Measurement of high-Q^2 charged current cross sections in e^+p deep inelastic scattering at HERA

Inaugural-Dissertation
zur
Erlangung der Doktorwürde
der
Mathematisch-Naturwissenschaftlichen Fakultät
der
Rheinischen Friedrich-Wilhelms-Universität
zu Bonn

vorgelegt von
Julian Rautenberg

Bonn 2004

Measurement of high-Q^2 charged current cross sections in e^+p deep inelastic scattering at HERA

von
Julian Rautenberg

Cross sections for charged current deep inelastic scattering have been measured in e^+p collisions at a center-of-mass energy of 318 GeV. The data collected with the ZEUS detector at HERA in the running periods 1999 and 2000 correspond to an integrated luminosity of 61 pb^{-1}. Single differential cross sections $d\sigma/dQ^2$, $d\sigma/dx$ and $d\sigma/dy$ have been measured for $Q^2 > 200\,\mathrm{GeV}^2$, as well as the double differential reduced cross section $d^2\tilde{\sigma}/dxdQ^2$ in the kinematic range $280\,\mathrm{GeV}^2 < Q^2 < 17\,000\,\mathrm{GeV}^2$ and $0.008 < x < 0.42$. The results are compared with the predictions of the Standard Model as well as with measurements of e^-p charged current deep inelastic scattering cross sections. The helicity structure is investigated in particular. The mass of the space-like W boson propagator has been determined from a fit to $d\sigma/dQ^2$.

Diese Arbeit wurde als Dissertation von der Mathematisch-Naturwissenschaftlichen Fakultät der Universität Bonn angenommen.

Referent:	Prof.Dr. E. Hilger
Korreferent:	Prof.Dr. M. Kobel
Tag der Promotion:	24.05.2004

Mein Vater,
der (Werte-) Horizont,

hinter dem tiefe Dunkelheit und grollende Gewitter drohen.
Doch mit Sicherheit erwarten wir den Aufgang der Sonne,
deren Strahlen stärker sind als jeder Stern,
bis eines Tages die Gewißheit einzieht,
daß sie nur noch in unseren Gedanken leuchtet.

Schnell dreht sich der Horizont in meinem Geiste,
mal oben, mal unten.
Doch der Glaube läßt uns erstarken, erkennen,
wo rechts — wo links?

Es ist seine Liebe die hinter dem Horizont leuchtet,
und wärmt mein bitterkaltes Herz.

Von Stolz erfüllt überglücklich
wärst Du an diesem Tag gewesen,
dem dieses Werk gewidmet.
Du standest vor mir und ich habe dein Strahlen gesehen,
hinter mir und Du hast durch mich geleuchtet.

Contents

List of Figures

List of Tables

Chapter 1

Introduction

With the operation of the HERA accelerator at DESY located in Hamburg, Germany, the opportunity to study two complementary parts of the so far well tested description of particle physics called the standard model (SM) is given. Colliding a lepton and a hadron makes it possible to test both the electro-weak theory (EW) as well as quantum chromodynamics (QCD) with the same experimental set-up. The propagators and the couplings are given by the EW sector of the SM, while QCD describes the evolving partonic structure of the proton.

Depending on the electro-magnetic charge of the exchanged boson the lepton-proton scattering process is called neutral current (NC) or charged current (CC), respectively. In deep inelastic scattering (DIS) the incoming proton breaks into a complex hadronic system in the final state. Not distinguishing the hadronic final state into special, exclusive, types renders the measurement as being inclusive. The topic presented in this thesis is only one out of the rich physics program of HERA, the measurement of the inclusive CC DIS positron-proton cross section.

CC DIS has been measured before in fixed-target neutrino-nucleus scattering experiments [1, 2, 3, 4] at relatively low center-of-mass energies. With the operation of HERA a new kinematic region has been explored. For the preceeding running periods until 1999 both collider experiments, H1 [5, 6, 7, 8, 9] and ZEUS [10, 11, 12, 13], have published CC measurements with lower statistics, and either at lower center-of-mass energy or when HERA operated electrons instead of positrons. The work presented here essentially contributed to the publication [14] of the ZEUS measurement for $61\,\mathrm{pb}^{-1}$ of data collected in the running periods 1999 and 2000, where HERA collided 27.5 GeV positrons on 920 GeV protons, yielding a center-of-mass energy ($\sqrt{s}$) of 318 GeV. The corresponding measurement by H1 for this data period has also been published [15]. In addition, CC has been studied in several theses of ZEUS-BONN group members before, specializing on implementing an extra detector component [16], on an earlier data set [17] and leading to preliminary ZEUS-results [18].

The measurements presented in this thesis are the single differential CC DIS e^+p cross sections $d\sigma/dQ^2$, $d\sigma/dx$ and $d\sigma/dy$ for $Q^2 > 200\,\mathrm{GeV}^2$, as well as the double differential reduced cross section $d^2\tilde{\sigma}/dxdQ^2$ in the kinematic range $280\,\mathrm{GeV}^2 < Q^2 < 17\,000\,\mathrm{GeV}^2$

and $0.008 < x < 0.42$. The measurements are based on the ZEUS data collected in the 1999 and 2000 e^+p HERA running periods corresponding to an integrated luminosity of $61\,\mathrm{pb}^{-1}$. The results are compared to the SM prediction. In particular, the helicity structure of the SM is investigated. From the cross section $d\sigma/dQ^2$ the mass of the space-like W boson propagator is inferred.

In the second chapter the experimental setup is introduced with special emphasis on the detector components relevant for this work, including calorimetry, luminosity detector as well as the trigger and data acquisition system.

The third chapter will present the theoretical background for the measurement, the kinematics of a DIS event, and the SM descriptions of the charged and neutral current reactions. Also described are the parton density functions, which are a crucial input to the standard model.

The detailed chapter four will elaborate on the data analysis preceeding the cross section measurement. The Monte-Carlo simulation of the relevant physics processes and the detector response is an essential tool for the analysis. The reconstruction of the raw data requires several corrections and algorithms to extract the kinematic variables as well as those necessary for the selection of the signal event-sample in the following section. This has to be evaluated to provide a signal sample with as little background contamination as possible still preserving the significance of the signal. This goal is already faced by the trigger logic. Sophisticated algorithms are developed on the reconstructed offline quantities. The final signal sample will be presented. The techniques for the extraction of the cross sections from the signal sample include the proper definition of the bins, the validation of acceptance, purity and efficiency, the background subtraction, the theoretical correction for radiative effects as well as ultimately the unfolding procedure. The section closes with a detailed study of the measurement uncertainty due to systematic effects.

The results of this work will be presented in chapter five. The single differential cross sections and the double differential reduced cross sections will be stated. The discussion of these results includes the "helicity" representation and the determination of the M_W mass.

I will summarize the dissertation in chapter six.

In addition to the topic presented in this work I had several responsibilities as a PhD-student in the ZEUS group in Bonn and as a member of the ZEUS Collaboration. Most of the time I have been responsible for the maintenance of the PC-cluster with demilitarized zone and web-server. A client-server architecture for the Linux PC-cluster has been developed, including e.g. automatic client installation. I added further tools and optimizations to the cluster. I maintained the web-server and introduced new PHP and MySQL based services. For the benefit of ZEUS I adapted a java-based event-display tool to the ZEUS software environment as a proto-type for a new event visualization tool. For the final event visualization tool ZEVis [19] based on root I have been responsible for the online event chain from the raw event provided by the data acquisition via reconstruction to the event in root-format as accessed by the client using http.

Chapter 2

The ZEUS detector at the HERA collider

To perform an experiment at such exceptionally high energies requires a huge effort of a large collaboration of physicists. On the one hand, the machine group provides the beams which produce the luminosity and, on the other hand, the ZEUS Collaboration has built, maintains and runs the ZEUS detector to collect the data. While the first subsection introduces the work of the former group, the main part of this chapter explains the detector with emphasis on those parts which are relevant to this analysis.

2.1 The HERA collider at DESY

The Hadron-Elektron-Ringanlage (HERA) is situated at the research center Deutsches Elektronen Synchrotron (DESY) in Hamburg, Germany. It is the only running facility colliding a lepton and a proton beam, thus offering unique possibilities of probing the dynamic structure of the proton with the point-like electron[1].

This field of timely research is at the heart of this analysis. To give an example for the universality of this experimental set-up, in a different kinematic region the partonic structure of the photon emitted by the lepton is probed by the parton within the proton.

A map of the HERA collider and its pre-accelerator chain is given in Fig. 2.1. The leptons enter the former Positron-Elektron-Tandem-Ringanlage (PETRA) via LINAC 2, the positron intensity accumulator PIA and the synchrotron DESY II. The protons enter PETRA via LINAC 3 and DESY III. Both DESY II/III are installed in the tunnel of the former DESY I synchrotron. Coming from separated beam lines of PETRA both beams enter HERA. Here the electrons are accelerated from 12 GeV to 27.5 GeV and the protons from 40 GeV to — since the year 1998 — 920 GeV, both in separated accelerators in the HERA tunnel. The beams are structured over the total circumference of 6.3 km into 220

[1] If not explicitly noted the term electron is used denoting both particle as well as anti-particle, i.e. electron and positron, as HERA is able to operate both.

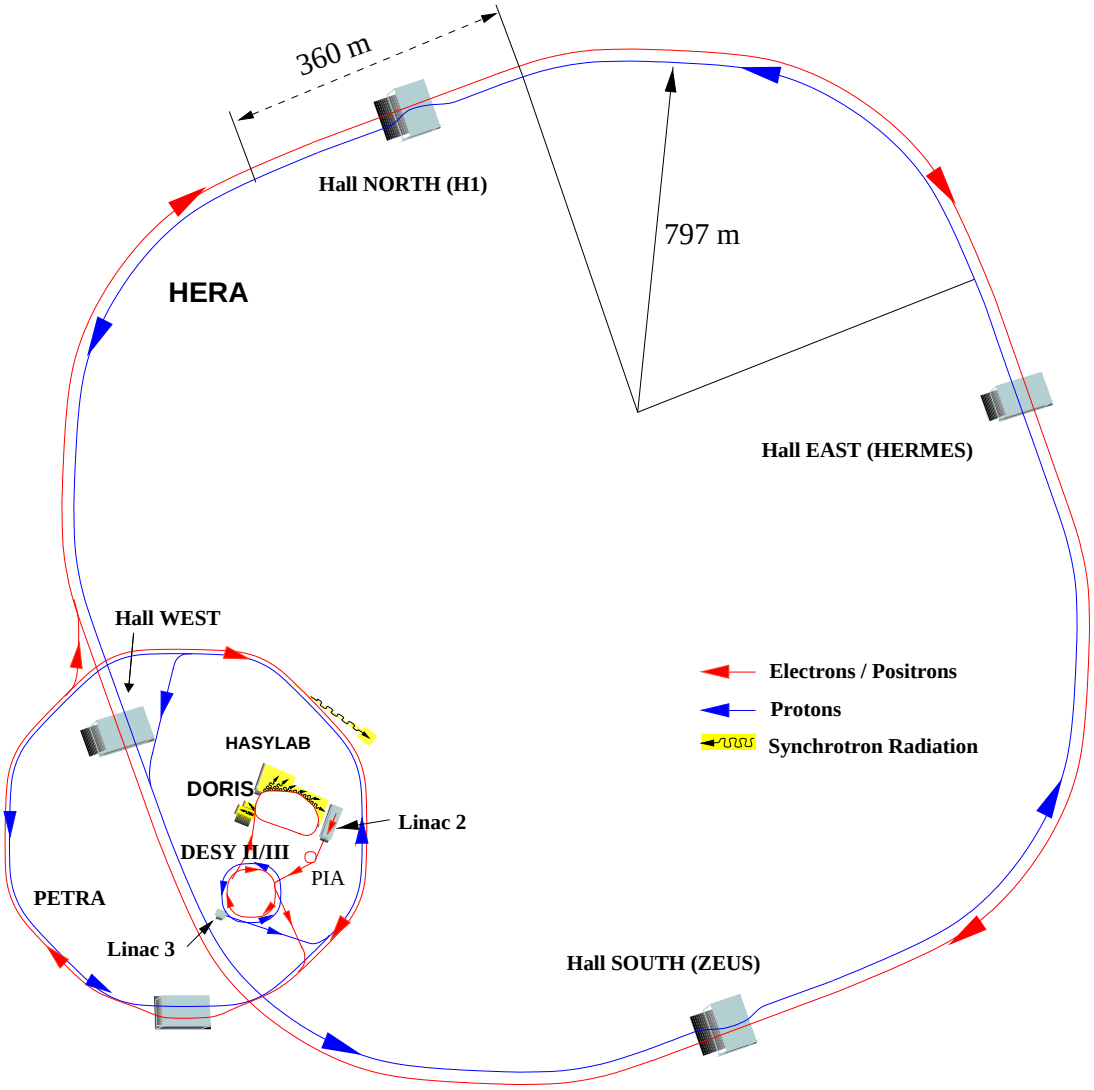

Figure 2.1: Design of the accelerator chain for HERA.

buckets yielding a time distance between two crossings of 96 ns. A bunch is a bucket filled with approximately 10^{10} particles. Not all buckets are filled, which means the number of bunches for each beam is less than 220. The empty bunches provide crossing times when only one type of bunch passes the nominal interaction point (IP). These unpaired "crossings" are valuable for systematic studies, as will be described in Section 4.3.9.

The large mass difference of proton and electron leads to different designs of the two HERA accelerators. The radiative energy-loss ΔE per revolution with radius R of a simply charged particle with mass m_0 and energy E is:

$$\Delta E \approx \frac{E^4}{m_0^4\, R}. \tag{2.1}$$

Therefore the 13 MW power provided by the radio-frequency resonators for the lepton beam are the limiting factor for the maximum energy of the light leptons. The mag-

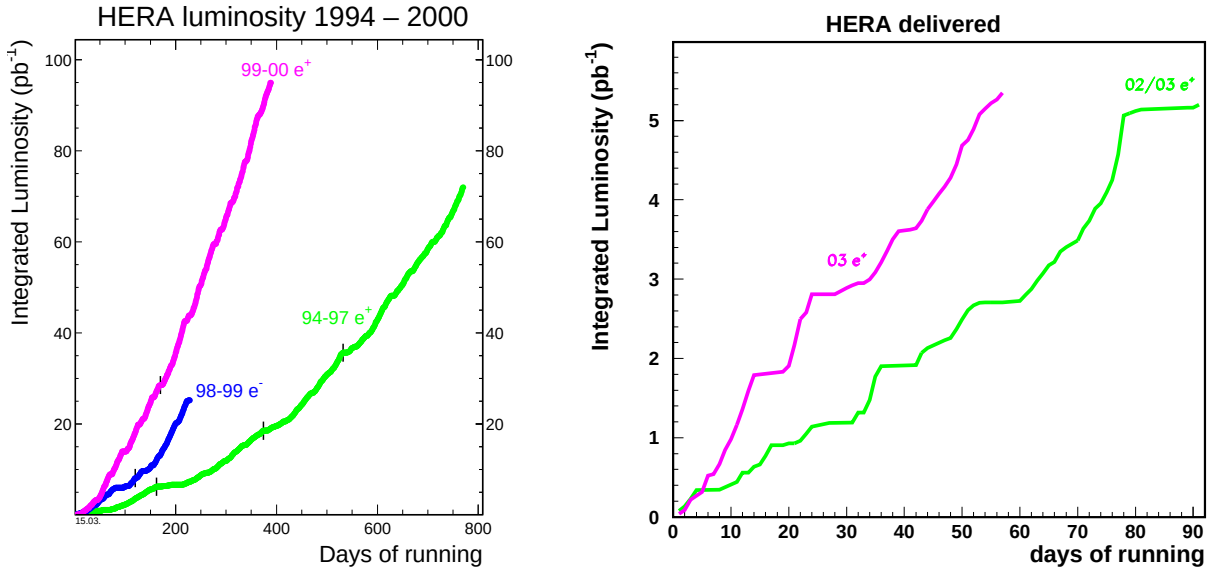

Figure 2.2: Integrated luminosity as delivered by the HERA machine versus day of operation. On the left for the three operation conditions of HERA I, positrons at lower center-of-mass energy until 1997 and electrons and protons thereafter. On the right the slow progress at startup of HERA II is shown.

netic field of 5T produced by the superconducting dipole magnets needed to bend the heavy protons on the circumference of radius 797 m limits the proton energy. The beams provided are collided head-on at two interaction regions, where the detectors H1, in hall north, and ZEUS, in hall south, are situated. In hall east the fixed-target HERMES experiment uses only the electron beam. Here the transverse polarization of the beam is flipped by rotators before and after the HERMES interaction region. By scattering longitudinally polarized electrons on a target of polarized protons the spin structure of the proton is investigated.

For the 1998 running period HERA operation was switched to electrons while having been operated mainly with positrons before. In addition, the proton beam energy was raised from 820 GeV to 920 GeV, corresponding to an increase in the center-of-mass energy from 300 GeV to 318 GeV. In the middle of the 1999 running period the operation was switched back to positrons. Until the end of the first phase of HERA running in August 2000 the integrated luminosity has improved steadily as can be seen in Fig. 2.2.

This analysis is based on data of the running period from the middle of 1999 when HERA switched to positron operation until August 2000. Since then major modifications of the machine took place for HERA phase II. For an increase of the specific luminosity by stronger foci of the beams quadrupole magnets were positioned closer to the interaction point and entered the detector region. In addition, spin rotators as used already at HERMES were installed also at the interaction regions of colliding beams providing longitudinally polarized electron beams. The startup has been delayed due to problems with synchrotron radiation in the detector region produced by the closer positioned magnetic fields as well as due to vacuum problems in the interaction region caused by the smaller

intersection of the beam pipe and no access for vacuum pumps near the IP due to the closely placed quadrupole magnets. Modifications during a recent shutdown in 2003 have reduced the problems due to synchrotron radiation.

2.2 The ZEUS Detector

To cover the vast research field accessible with the HERA kinematics a complex system of particle detectors is necessary. The ZEUS collaboration of approximately 450 scientists from 51 institutes spread over 13 countries built the detector system called ZEUS and has the responsibility of maintaining and operating it. A detailed description of the multi-purpose ZEUS detector can be found in [20]. The design of the ZEUS detector is given in Fig. 2.3. Below the most relevant components of the detector are described.

2.2.1 The central tracking detector

Charged particles are tracked in the cylindrical central tracking detector (CTD), which operates in a magnetic field of 1.43 T provided by the surrounding superconducting coil. The CTD consists of 576 cells in 72 cylindrical drift chamber layers, organized in 9 superlayers. In total the CTD has 4608 signal wires and 19584 potential wires, making it 8 and 34 for one cell. The wires are arranged as shown in Fig. 2.4. In five superlayers the wires are parallel to the beam-line, while in four the wires are inclined by a stereo angle. These stereo layers allow for the reconstruction of the z-position[2] of a hit with an accuracy of around 1 mm. In addition, z can be reconstructed by timing with a much worse resolution of 4.5 cm. The latter information is fast enough to be used for triggering. The CTD volume measures 18.2 cm to 79.4 cm radially and -100 cm to 105 cm in z-direction, covering the polar-angle region $15° < \theta < 164°$. The transverse-momentum resolution for full-length tracks is $\sigma(p_T)/p_T = 0.0058p_T \oplus 0.0065 \oplus 0.0014/p_T$ [3], with p_T in GeV.

2.2.2 The calorimeter

The high-resolution calorimeter (CAL) [21] is built as a sandwich of scintillator and depleted uranium plates. The design of the plate thicknesses yields the compensating character of the CAL, i.e. responding equally to hadronic and electromagnetic energy deposits. The CAL consists of three parts: the forward (FCAL), the barrel (BCAL) and the rear (RCAL) calorimeters. Each part is subdivided transversely into towers and longitudinally into one electromagnetic section (EMC) and either one (in RCAL) or two (in BCAL and

[2]The ZEUS coordinate system is a right-handed Cartesian system, with the Z axis pointing in the proton beam direction, referred to as the "forward direction", and the X axis pointing left towards the center of HERA. The coordinate origin is at the nominal interaction point. The pseudorapidity is defined as $\eta = -\ln\left(\tan\frac{\theta}{2}\right)$, where the polar angle, θ, is measured with respect to the proton beam direction.

[3]$\oplus$ denotes the quadratic sum

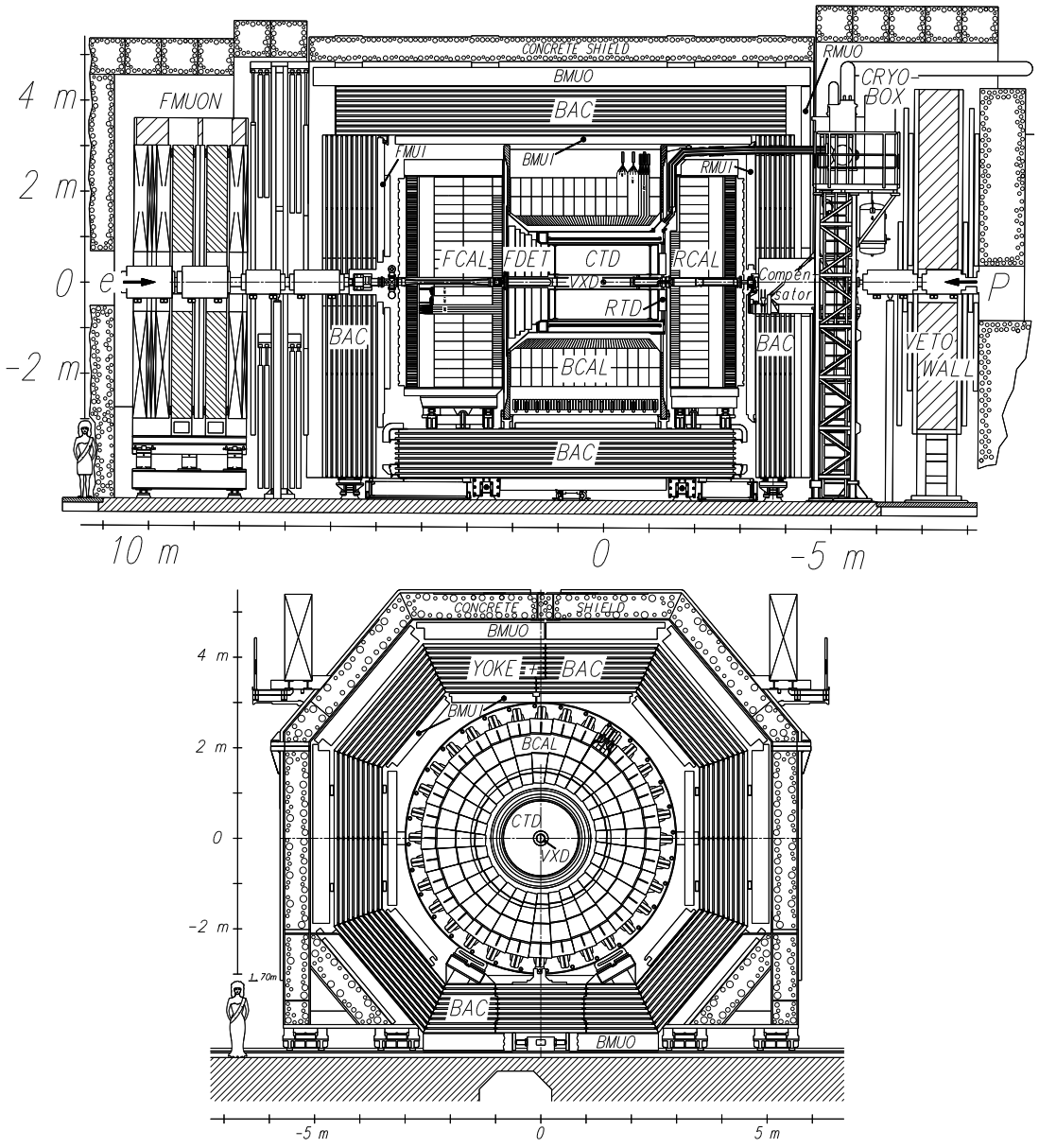

Figure 2.3: The design of the ZEUS detector in z-y (top) and x-y (bottom) cut.

FCAL) hadronic sections (HAC)[4]. The cylindrical BCAL is segmented in r-φ and the planar F/RCAL in x-y. The towers are grouped mechanically into modules, vertical ones for F/RCAL and wedges for BCAL. The smallest subdivision of the calorimeter is called a cell. On each side in x (φ) in F/RCAL (BCAL) of the cell the light is transmitted by a wavelength shifter to a photomultiplier (PM) located at the end of the tower. As an example the design of a single FCAL module is given in Fig. 2.5. The CAL energy resolutions, as measured under test-beam conditions, are $\sigma(E)/E = 0.18/\sqrt{E} \oplus 1\%$ for electrons and $\sigma(E)/E = 0.35/\sqrt{E} \oplus 2\%$ for hadrons (E in GeV).

[4]If referenced individually the hadronic sections of the calorimeter are denoted by BHAC1 and BHAC2 in BCAL and FHAC1 and FHAC2 in FCAL.

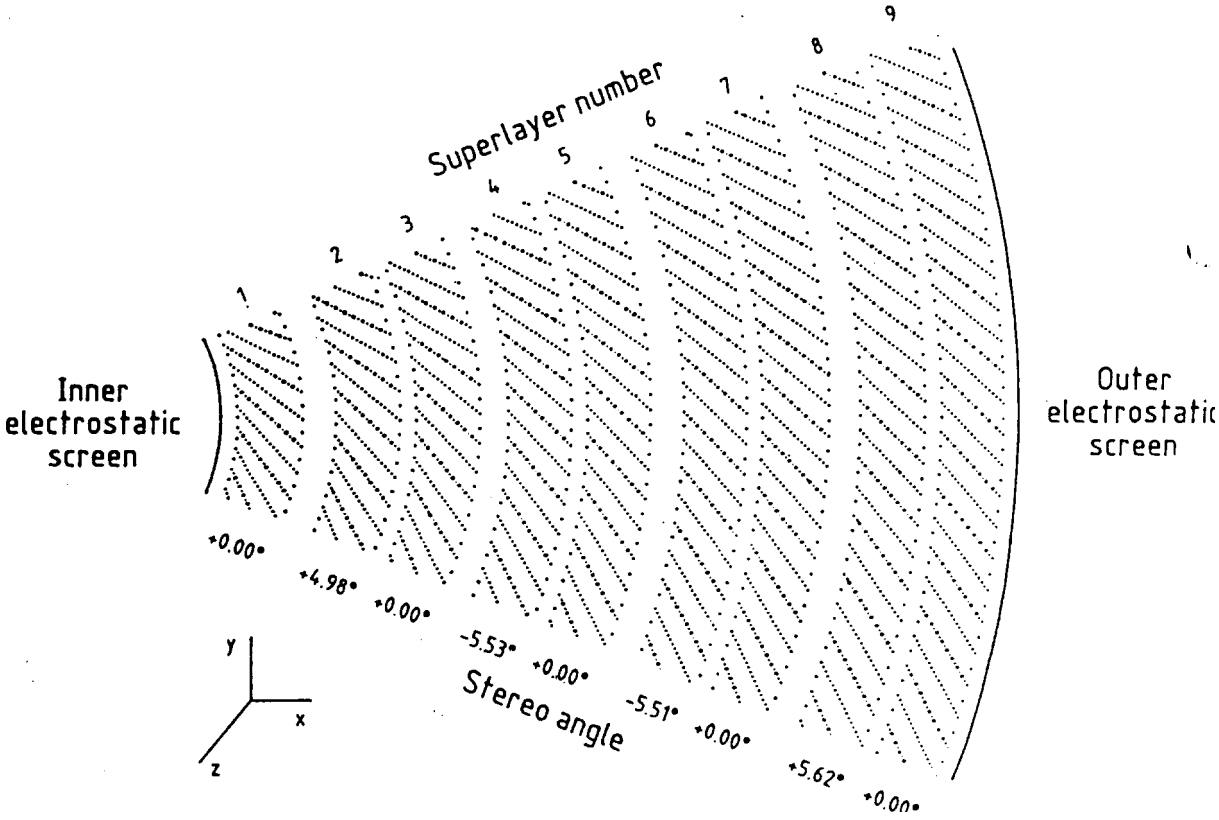

Figure 2.4: The layout in x-y of signal and potential wires for an octant of the CTD.

2.2.3 The backing calorimeter

The iron that returns the magnetic flux of the solenoid providing the magnetic field for the CTD is instrumented with layers of aluminum proportional tubes. This detector component is called Backing Calorimeter (BAC). Its purpose is to cover large hadronic showers which are not fully contained in the CAL and leak into the BAC, and to separate muons from hadronic showers.

2.2.4 The luminosity detector system

The measurement of the luminosity is performed at ZEUS independent of the beam geometry by measuring the QED-bremsstrahlungs process (Bethe-Heitler-process) $ep \rightarrow ep\gamma$. The uncertainty of its cross section calculation is 5‰ [22]. For the measurement in ZEUS two lead-scintillator calorimeters are used. One, Lumi-γ, is positioned at $z = -107\,\mathrm{m}$ and detects photons emitted at the IP within a cone of 0.5 mrad. The other, Lumi-e, at $z = -35\,\mathrm{m}$ detects electrons in the energy range of 7 GeV to 22 GeV which are deflected by the beam optics to the ring-inward side of the beam line. The uncertainty for the luminosity of the running period exploited in this analysis amount to 2.25% and has been achieved using only Lumi-γ [23].

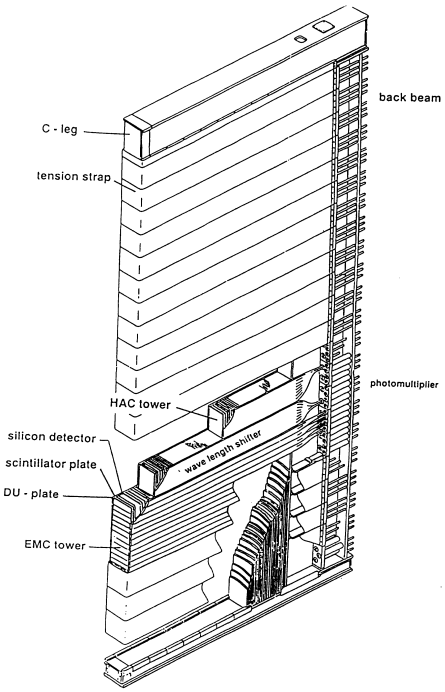

Figure 2.5: The design of an FCAL module as described in the text.

2.2.5 Trigger and data acquisition

With crossings every 96 ns and in total 250 000 readout channels the theoretical maximum for the data volume from the detector is 10 TB/s, though mostly due to background or uninteresting reactions. The connection from the ZEUS control room to the DESY data center, where the data are stored for offline processing, is capable of less than 1MB/s. As a consequence the event rate has to be reduced by a factor of 10^6. For this enormous task a three-level trigger system has been designed and installed. It not only has to identify non-collision background to be rejected, but also has to select the interesting physics events. With over the years increasing instantaneous luminosity even physics events have to be prescaled or limited to the more interesting kinematic regions. The data flow in the trigger system, with scales of data volume and of rates at each level, is displayed in Fig. 2.6.

2.2.5.1 First level trigger (FLT)

To get a decision every 96 ns is even too hard a task for analog electronics. Therefore the raw data are stored for 5 µs in a pipeline. 25 cycles are given to the individual detector components to reach a decision locally. The next 20 cycles are used by the global FLT (GFLT) to collect the decisions of the single components and come to a final decision. Until this step the detector is dead-time free. The slow transport of the readout values to the next level leads to a dead time which is, however, less than 2% at a GFLT rate of 1 kHz.

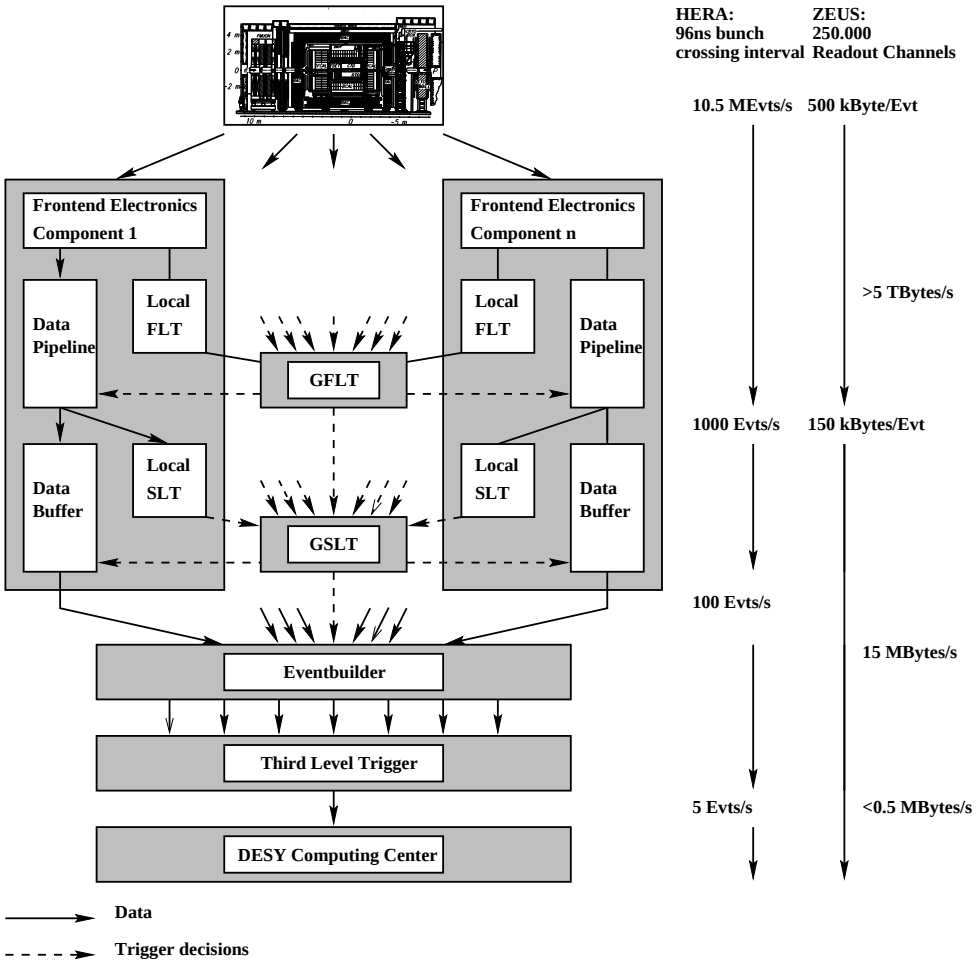

Figure 2.6: The data flow for the ZEUS data acquisition. On the right the scale of frequency and data volume is given for each level.

2.2.5.2 Second level trigger (SLT)

On the second level an asynchronous pipeline allows for complex algorithms to be executed, e.g. calculating $E - P_z$. The decisions of the individual detector components are collected by the global SLT (GSLT). It assigns an event number that allows the event builder to identify the pieces of data collected from the components.

2.2.5.3 Third level trigger (TLT)

The TLT has access to the global event data as assembled by the event builder, in contrast to the previous levels which process data only component-wise. The TLT is implemented in a computer farm. This allows complex computer code to be executed similar to the reconstruction code on the offline events. The quantities available differ only slightly from the final reconstructed values. The main difference originates from the calibration constants which are not available at run-time as they are extracted on run basis.

Chapter 3

Charged current in deep inelastic scattering

At HERA we investigate the various reactions of electrons scattering off protons. The most general feature of the final state is a lepton that conserves lepton number at the lepton vertex and a system of hadrons. The hadronic final state is not distinguished into special, exclusive, types of the hadronic system, rendering the measurement as being inclusive. The generic Feynman graph is depicted in Fig. 3.

The physics of the leptonic vertex is very well described by the EW theory. The incoming lepton can interact with the proton exchanging either an electro-magnetically neutral EW boson, γ or Z, and stay the same, or a charged EW boson, $W^{\pm}$, and become the neutral lepton of the same family, an electron neutrino ν_e. Corresponding to the electromagnetic charge of the boson the interaction is classified as charged current (CC) or neutral current (NC). For easier comparison the cross section is usually stated in leading order of the electro-magnetic coupling α_{EM}. Since this is not what we measure in the laboratory when counting events, the final result is obtained by unfolding using higher order QED calculations, which are tested to a very precise level [24]. This is denoted by calling the cross section as Born-level. The Feynman graphs for the correction of the CC DIS cross section corresponding to proper first order EW radiative effects are displayed in Fig. 3.2, and those to EW single loops in Fig. 3.3.

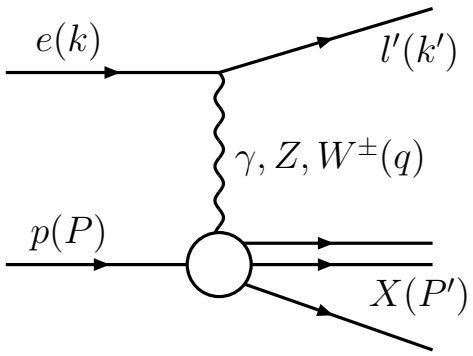

Figure 3.1: General Feynman graph for the scattering of electrons e on protons p by the exchange of a boson γ, Z or $W^{\pm}$ to the final state lepton l' and inclusive hadronic final state X

The proton is a complex strongly bound system of partons. One way to approach the description of the process of a lepton interacting with the proton as a hadron is from the macroscopic side. This way one obtains a set of observables, the structure functions, which, however, are difficult to interprete. By considering the partons inside the proton

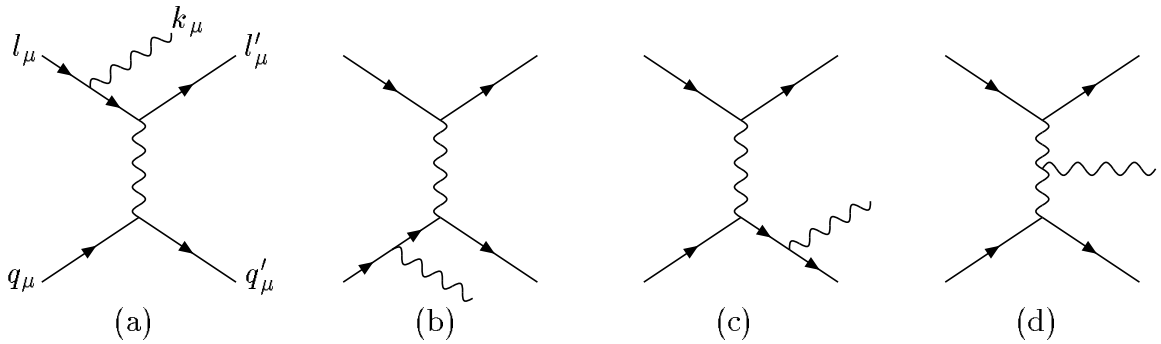

Figure 3.2: Feynman graphs for EW radiative corrections of incoming lepton (a), incoming (b) and outgoing (c) quark and of the exchanged boson (d).

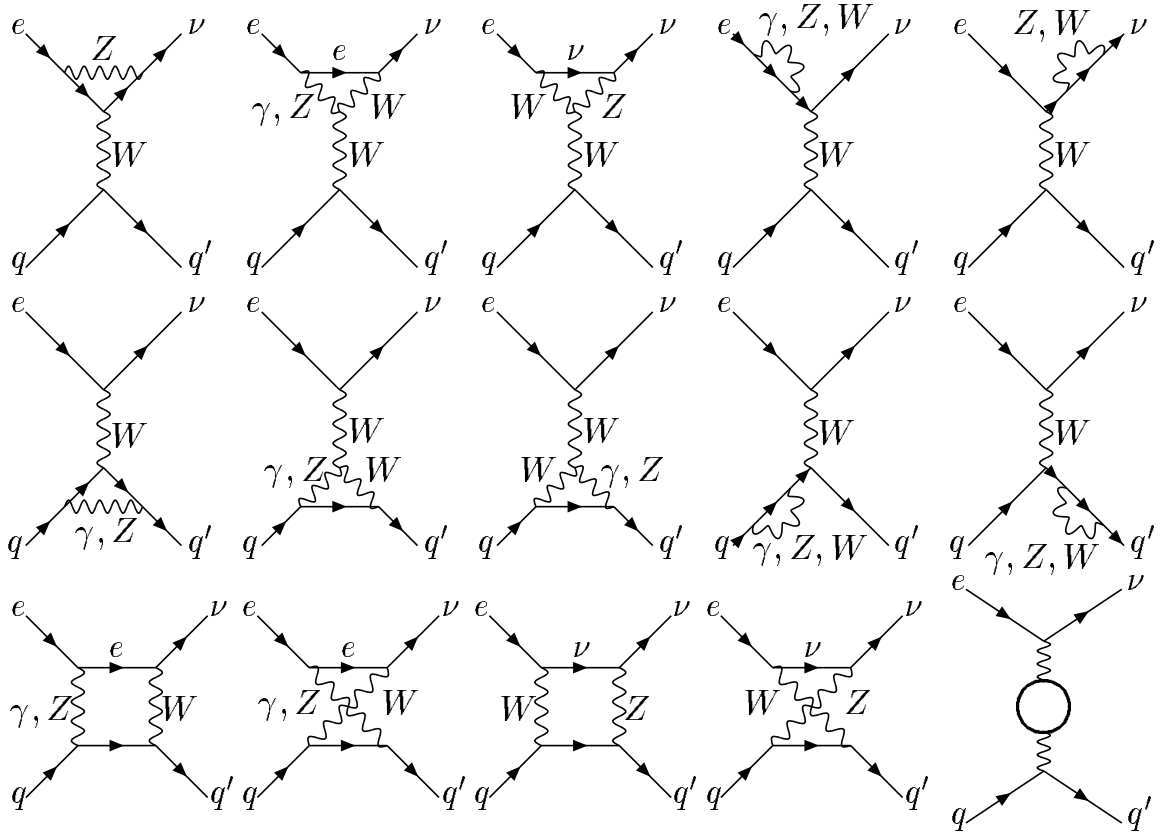

Figure 3.3: Feynman graphs for single loop EW corrections.

we have the possibility to interprete the structure functions. We make the transition from an ep scattering process to an eq scattering process. Then we can define parton density functions (PDF) as probabilities of finding a particular parton with the given kinematic variables x, Q^2 inside the proton. The PDFs are therefore the key relating parton model and macroscopic measurement. The underlying color theory of the nucleon, which is to some degree calculable and of predictive power, is Quantumchromodynamics (QCD). In leading order (LO) QCD, that refers to the order of the perturbative expansion in powers of the strong coupling constant, we have the picture of constituents in the proton. In the naive parton model the proton is built out of three of them, called quarks, which are bound by the exchange of gluons. Since the gluons themselves carry QCD color charge they can interact strongly without the necessity of a quark being present. QCD does not only describe the static quark content of the proton but also the dynamic structure evolving from the interaction of the partons within the proton. Therefore the picture of 3 constituents is only valid under a very restricted set of conditional parameters. The quarks are only free, e.g. not feeling the strong force that binds them together, if the system is boosted to the so called infinite momentum frame. Here the ratio of longitudinal to transverse momentum is so large, that we can expect the partons to be 'free' of mutual interactions in the transverse direction. If we take an ever closer look into the proton with increasing spatial resolution we will see more and more partons that temporarily emerge from the field of the strong interaction. Then we are far from seeing just the three constituents. The higher orders in the coupling of the strong force, α_S, are not at all so easy to unfold and are absorbed in the set of structure functions F_i which parameterize our lack of knowledge of the detailed behavior of strongly interacting partons found inside the proton.

3.1 Kinematic of a DIS event

The kinematic of a DIS event is defined by the four-momenta of the incoming and outgoing lepton, k, k', the four-momentum of the incoming proton, P, and that of the outgoing hadronic final state, P'. The four-momentum of the boson exchanged between the leptonic and the hadronic side is then defined as

$$q = k - k' = P' - P. \tag{3.1}$$

The squared center-of-mass (CMS) energy of the lepton-hadron system, s, and that of the boson-hadron subsystem, W^2, are given by

$$s = (k + P)^2, \tag{3.2}$$
$$W^2 = (q + P)^2 = P'^2. \tag{3.3}$$

To describe DIS processes kinematically the following Lorentz invariants are in use:

$$Q^2 = -q^2 = (k-k')^2 = (P'-P)^2 \tag{3.4}$$

$$x = \frac{Q^2}{2P\cdot q} \tag{3.5}$$

$$y = \frac{P\cdot q}{P\cdot k} \tag{3.6}$$

$$\nu = \frac{P\cdot q}{M_p} = \frac{Q^2}{2\,x\,M_p}. \tag{3.7}$$

The (positive) virtuality of the exchanged boson, Q^2, can be interpreted as the 'resolving power' of the interaction with a spatial resolution corresponding to

$$\Delta d \sim \frac{\hbar c}{\sqrt{Q^2}} = \frac{0.197}{\sqrt{Q^2}}\,\mathrm{GeV}\cdot\,\mathrm{fm}. \tag{3.8}$$

At HERA this yields a resolution of up to $10^{-18}\,\mathrm{m}$, which is why HERA, or more precisely the detector ZEUS, is called a super-microscope, looking deeply into the structure of the proton. Though x, y and ν are Lorentz invariants, their interpretation is intuitive only in special frames. In the infinite momentum frame x is the fraction of the proton momentum P carried by the struck quark. In the proton's rest frame we can identify ν (and y) to be the energy (and the energy fraction) transfered from the lepton to the hadronic vertex. Since these quantities are related by

$$Q^2 = s\,x\,y \tag{3.9}$$

for fixed s like at HERA only two variables of Q^2, x and y are necessary for a complete kinematic description of an inclusive event. Motivated by the PDFs Q^2, x are chosen in the following.

3.2 CC cross section

The differential ep cross section may be written in terms of the reaction amplitude A, which can be factorized in a product of the leptonic tensor $L_{\mu\nu}$ and the hadronic tensor $W^{\mu\nu}$, here for the CC case:

$$\frac{d^2\sigma^{\mathrm{cc}}}{d\Omega dE'} = \frac{G_F^2}{4\pi^2}\frac{M_W^2}{M_W^2+Q^2}\frac{E'}{E}|A^{\mathrm{cc}}|^2 \equiv \frac{\alpha^2}{Q^2}\frac{E'}{E}L^{\nu}_{\mu\nu}W^{\mu\nu}. \tag{3.10}$$

The leptonic tensor is calculable in EW theory and is:

$$L^{\nu}_{\mu\nu} = \frac{1}{2}\sum_{s'}\overline{u}(k's')\gamma_\mu(1-\gamma_5)u(ks)\overline{u}(ks)\gamma_\nu(1-\gamma_5)u(k's') \tag{3.11}$$

$$= k_\mu k'_\nu + k'_\mu k\nu - g_{\mu\nu}k\cdot k' \pm i\epsilon_{\mu\nu\lambda\sigma}k^\lambda k'^\sigma. \tag{3.12}$$

The hadronic tensor is given in terms of the currents:

$$W_{\mu\nu} = \frac{1}{2}\sum_n < p|J_\mu^+|X_n >< X_n|J_\nu|p > (2\pi)^3\delta^4(P+q-P'). \tag{3.13}$$

We do not know very much about the hadronic tensor so that we have to parameterize our lack of knowledge in the most general form. At the hadronic vertex we have two independent four-momenta, that of the incoming proton, P, and that of the exchanged boson, q. The most general form of combining the independent four momenta P, q is [25]:

$$W_{\mu\nu} = -g_{\mu\nu}W_1 + \frac{P_\mu P_\nu}{M^2}W_2 - \frac{i\epsilon_{\mu\nu\alpha\beta}P^\alpha P^\beta}{2M^2}W_3 + \frac{q_\mu q_\nu}{M^2}W_4 + \frac{P_\mu q_\nu + q_\mu P_\nu}{M^2}W_5 + i\frac{P_\mu q_\nu - P_\nu q_\mu}{M^2}W_6. \tag{3.14}$$

Here the scalars W_i are structure functions which depend on two kinematic variables. The terms containing W_4, W_5 and W_6 are suppressed by the small lepton mass for they lead in combination with the lepton tensor to terms like:

$$q^\mu L_{\mu\nu} = q_\mu L^{\mu\nu} \cong 0. \tag{3.15}$$

This is the only simplification we can achieve for vector-axial $(V-A)$ currents.

In DIS the rescaled structure functions F_i are in use:

$$MW_1(\nu, Q^2) = F_1(x, Q^2), \tag{3.16}$$
$$\nu W_{2,3}(\nu, Q^2) = F_{2,3}(x, Q^2). \tag{3.17}$$

The $F_i(x, Q^2)$ were found to scale [26, 27], i.e. are independent of Q^2 for a certain x range. The complete double differential cross section is then:

$$\frac{d^2\sigma^{\mathrm{CC}}}{dQ^2dx} = \frac{G_F^2}{2\pi x}\left(\frac{M_W^2}{Q^2+M_W^2}\right)^2\left[y^2xF_1^{\mathrm{CC}} + (1-y)F_2^{\mathrm{CC}} \mp (y-\frac{y^2}{2})xF_3^{\mathrm{CC}}\right]. \tag{3.18}$$

With the definitions:

$$F_L = F_2 - 2xF_1 \tag{3.19}$$
$$Y_\pm = 1 \pm (1-y)^2 \tag{3.20}$$

the cross section is:

$$\frac{d^2\sigma^{\mathrm{CC}}}{dQ^2dx} = \frac{G_F^2}{4\pi x}\left(\frac{M_W^2}{Q^2+M_W^2}\right)^2\left[Y_+F_2^{\mathrm{CC}} \mp Y_-xF_3^{\mathrm{CC}} - y^2F_L^{\mathrm{CC}}\right]. \tag{3.21}$$

The motivation for (3.19) is that in the naive parton model $F_L = 0$, also known as Callan-Gross relation [28]. At higher orders its contribution to the cross section is small, and in addition, because of the coefficient of y^2, negligible everywhere but at high y. Also the parity-violating structure function F_3 is small for $Q^2 \ll M_Z^2$. Defining the reduced cross section:

$$\frac{d^2\tilde{\sigma}^{\mathrm{CC}}}{dxdQ^2} = \frac{2\pi x}{G_F^2}\left(\frac{Q^2+M_W^2}{M_W^2}\right)^2\frac{d^2\sigma^{\mathrm{CC}}}{dxdQ^2} \tag{3.22}$$

removes the kinematic coefficient.

Since electromagnetic charge is conserved, not all of the quarks can take part in the interaction via $W^{\pm}$ exchange as the $W^{\pm}$ can only couple to quarks with the proper sign of charge. For e^+ (e^-) it can couple only to negatively (positively) charged quarks. Therefore also the $F_i^{\mathrm{CC},e^{\pm}p}$ depend on the charge of the initial lepton. A singlet term comparable to F_2^{NC} is then obtained by the sum $F_2^{\mathrm{CC},e^+p} + F_2^{\mathrm{CC},e^-p}$. Experimentally this has been measured in DIS of an (anti-) neutrino beam on nucleon targets [29].

3.3 CC cross section on the parton level

On the parton level we can investigate the scattering of an electron on a quark q. The Born-level cross section can then be written in terms of diagrams as:

$$\frac{d\sigma^{e^{\pm}q\to\overset{(-)}{\nu}q'}}{dQ^2} \propto \sum_{q'} |V_{qq'}|^2 \left| \begin{array}{c} e \\ \\ q \end{array} \begin{array}{c} \overset{v_q^{\mathrm{CC}},a_q^{\mathrm{CC}}}{\longrightarrow} \\ W^{\pm} \\ \underset{v_e^{\mathrm{CC}},a_e^{\mathrm{CC}}}{\longleftarrow} \end{array} \begin{array}{c} \overset{(-)}{\nu} \\ \\ q' \end{array} \right|^2 . \tag{3.23}$$

This is a purely weak exchange diagram. In this case the couplings are not quark-flavor dependent and are not included in the F_i but moved to the coefficient in (3.21). In the transition from eq to ep scattering we have to sum over all parton densities. Because of the charge of the W boson we already saw that for e^+ (e^-) only negatively (positively) charged quarks contribute. In addition, because of the center-of-mass energy available at HERA and the small off-diagonal elements of the CKM matrix the third family quarks can be ignored here [30]. Therefore the F_i contain only the following up- and down-type (anti-) quark densities:

$$F_2^{e^+p}(x,Q^2) = x \sum_{q=1,2} \left[d_q(x,Q^2) + \overline{u}_q(x,Q^2) \right] \tag{3.24}$$

$$xF_3^{e^+p}(x,Q^2) = x \sum_{q=1,2} \left[d_q(x,Q^2) - \overline{u}_q(x,Q^2) \right] . \tag{3.25}$$

Inserting this in (3.22), with $F_L = 0$ at LO, yields:

$$\tilde{\sigma}^{e^+p} = x\left[(\bar{u}+\bar{c}) + (1-y)^2(d+s) \right] \tag{3.26}$$

$$\tilde{\sigma}^{e^-p} = x\left[(u+c) + (1-y)^2(\bar{d}+\bar{s}) \right] . \tag{3.27}$$

Because of the helicity structure of the weak interaction represented in the term $(1-y)^2$, the down-type (anti-) quarks are suppressed for increasing y in either case. This can be understood by looking at the sum of spins in the center-of-mass system as sketched in Fig. 3.4. Since the positron has to be right-handed and the (anti-) quark has to be (right-) left-handed to couple to the W-Boson, the sum of the spins in the center-of-mass frame is 0 for positron anti-quark scattering, but is 1 for positron quark scattering. While the first case does not restrict the scattering angle and leads to an isotropic distribution,

Figure 3.4: Sketch of the spin sum in center-of-mass system for $e^+\bar{q}_u$ and $e^+\bar{q}_d$.

the distribution from the latter one peaks in the forward direction. The suppression in $\cos\theta_{\rm CMS}$ can be related to y:

$$(1-y)^2 = \frac{(1+\cos\theta_{\rm CMS})^2}{4}. \tag{3.28}$$

3.4 NC cross section

In analogy to CC the differential cross section for NC may be written in terms of the amplitude A or as the tensor product:

$$\frac{d^2\sigma^{\rm NC}}{d\Omega dE'} = \frac{\alpha^2}{Q^2}\frac{E'}{E}|A^{\rm NC}|^2 \equiv \frac{\alpha^2}{Q^2}\frac{E'}{E}L^e_{\mu\nu}W^{\mu\nu}. \tag{3.29}$$

The leptonic tensor for NC is:

$$\begin{aligned} L^e_{\mu\nu} &= \frac{1}{2}\sum_{spin}\overline{u}(k')\gamma_\mu u(k)\overline{u}(k)\gamma_\nu u(k') && (3.30)\\ &= k_\mu k'_\nu + k'_\mu k\nu - g_{\mu\nu}(k\cdot k' - m^2). && (3.31)\end{aligned}$$

For the hadron tensor we start with the general ansatz of (3.14). As before we can ignore the lepton-mass suppressed terms with W_4, W_5 and W_6. In addition, for low $Q^2 \ll M_Z^2$ we approximately have γ-only exchange, i.e. pure vector current. Then the parity violating term W_3 cannot contribute. The asymmetric term of W_6 cannot contribute either, since the leptonic tensor is symmetric. Therefore we have

$$W_3^{\rm em} = 0 \qquad \text{and} \qquad W_6^{\rm em} = 0. \tag{3.32}$$

In addition, current conservation leads to $q^\mu W_{\mu\nu} = q_\mu W^{\mu\nu} = 0$ [28] and therefore to the following relations:

$$W_4^{\rm em} = \frac{P\cdot q}{q^2}W_2^{\rm em} + \frac{M^2}{q^2}W_1^{\rm em} \qquad \text{and} \qquad W_5^{\rm em} = -\frac{P\cdot q}{q^2}W_2^{\rm em}, \tag{3.33}$$

so that (3.14) is reduced to two independent structure functions:

$$W_{\mu\nu}^{\rm em} = \left(-g_{\mu\nu} + \frac{q_\mu q_\nu}{M^2}\right)W_1^{\rm em} + \frac{1}{M^2}\left[\left(p_\mu - \frac{q_\mu\, q\cdot P}{q^2}\right)\left(p_\nu - \frac{q_\nu\, q\cdot P}{q^2}\right)\right]W_2^{\rm em}. \tag{3.34}$$

For the general cross section including Z exchange one obtains with the transition to F_i (3.16, 3.17) and the definitions (3.19, 3.20):

$$\frac{d^2\sigma^{\mathrm{NC}}}{dQ^2dx} = \frac{2\pi\alpha^2}{xQ^4}\left[Y_+F_2^{\mathrm{NC}} \mp Y_- xF_3^{\mathrm{NC}} - y^2F_L^{\mathrm{NC}}\right]. \tag{3.35}$$

In analogy to (3.22) we define the reduced cross section for NC:

$$\frac{\tilde{\sigma}^{\mathrm{NC}}}{dxdQ^2} = \frac{xQ^4}{2\pi\alpha^2 Y_+}\frac{d^2\sigma^{\mathrm{NC}}}{dxdQ^2}. \tag{3.36}$$

This definition removes the kinematic coefficient and since F_2^{NC} is dominant $\tilde{\sigma}^{\mathrm{NC}}$ gives approximately F_2^{NC} in most of the kinematic plane.

3.5 NC cross section in the parton model

Next we can replace the proton on the hadronic side of the diagram in Fig. 3 by a quark, carrying the momentum fraction x of the protons momentum. To obtain an expression for the cross section we have to calculate the following diagrams:

$$\frac{d\sigma^{e^\pm q\to e'q'}}{dQ^2} \propto \left| \right. \tag{3.37}$$

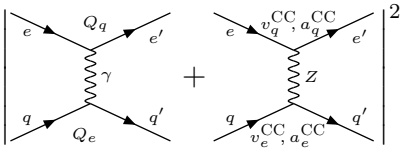

$$\left. \right|^2 .$$

For NC we have the electromagnetic and the weak diagram, which will lead to interference terms. This is reflected in the complicated quark-flavor dependent couplings in the cross section for NC:

$$v_f = \frac{-I_f^3 + 2\sin^2\theta_W Q_f}{2\sin\theta_W\cos\theta_W} \qquad \text{and} \qquad a_f = \frac{-I_f^3}{2\sin\theta_W\cos\theta_W}, \tag{3.38}$$

where I_f^3 is the third component of the weak isospin and Q_f the electromagnetic charge of the quark.

When we want to come back from the eq to the ep cross section, we just have to take every parton into account that might be in the proton and contribute to the cross section. This leads to a sum of probability functions of finding a parton with a specific x and Q^2 within the proton. The sum runs over all quark-flavors accessible with the HERA CMS energy and contains the couplings. It is splitted into two parts, one with term that couple with equal signs to quarks and anti-quarks, and another with terms that couple with opposite signs to quarks and anti-quarks. This separates the parity conserving and parity violating terms:[1]

$$F_2^{\mathrm{NC}}(x,Q^2) = x\sum_{q=d,u,s,c,b} A_q(Q^2)\left[q(x,Q^2) + \overline{q}(x,Q^2)\right], \tag{3.39}$$

$$F_3^{\mathrm{NC}}(x,Q^2) = \sum_{q=d,u,s,c,b} B_q(Q^2)\left[q(x,Q^2) - \overline{q}(x,Q^2)\right]. \tag{3.40}$$

[1] Strictly speaking this is only true for unpolarized beams, see [31]

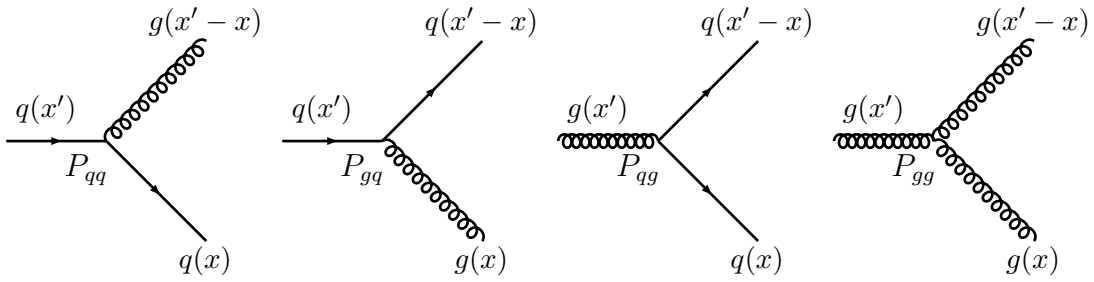

Figure 3.5: Splitting graphs for lowest order in α_s.

Here the coefficient functions are

$$A_q(Q^2) = Q_q^2 - 2Q_q v_e v_q P_Z + (v_e^2 + a_e^2)(v_q^2 + a_q^2)P_Z^2 \quad (3.41)$$

$$B_q(Q^2) = -2Q_q a_e a_q P_Z + 4 v_e a_e v_q a_q P_Z^2 \quad (3.42)$$

with

$$P_Z = \frac{1}{4\sin^2\theta_W \cos^2\theta_W} \frac{Q^2}{Q^2 + M_Z^2}. \quad (3.43)$$

Note that Q_q is always the electric charge of the particle, also for the corresponding anti-particle [32].

3.6 QCD evolution

The biggest simplification in the derivation of the cross section under the assumption of the parton model, like in Sects. 3.3 and 3.5, is to ignore higher orders in QCD. This is also the difference in the definitions of F_2^{NC} between the heuristic parton model (3.39) and the one following the definition (3.14), which comes from the experimentally measured cross section. Now like in QED we also have in QCD radiative effects, here splitting graphs as sketched in Fig. 3.5, that make things more complicated. To be more explicit, a quark with a momentum fraction x does not have to exist a priori but could be the result of a quark with a higher x that just radiated a gluon before interacting, reducing its momentum to the x under inspection. These QCD effects offer also a handle to study and test the theory itself.

The dependences of these graphs on x and Q^2 are described in QCD by the DGLAP evolution equations. QCD is not able to give absolute values of the parton densities, but with a given input at a fixed Q^2 the DGLAP equations predict the evolution of the PDFs. This way by studying the structure functions one obtains information on QCD. It allows to test QCD to the limits of its expected validity, especially towards low Q^2, where the perturbative expansion is expected to break down due to α_s becoming large.

	p_1	p_2	p_3	p_5
xu_v	$(1.69 \pm 0.01 \pm 0.06)$	0.5	$4.00 \pm 0.01 \pm 0.08$	$5.04 \pm 0.09 \pm 0.64$
xd_v	$(0.96 \pm 0.01 \pm 0.08)$	0.5	$5.33 \pm 0.09 \pm 0.48$	$6.2 \pm 0.4 \pm 2.3$
xS	$0.603 \pm 0.007 \pm 0.048$	$-0.235 \pm 0.002 \pm 0.012$	$8.9 \pm 0.2 \pm 1.2$	$6.8 \pm 0.4 \pm 2.0$
xg	$(1.77 \pm 0.09 \pm 0.49)$	$-0.20 \pm 0.01 \pm 0.04$	$6.2 \pm 0.2 \pm 1.2$	0
$x\Delta$	$0.27 \pm 0.01 \pm 0.06$	0.5	$(10.9 \pm 0.2 \pm 1.2)$	0

Table 3.1: The PDF parameters of the ZEUS-S QCD NLO fit. Given are the statistical as well as uncorrelated and correlated uncertainties of the parameters. Values in brackets are constrained by sum-rules, and values without error have been fixed in the fit.

3.7 PDF parameterizations

The ZEUS data can be used to determine the input parameters of the DGLAP evolution, which describes DIS measurements over a broad kinematic range, like the PDFs and the value of the strong coupling constant, α_s, at a given scale. On the one hand the PDFs are needed to evaluate the SM prediction for the CC DIS cross section, on the other hand the measured cross sections contain the information on the real PDFs, which can be extracted. Therefore PDF parameterizations as a result of fits to data are obtained in an iterative procedure with the cross section measurements. The next generation of PDF fits will use these ZEUS measurements as additional input to improve the quality of the fits and therefore of the resulting PDFs. The measurement of the cross section, however, depends only marginally on the PDFs, as will be explained in Sect. 4.6.6.

The ZEUS-S fit [33] uses ZEUS data from 1996/97 [34] together with fixed-target data to extract PDFs. The fixed-target data included are F_2 measurements from BCDMS [35], NMC [36] and E665 [37], deuterium-target data from NMC [36] and E665 [37] to separate $\bar{u}$ and $\bar{d}$, the ratio F_2^D/F_2^p from NMC [38] which determine the ratio of d to u valence quark, and xF_3 from CCFR [39] in the range $0.1 \leq x \leq 0.65$ constraining the valence quark PDFs at high-x. By adding α_s as a free fit-parameter in the ZEUS-α_s fit α_s is estimated while taking correlations of the PDFs fully into account. A cut $Q^2 \geq 2.5\,\mathrm{GeV}^2$ ensures the applicability of pQCD while a cut $W^2 > 20\,\mathrm{GeV}^2$ reduces higher mass and higher twist sensitivities. The kinematic range of the data input to the fits is shown in Fig. 3.6 and covers $6.3 \times 10^{-5} \leq x \leq 0.65$ and $2.5 \leq Q^2 \leq 30\,000\,\mathrm{GeV}^2$. The fit was performed at leading twist. The DGLAP evolution equations at NLO were solved in the $\overline{\mathrm{MS}}$ scheme [40, 41, 42] with the renormalization and factorization scales chosen to be Q^2. For treatment of the heavy-quark sea the variable-flavor number-scheme of Thorne and Roberts [43, 44, 45, 46] (TRVFN) has been used to interpolate between correct threshold and correct large-Q^2 behaviors. The PDFs u-valence, $xu_v(x)$, d-valence, $xd_v(x)$, total sea, $xS(x)$, gluon, $xg(x)$, and the difference between the d and u contributions to the sea, $x\Delta = x(\bar{d} - \bar{u})$, were parameterized each at $Q_0^2 = 7\,\mathrm{GeV}^2$ by:

$$xf(x) = p_1 x^{p_2}(1-x)^{p_3}(1+p_5 x). \tag{3.44}$$

Additional constraints, e.g. number or momentum sum rules, fix 9 of these parameters. leaving 11 free parameters. The results of the ZEUS-S fit given with statistical as well as

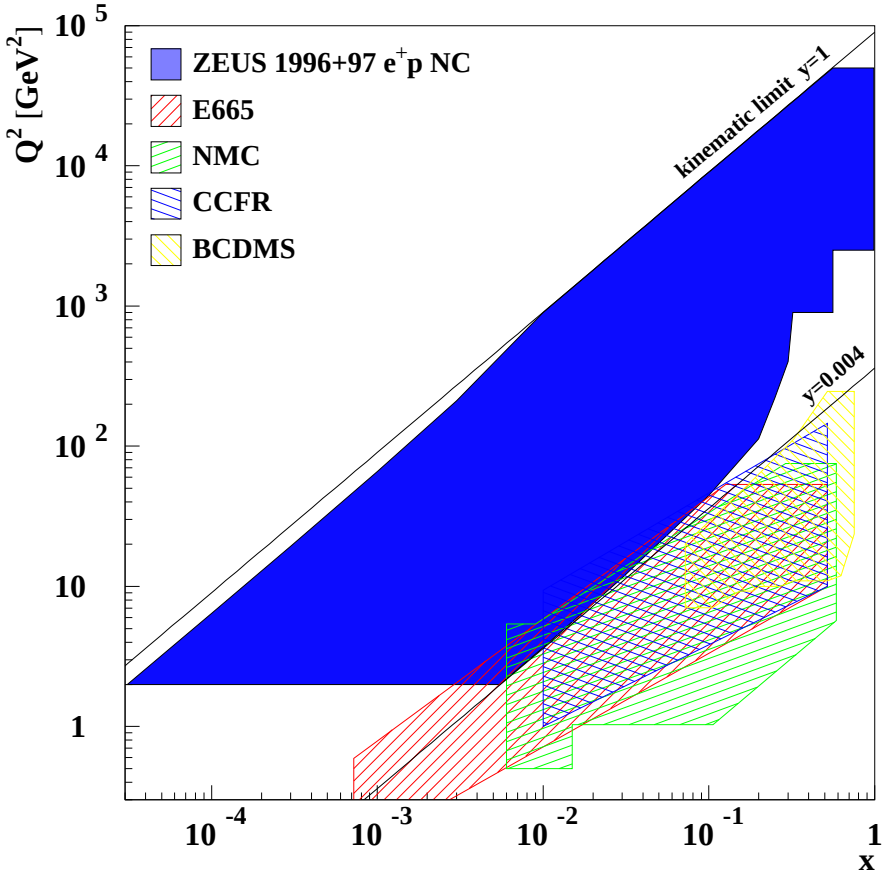

Figure 3.6: The kinematic range covered by the data input to the ZEUS-S QCD NLO fit.

uncorrelated and correlated uncertainties are given in Table 3.1. Values given in brackets are constrained. Those given without uncertainties have been fixed. The resulting PDFs $xu_v(x)$, $xd_v(x)$, $xS(x)$ and $xg(x)$ are plotted in Fig. 3.7 for $Q^2 = 10\,\mathrm{GeV}^2$ together with the total uncertainties. They are compared to the alternative global PDF fits CTEQ6D and MRST(2001), and are found to be compatible. In Fig. 3.8 $xg(x)$ and $xS(x)$ are displayed for the ZEUS-S result with the uncertainty bands, where the correlated systematic uncertainties were found to be dominant. The gluon density has been found to rise towards low x not quite as dramatically as expected for low Q^2. It even becomes negative. Since PDFs, in particular $xg(x)$, are not physical observables, contrary to structure functions such results are not unphysical. They might, however, indicate the breakdown of pQCD.

The PDF fit is especially affected by this measurement at the high-x $xd_v(x)$, as the charged boson exchanged couples only to negatively charged quarks, and at high-x valence quark densities dominate over the sea-quark densities. Preliminary results for a ZEUS PDF-fit using exclusively ZEUS data from the data taking periods 1994 to 2000 as input reaches now a compatible precision as the fits including fixed-target data [47].

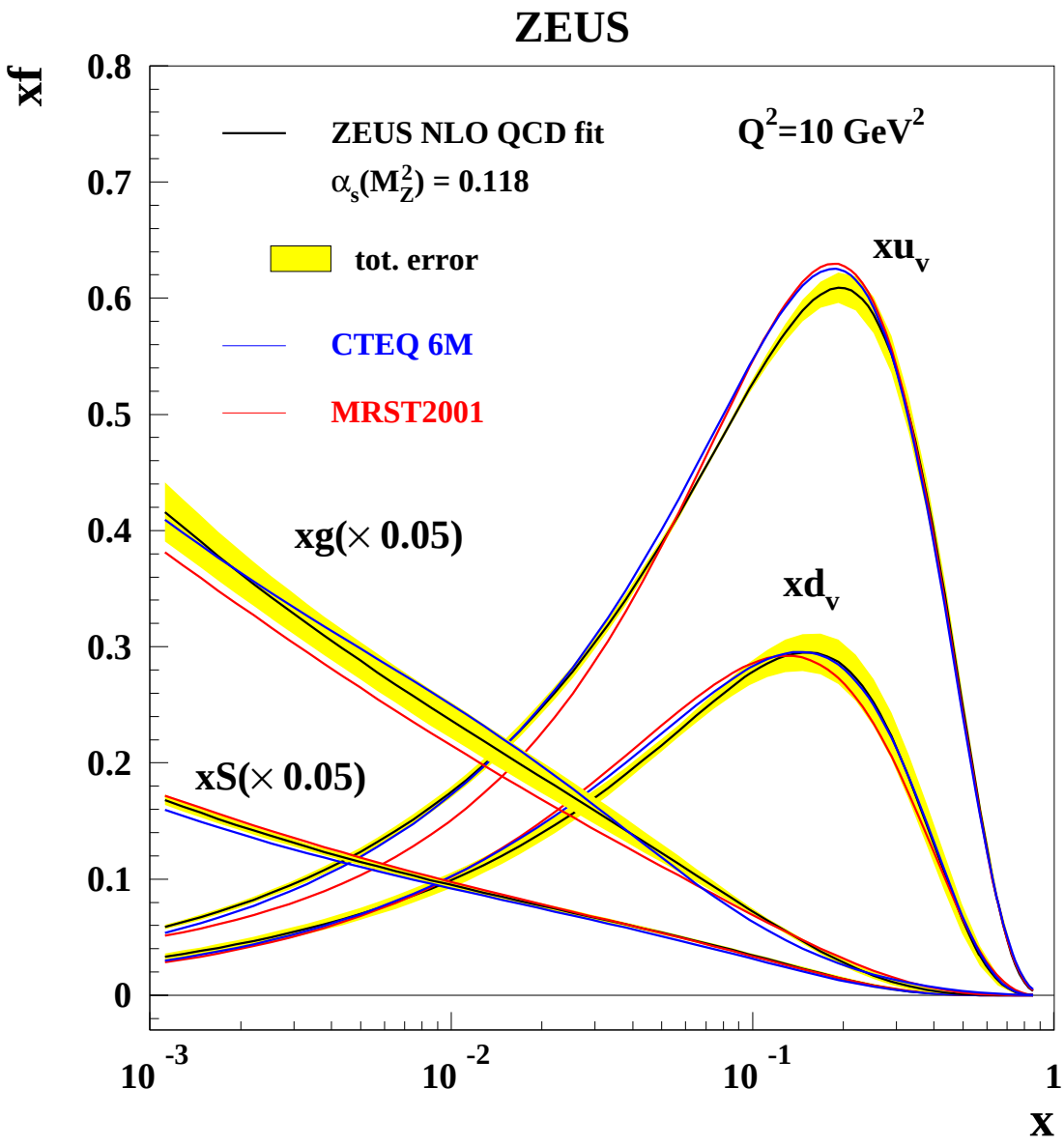

Figure 3.7: The ZEUS-S PDFs $xu_v(x)$, $xd_v(x)$, $xS(x)$ and $xg(x)$ for $Q^2 = 10\,\mathrm{GeV}^2$ with total uncertainty and compared to the alternative global PDFs CTEQ6D and MRST(2001).

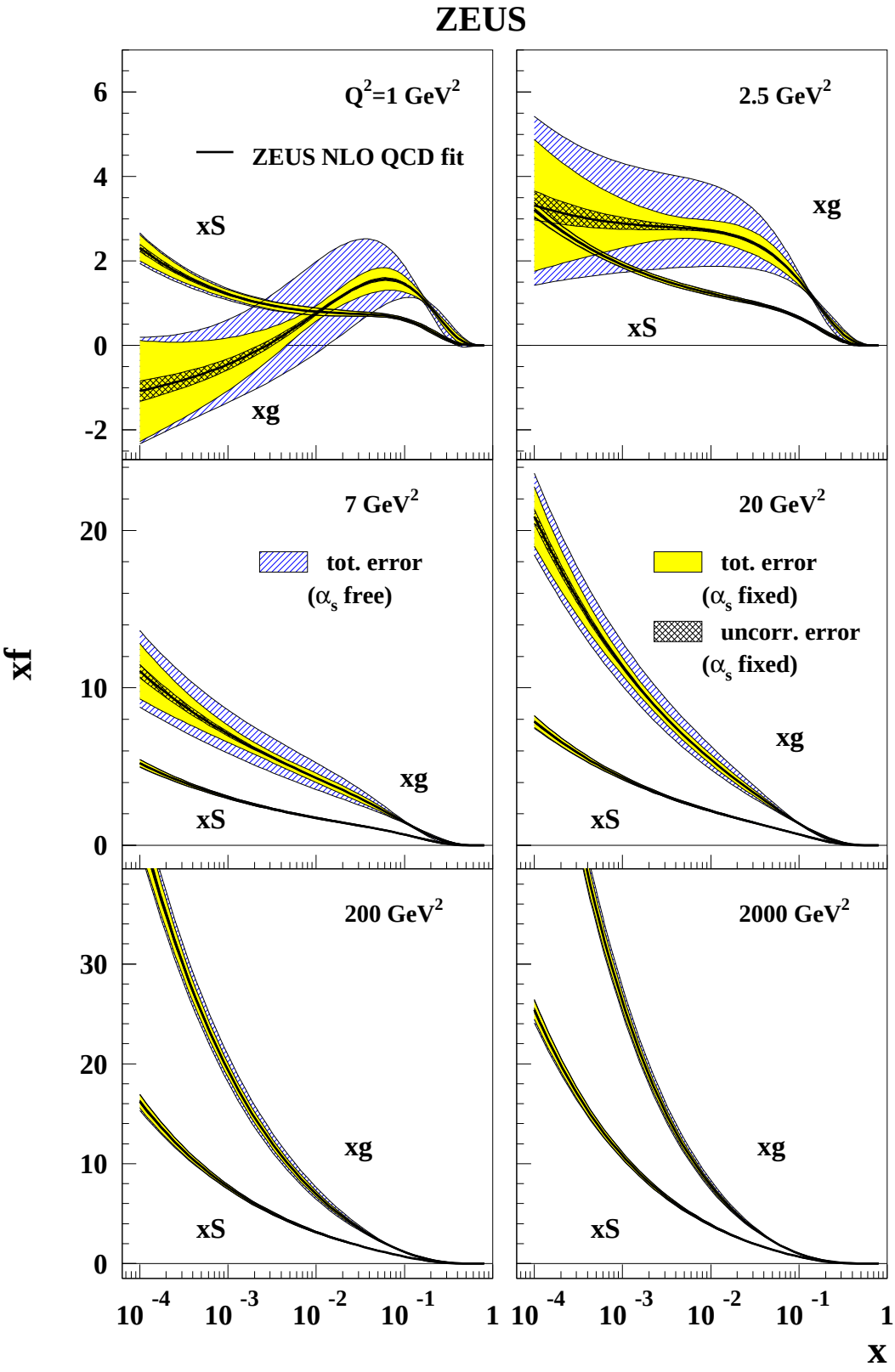

Figure 3.8: The ZEUS-S PDFs $xS(x)$ and $xg(x)$ in bins of Q^2 with only uncorrelated uncertainty and total uncertainty.

Chapter 4

Data Analysis preceeding the CC measurements

This section presents the basics of the preparatory analysis preceeding the final measurements in Sect. 5. A basic tool for analyzing the properties of an event class is the Monte-Carlo (MC) simulation. Such MC samples, as presented in Sect. 4.1, that contain the 'true' event-information, help to study and optimize reconstruction and event selection. Section 4.2 introduces the reconstruction of the event parameters including optimizations for CC-type event-topologies. The reconstruction is not only needed to obtain the kinematic variables for the cross section measurements, but also for additional evaluated quantities used for selecting the signal sample. In Sect. 4.3 the selection of the signal sample including criteria to suppress special background contributions is described. The resulting final signal sample is presented in the following section. Finally the technique for obtaining the measurement results from the final event-sample are described. This includes experimental issues like binning and acceptances, as well as theoretical corrections and the method applied for estimating the systematic uncertainty.

4.1 Monte-Carlo simulations

A sophisticated Monte-Carlo simulation (MC) is employed to estimate properties like the acceptance of such a complex device as the ZEUS detector for the reaction under study. The production of an MC sample is a process of several layers, the flow-diagram of which is shown in Fig. 4.1.

4.1.1 Physic generators

Generators produce simulated events of physical reactions under study and respect additional constraints like the proper kinematic range. The generation of the CC signal sample is described in Sect. 4.1.1.1. As will be shown in Sect. 4.3, the signal region for CC events is not completely separable from events of background processes. The gener-

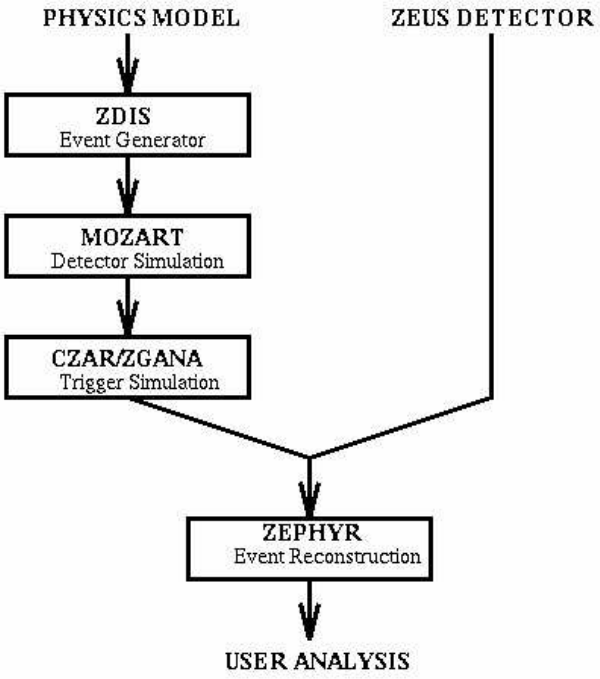

Figure 4.1: Software flow-diagram for MC simulation of ZEUS events

ators and the employed MC samples simulating the contributing background processes are described in Sects. 4.1.1.2 to 4.1.1.5.

4.1.1.1 **Signal** CC MC

CC events were generated using DJANGOH 1.1[48]. This is an interface between several pieces of the simulation process. HERACLES 4.6.1[49] simulates the QED part on the leptonic side, including initial state radiation of the lepton, vertex and propagator corrections as well as two-boson exchange processes. The sub-process of boson scattering on the parton is simulated by LEPTO 6.5.1 [50]. The final state is calculated on the parton level using either the color dipole model (CDM) implemented in ARIADNE 4.10 or the matrix element plus parton shower model (MEPS) as implemented in LEPTO. Gluon emission is treated in the CDM by radiation of the color dipole between q and $\bar{q}$, one being struck by the lepton and the other being in the remnant. This description includes QCD-Compton scattering (QCDC), while boson-gluon fusion (BGF) is left as an additional process. MEPS simulates parton-level interactions according to DGLAP-type splitting functions which corresponds to a leading-log approximation of the gluon emission. Finally, JETSET 7.4 [51] uses the Lund string model to simulate the fragmentation into hadrons. The EW parameters were used as given by the particle data group (PDG)[24]. The PDFs were generated using the CTEQ5D parameterization [52].

For this analysis ARIADNE has been used to generate signal events. A sample generated using MEPS has been employed as systematic check, as described in Sect. 4.6.6.

Hadronisation	Q^2 threshold	σ/ pb	N_{evt}	$\mathcal{L}$/ pb^{-1}
ARIADNE	$Q^2 >$ 10 GeV^2	45.20	25k	553
ARIADNE	$Q^2 >$ 100 GeV^2	39.77	25k	629
ARIADNE	$Q^2 >$ 5 000 GeV^2	3.20	15k	4688
ARIADNE	$Q^2 >$ 10 000 GeV^2	0.68	5k	7323
ARIADNE	$Q^2 >$ 20 000 GeV^2	0.062	5k	80775
MEPS	$Q^2 >$ 10 GeV^2	45.20	25k	553
MEPS	$Q^2 >$ 100 GeV^2	39.77	25k	629
MEPS	$Q^2 >$ 5 000 GeV^2	3.20	15k	4688
MEPS	$Q^2 >$ 10 000 GeV^2	0.68	10k	14633
MEPS	$Q^2 >$ 20 000 GeV^2	0.062	10k	161551

Table 4.1: Samples of CC-signal MC used in this analysis.

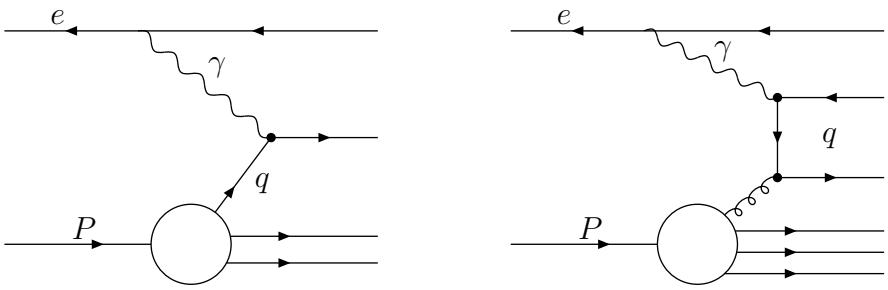

Figure 4.2: Feynman graph for direct (left) and resolved (right) photoproduction in e^+p scattering.

The signal MC has been generated in several samples with different lower cuts in Q^2. This ensures negligible statistical uncertainty of the MC sample without consuming too much computing-time for kinematical regions of high cross sections. Each event has been weighted by the ratio of the data luminosity to the summed luminosity of all samples covering the Q^2 of the event. The samples used in this analysis are listed in Table 4.1. The statistics of the signal MC is at least a factor 100 higher then the integrated data luminosity. The statistical contribution from the MC to the uncertainty of the cross section measurement is thus negligible, but not ignored in the analysis.

4.1.1.2 **Photoproduction background** MC

The Photoproduction (PHP) process, where a quasi-real photon ($Q^2 \approx 0\,\text{GeV}$) is exchanged between the lepton and the proton, has a much larger cross section than CC. In PHP one can differentiate whether the photon scatters directly on a quark within the proton (direct PHP), or whether a gluon from within the proton scatters on a parton within the resolved partonic structure of the photon (resolved PHP). The diagrams for the two processes are depicted in Fig. 4.2. For PHP the scattered electron is not detected at the small scattering angles resulting from the small Q^2 (see (4.4)) and escapes

Process	E_t threshold	P_t threshold	$\sigma/\,\mathrm{pb}$	N_{evt}	C_{PHP}	$\mathcal{L}/\,\mathrm{pb}^{-1}$
Resolved	$E_t > 30\,\mathrm{GeV}$	$P_t > 6\,\mathrm{GeV}$	13410	3.2M	0.84	274
Direct	$E_t > 30\,\mathrm{GeV}$	$P_t > 6\,\mathrm{GeV}$	2849	1.1M	0.84	386

Table 4.2: MC samples of PHP used in the analysis. The luminosities given are after the correction described in the text has been applied.

detection through the beam pipe. The hadronic final state measured in the main detector should have a balanced P_t, since the scattered electron carries almost no P_t. In rare cases the hadronic final state can be mismeasured either due to detector failures or incomplete acceptance or due to intrinsic physical reasons like the energy of muons or neutrinos within the hadronic final state not being measured in the calorimeter. This can result in an imbalance of the transverse momentum so that these events mimic the signature of CC-events. The probability for such cases to occur is quite small, but since the PHP cross section is so large, PHP events constitute the main *ep* collision background. These circumstances create a technical difficulty, since a very large number of PHP events has to be simulated to obtain a reasonably large number of events that, after selection, contribute to the CC signal sample. To increase the production efficiency samples with events that exceed a threshold in either P_t or E_t were produced. Only samples with the condition $P_t > 30\,\mathrm{GeV}$ **or** $E_t > 6\,\mathrm{GeV}$ where used to analyze the PHP background since samples with lower thresholds where found to give negligible contributions to the signal [53]. Samples for direct and resolved PHP have been generated using HERWIG 5.9 [54]. The complete list of PHP MC event samples is given in Table 4.2. The theoretical cross section of PHP is not well estimated. The normalization of the PHP MC samples is fitted to the data, rendering the analysis insensitive to theoretical uncertainties. This is done using the P_t/E_t distribution of a CC data sample with an enriched PHP contribution. Anticipating the terminology of the event selection which will be introduced in Sect. 4.3 this sample was obtained by applying all final cuts excluding the P_t/E_t cut to the high-γ sample and requiring in addition $P_t < 20\,\mathrm{GeV}$. A fit of the absolute normalization to the region $0.12 < P_t/E_t < 0.72$ using the theoretical relative normalisation between direct and resolved PHP yields a normalization correction factor $C_{\mathrm{PHP}} = 0.84 \pm 0.11$ with a good $\chi^2/\mathrm{ndf} = 8.91/14$. Figure 4.3 shows the good agreement of the P_t/E_t distribution with the normalization of the PHP corrected by the fit result and the χ^2 distribution for the fit parameter. The impact of the fit uncertainty on the final measurement will be addressed in Sect. 4.6. If the relative normalization of the direct to the resolved PHP samples is included as a second fit parameter this yields the ratio 0.64 ± 1.88 and the uncertainty on the absolute normalization is increased by a factor of three. Because of the large uncertainty it is concluded that this method is not sensitive to the relative normalization and the theoretical prediction is kept.

4.1.1.3 NC **background** MC

In analogy to the PHP process the final state in an NC event can be mismeasured to produce a misbalanced P_t. However, the cross section of NC reactions is much smaller

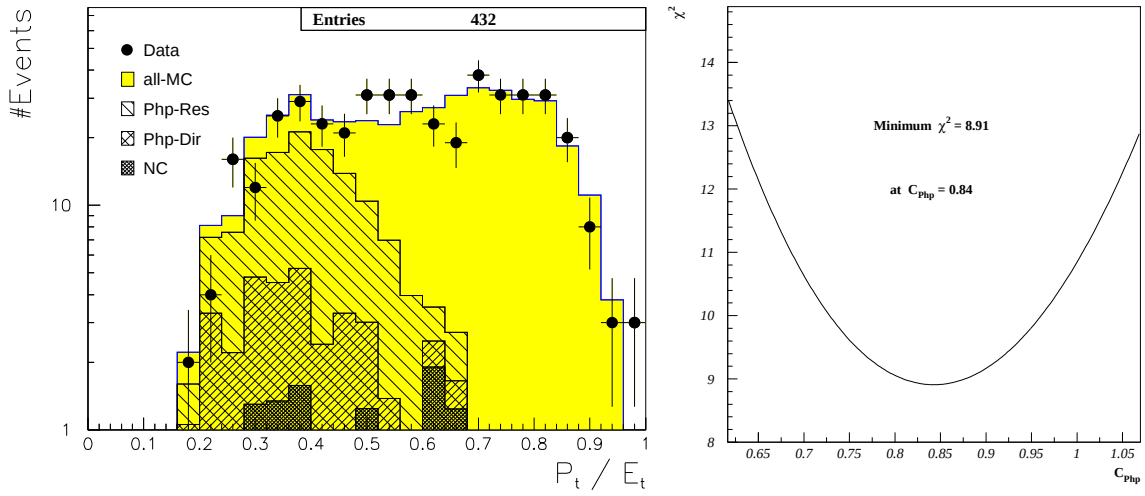

Figure 4.3: P_t/E_t distribution for the PHP enriched sample after normalization correction (left) and the χ^2 distribution of the fit function (right).

Process	Q^2 threshold	$\sigma/\,\mathrm{pb}$	N_{evt}	$\mathcal{L}/\,\mathrm{pb}^{-1}$
NC	$Q^2 > 100\,\mathrm{GeV}$	8.12	1.0M	123

Table 4.3: MC sample of NC used in the analysis.

compared to the cross section of PHP reactions. In addition, a detectable scattered electron in the detector makes this process easier to suppress. The NC sample was produced similarly to the signal MC as described in Sect. 4.1.1.1 using Djangoh 1.1 with Heracles 4.6.1, Lepto 6.5.1, the CDM of Ariadne 4.10. and Jetset 7.4. The sample is listed in Table 4.3.

4.1.1.4 **Di-lepton background** MC

Lepton pair production can be produced by the Bethe-Heitler reaction as depicted in Fig. 4.4 or with a much lower cross section by a Z decay. On the proton side we can separate the processes into elastic, quasi-elastic and DIS, depending on the proton to stay intact, form a resonant state or interact via its constituents to a hadronic final state. While di-electron events should be well contained and lead to a balanced event P_t, di-muon events might produce a misbalanced P_t because of the small energy loss of the muons in the calorimeter. For di-tau production the undetected neutrinos in the final state of the leptonic decays can, in addition to muons, produce a P_t. Therefore only di-muon and di-tau processes have been used to estimate the background. Because of the small cross sections for these processes they contribute only marginally to the CC signal sample. The MC samples used and given in Table 4.4 where produced using Grape [54].

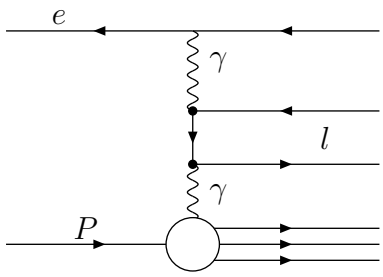

Figure 4.4: Feynman graph for di-lepton production in e^+p scattering via Bethe-Heitler process.

Process	σ/ pb	N_{evt}	$\mathcal{L}$/ pb^{-1}
DIS $eu \Rightarrow eX\mu\mu$	12.98	26000	2004
DIS $e\bar{u} \Rightarrow eX\mu\mu$	2.68	5500	2051
DIS $ed/s \Rightarrow eX\mu\mu$	2.37	5000	2107
DIS $ed/\bar{s} \Rightarrow eX\mu\mu$	1.21	3000	2474
Quasi elastic, $M_{\text{had}} > 5\,\text{GeV}$	0.17	3000	18001
Quasi elastic, $1.08\,\text{GeV} < M_{\text{had}} < 5\,\text{GeV}$	4.97	10000	2013
Elastic	10.20	21000	2059
DIS $eu \Rightarrow eX\tau\tau$	5.23	11k	2104
DIS $e\bar{u} \Rightarrow eX\tau\tau$	1.05	3k	2868
DIS $ed/s \Rightarrow eX\tau\tau$	0.95	3k	3153
DIS $ed/\bar{s} \Rightarrow eX\tau\tau$	0.48	3k	6279
Quasi elastic, $M_{\text{had}} > 5\,\text{GeV}$	0.10	3k	28686
Quasi elastic, $1.08\,\text{GeV} < M_{\text{had}} < 5\,\text{GeV}$	3.56	7.5k	2106
Elastic	6.35	13k	2049

Table 4.4: MC samples to simulate di-lepton background generated with GRAPE.

4.1.1.5 $W^{\pm}$ production background MC

In ep scattering a real $W^{\pm}$ can be produced in the final state in both, NC and CC. The cross section for the CC part is much smaller, so only the NC process

$$ep \rightarrow eW^{\pm}X \tag{4.1}$$

is considered as a background contribution to the CC sample. The Feynman graphs for the main leading order processes are depicted in Fig. 4.5. Again neutrinos or muons in the final state of the leptonic decays of the $W^{\pm}$ can lead to a non-zero P_t. In analogy to PHP the real $W^{\pm}$ can be produced either directly from the proton structure or from the resolved photon structure. For both processes and both charges MC samples where produced using EPVEC, as listed in Table 4.5. In contrast to all the other backgrounds the cross section for this process is rising with Q^2 for the Q^2 range covered by this analysis. Therefore it is the only background contribution at high Q^2.

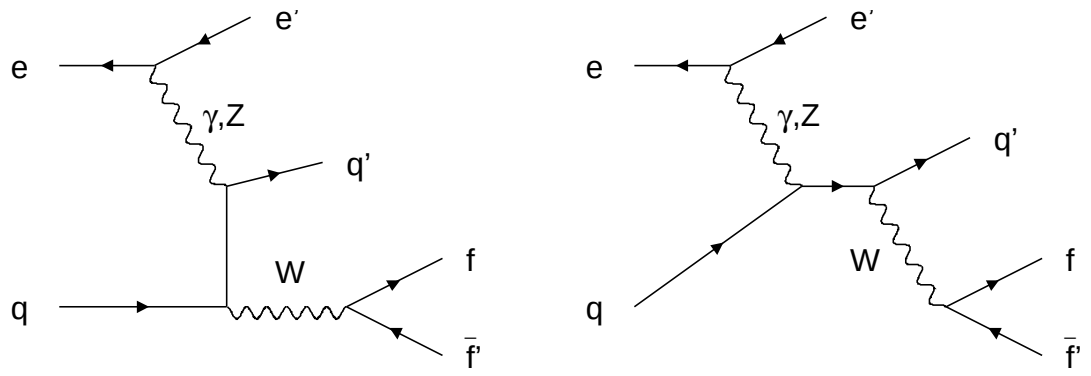

Figure 4.5: Main leading order Feynman diagramms for real $W^{\pm}$ production $e^+p \to e^+W^{\pm}X$ on parton level.

Process	$\sigma/\,\mathrm{pb}$	N_{evt}	$\mathcal{L}/\,\mathrm{pb}^{-1}$
DIS $e^+p \Rightarrow e^+W^-X$	0.087	10k	114754
Resolved $e^+p \Rightarrow e^+W^-X$	0.026	10k	379453
DIS $e^+p \Rightarrow e^+W^+X$	0.106	10k	94224
Rsolved $e^+p \Rightarrow e^+W^+X$	0.033	10k	302098

Table 4.5: MC samples to simulate real W-production background generated with EPVEC.

4.1.2 Detector simulation

The detector response to the final state of generated events is simulated by means of the MOZART software package using a detector simulation based on GEANT 3.13 [55]. The trigger is a mixture of detector hardware and software. This means that the data acquisition by the early trigger levels have to be simulated as well as the algorithms of the later levels. This is done by the package ZCAR for first and second levels, and ZGANA for the third level. After the trigger simulation the complete MC event is available in the same data structure as real data events.

4.1.3 MC-event reconstruction

The simulated events undergo the same reconstruction as real events using the ZEPHYR package, as illustrated in the flow-diagram in Fig. 4.1. This way an event with a data structure identical to a real event is obtained, only that the "true" quantities that were inputs to the detector simulation are available in addition. The details of the reconstruction for data are described in Sect. 4.2.

4.2 Reconstruction

In Sect. 3.1 we introduced the kinematic variables describing a DIS event. The purpose of this section is to show how these quantities are determined from the detector based quantities, e.g. calorimeter deposits. The reconstruction includes also corrections applied to the raw detector information. Some of these are applied in the early stage of the reconstruction, since they have an effect on the quantities reconstructed later.

4.2.1 Calorimeter noise suppression

The radioactivity of the uranium used as absorber in the calorimeter causes background noise in the photomultipliers. To reduce the data volume of an event an energy cut on EMC (HAC) cells of 60 MeV(110 MeV) has been applied before recording. A harder offline cut of 80 MeV(140 MeV) is applied on *isolated* cells in the reconstruction.

A photomultiplier (PM) may have the defect to produce either no (dead) or a random (noisy) signal. Dead PMs are identified in the data quality monitoring. In the reconstruction they are set equal to the energy deposit measured by the opposite PM of the cell. The case when both PMs of a cell are dead is called a 'hole', since the energy is then lost. During the running period special care was taken to limit the number of holes. Noisy PMs are identified by a sophisticated algorithm [56]. Cells are marked if their average firing exeeds the mean of all cells' average firing by more than 5 standard deviations. Such cells are not taken into account in the reconstruction.

In addition PM bases may discharge spontaneously faking a high energy deposit. The effect of such 'sparks' is reduced by removing isolated cells with a high imbalance of the energy measured by the left, E_L, and right, E_R, PM of the cell, thus requiring:

$$A_{\text{imb}} = \frac{|E_L - E_R|}{E_L + E_R} < 0.7. \tag{4.2}$$

4.2.2 Calorimeter energy rescaling

The global energy scale was corrected by scaling the measured energies of the cells by a common scale factor of 1.000/1.050/1.022 for FCAL/BCAL/RCAL. These scale factors were mainly obtained by measuring the scattered electrons. This method implies limited statistics in the forward direction corresponding to large electron scattering angles, while in backward direction within 70 cm to the beam pipe statistics is large enough to extract a scale-factor on cell basis. In forward direction a study on hadronic energies showed an improved agreement if a scale factor of 1.003/1.044/1.024/0.941 for BEMC/BHAC/FEMC/FHAC was applied.

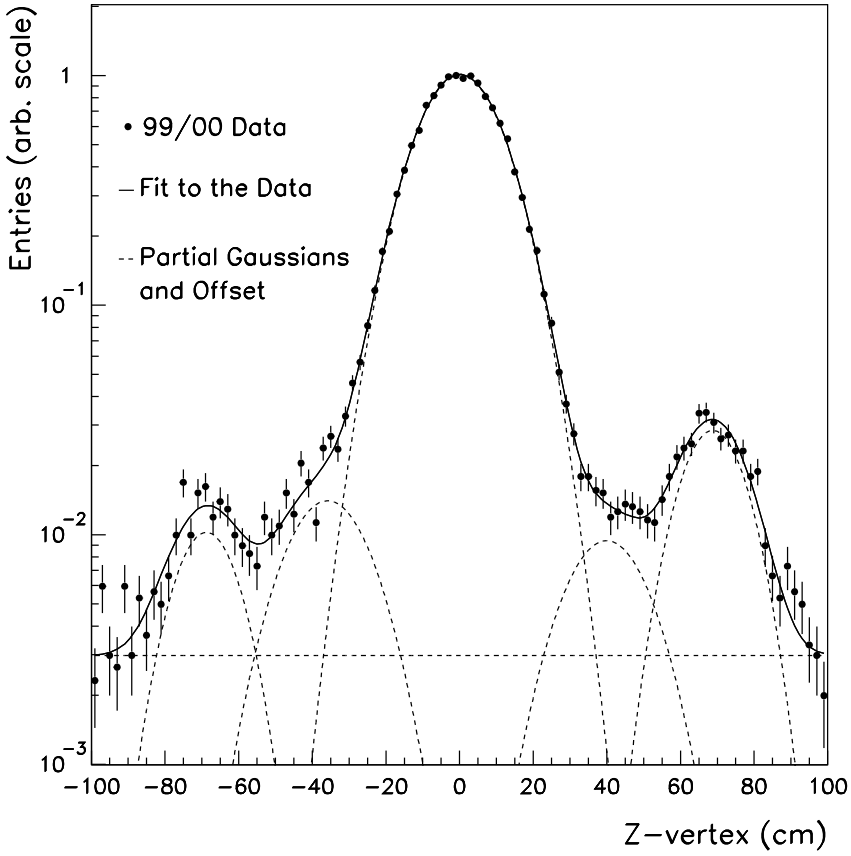

Figure 4.6: The z-vertex distribution obtained from a minimum bias sample with the fit result of a parameterization of five Gaussians and an offset. From [59].

4.2.3 Tracking and Event vertex

A sophisticated algorithm is used to reconstruct the CTD hits, tracks and the event vertex [57, 58].

Due to the extended longitudinal beam profile provided by the HERA machine the interaction can take place in a region around the nominal collision point of about 1 m. The extracted z-vertex distribution in Fig. 4.6, as it is used in the simulation, was obtained by fitting an overlay of five Gaussians with z-offsets to a vertex distribution of a minimum bias event sample. This sample has been selected with special care to ensure that it is not influenced by the detector, e.g. by trigger efficiencies, but reflects only the machine property. Most of the events lie within ± 30 cm around the nominal z-position, however satellites in the proton beam structure result in secondary peaks that are centered at about ± 70 cm.

The reconstruction algorithm uses all CTD tracks to fit a vertex position, taking possible secondary vertices into account. In the first step this algorithm discards tracks not originating from the beam line. Then a simple fit is repeated iteratively where tracks producing an unreasonable χ^2 are removed. The final vertex fit refits all tracks with the

vertex as an additional point. The resulting new vertex is used as input to a new fit. This fit procedure is repeated until it converges. The transverse resolution of the vertex fit does not reach the $0.3 \times 0.1\,\mathrm{mm}^2$ transversal intersection region of the proton-electron beams. Therefore the x and y coordinates of the vertex are always set to the nominal interaction point ($x_{vtx} = y_{vtx} = 0\,\mathrm{cm}$).

In case there are no tracks within the acceptance of the CTD the z-vertex position is reconstructed from the arrival time of hadrons in the FCAL, i.e. the mean energy deposit time in FCAL, as described in [60]. The high timing resolution allows this reconstruction method. The timing resolution of a single ZEUS calorimeter-PM is better than 1 ns for energies above a few GeV [61]. The absolute calorimeter timing shows run-dependent shifts on the order of 1 ns. To avoid run-dependent shifts in the calorimeter-reconstructed z_{vtx} corresponding to the order of 30 cm the mean z_{vtx}^{cal} is corrected on a run-by-run basis to reflect the mean position reconstructed using the CTD. For the running period analyzed here the estimation of the run constants is described in [18]. The resolution obtained with this reconstruction method is about 9 cm for events with an energy deposit in FCAL above 25 GeV and improves to 7 cm for deposits above 100 GeV.

For the later stage of the analysis it is necessary to identify "good tracks". These tracks have to fulfill several quality criteria. They have to be reconstructed as originating from the primary vertex with a not too large distance of closest approach (D_0). To ensure good tracking quality the reconstructed track has to have a minimum track-P_t and a polar angle (θ) lying well within the geometrical acceptance of the CTD. The requirement for a "good track" are:

$$P_t^{\mathrm{track}} > 0.2\,\mathrm{GeV} \quad \textbf{and} \quad 15^\circ < \theta^{\mathrm{track}} < 164^\circ \quad \textbf{and} \quad D_0^{\mathrm{track}} < 1.5\,\mathrm{cm}. \tag{4.3}$$

4.2.4 Reconstruction of kinematic variables

First we can formulate the kinematic variables in terms of energy and scattering angle of the particles e, l', p and X as depicted in the Feynman graph in Fig. 3. The four momenta of l and p are defined by the initial state, therefore E_p and E_e are well known. As l and p collide head-on they define a natural orientation of the reference system.

For NC we measure the scattered lepton and the event quantities available are therefore E'_e, θ_e, E_h and γ_{h}, where h denotes the hadronic final state X and e the scattered lepton l'. Because of four-momentum conservation this is of course an over-constrained system. Therefore one can use different methods which choose two of these quantities to reconstruct the kinematic variables. An obvious choice would be the variables of the scattered

lepton. This is called the electron method (EL) and the formulae are:

$$Q^2_{EL} = 2E_e E'_e(1+\cos\theta_e) \tag{4.4}$$

$$x_{EL} = \frac{E_e}{E_p}\frac{E'_e(1+\cos\theta_e)}{2E_e - E'_e(1-\cos\theta_e)} \tag{4.5}$$

$$y_{EL} = 1 - \frac{E'_e}{2E_e}(1-\cos\theta_e). \tag{4.6}$$

The double-angle (DA) method uses θ_e and $\gamma_{\rm h}$:

$$Q^2_{da} = 4E_e^2\frac{\sin\gamma_h(1+\cos\theta_e)}{\sin\gamma_h + \sin\theta_e - \sin(\gamma_h+\theta_e)} \tag{4.7}$$

$$x_{DA} = \frac{E_e}{E_p}\frac{\sin\gamma_h + \sin\theta_e + \sin(\gamma_h+\theta_e)}{\sin\gamma_h + \sin\theta_e - \sin(\gamma_h+\theta_e)} \tag{4.8}$$

$$y_{DA} = \frac{\sin\theta_e(1-\cos\gamma_h)}{\sin\gamma_h + \sin\theta_e - \sin(\gamma_h+\theta_e)}. \tag{4.9}$$

In CC the scattered lepton leaves no signal in the detector, so we have no choice anymore. Only the hadronic final state is available for reconstruction. For this Jacquet and Blondel (JB) have proposed a method [62]:

$$y_{JB} = \frac{(E-P_z)_h}{2E_e} \tag{4.10}$$

$$Q^2_{JB} = \frac{P^2_{t,h}}{1-y_{JB}} \tag{4.11}$$

$$x_{JB} = \frac{Q^2_{JB}}{s\cdot y_{JB}}. \tag{4.12}$$

Here $P^2_{t,h}$ is the squared transverse momentum of the hadronic final state. The squared transverse momentum of a CC-event, P^2_t, originates from the non-measured 'missing' transverse momentum of the neutrino, $\not{P}^2_t$. The transverse momentum of the neutrino is of equal size but opposite direction as the transverse momentum of the hadronic final state, which is the total event transverse momentum, and therefore:

$$\not{P}^2_t = P^2_{t,h} = P^2_t. \tag{4.13}$$

In the following the detector-based P^2_t is used. The hadronic energy and angle are then:

$$\cos\gamma_{\rm h} = \frac{P^2_t - (E-P_z)^2_{\rm h}}{\not{P}^2_t + (E-P_z)^2_{\rm h}}, \tag{4.14}$$

$$E_{\rm h} = \frac{P_t}{\sin\gamma_{\rm h}}. \tag{4.15}$$

The advantage of this method is, that $E-P_z$ is not sensitive to energy-loss through the forward hole in the calorimeter around the beam pipe, since at small angles and ignoring the masses $E_i = P_{z,i}$ and $P_{t,i} = 0$. This holds in particular for the proton remnant.

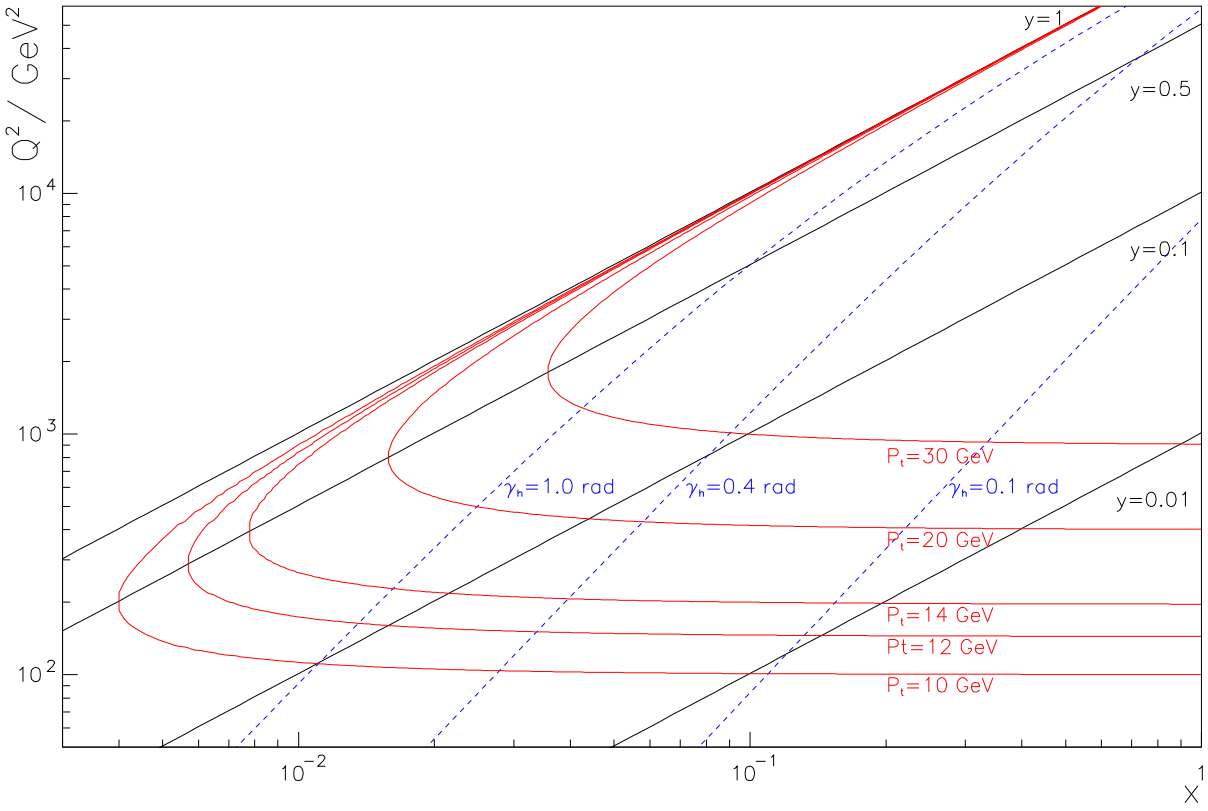

Figure 4.7: Representation of the kinematic plane in Q^2 and x with lines of fixed y, γ_{h} and P_t

In general one should note, that the input variables for the JB method are P_t^2 and $E - P_z$. Furthermore, the kinematic variables are not independent as explained in Sect. 3.1 and given in (3.9). If we choose the two independent kinematic quantities to be Q^2 and x, we can locate each event in the plane spanned by these two variables. In addition, the other variables can be expressed by these two, which is equivalent to lines of fixed values for these quantities in the Q^2-x plane. Figure 4.7 shows the Q^2-x plane with some iso-γ_{h}, iso-y and iso-P_t lines. The interest in this plot lies in allowing the translation of a region of special characteristics in one variable into those kinematic variables in which the cross sections is measured. As an example we can see from this plot, that the low-γ_{h} region which, as a result of the limited geometrical acceptance has a very low tracking probability, corresponds to the region of high-x and rather low Q^2.

4.2.5 Reconstruction and corrections of the hadronic final state

The preceding section explained the reconstruction method using only the hadronic final state, as inescapable in CC. Therefore special care has to be taken to correctly estimate the hadronic energy and its spatial distribution.

The naive estimation of the hadronic four-momentum is on calorimeter-cell basis:

$$\begin{pmatrix} E \\ p_x \\ p_y \\ p_z \end{pmatrix} = \begin{pmatrix} \sum_i E_i \\ \sum_i E_i \cos\theta_i \cos\phi_i \\ \sum_i E_i \cos\theta_i \sin\phi_i \\ \sum_i E_i \sin\theta_i \end{pmatrix}, \tag{4.16}$$

where for cell i E_i, θ_i and ϕ_i are the energy deposit, the polar and the azimuthal angle with respect to the previously determined interaction vertex. The sums run over all cells i of the hadronic final state, so excluding those identified as belonging to a scattered electron. In the CC analysis we expect no scattered electron in the final state, thus the quantities presented in the following always include all deposits.

Several effects require corrections of the measured energy on calorimeter-cell basis to enhance the quality of the estimators for e.g. γ_{h} and E_{h}. These are part of the software package Cor&Cut [63].

4.2.5.1 Island clustering

The energy deposits in the calorimeter cells are clustered to 3D objects called islands. This way the resolution of the center of these objects is increased in comparison to the cell size. The sums in Equation (4.16) then run over these islands instead of cells.

The algorithm works in two steps. In a first step, cells within a calorimeter part and type, e.g. FEMC or BHAC1, are joined to the neighboring cell with the highest energy. This way 2D-islands are created around local maxima, as illustrated in Fig. 4.8. In the second step, these islands are combined to cone-islands according to a probability function of the angular separation. This step does not respect calorimeter part or type boundaries, resulting in cone-islands that can include e.g. cells in BEMC as well as FHAC1. The resulting 3D cone-islands are referred to later as just 'islands'. The island position is reconstructed from the energy weighted positions of the contributing cells. The resulting resolution for the composed object is therefore enhanced with respect to the simple cell based positions.

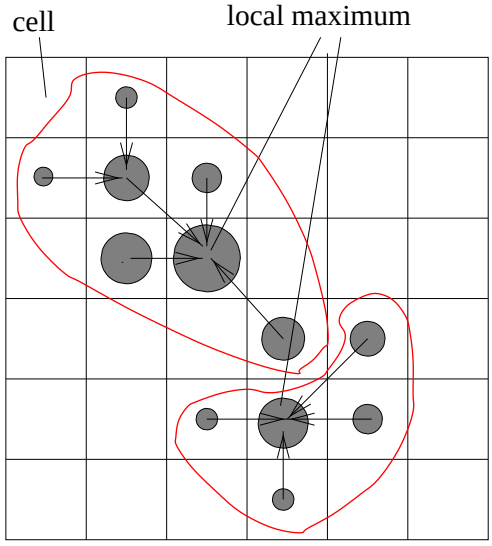

Figure 4.8: Schematic illustration of the island clustering-algorithm

4.2.5.2 Backsplash correction

Particles coming from an interaction may scatter or shower in material, or back-scatter from the calorimeter across the detector to be detected at a completely different position.

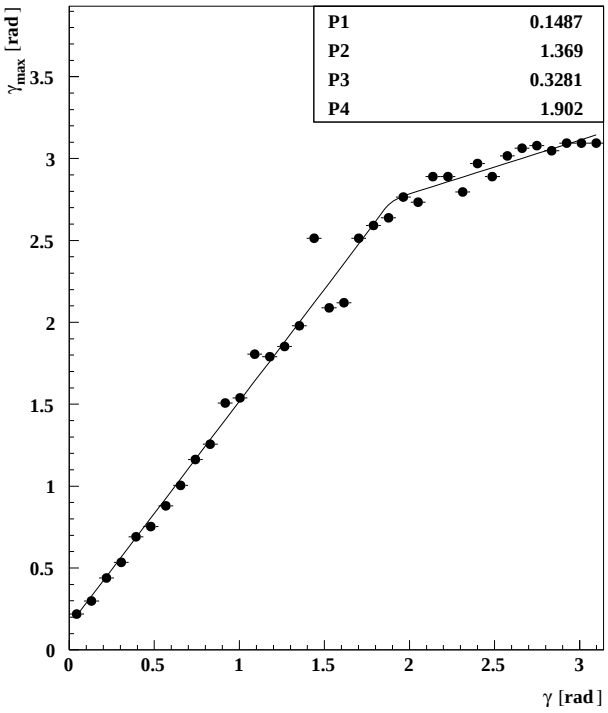

Figure 4.9: Maximum polar angle $\gamma_{\max}(\gamma_{\mathrm{h}})$ as defined in the text with the fit result for the parameterization in Equation (4.17). From [64]

Such energy deposits can affect significantly the reconstruction of the hadronic final state. Though their energy is usually less than 3 GeV, the big distance to the nominal position constitutes a large lever arm. The spatial distance to the closest island with energy $E > 3\,\mathrm{GeV}$ was found not to be an efficient discriminant. Instead only the polar angle θ of the island was used to discriminate against those islands, that have a θ bigger than $\gamma_{\max}(\gamma_{\mathrm{h}})$ defined below. From MC study it was found that the best agreement between the reconstructed and the true γ_{h} in terms of χ^2 was achieved by removing less than 1% of the non-backsplash islands. This defines $\gamma_{\max}$ of an event as the minimum polar angle of islands to be removed such that less than 1% of the non-backsplash islands are removed. The $\gamma_{\max}(\gamma_{\mathrm{h}})$ has been determined as displayed in Fig. 4.9 and found to be well parameterized by:

$$\gamma_{\max} = \begin{cases} P_1 + P_2 \cdot \gamma_{\mathrm{h}}, & \gamma_{\mathrm{h}} < P_4 \\ P_1 + P_2 P_4 + P_3 \cdot (\gamma_{\mathrm{h}} - P_4), & \gamma_{\mathrm{h}} > P_4. \end{cases} \tag{4.17}$$

The correction routine uses the extracted $\gamma_{\max}(\gamma_{\mathrm{h}})$ to ignore islands with $\theta_i > \gamma_{\max}(\gamma_{\mathrm{h}})$ in calculating the hadronic final state.

4.2.5.3 Dead material correction

The particles that are measured in the calorimeter undergo energy-loss in un-instrumented material on their way from the interaction point to the calorimeter. For the ZEUS

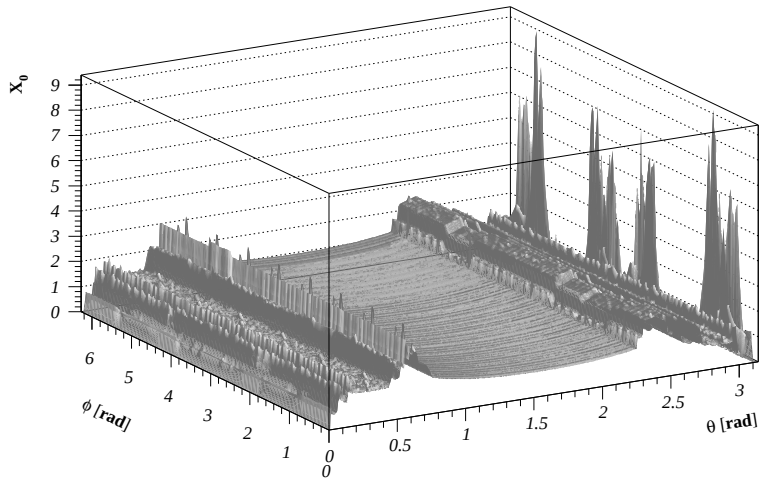

Figure 4.10: Dead material distribution of the ZEUS detector in polar coordinates from the nominal interaction vertex to the calorimeter surface. The map has been smoothed to one fourth of the original resolution, which has a peak maximum of $11.5 X_0$.

detector there is a 'map' of dead material in units of the electromagnetic interaction length X_0, as displayed in Fig. 4.10. This map depends on the interaction vertex. The actual map-value for a given z_{vtx} is obtained by interpolating between X_0-maps for $z_{vtx} = [0\,\text{cm}, \pm 8\,\text{cm}, \pm 45\,\text{cm}]$. A correction of the islands energy for energy loss in dead material based on this map has been obtained by fitting the ratio of the energy measured in the island, E_{isl}, to the true energy, E_{true}, in three bins in X_0. This has been done separately for purely electromagnetic islands ($f_{\text{isl}}^{\text{EMC}} \equiv E_{\text{isl}}^{\text{EMC}}/E_{\text{isl}} = 1$) and hadronic islands ($f_{\text{isl}}^{\text{EMC}} < 1$). The fit result is a function of X_0 and is used to correct the energy of the islands. The separation in hadronic islands is done since their energy is overestimated for small energies $E_{\text{isl}} < 7\,\text{GeV}$ as hadrons have a higher probability to ionize than to shower. A correction for this effect is applied separately in this energy region.

4.2.5.4 Supercrack correction

The mechanical design of the three main calorimeter parts was chosen in a way that they overlap in the polar angle with respect to the nominal interaction point. Yet energy can 'leak' through the calorimeter, resulting in the calorimeter measurement underestimating the energy. The leakage is enhanced in the supercrack regions between the main calorimeter parts, necessitating an interaction-vertex dependent correction.

non-*ep* background	*ep* background
Beam-gas Halo muon Cosmic muon	Photoproduction (resolved & direct) Neutral current Di-lepton production $W^{\pm}$ production

Table 4.6: Background classes for a CC analysis.

4.2.5.5 Effect of the corrections

The effect of the correction on the reconstructed kinematic variables has been checked using the complete signal MC. The relative deviations of the uncorrected variables Q^2, x, y and P_t reconstructed on cell basis and the corrected ones from the 'true' value as given in the MC are plotted in Fig. 4.11 to 4.14 versus the 'true' value. The correction reduces considerably the bias of the reconstructed variables. Especially P_t is very well reconstructed after the correction with a bias of less than 3%. The RMS values for Q^2 and low x are increased by the correction, though, because a small number of events is not shifted by the correction towards the proper mean value.

4.3 Event selection

The aim of the event selection is to identify the events produced via the process under study. The quality of the selected sample can be given in terms of efficiency, purity and statistical relevance. Restricting the sample to a smaller region in event variables might reduce the background contribution, but also reduces the statistical significance of the sample. The aim is to find optimized cut values that guarantee a large signal-to-background ratio while keeping high statistics.

In the following the different measures taken to separate the signal from the background at the different stages are presented. Throughout the selection one should keep in mind, that there are two classes of backgrounds, which are listed in Table 4.6. The first one contains the events not coming from positron-proton beam collisions, non-*ep* background, while the second class originates from *ep*-collisions, but not from the CC-interaction under study here. For the non-*ep* background there are several contributions. There are events from the interaction of the beam with the residual gas in the beam pipe, called beam-gas events. Muons that are produced far up-beam by an interaction and proceed almost parallel to the beamline through the detector or are stopped in the FCAL, are called halo-muons. In addition, cosmic rays hit the detector and can mimic the signature of an CC event. Non-*ep* background has the big disadvantage that it is not modeled by MC, so predictions on the properties of these types of background are vague and only possible by preparing

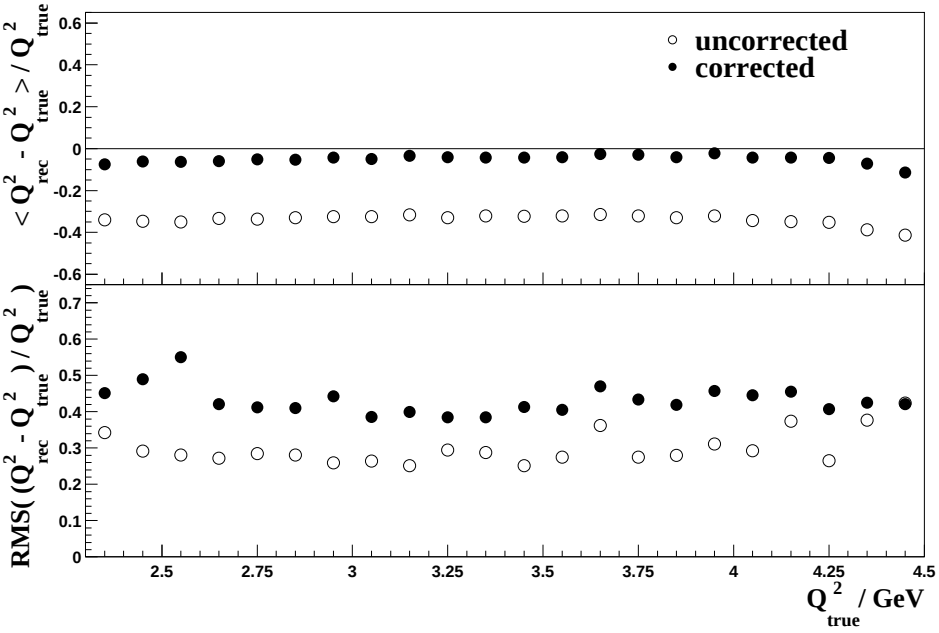

Figure 4.11: Relative deviation of the reconstructed Q^2 from the 'true' Q^2 versus the 'true' value for uncorrected (open circles) and corrected (closed circles) Q^2.

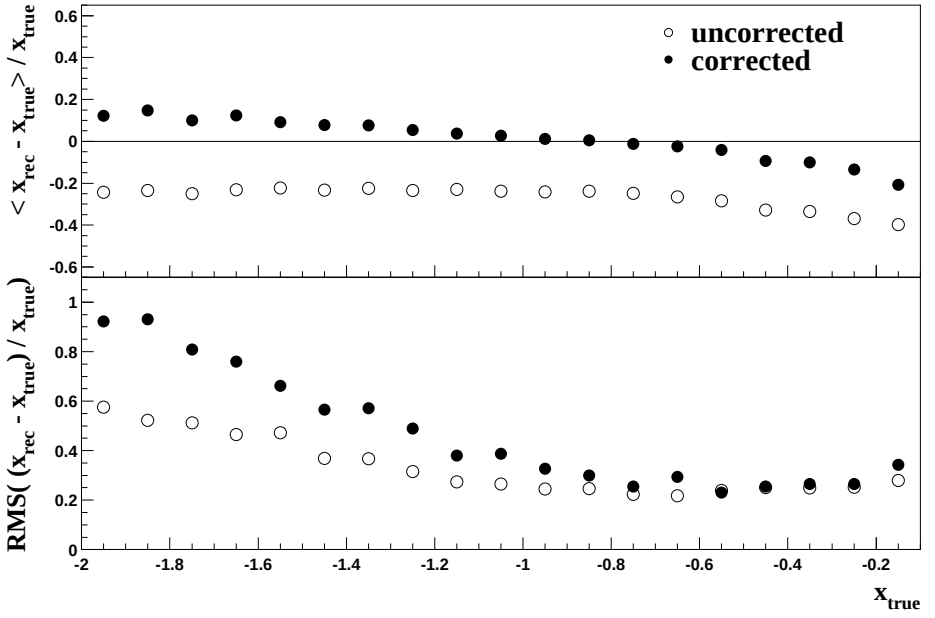

Figure 4.12: Relative deviation of the reconstructed x from the 'true' x versus the 'true' value for uncorrected (open circles) and corrected (closed circles) x.

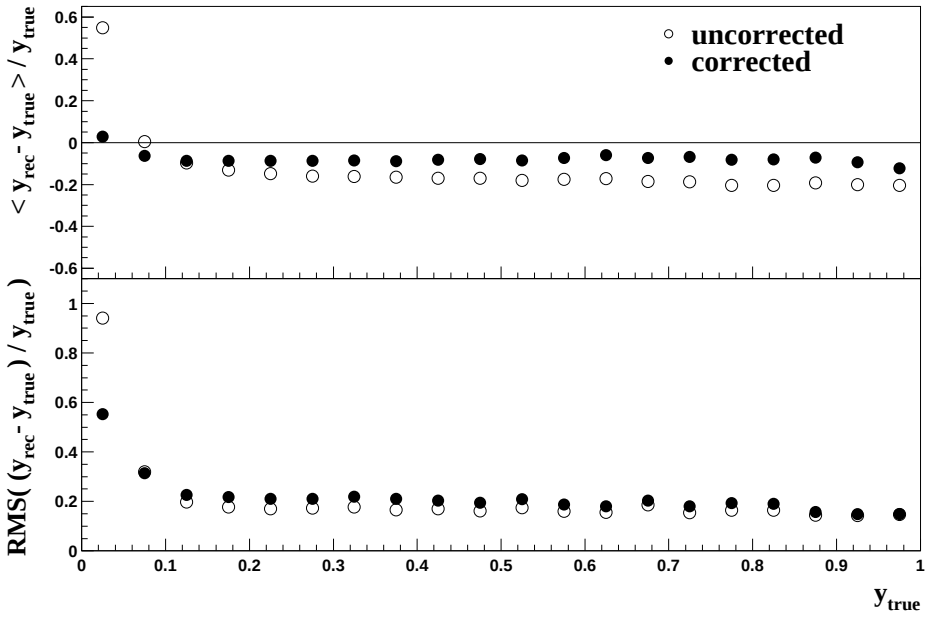

Figure 4.13: Relative deviation of the reconstructed y from the 'true' y versus the 'true' value for uncorrected (open circles) and corrected (closed circles) y.

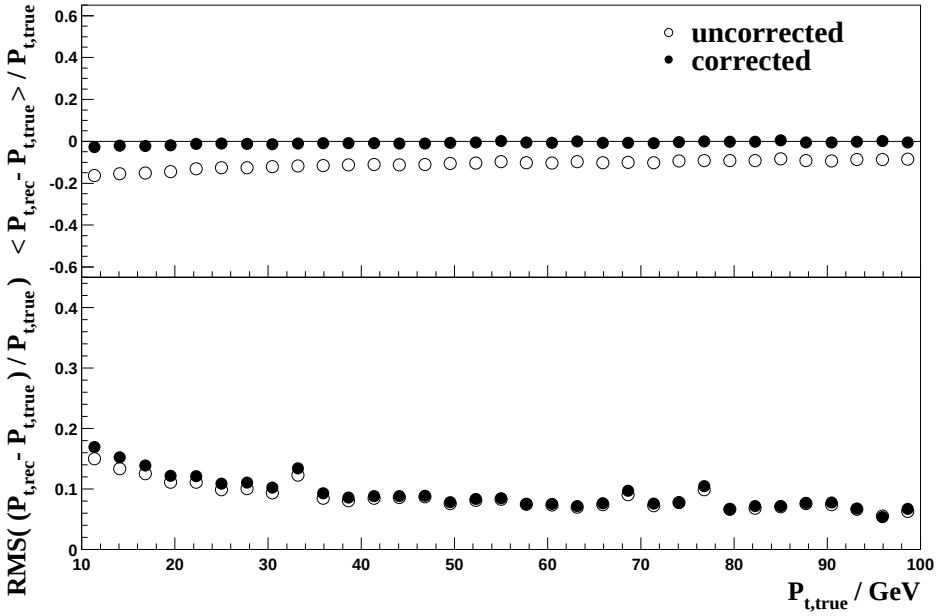

Figure 4.14: Relative deviation of the reconstructed P_t from the 'true' P_t versus the 'true' value for uncorrected (open circles) and corrected (closed circles) P_t.

an enriched background data sample. Non-CC *ep* interactions come again in two kinds. Either they have a much higher cross section than CC but are only seldomly faking a CC signal, mostly by mismeasurement of the hadronic final state like in photoproduction and NC. Or they are rare processes but have an indistinguishable signature, like W and di-lepton production. These backgrounds can be studied in detail by using the MC samples described in Sects. 4.1.1.2 to 4.1.1.5. In addition, since background and signal are overlapping and thus are not completely separable, the MC samples have to be used to estimate the contribution from these processes and subtract the residual contribution statistically.

An additional complication arises when a non-*ep* background event, which fakes the CC signature, happens within the crossing time of an *ep* collision event of the more probable types, e.g. a halo or cosmic muon producing missing transverse momentum overlayed with a PHP event. These events are rare and hard to reject by means of simple cuts, since they do not have the properties of a clean halo-muon event. Some of them are only identified by eye-scanning the visualized event as discribed in Sect. 4.3.14.

4.3.1 Low/high γ sample separation

The geometry of the ZEUS detector, explicitly the geometrical acceptance of the CTD, poses a crucial point in the selection of signal events and rejection of background events. The event sample has to be split in two subsamples, one where the hadronic final state lies within the acceptance of the CTD and a tracking is guaranteed, and another where no tracking is reliably available. The two subsamples are treated differently with respect to the selection cuts. Tracking quantities allow to reduce background efficiently. In case of no reliable tracking the thresholds for the rejection cuts based on calorimetry have to be increased. Some backgrounds like halo muons cannot produce a good track. Therefore special measures to reject these events described in Sect. 4.3.10 are only necessary when not requiring tracking.

The CC event variable which reflects best the probability of tracks to be within the CTD acceptance is the angle of the hadronic final state γ_0, which is used to separate the sample in a high-γ sample with guaranteed tracking and a low-γ sample. Here γ_0 is the angle of the hadronic system with respect to the nominal interaction vertex. For the decision which method will be used for vertex reconstruction, based on tracking or alternatively using calorimeter timing as described in Sect. 4.2.3, has to be taken by inspecting γ_0, which is not biased by any vertex reconstruction method. However, for the reconstruction of γ_{h} the properly reconstructed vertex is used. The optimum value of γ_0 for separation of the samples is detemined by inspecting the tracking vertex efficiency, $\epsilon_{\mathrm{vtx-ctd}}$, defined as the number of events with reconstructed tracking vertex divided by all events, versus γ_0, as shown in Fig. 4.15. The event samples used for this plot were obtained by applying the final selection cuts for the low-γ sample as summarized in Sect. 4.4 over the whole γ_0 range shown. A turn-on curve of the form

$$\epsilon_{\mathrm{vtx-ctd}} = 0.5 \cdot \tanh\left(\frac{\gamma_0 - P_1}{P_2}\right) + 0.5 \tag{4.18}$$

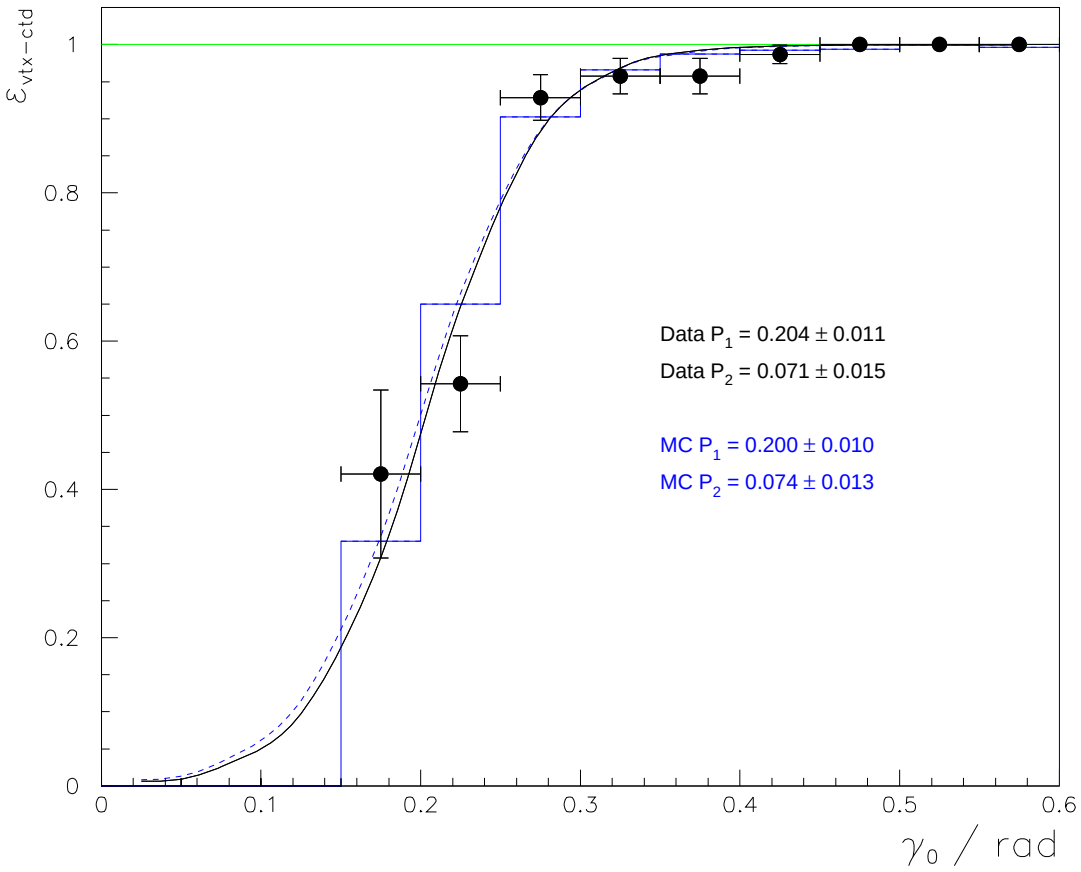

Figure 4.15: Efficiency of finding a tracking vertex versus γ_0 for data (points) and MC (histogram) with the fit result of a turn-on curve (4.18) to the data (solid line) and the MC (dashed line).

has been fitted separately to data and the signal MC. A comparison of the results for data and the signal MC proves that the tracking vertex efficiency is well described by the MC. The absolute value above which to expect a tracking vertex is determined from this figure to be $\gamma_0 > 0.4\,\text{rad}$ and is used to separate high-γ and low-γ sample.

4.3.2 Online trigger

As described in Sect. 2.2.5 the ZEUS data acquisition system contains a three-leveled trigger system which reduces the event rate to roughly 3 Hz. This represents the online selection of events while taking data. On each level there are dedicated logics, called slots, which are specifically designed to select CC events. The logics of the slots used in this analysis are listed in detail in Table 4.7 and are described in the following. This description is rather technical and detailed as a complete description is missing elsewhere and retrieving it is quite difficult.

In Fig. 4.16 the hit distribution of the slots that triggered the events of the final CC sample

FLT 41	$E_t^{-2\mathrm{ir}} > 21\,\mathrm{GeV}$
FLT 42	$N_{\text{good-trk}} > 0$ **and** $\begin{pmatrix} E_{\mathrm{CAL}} > 15.0\,\mathrm{GeV} \\ \textbf{or } E_{\mathrm{EMC}} > 10.0\,\mathrm{GeV} \\ \textbf{or } E_{\mathrm{BEMC}} > 3.4\,\mathrm{GeV} \\ \textbf{or } E_{\mathrm{REMC}} > 2.0\,\mathrm{GeV} \end{pmatrix}$
FLT 43	$N_{\text{good-trk}} > 0$ **and** $E_t^{-2\mathrm{ir}} > 11.6\,\mathrm{GeV}$
FLT 44	$E_{\mathrm{REMC}} > 3.4\,\mathrm{GeV}$ **or** ($E_{\mathrm{BEMC}} > 4.8\,\mathrm{GeV}$ **and** $N_{\mathrm{trk}} > 0$)
FLT 60	$P_t > 5.1\,\mathrm{GeV}$ **and** $E_t^{-2\mathrm{ir}} > 5.1\,\mathrm{GeV}$ **and** $N_{\text{good-trk}} > 0$) **or** $P_t > 8.0\,\mathrm{GeV}$ **and** $\begin{pmatrix} N_{\mathrm{track}} > 0 \\ \textbf{or } E_{\mathrm{FCAL}} > 10.0\,\mathrm{GeV} \end{pmatrix}$
FLT 61	$N_{\text{good-trk}} > 0$ **and** $P_t > 3.0\,\mathrm{GeV}$ **and** $E_{\mathrm{FCAL-BP}} < 1.3\,\mathrm{GeV}$
SLT EXO 4	$\begin{pmatrix} P_t > 9\,\mathrm{GeV}$ **and** $\begin{pmatrix} P_t^{-ir} > 8\,\mathrm{GeV}$ **and** $E_{\mathrm{FCAL}} > 20\,\mathrm{GeV} \\ \textbf{or } P_T^2/E_T > 4.4\,\mathrm{GeV}$ **and** $E_{\mathrm{FCAL}} > 80\,\mathrm{GeV} \end{pmatrix}$ **or** $\begin{pmatrix} P_t > 6\,\mathrm{GeV}$ **and** $E_t^{-2ir} > 6\,\mathrm{GeV} \\ \delta > 6\,\mathrm{GeV}$ **and** $P_t^2/E_t > 2.3\,\mathrm{GeV} \end{pmatrix}$ **and** $\begin{pmatrix} N_{\text{good-trk}}^{\mathrm{FLT}} > 0 \\ \textbf{or } N_{\mathrm{trk}} > 0 \end{pmatrix}$ $\end{pmatrix}$ **and** $\begin{pmatrix} \lvert t_{\mathrm{global}}\rvert < 7\,\mathrm{ns}$ **and** $N_{\mathrm{PMs}} > 1 \\ \textbf{or } N_{\mathrm{trk}} > 0$ **and not** Beam-Gas $\end{pmatrix}$ **and not** $(\lvert Py\rvert < 3\,\mathrm{GeV}$ **and** $P_t < 15\,\mathrm{GeV}$ **and** $P_t^{-ir} < 6\,\mathrm{GeV}$ **and** $P_t/P_z < 0.06)$
TLT EXO 2	$P_t > 6\,\mathrm{GeV}$ **and** $N_{\text{good-trk}} > 0$ **and** GoodVertex **and** UDTimeOK
TLT EXO 6	$P_t > 8\,\mathrm{GeV}$ **and** EXO SLT 4 **and** UDTimeOK **and not** BeamGasVertex **and** $\begin{pmatrix} \textbf{not } \text{TooManyBeamGasTracks} \\ \textbf{or } \text{TwoTrackGoodVertex} \end{pmatrix}$ **and** $\begin{pmatrix} N_{CTD-Hits} < 2500 \\ \textbf{or } P_t^{-ir} > 10\,\mathrm{GeV} \end{pmatrix}$ **and** $\begin{pmatrix} E_{\mathrm{FCAL}} > 10\,\mathrm{GeV} \\ \textbf{or } N_{\text{good-trk}}^{FLT} > 0 \end{pmatrix}$ **and not** $\begin{pmatrix} \lvert Py\rvert < 4\,\mathrm{GeV}$ **and** $P_t < 25\,\mathrm{GeV}$ **and** $P_t^{-ir} < 10\,\mathrm{GeV} \\ \textbf{and } P_t/P_z < 0.08$ **and** $P_t/E_t < 0.7$ **and** $\delta < 10\,\mathrm{GeV} \end{pmatrix}$
DST 34	$P_t > 7\,\mathrm{GeV}$ **and** $\begin{pmatrix} \text{TLT EXO 2} \\ \textbf{or } \text{TLT EXO 6} \\ \textbf{or } P_t^{-ir} > 6\,\mathrm{GeV} \end{pmatrix}$

Table 4.7: Definition of the trigger slots. If not stated otherwise the quantities are reconstructed with the algorithm of the corresponding level.

is shown. In addition the number of events triggered exclusively by one slot of a level are given. The calorimeter information used for the trigger decision are the energies of a part (F/B/R) or of a section (EMC/HAC) or any combination of it, e.g. E_{BEMC} denotes the energy in the electromagnetic section of the barrel part of the calorimeter. Important are the scalar and vector sums of the transversal energies, E_t and P_t, respectively.

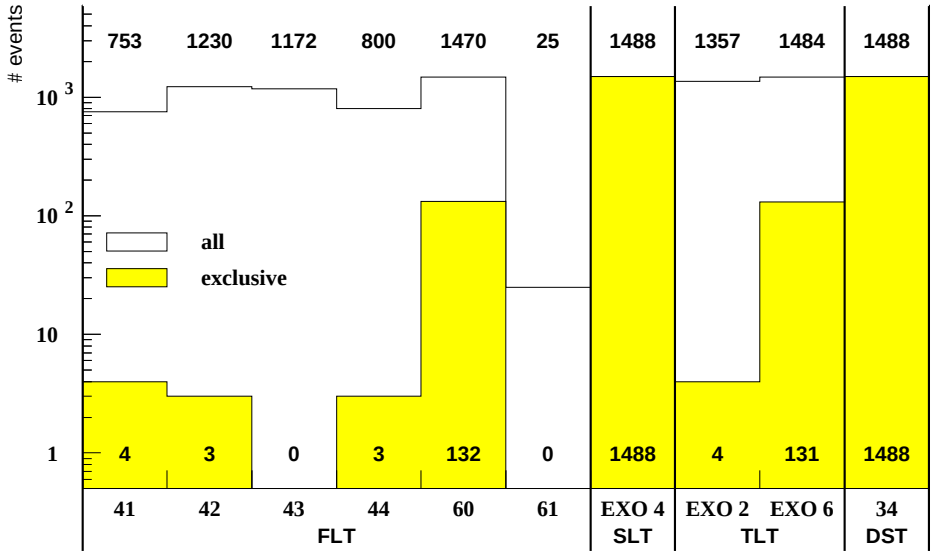

Figure 4.16: Distribution of the slots which triggered the events of the final CC-signal sample. In addition the number of events triggered exclusively by one slot of a trigger level are given.

4.3.2.1 First level trigger

The FLT quantities are restricted only coarsely due to the short time for their acquisition. While some quantities like the calorimeter energies are available in limited precision, others like a reconstructed vertex are not available at all. From tracking the number of tracks (N_{trk}) and the number of good tracks ($N_{\text{good-trk}}$), which are coarsely pointing to the nominal interaction point, are available. On the FLT-level E_t does not include the two innermost rings of towers around the beam pipe in the forward direction, and thus is denoted as E_t^{-2ir}. Excluding the innermost rings suppresses interactions of protons with the rest gas in the beam pipe that can lead to large contributions of their energy deposit in these towers, as the center-of-mass system in these interactions is heavily boosted in the forward direction and allows energy deposits only in a restricted angular region around the beam pipe.

There are six first level slots that select CC events:

FLT 41 is based solely on a rather high threshold for the cut on the transverse energy excluding the two innermost rings of calorimeter towers around the beam pipe in the forward direction.

FLT 42 requires in addition to a good FLT-track an energy deposit in the total or some part or some section of a part of the calorimeter.

FLT 43 features a lower threshold on the transverse energy than slot FLT 41, but requires a good FLT-track in addition.

FLT 44 requires an energy deposit in the EMC section of the rear or barrel calorimeter in addition to an FLT track.

FLT 60 is the main slot which selects almost all CC events. While events with a lower missing energy are required to have also some transverse energy and a good FLT-track, those with higher missing energy are selected in case of an FLT-track or a large energy deposit in FCAL. The latter requirement is especially designed for CC events where the hadronic final state is at small angles, thus outside the acceptance of the CTD, and should lead to large energy deposits in FCAL.

FLT 61 requires in addition to a moderate missing energy and a good FLT-track only a limited energy deposit around the beam pipe in the forward direction. This corresponds to the signature of diffractive events (see Sect. 4.6.2), for which this slot is especially designed.

One should note that only slot 41 and one of the **or**-ed requirements of slot 60 are selecting events without a track requirement, thus events where the hadronic final state is outside the CTD acceptance. As can be seen from the distribution of the trigger information in Fig. 4.16 the signal sample has almost completely (1470 of 1488 events) been triggered by FLT 60. The role of the other slots is mainly to allow for independent cross checks, as in Sect. 4.3.4, and to cover minor deficits of FLT 60 at high-y and low-P_t.

4.3.2.2 Second level trigger

On the second level some calculated quantities are available like P_t^2/E_t, $\delta = E - P_z$ and the transverse momentum excluding the towers in the innermost ring around the beam pipe in the forward direction (P_t^{-ir}). In addition, timing information of the calorimeter deposits (t_{global}) can be used to suppress non ep-collision background, as long as the number of PMs (N_{PMTs}) used in the timing reconstruction is large enough. A coarse tracking results in a vertex, which in case of being far outside of the CTD range leads to the Beam Gas veto rejecting the event. In the data taking period of 98/99 where Hera was operated using electrons the beam-gas background worsened considerably, a phenomenon which was called Off-Beam Protons. These events led to an asymmetric distribution in the azimuthal angle of the P_t, typically at $P_x < 0\,\text{GeV}$ and $|P_y|$ some few GeV. To avoid high dead-time by triggering on these beam-gas events an additional logic, the last line of the SLT EXO 4 description in Table 4.7, was set up to especially suppress this event class without affecting the CC signal. The positron data-taking period under study did not show this problem anymore, the logic in the trigger remained, though. Only SLT-slot 41 is designed to trigger especially CC events. Except for the vetos described above it consists of four branches. The first two do not contain a tracking requirement, but require an energy deposit in the FCAL. The latter two require a track and thus lower the P_t condition to 6 GeV.

4.3.2.3 Third level trigger

On the third level the event information is already close to offline quality. This calls for complex logics. The ones used are described in the following:

UDTimeOK This checks the difference in the timing of the energy deposits in different calorimeter parts. Cosmics typically hit the upper half of the calorimeter several ns earlier than the lower half. The veto is set if the difference is larger than 8 ns or three times the reconstruction uncertainty.

BeamGasVertex If the z-position of the reconstructed vertex is too far off the nominal interaction vertex ($z_{vtx} < -80\,\mathrm{cm}$) and if there is a minimum number of tracks ($N_{\mathrm{trk}} \geq 5$) from this vertex it is considered to be a beam-gas event.

TooManyBeamGasTracks This veto is set if the number of tracks, N_{trk}, exceeds 25 and the number of those with trajectories closest to the beam line far outside the interaction region ($< -80\,\mathrm{cm}$) exceeds 8.

TwoTrackGoodVertex For this flag the vertex has to lie within $\pm 60\,\mathrm{cm}$ of the nominal interaction vertex with at least two tracks pointing at it.

There are two slots for triggering CC events on the third level, TLT EXO 6, which is the main slot, and TLT EXO 2 which was needed for four additional events, as seen from Fig. 4.16. While TLT EXO 2 contains a track requirement, therefore does not trigger events with the hadronic final state outside the CTD acceptance, TLT EXO 6 requires a good FLT track *or* an energy deposit in the FCAL. In addition to the tracking vetoes described above to reject cosmic and beam-gas events, TLT EXO 6 has an off-beam proton suppression. The P_t cut is raised for this slot to $P_t > 8\,\mathrm{GeV}$.

4.3.3 Performance of the calorimeter FLT

Since the calorimeter quantities are of crucial importance to the analysis the part of the FLT which is responsible for the calorimeter information (CFLT) has been studied thoroughly. Events not triggered by the CFLT are unrecoverably lost for the analysis and could create a bias located at a kinematic region corresponding to the P_t of the lost events.

Special attention has been devoted to the threshold behavior of the P_t cut in the FLT 60, which triggers most of the final signal events. For this reason a data quality monitoring job fills for each run a histogram containing the number of events versus P_t as reconstructed by the trigger simulation on calorimeter-cell basis. The efficiency is obtained by dividing the number of events that passed the online trigger, i.e. had an online P_t above threshold, by the total number of events. This is done for a subsample of events that passed an orthogonal trigger to ensure that the event selection is unbiased. A turn-on curve is fitted to the region $0.5 - 15.0\,\mathrm{GeV}$ of this histograms, of the form:

$$f = 1 - \frac{1}{e^{P_s \cdot (x - P_t)} + 1}. \tag{4.19}$$

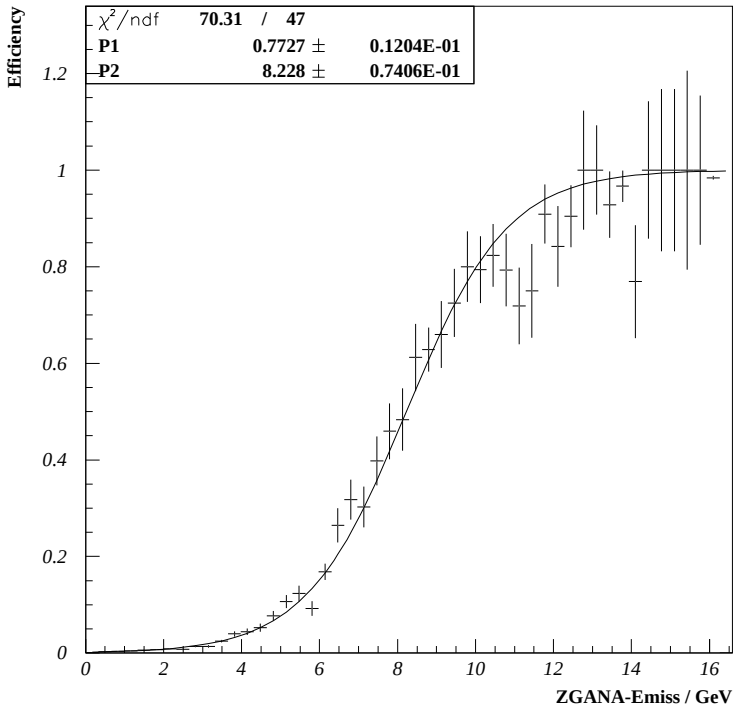

Figure 4.17: Efficiency of the CFLT versus P_t as reconstructed by the trigger simulation with the fit of the turn-on curve Equation (4.19) for an example run. The last bin contains all events with $P_t > 16\,\text{GeV}$.

An example of the fit to the histogram for one run is given in Fig. 4.17. Note that the last bin contains the overflow, i.e. all events with $P_t > 16\,\text{GeV}$. The resulting fit-parameters, turning point (P_t) and slope at turning point (P_s), are then plotted in Figs. 4.18 and 4.19 versus the run index of all physics runs of the data taking period. The runs showing a deviation from the mean value of the fit parameters of more than three standard deviations were checked individually. They have either low statistics resulting in a misled fit, or have a lower turning point. The latter is not expected to be a problem, because the logics of the following levels raise the cut in P_t consecutively, yielding insensitivity to the low side of the turning point. The operation of the CFLT is thus shown to be stable, as the fit parameters show no significant dependence on the run index.

4.3.4 FLT 60 efficiency

Since the FLT slot 60 plays an important role in selecting CC events the performance of the complete slot, not just the calorimeter FLT, is compared to the MC simulation. Also here the turn-on behavior is of key interest. The branch of FLT 60 with the track requirement has a P_t threshold of 8 GeV. This can be tested by the independent trigger slot FLT 42, which requires also a track, together with a logical **or** of several conditions on the calorimeter energy deposits given in Table 4.7, and is sensitive to much lower values of P_t. The efficiency of slot FLT 60 is then defined as the number of events that pass both trigger slots, FLT 42 & 60, divided by those passing FLT 42. For the comparison with

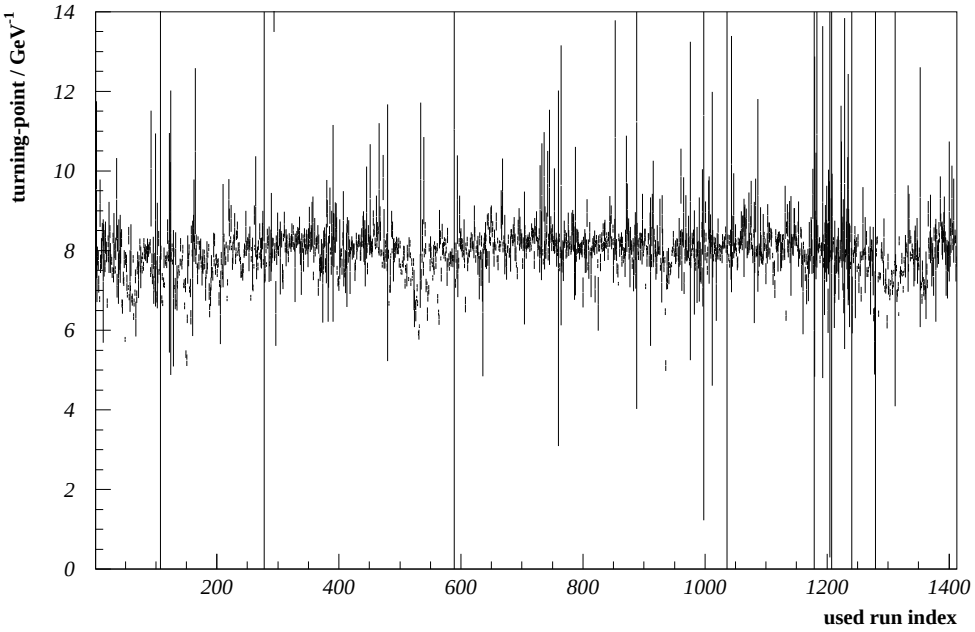

Figure 4.18: The fit parameter "turning point" P_t versus run index

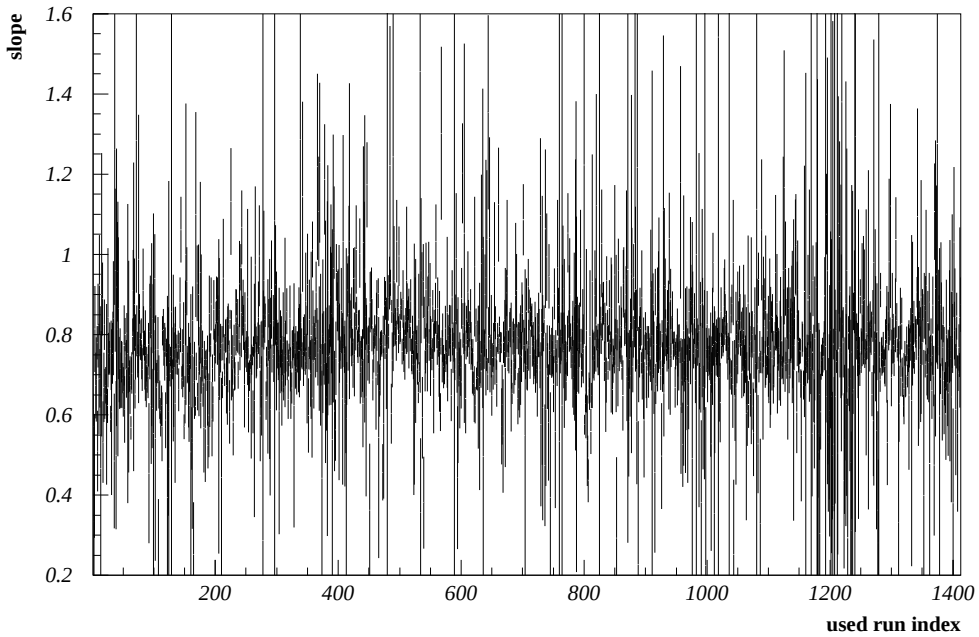

Figure 4.19: The fit parameter "slope at turning point" P_s versus run index

MC the data event-sample has to be specially prepared. The sample has to be cleaned from background since non-CC events may have a deviating triggering efficiency. The final CC selection, however, is not very well suited as it cuts in various ways into the P_t distribution. Hence, the event sample for this efficiency comparison has been selected by requiring the SLT and TLT trigger decisions in addition to a reconstructed vertex within 50 cm of the nominal interaction vertex to suppress non-beam-gas background and a loose

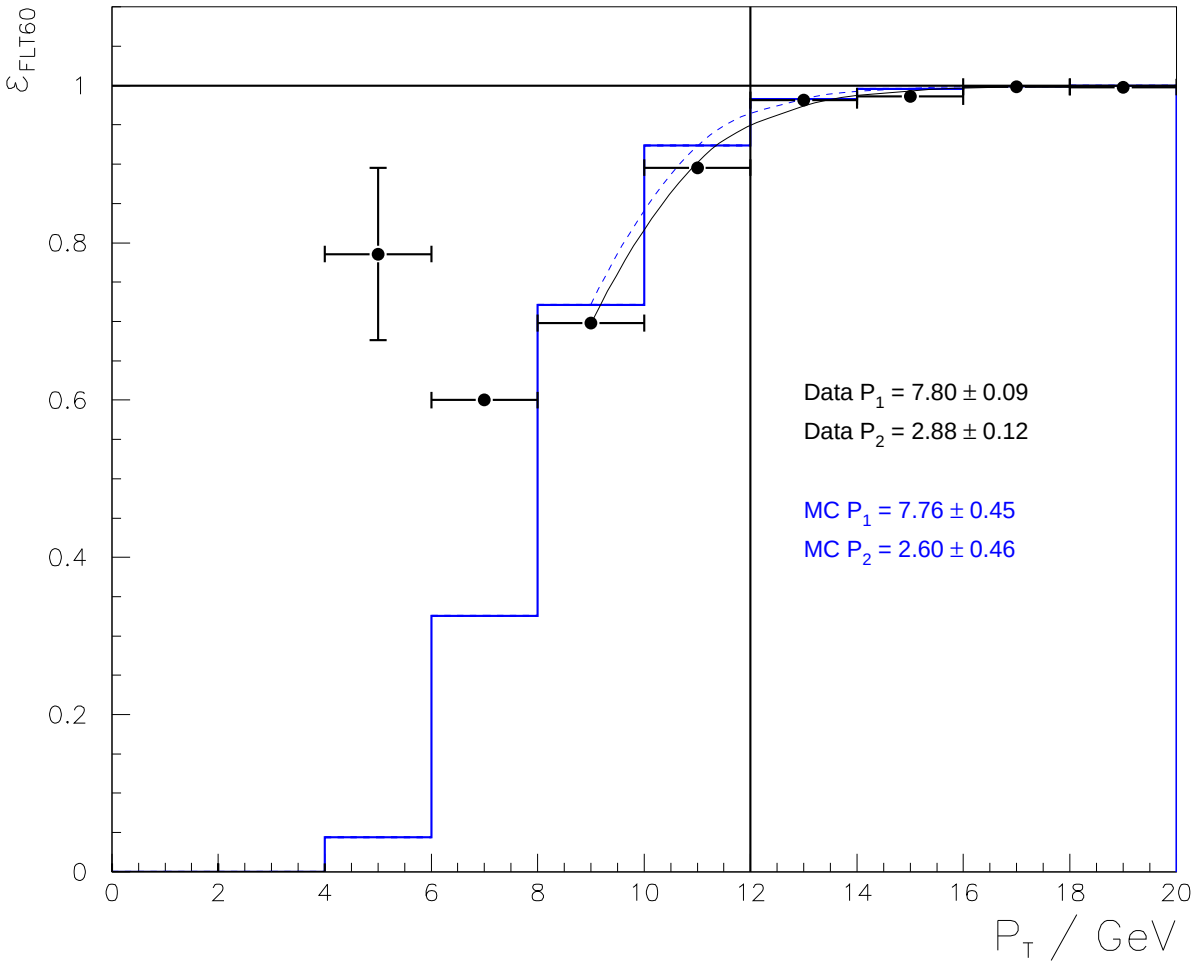

Figure 4.20: Efficiency of FLT 60 versus P_t for events triggered with FLT 42. The points show data and the histogram the MC. The solid (dashed) line shows the fit result of a turn on-curve (4.20) to the data (MC).

cut $P_t/E_t > 0.4$ to reduce photoproduction events. The efficiency is plotted versus P_t for data and MC in Fig. 4.20. In addition, the result of a turn-on curve parameterized as

$$\epsilon_{\text{flt}} = 0.5 \cdot \tanh\left(\frac{P_t - P_1}{P_2}\right) + 0.5 \tag{4.20}$$

is shown for both data and MC. The fit of the turn-on curve has been restricted to $P_t > 8\,\text{GeV}$. Below this threshold the data and MC show a disagreement due to background events in the special prepared data sample, which has no effect on the analysis since it is far below the offline threshold. The effect of a slight disagreement in the turn-on behavior has been studied in [65] by re-weighting the MC events with the ratio of the parameterizations using the fit result for data and MC. This procedure yielded an effect on the cross-section measurements which is negligible, especially when considering that the uncertainty of the estimated efficiency has been ignored in this study. Therefore it is neglected in this analysis.

4.3.5 Overall online trigger efficiency

The overall efficiency of the online trigger has been determined using the MC simulation. It is 96% for the whole kinematic region of the cross section measurements (Sect. 4.3.13). For single double-differential cross-section bins it is never below 78%.

4.3.6 Run selection

The offline selection starts with the Data Summary Tape (DST) selection bit 34. This bit selects events with $P_t > 7\,\text{GeV}$ and either TLT EXO 2, TLT EXO 6 or $P_t^{\text{-}ir} > 6\,\text{GeV}$. For the positron running period 1999/2000 the database contains 1185048 events in 1558 runs in the run-number range between 33125 and 37715 with DST 34 set. This list contains only runs, that passed the ZEUS data quality monitoring (DQM). In addition a list provided by the DQM of the physics group gave reasons to exclude another 200 runs with a combined integrated luminosity of $5.4\,\text{pb}^{-1}$. The remaining 1358 runs make up a total integrated luminosity of $60.9 \pm 2.25\%\,\text{pb}^{-1}$ used in this analysis. The distribution of luminosity per run is shown in Fig. 4.21. Except for the first bin corresponding to the sum of runs below $100\,\mu\text{b}^{-1}$ it is well described by an exponential function with a fit giving a mean run length equivalent to $485\,\mu\text{b}^{-1}$.

A check how seriously the quality of the data may be corrupted, especially for a CC analysis, is given by the yield Y defined as number of selected events per luminosity.

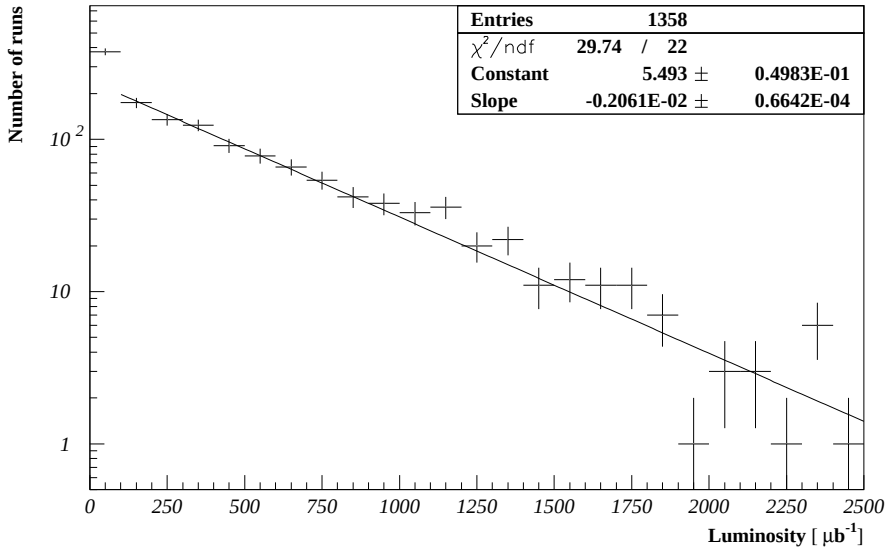

Figure 4.21: Distribution of the luminosity per run for the 1358 runs used for the analysis. A fit excluding the first bin of runs with $\mathcal{L} < 100\,\mu\text{b}^{-1}$ gives a "lifetime" of $485\,\mu\text{b}^{-1}$.

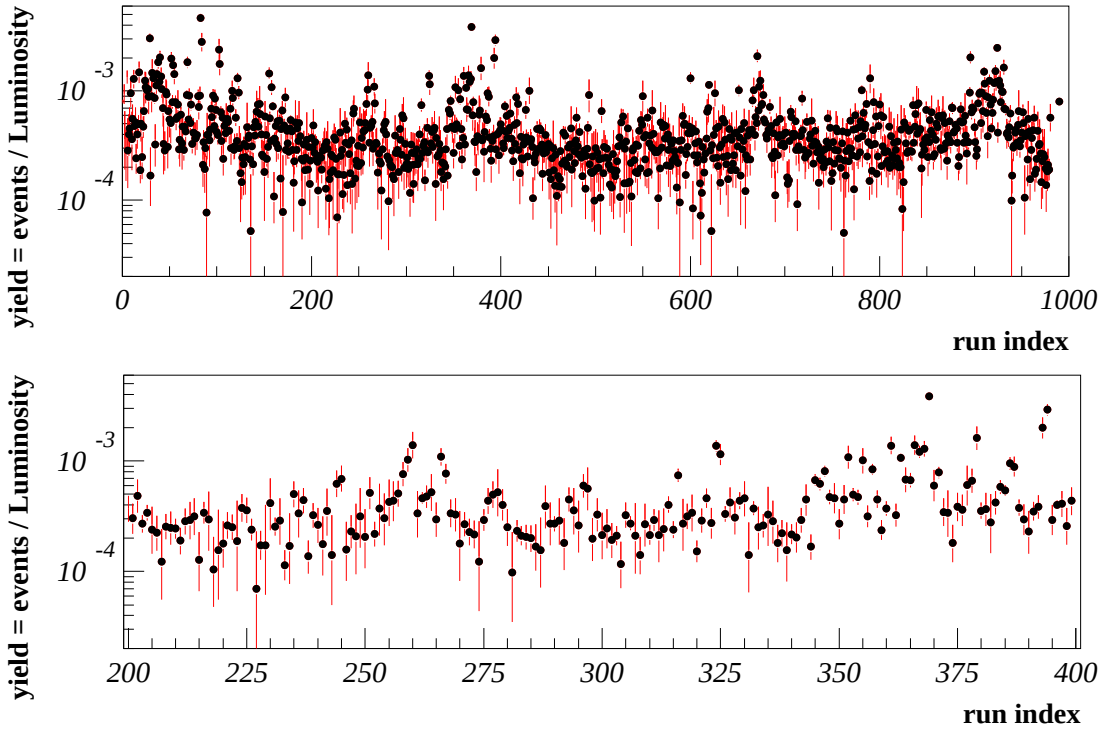

Figure 4.22: Yield defined as number of events per luminosity after preselection versus the index of the selected runs (top) and a zoomed example region (bottom)

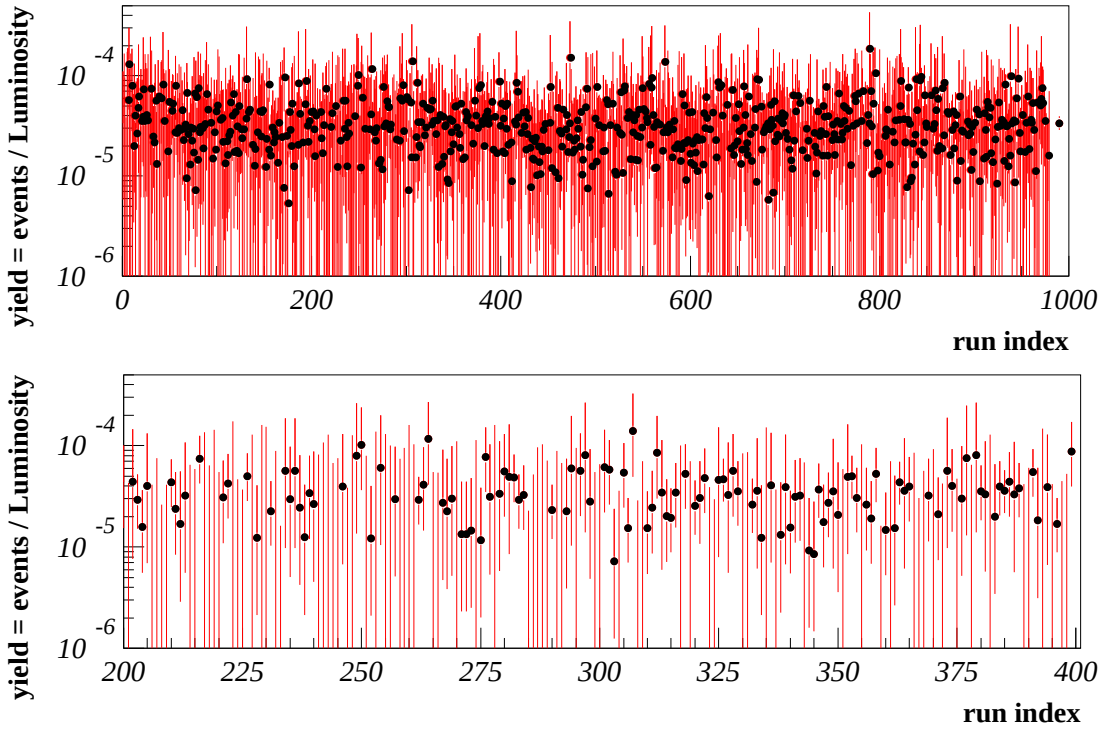

Figure 4.23: Yield for the final CC-signal selection per luminosity versus the index of the selected runs (top) and a zoomed example region (bottom)

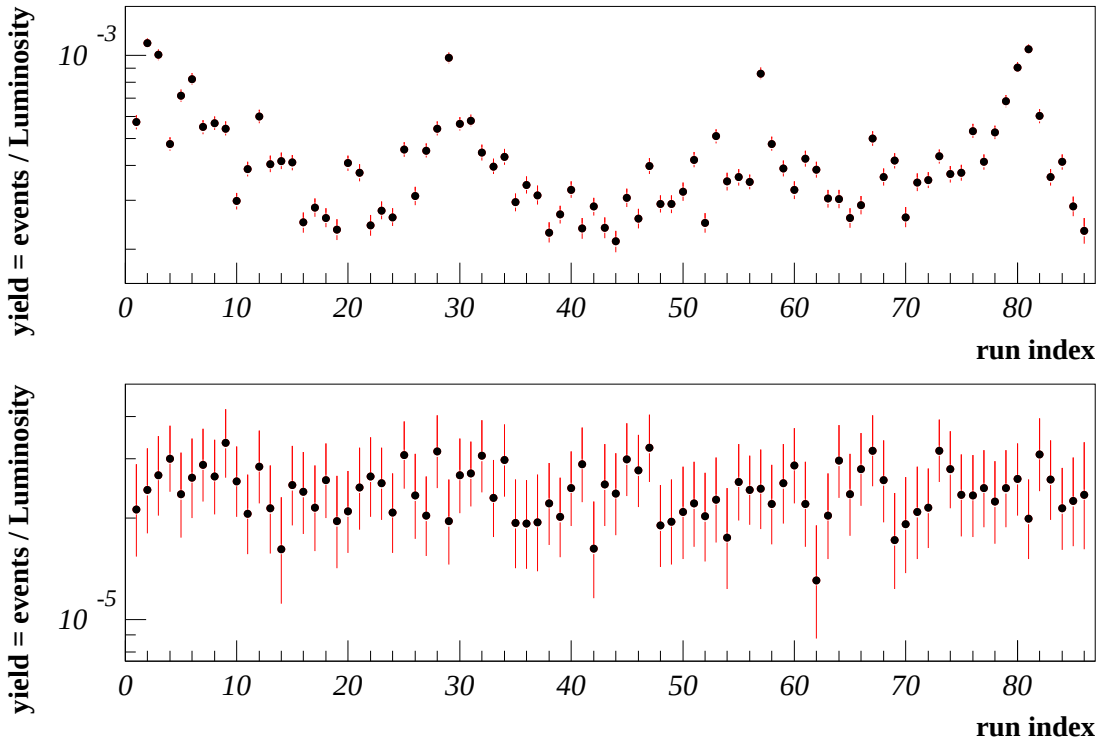

Figure 4.24: Yield defined as number of events per luminosity after preselection (top) and the final CC-signal selection (bottom) in bins of minimum $0.6\,\mathrm{pb}^{-1}$ as described in the text.

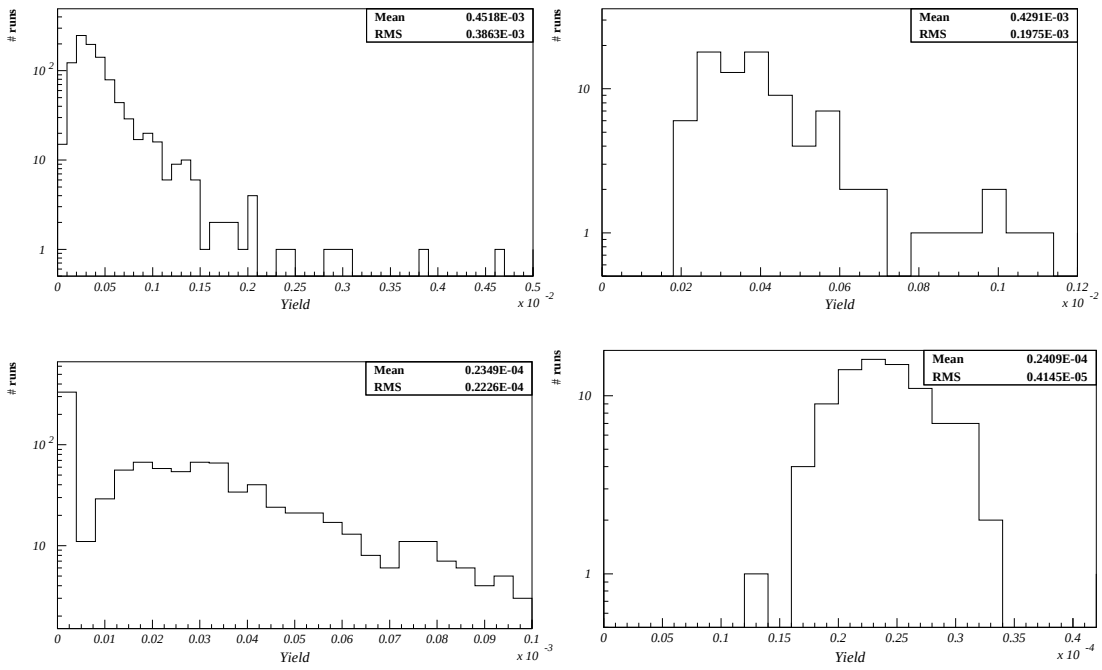

Figure 4.25: Distribution of yield per run (top) and per bin of runs of minimum $0.6\,\mathrm{pb}^{-1}$ as described in the text (bottom) after preselection (left) and after the final CC signal selection (right).

Within statistical fluctuations Y should be constant over the complete run period. A too small or a too large yield immediately points at data quality problems. Most of them are caused by parts of the calorimeter giving either no or a constant signal, or by bad beam conditions. The problem here is to choose the right selection for the events entering the yield calculation. Using the final signal selection would not leave enough statistics for a significant determination of the run quality. A selection which is too loose, however, could suffer from problems that may get removed later by the appropriate cuts, i.e. indicate a quality problem which is coped with by further selection mechanisms. In Fig. 4.22 the yield for selected runs of the running period is plotted per run. To be not misled by runs with small luminosity those with a luminosity of less than $100\,\mu\mathrm{b}^{-1}$ are combined in one run to yield significant statistics. The plot showing the yield at preselection level as defined in Sect. 4.3.7 hints at specific runs incompatible with a constant yield. The analog plot in Fig. 4.23 for the CC signal events after the selection cuts shows no incompatibility, but lacks statistics for a definitive conclusion. A better test is obtained by combining runs in chronological order in bins of at least $0.6\,\mathrm{pb}^{-1}$. This demonstrates much better the effect of the final CC signal-event selection on the data quality, as is shown in Fig. 4.24. While the preselection still leaves signs of varying data quality the final CC signals are consistent with a constant yield. Small runs with quality problems, however, could be hidden within the bins, but this has been excluded by the more detailed yield per run study above. This conclusion can be drawn from the distribution of the yield, which is approximately Gaussian for the CC signal but has a tail towards higher values at preselection, as shown in Fig. 4.25.

The arguments provided establish the necessary data quality after the run-selection, but only by anticipating the background suppressing effect of the CC signal selection cuts.

4.3.7 Offline preselection

The offline preselection proceeds in two steps and has the aim at the first step of reducing the data processing time to obtain the data volume for analysis and in the second step to reduce the data volume itself. Both steps must not affect signal events. Therefore the efficiency for the signal has to be 100% while the signal-to-background ratio will not necessarily be increased optimally. For the first step, the reduction of the processing time, the variables available do not include final corrections of the reconstructed quantities, as described in Sect. 4.2. The cuts used at this stage are not needed in the end for the separation of signal from background, because other more efficient cuts will be presented. For the second step, after processing the event, the event sample is reduced by applying some cuts on the signal signature. The cuts used are described in the following paragraphs. In the ensuing documentation the event sample referred to is the one after the preselection described here, except for the documentation of some special cuts, where a more general preselection is needed to obtain a sample with sufficient background contribution to study the signature of a specific event class. The total number of events after the preselection is 50724, This means that the data-volume is reduced already by 95.7% compared to the number of events writen to tape with DST bit 34 (see Sect. 4.3.6).

4.3.7.1 Halo muon suppression by P_t/E_t

A major background are halo-muon events. One way of rejecting them at an early stage is inspecting P_t/E_t, where P_t and E_t are the vector and scalar sums of the transversal energies, respectively. Since halo muons traverse the detector parallel to the beam axis they deposit energy in the calorimeter at the same position in the perpendicular plane. This results in the equivalence of vector and scalar sum. Hence, for halo muon events we expect $P_t/E_t \approx 1$. Figure 4.26 shows the region close to 1 of the P_t/E_t distribution, where P_t/E_t is reconstructed on calorimeter cell basis (Cal P_t/E_t), which is available at the preselection stage, and for the final value after all corrections have been applied (Cor&Cut P_t/E_t). In both cases there is an accumulation of data events very close to unity, while the MC is completely depleted in that region. The correlation between the two reconstruction stages are displayed in Fig. 4.27 for data and MC. In addition to highly correlated events there is another band of events which have a final P_t/E_t close to unity while the cell based one is slightly reduced for the data. This is caused by the corrections described in Sect. 4.2.5 which remove additional energy deposits, leaving only the ones caused by the halo muon. To ensure that the data selection is not affected by this preselection, which is only applied to data, a tighter cut is used for the final selection. The cut applied for the preselection is:

$$\frac{P_t^{\mathrm{Cal}}}{E_t^{\mathrm{Cal}}} < 0.995. \tag{4.21}$$

For the final selection the following cuts have been applied:

$$\frac{P_t^{\mathrm{Cal}}}{E_t^{\mathrm{Cal}}} < 0.994 \qquad \text{and} \qquad \frac{P_t^{\mathrm{Cor\&Cut}}}{E_t^{\mathrm{Cor\&Cut}}} < 0.997. \tag{4.22}$$

This modification has, however, no effect on the final event sample.

4.3.7.2 Halo muon suppression by electromagnetic-to-hadronic energy ratio

Particles coming from the interaction point leave some amount of their energy in the electromagnetic section of the calorimeter, especially if we consider only the BCAL. Events that have a minimum energy deposit in the hadronic section but a very low fraction of energy deposit in the electromagnetic section can only be caused by halo muons, that traverse the BCAL parallel to the beam line, i.e. either through BEMC or BHAC, or cosmic muons, which hardly deposit any energy in the calorimeter anyway. The distribution of the BEMC energy fraction for events with more than 2 GeV energy deposit in the hadronic section of the BCAL is displayed in Fig. 4.28. The distribution for data is dominated by background, resulting in a bad decription of the shape by the signal MC distribution. The signal MC has been arbitrarily scaled up for a better comparison. Figure 4.28 indicates that rejecting the very lower end of the distribution has a background reducing effect on the data while maintaining the CC signal. Thus in the preselection the event is required to fulfill the following condition:

$$E_{\mathrm{BHAC}} < 2\,\mathrm{GeV} \quad \textbf{or} \quad \frac{E_{\mathrm{BEMC}}}{E_{\mathrm{BHAC}}} > 0.1. \tag{4.23}$$

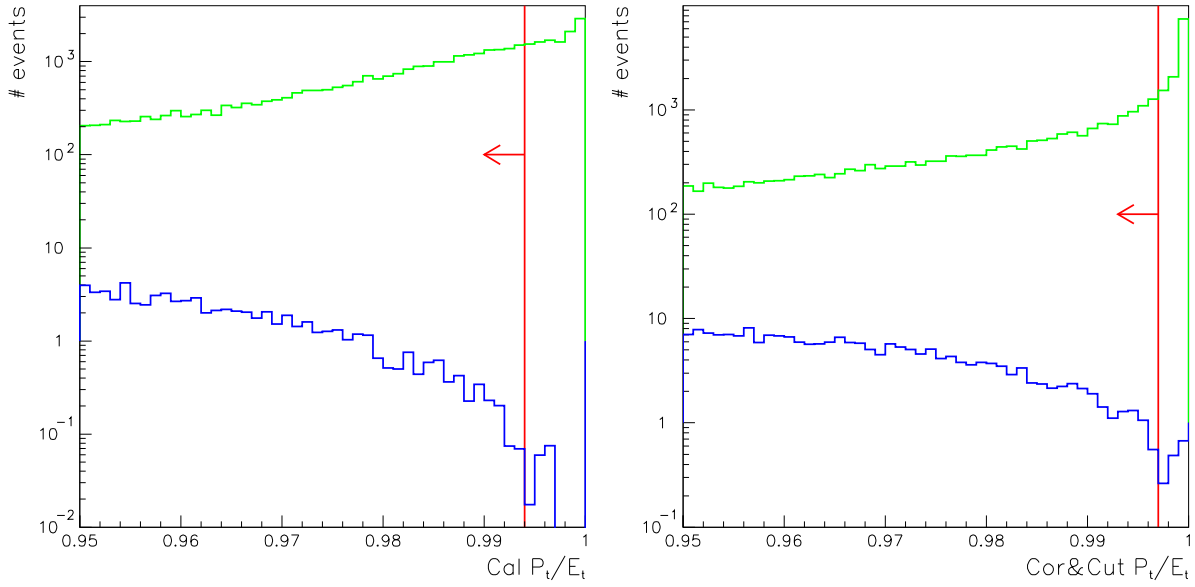

Figure 4.26: P_t/E_t for data (green) and MC (blue) as reconstructed on calorimeter-cell basis (left) and for the final corrected values (right). The vertical lines indicate the cut threshold.

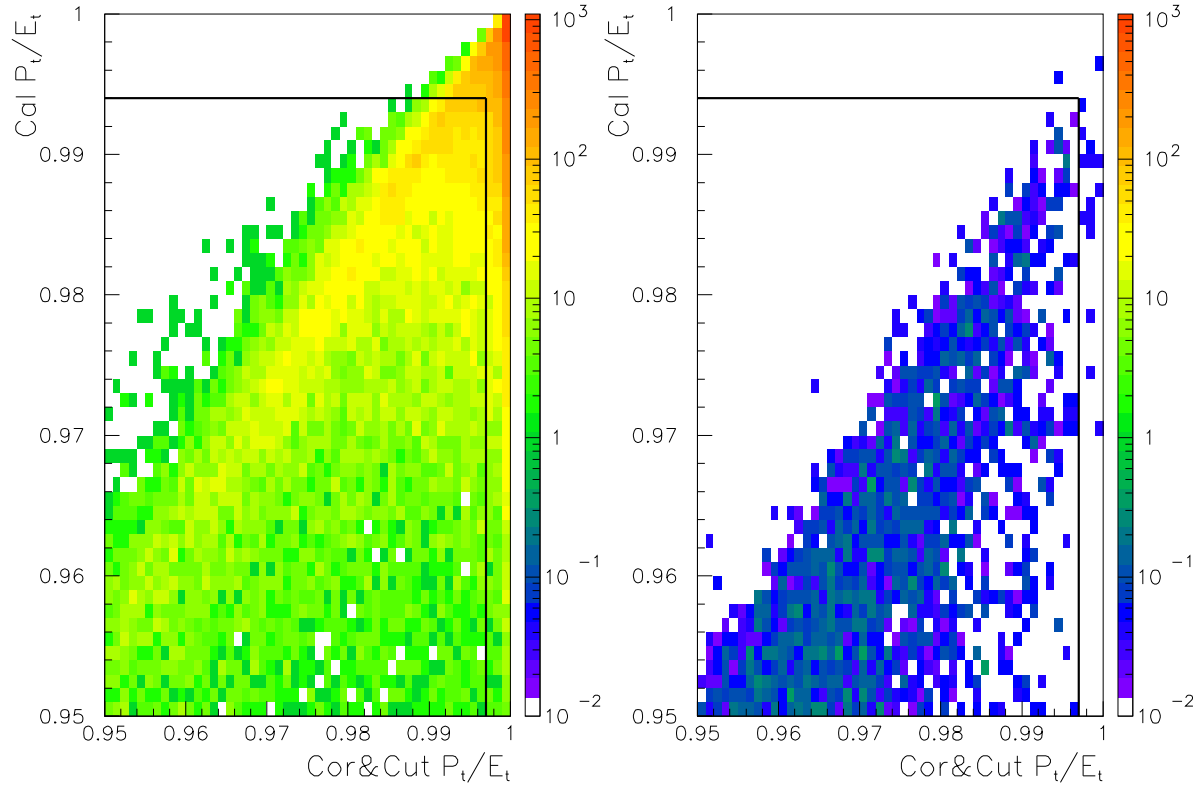

Figure 4.27: P_t/E_t as reconstructed on calorimeter-cell basis versus final corrected values for data (left) and MC (right). The color indicates the number of events in each bin on a logarithmic scale as shown on the right.

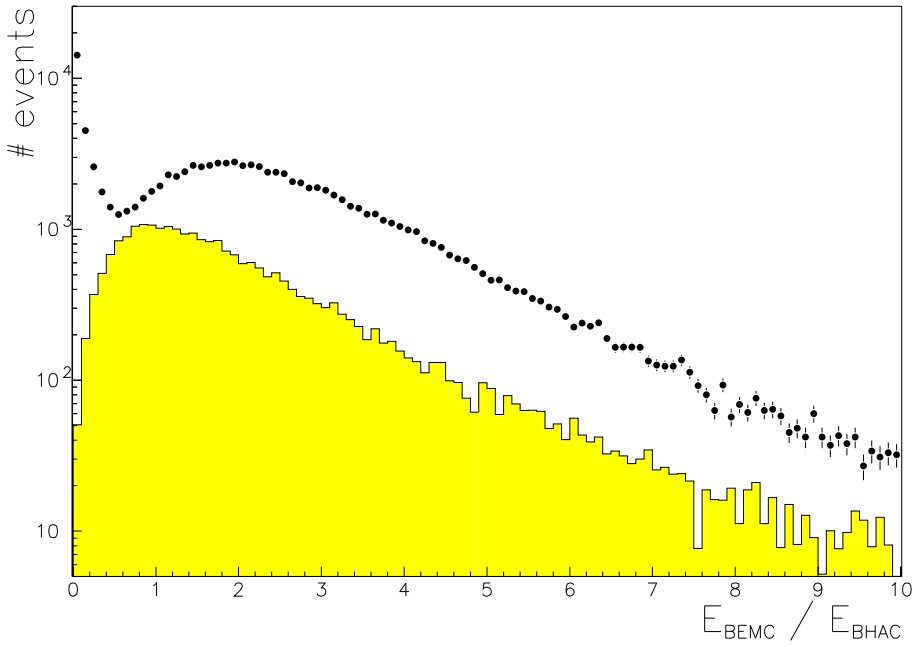

Figure 4.28: Ratio of energy deposits in the electromagnetic and hadronic sections of the BCAL for events with at least 2 GeV energy deposited in the hadronic section. The points represent the data and the histogram the arbitrarily scaled signal MC.

4.3.7.3 Non-*ep* background suppression

For the high-γ sample the tracking is an essential tool for suppressing non-*ep* background like beam-gas reactions. At least one good-track as defined in (4.3) is required for events of the high-γ sample.

4.3.7.4 Preselection of signal region

To reduce the amount of data to be investigated further, some cuts on the signal regions are anticipated. These cuts are not as tight as the final ones to allow for variation of the thresholds in the study of systematic checks in Sect. 4.6. For low P_t the PHP background is overwhelming and a P_t cut is already the main cut of the trigger preselection. The events in the preselected sample are required to exceed $P_t > 10\,\text{GeV}$. The signal region will be reduced later to $Q^2 > 200\,\text{GeV}^2$, but for the preselection a cut of $Q^2 > 180\,\text{GeV}^2$ is anticipated.

4.3.8 Cleaning for technical reasons

There are events that are not excluded in the preselection, but are not signal events because of rather technical reasons.

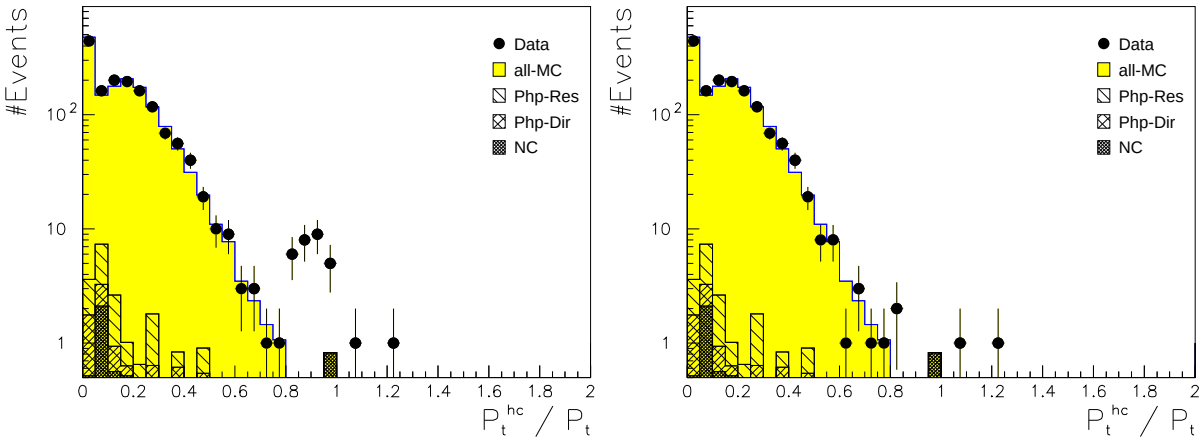

Figure 4.29: Fraction of highest energetic cell over total event transverse momentum P_t^{hc}/P_t, for the final event sample without (left) and with (right) the cut of (4.24) applied.

4.3.8.1 Spark and dead PM coincidence

In Sect. 4.2.1 we already found that spontaneously discharging PMs can fake a non-negligible energy deposit. Usually these are identified by the imbalance between the two PMs of a calorimeter cell. Now if one of them is dead it is reconstructed to the same energy as the good one, as described in Sect. 4.2.1. Therefore the imbalance of cells with one dead PM is always equal to zero. If a spark happens to be in a cell, where the other PM is dead, it can not be detected by means of imbalance, A_{imb}, as given in (4.2). The energy deposit is then twice the spark energy, which can cause a substantial P_t. To detect these kind of events the calorimeter cell with the highest energy is identified. A class of suspicious events where the cell with the highest energy contributed more than half of the event-P_t ($P_t^{\mathrm{hc}}/P_t > 0.5$) has been scanned visually. In combination with the imbalance information of the cell with the highest energy, $A_{\mathrm{imb}}^{\mathrm{hc}}$, it was found that all events visually classified as sparks could be identified by the imbalance $A_{\mathrm{imb}}^{\mathrm{hc}}$ being equal to zero. This detector defect is not simulated in the MC-samples. The acceptance determined using the MC would be overestimated rejecting all events with such a spark. Therefore only those events where this spark faked the CC event-signature, which means it produced a significant amount of the event-P_t, can be excluded. The excess in the fraction of P_t^{hc}/P_t for the signal sample without a cut on $A_{\mathrm{imb}}^{\mathrm{hc}}$ is shown in Fig. 4.29. A clear overshooting of the data is visible that sets on at $P_t^{\mathrm{hc}}/P_t > 0.5$. By rejecting events with a spark and a dead PM in a cell for this region the data signal is well described by the MC. The resulting condition for signal events is:

$$P_t^{\mathrm{hc}}/P_t < 0.5 \qquad \textbf{or} \qquad A_{\mathrm{imb}}^{\mathrm{hc}} \neq 0. \tag{4.24}$$

4.3.8.2 Collision crossing

As described in Sect. 2.1 not all buckets are filled with protons or electrons. There are crossings, where e.g. a filled proton bucket meets an empty electron bucket. Events from such a crossing must be non-*ep* interactions. Single-bunch events are valuable as event source for background studies, as will be used in Sect. 4.3.9. At this stage one has to make sure that only collision crossing events enter the signal sample.

4.3.9 Reduction of beam-gas interactions

Interactions of a beam with rest-gas in the beam pipe can lead to a considerable activity in the detector components. These should have a balanced P_t, though. If, however, the final state is mismeasured in the calorimeter it fakes a missing momentum. A signature of beam-gas events is bad tracking. First of all the reconstructed vertex may be not compatible with the interaction region. As described in Sect. 4.3.2 the TLT already makes use of this. For the trigger the final tracking is not available. Therefore a cut on the vertex position does improve the beam-gas rejection with respect to the trigger level. For a high-γ event with a good vertex we can expect at least one good track as defined in (4.3). In addition, the ratio of good tracks ($N_{\text{good-trk}}$) to all tracks (N_{trk}) provides a handle to discriminate against beam-gas events. Since the final offline criteria for a good-track is applied the offline cut is tighter than a similar cut in the trigger on the FLT number of good tracks as described in Sect. 4.3.2. In Fig. 4.30 the distribution of $N_{\text{good-trk}}$ versus N_{trk} is displayed. For only trigger-selected data the beam-gas background is clearly visible at low $N_{\text{good-trk}}$ and high N_{trk}. For the high-γ sample with all cuts applied except those on tracking quantities the signal shows the same shape as the high-γ sample of the signal MC. The comparison suggests a two-dimensional cut in addition to requiring at least one good track. The offset is chosen to be minus 20. For the slope the graph of $(N_{\text{trk}} - 20)/N_{\text{good-trk}}$ in Fig. 4.31 suggests 4 as optimal cut value. The final condition as indicated by a line in Figs. 4.30 and 4.31 is

$$\frac{N_{\text{trk}} - 20}{N_{\text{good-trk}}} < 4. \tag{4.25}$$

The tracking cuts are not applied to the low-γ sample, since the complicated dependence of the tracking acceptance on several other variables would render these cuts biased.

In addition the shape of beam-gas background has been studied by looking at proton pilot-bunch events. The shape of these events after preselection shows only very small overlap with the signal, while no p pilot-bunch event passes all final selection cuts. Therefore it is concluded that the contamination of beam-gas events remaining in the signal sample is negligible.

4.3.10 Rejection of muons

In Sect. 4.3.7 we introduced already rather coarse methods to reject clean halo-muon events using P_t/E_t and $E_{\text{BEMC}}/E_{\text{BHAC}}$. For the final signal sample we have to reach

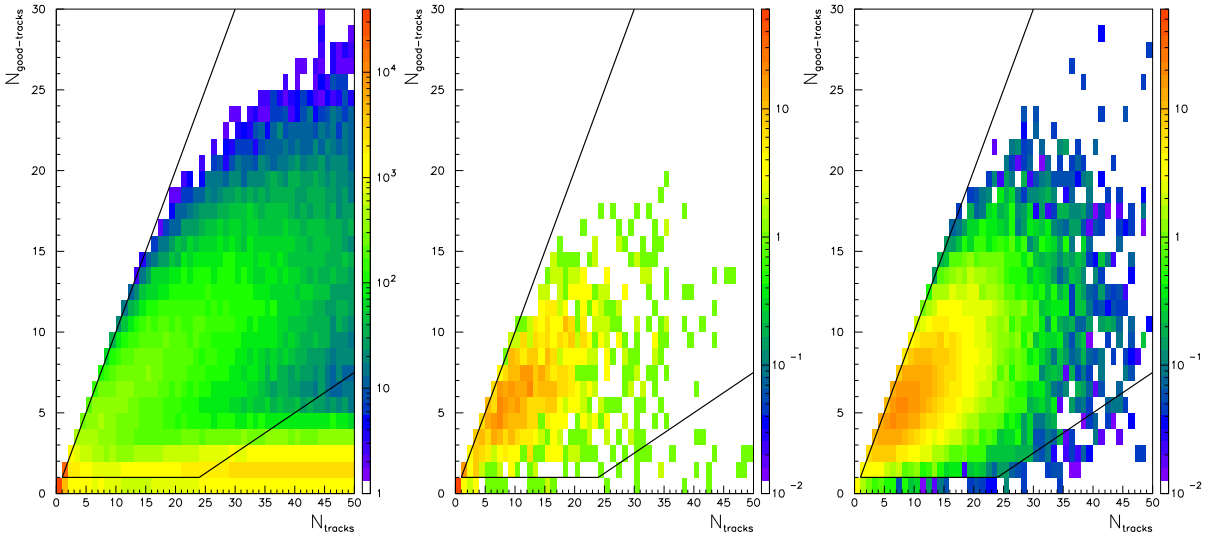

Figure 4.30: The number of good tracks ($N_{\text{good-trk}}$) as defined in (4.3) versus the number of all tracks (N_{trk}) for data before selection-cuts (left), the high-γ data sample with all cuts except on tracking quantities applied (middle) and the high-γ sample of the signal MC (right). The line shows the cut applied on the high-γ sample.

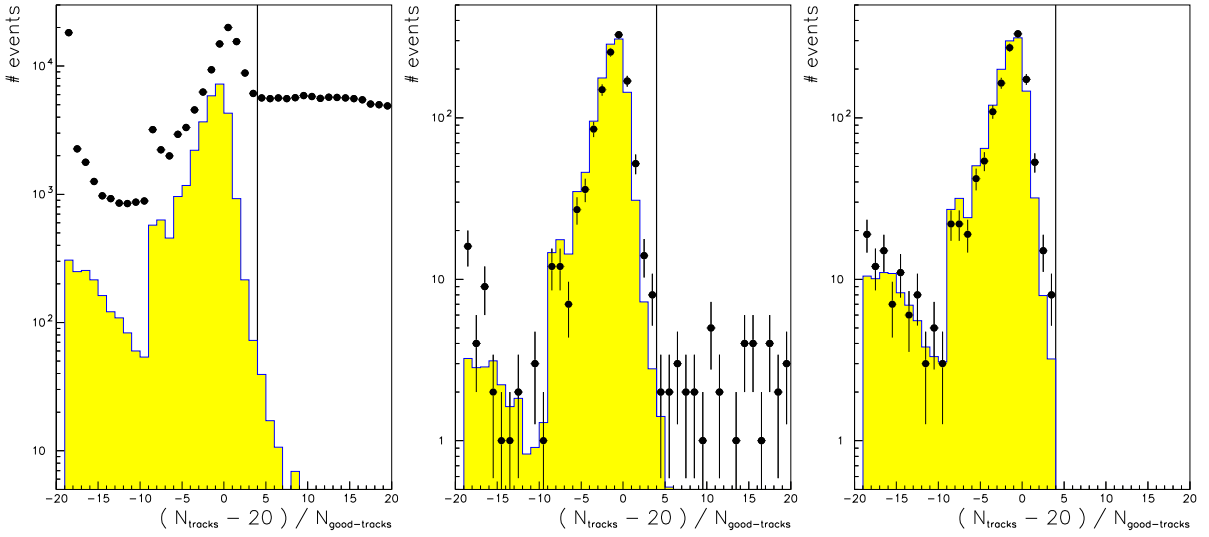

Figure 4.31: Ratio $(N_{\text{trk}} - 20)/N_{\text{good-trk}}$ for data (points) and signal MC (line) for data before selection cuts with the signal MC arbitrarily scaled (left), the high-γ with all cuts except on tracking quantities applied (middle) and the final signal sample (right). The vertical line shows the cut-value of 4.

a very high purity excluding completely a contamination from halo-muon events. The most significant muon signature is the shower shape in the calorimeter. Most muons traverse many interaction lengths X_0 of material without depositing more than a minimal ionizing particle. Halo muons are going through the detector parallel to the beam line, i.e. parallel to the segmentation of the calorimeter. The signature of a track-like cluster is therefore preserved in the calorimeter geometry within the horizontal segmentation as number of cells of the EMC/HAC section belonging to a cluster. This does not apply to cosmic muons, which have an arbitrary angle with respect to the segmentation axis of the calorimeter. Here, to determine track-likeness requires to take into account the absolute positions of cells with energy deposits. This is quite complicated and a software tool called MUFFIN [66] has been developed to identify not only halo but also cosmic muons. This code has been used to analyze all preselected events and they are rejected from the analysis if the output of MUFFIN identifies the event as halo or cosmic muon. While MUFFIN has 100% acceptance when applied to the signal MC sample, it does not identify all halo-muon events, as will be explained further in Sect. 4.3.14. For halo-muons the other method used is based on the shower characteristics of the condensate with the highest energy in the FCAL. For this condensate number of cells and energy per calorimeter section are reconstructed as event quantities. The shower width corresponds to the number of cells in a section, since cells are the horizontal segmentation. Energy fractions for the sections are used to identify the non-hadronic and non-electromagnetic but MIPS character of the muons. If the total energy in FCAL exceeds 2 GeV the event is rejected if one of the following conditions is fulfilled:

$$\begin{aligned} E_{\mathrm{FEMC}}/E_{\mathrm{FCAL}} &< 0.15 \\ E_{\mathrm{FHAC1}}/E_{\mathrm{FCAL}} &< 0.1 \\ E_{\mathrm{FHAC2}}/E_{\mathrm{FCAL}} &> 0.6 \\ N_{\mathrm{FHAC1}} &\leq 4 \\ E_{\mathrm{FHAC1}} &\leq 5\,\mathrm{GeV}. \end{aligned} \tag{4.26}$$

The cuts on the FHAC2 quantities are not more sensitive than the cuts applied to the FEMC and FHAC1 quantities. As a consequence no cuts are imposed on N_{FHAC2} and E_{FHAC2}. In Fig. 4.32 and 4.33 the effect of the cuts on these quantities used by the cuts can be seen. The rejection of events using MUFFIN further improves the agreement of data and signal MC.

The cuts (4.26) are not applied to the high-γ sample. It is not necessary, since halo-muon events are usually rejected by the good-track criteria in the high-γ sample. In addition, the hadronic final state is mainly in the BCAL for events of the high-γ sample, making this cut sensitive to energy deposits of the proton remnant only. Since the proton remnant has in some cases unusual shower properties the event might be rejected by the cuts.

4.3.11 Reduction of photoproduction background

As described in Sect. 4.1.1.2, mismeasurement of the hadronic final state can result in a non-balanced P_t and mimic the CC signature. In addition, $P_t \neq 0$ can be produced by an overlay with a halo-muon. Though these probabilities to fake a P_t are small, the high

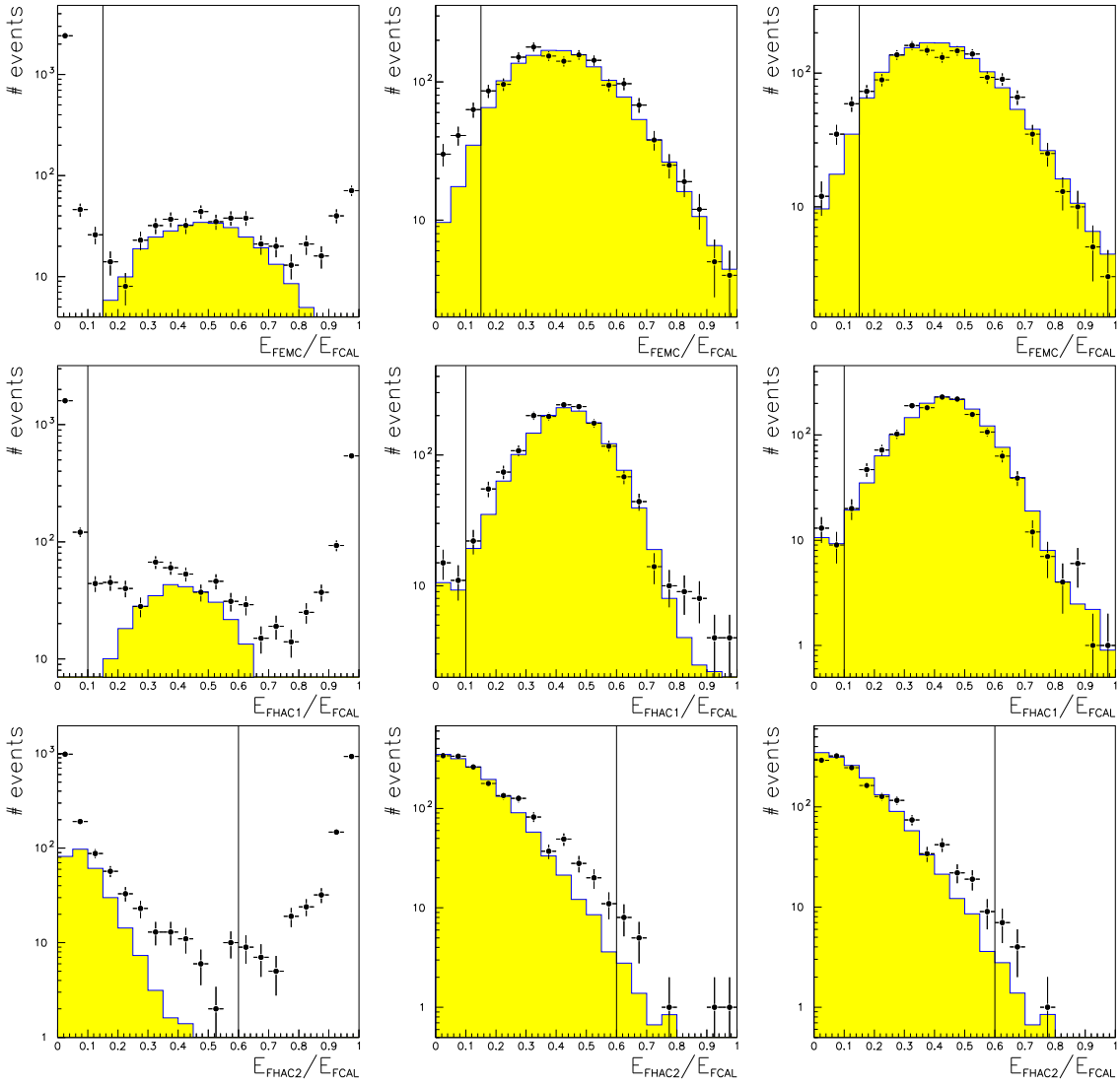

Figure 4.32: Energy-fraction of FEMC (top), FHAC1 (middle) and FHAC2 (bottom) for the highest energetic condensate in the FCAL, for the low-γ sample after all cuts applied except for the ones on condensate quantities (left) and for the final signal without (middle) and with (right) MUFFIN rejection. The points present the data, the histogram the signal MC. The vertical lines indicate the cut thresholds.

cross section of PHP in comparison to the CC cross section renders these backgrounds sizeable. In any case the probability to imitate the CC signature drops rapidly with increasing P_t. The best discrimination would be to raise the cut threshold for P_t. But as described in Sect. 4.2.4 and visible in Fig. 4.7 P_t is highly correlated with the kinematical quantities, since it is an input for the reconstruction formulae of the Jacquet-Blondel method in (4.10).

An efficient way to discriminate against PHP is by looking at an observable that measures the sphericallity of the energy deposits in an event. The PHP event itself should be balanced in transverse momentum. Even though there is an extra or missing energy

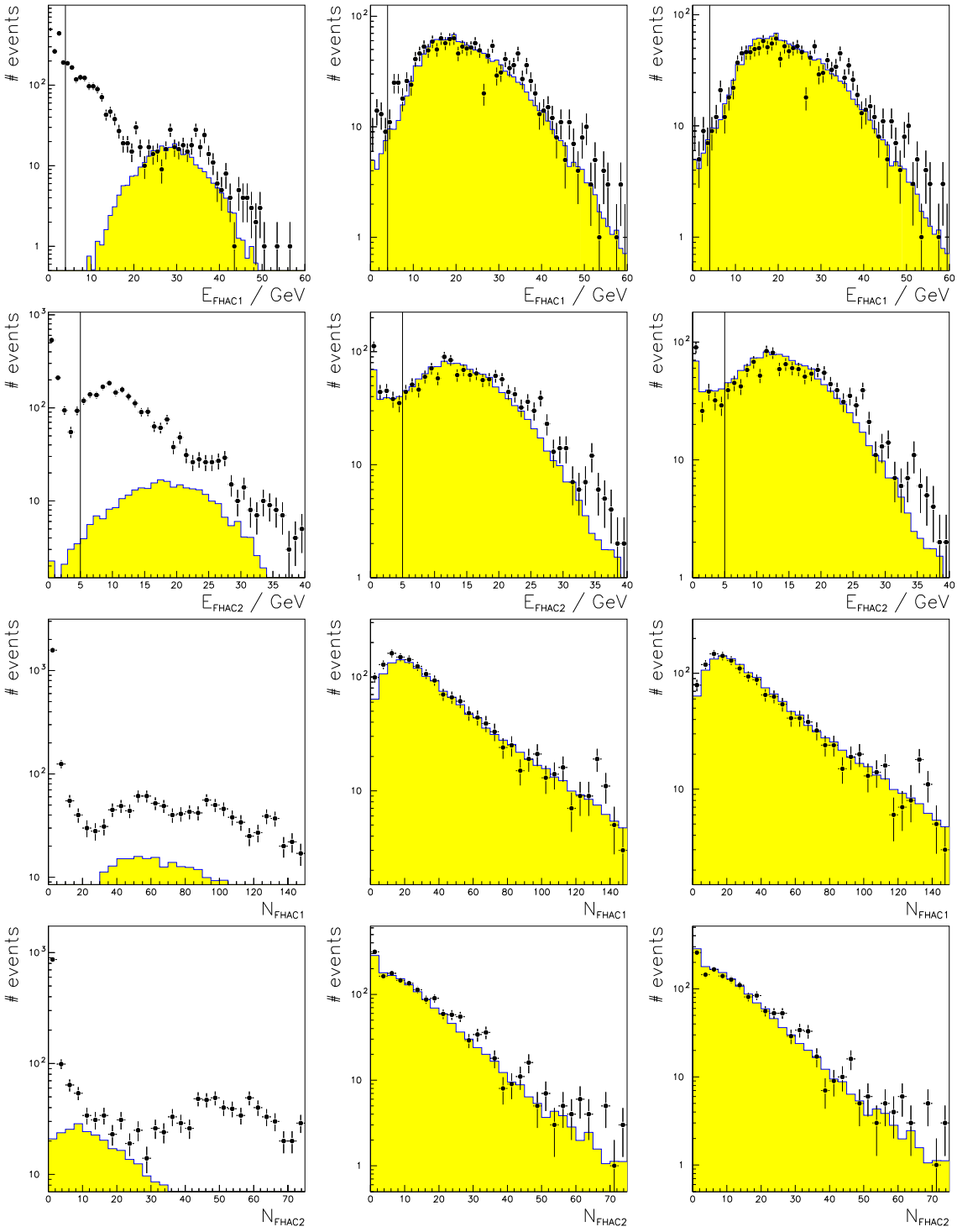

Figure 4.33: From top to bottom energy in FHAC1/FHAC2 and number of cells in FHAC1/FHAC2 for the low-γ sample after all cuts applied except for the ones on the condensate quantities (left), the final signal without (middle) and with (right) MUFFIN rejection. The points present the data, the histogram the signal MC. The vertical lines indicate the cut thresholds.

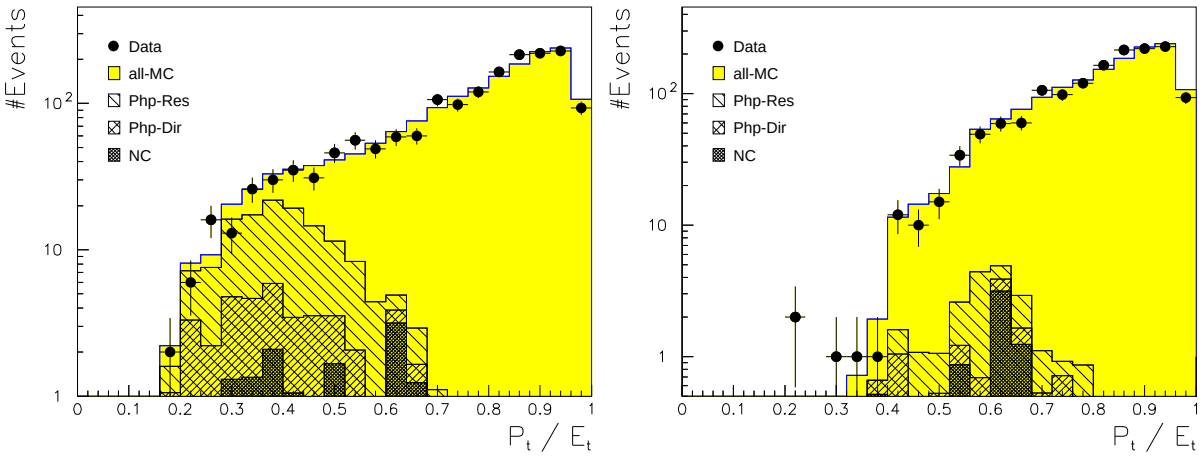

Figure 4.34: Distribution of P_t/E_t for data (points) and MC (histogram) after applying all cuts except that on P_t/E_t (left) and for the final signal sample (right).

deposit the rest of the event should still be rather isotropically distributed in the azimuthal angle. For a CC event we expect a jet-like hadronic final state that balances the missing momentum of the undetected neutrino. The reconstructable detector quantity which has such characteristics is P_t/E_t. We already discussed the properties of P_t/E_t in case of the halo-muon suppression in Sect. 4.3.7. If the energy deposit is confined to one cell only, the scalar (E_t) and vector (P_t) sums of the transversal energies are identical yielding $P_t/E_t = 1$. On the other hand, if the deposit is cylindrically distributed the vector sum vanishes yielding $P_t/E_t = 0$. Therefore we expect small values of P_t/E_t for PHP while larger ones for CC (halo muons with $P_t/E_t \simeq 1$ already excluded). As the PHP background depends strongly on P_t the necessity for a hard P_t/E_t-cut is reduced at higher P_t. The cut is therefore applied in steps of P_t, and is omitted for events with P_t above 30 GeV:

$$\begin{aligned} P_t/E_t > 0.65 \quad &\text{for} \quad P_t \leq 20\,\text{GeV} \\ P_t/E_t > 0.4 \quad &\text{for} \quad 20\,\text{GeV} \leq P_t < 30\,\text{GeV}. \end{aligned} \tag{4.27}$$

The distribution of P_t/E_t for data and MC simulation is displayed in Fig. 4.34. Note that the PHP MC is normalized to the P_t/E_t-distribution of a specially prepared sample as described in Sect. 4.1.1.2. Alternatively the quantity $P_t/\sqrt{E_t}$ has been investigated for suppressing PHP. This would be the natural choice, since it better reflects the calorimeter resolution. In addition, the cut condition (4.27) with the step in P_t could be replaced by a constant threshold. However, the discriminating power of P_t/E_t turned out to be superior.

Another tool to suppress PHP events is to check if the P_t measured in the calorimeter is consistent with P_t from the tracking. In some cases the tracking is not sensitive to the mismeasurement of the calorimeter. With the definition of good tracks in (4.3) one can use the momentum of the good tracks in the events to reconstruct the transverse momentum P_t^{trk} as the vector sum. The momentum from the tracking does only reflect the momentum of the charged tracks and therefore systematically deviates from the momentum measured with the calorimeter by the momentum of the neutral particles. A mismatching of the

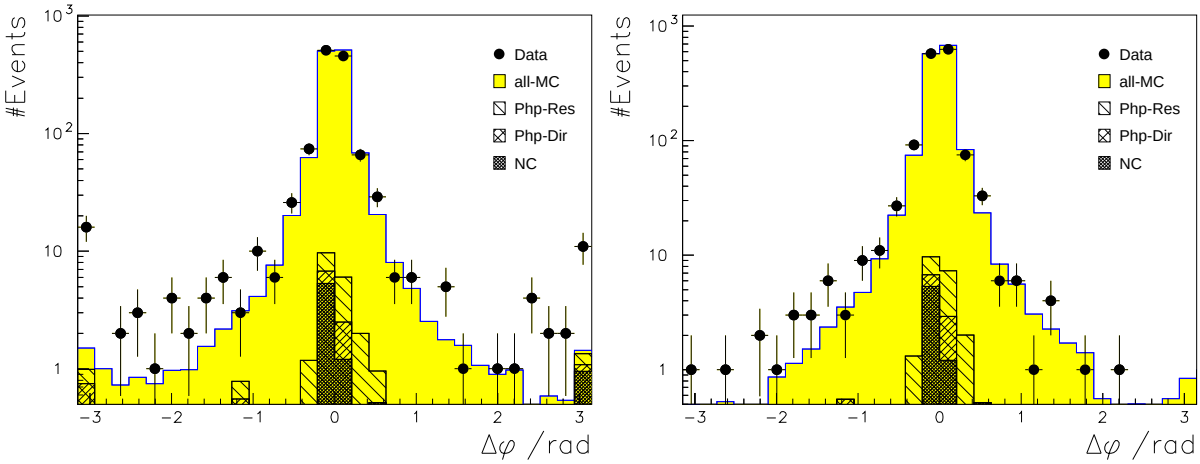

Figure 4.35: Distribution for data (points) and MC (histogram) of the difference in the azimuthal angle of P_t measured with calorimeter and CTD, $\Delta\varphi$, for the high-γ sample with all but the cut on $\Delta\varphi$ applied (left) and for the final signal sample (right).

absolute value of P_t reconstructed using calorimeter and good tracks can therefore not be used as an indication of calorimetry mismeasurement. The direction of P_t^{trk}, however, is almost independent of the fraction of neutral particles in the hadronic final state. Hence, the difference in the azimuthal angle of the transverse momenta as reconstructed from calorimetry and tracking, $\Delta\varphi$, can be used as a discriminant for PHP suppression. Since the PHP contribution at high P_t is much smaller this cut can be relaxed for higher P_t but has to be tighter at low P_t. The cut can only be applied on the high-γ sample where tracking acceptance is given. The final cuts applied are:

$$\begin{aligned} \Delta\varphi &< 0.5 \quad \text{for} \quad P_t < 20\,\text{GeV} \\ \Delta\varphi &< 2.0 \quad \text{for} \quad P_t \geq 20\,\text{GeV}. \end{aligned} \tag{4.28}$$

The $\Delta\varphi$ distributions for the high-γ sample before the cut and for the final signal sample are presented in Fig. 4.35. The cut not only removes simulated PHP background but also the non-simulated non-ep background at $\pm\pi$. The final $\Delta\varphi$-distribution shows a reasonable agreement between data and MC.

Yet another method which follows the same principle of track and calorimetry mismatch is to look at the asymmetry in the number of good tracks within an angle of 0.5 rad in the direction of the P_t as measured with the calorimetry, N^+, and those outside, N^- [67]. Events were rejected based on the conditions on N^- and the asymmetry as follows:

$$N^- \geq 2 \qquad \textbf{or} \qquad A^{\pm} \equiv \frac{N^+ - N^-}{N^+ + N^-} < 0.7. \tag{4.29}$$

4.3.12 Rejection of NC events

The detection of the scattered electron in the final state is the main signature of a DIS NC event. The scattered electron balances the transverse momentum of the hadronic

final state. For a fully contained NC event this yields a transverse momentum $P_t = 0$ and a longitudinal momentum $E - P_z = 2E_e = 55\,\text{GeV}$. One should note that $E - P_z$ is not affected by missing energy leaving the detector through the beam pipe in the proton direction as for those particles $E = P_z$. For CC signal events $E - P_z$ is not conserved because of the missing momentum of the neutrino. However, $E - P_z$ is strongly correlated with the kinematic variable y_{JB} as reconstructed using the Jacquet-Blondel method given in (4.10) and described in Sect. 4.2.4. Because of the longitudinal and transversal momentum conservation in NC events the NC-rejection is limited to events with $E - P_z > 30\,\text{GeV}$ and $P_t < 30$. For positive identification of a scattered electron which then leads to the rejection of the event specially designed algorithms exist within the ZEUS software, where the one used here is called SINISTRA95 [68]. This software package provides as output the probability P_e for a candidate to be a scattered electron. In addition several cuts on quantities of the electron candidate as estimated by SINISTRA95 are applied to ensure the quality of the electron finding in the data sample. These cuts are on the energy E_e of the electron candidate and the energy $E_e^{\text{outside-cone}}$ that is not within a cone in η, φ of 0.8 around the position of the electron candidate. If the electron candidate lies in the tracking acceptance of the CTD ($15° < \theta_e < 164°$) the candidate's track-momentum has to be greater than a quarter of its energy deposit in the calorimeter and the track must originate from the event vertex within a maximum distance of closest approach, d_e. If the candidate lies outside the CTD acceptance it has to have a minimum transverse energy, $P_{t,e}$. The conditions the event and the candidate have to fulfill to be identified as an NC event and therefore be rejected from the CC event sample are:

$$\begin{aligned}
P_t &< 30\,\text{GeV} \\
E - P_z &> 30\,\text{GeV} \\
P_e &> 0.9 \\
E_e &> 4\,\text{GeV} \\
E_e^{\text{outside-cone}} &< 5\,\text{GeV} \\
P_e^{\text{trk}} &> 0.25 \cdot E_e^{\text{cal}} \quad \text{for} \quad 15° < \theta_e < 164° \\
d_e &< 15\,\text{cm} \quad \text{for} \quad 15° < \theta_e < 164° \\
P_{t,e} &> 2\,\text{GeV} \quad \text{for } \mathbf{not} \quad 15° < \theta_e < 164°.
\end{aligned} \tag{4.30}$$

The probability of a mismeasured hadronic final state to fake a substantial P_t drops quickly as γ_{h} falls. The electron rejection yields no effect if applied to the low-γ sample and is therefore only applied to the high-γ sample. For this data set the condition for a scattered electron at low angle outside the CTD acceptance is found to effect no data event. The effect of the electron rejection on the data sample is not easy to visualize for lack of statistics of rejected electron candidates. But loosening cuts to increase the NC background signal does also increase the PHP contribution and is not separable from it. Hence, Fig. 4.36 shows the electron selection variables for the final signal with and without NC suppression with limited statistical significance.

4.3.13 Selection of signal region

The final sample is reduced in the kinematic variables to a well described region. The background processes, especially PHP, are not completely separable from the signal.

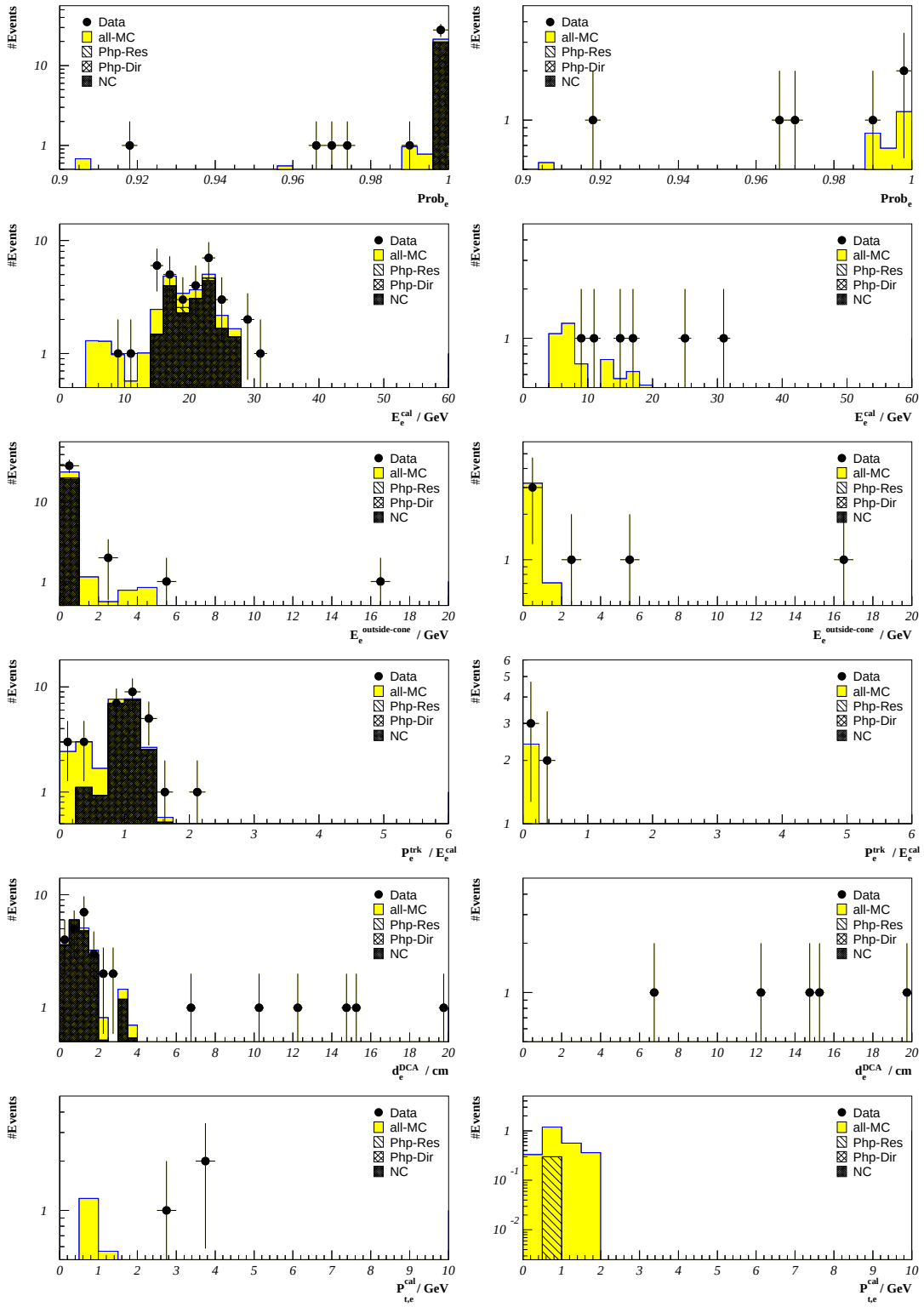

Figure 4.36: Inspected distributions for identification of a scattered electron for NC rejection (4.30). From top to bottom: probability of the electron finder (P_e), energy (E_e), energy outside cone ($E_e^{\text{outside-cone}}$), tracking to calorimetry matching ($P_e^{\text{trk}}/E_e^{\text{cal}}$), DCA ($d_e$) and transverse momentum ($P_{t,e,}$) for the electron candidate. The histograms show the final signal sample (right) and the sample before the NC rejection (left). For $P_e^{\text{trk}}/E_e^{\text{cal}}$ and d_e ($P_{t,e,}$) only events (not) fulfilling $15° < \theta_e < 164°$ are shown.

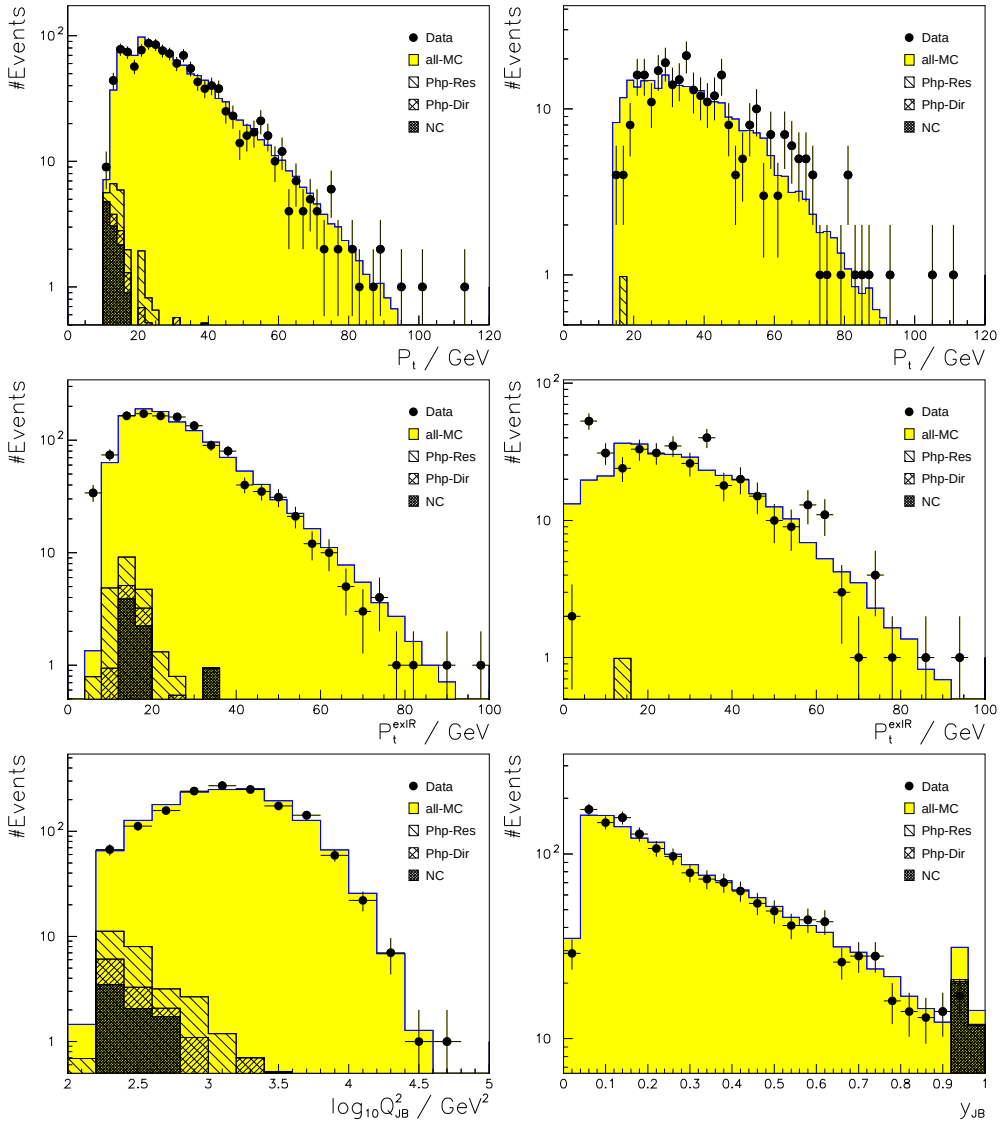

Figure 4.37: Limitations of the final sample by thresholds in the distributions of P_t (upper), P_t^{-ir} (middle), separately for high-γ (left) and low-γ (right), and in the kinematic variables Q^2 (lower left) and y_{JB} (lower right) for the whole sample. All distributions are for samples with the final set of cuts except for the cut on the quantity shown.

Almost all background contributions diminish rapidly with increasing P_t, favoring a hard cut in P_t. However, P_t is directly related to the kinematic variables, especially Q^2 and y_{JB} as visualized in Fig. 4.7. Hence, on the one hand, the cuts on those kinematic quantities have to be chosen in a way that they limit the measurement to a region of reasonable acceptance of the P_t cut. On the other hand, the P_t cut must not reduce the acceptance in the kinematic range of the mesaurement dramatically. So the cuts have to be balanced, optimised to a region of reasonable background contamination. The distributions for P_t, Q^2 and y_{JB} are shown in Fig. 4.37. However, their explanatory power suffers from the preselection, which in turn takes the trigger selection into account, but which is not applied to the MC. A reasonable description of the data by the sum of signal and background

Run Nr.	Event Nr.	Event typ
33468	186389	cosmic
33607	4728	halo muon
33875	8533	halo muon
34224	11199	halo muon
34448	62064	halo muon
35119	78187	halo muon
35119	97022	halo muon
35132	74484	halo muon
35327	13390	halo muon
35343	5916	halo muon
35343	8819	halo muon
35363	58249	cosmic
35450	86128	halo muon
35523	79409	halo muon
36548	119708	halo muon
37280	31595	halo muon

Table 4.8: Identification of the events classified as non *ep* background in the final scanning of the visiualized events.

MC is achieved by applying the following conditions for the whole sample:

$$\begin{aligned} Q^2 &> 200\,\mathrm{GeV}^2 \\ y_{\mathrm{JB}} &< 0.95. \end{aligned} \tag{4.31}$$

For the low-γ sample the cuts on P_t and $P_t^{\text{-}ir}$ (excluding the innermost ring, see Sect. 4.3.2.2) have to be raised, as Fig. 4.37 still shows a big discrepancy of data and MC including the simulated background processes. This deviation belongs to non-simulated non-*ep* background. For the high-γ sample the tracking helps to reduce this class of background, as discussed in Sect. 4.3.9. Since tracking is not reliably for the low-γ sample, the cuts on the calorimetry have to be increased as follows:

$$\begin{array}{ccc} \underline{\text{high}-\gamma} & & \underline{\text{low}-\gamma} \\ P_t > 12\,\mathrm{GeV} & \rightarrow & P_t > 14\,\mathrm{GeV} \\ P_t^{\text{-}ir} > 10\,\mathrm{GeV} & \rightarrow & P_t^{\text{-}ir} > 12\,\mathrm{GeV} \end{array} \quad . \tag{4.32}$$

4.3.14 Visualized event scanning

The 1504 events of the final sample have been scanned using a tool for visualization [19]. 14 events have been identified as halo-muon events and two as cosmics. They have been excluded from the final sample. The event identification is given in Table 4.8. One of these halo-muon events is shown as an example in Fig. 4.38 and a cosmic event in Fig. 4.39.

The halo-muon events have almost no energy deposit in the RCAL corresponding in x-y to the deposit in the FCAL. This renders them hard to identify by MUFFIN. The shower

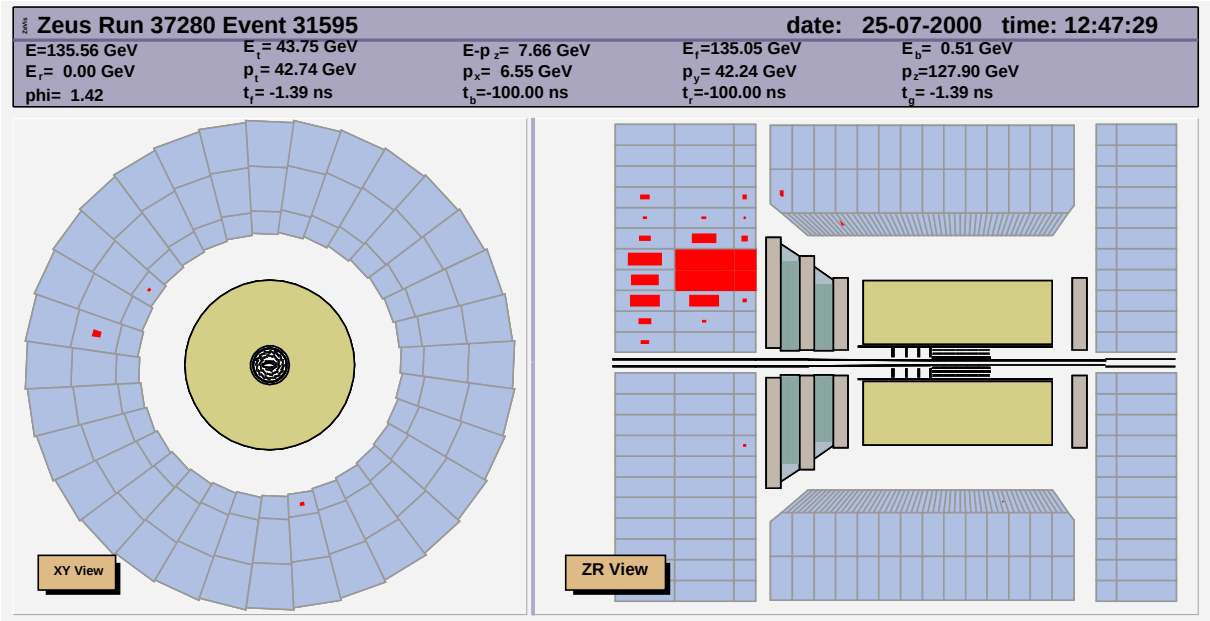

Figure 4.38: Visualized event identified as halo-muon event. The z-r view (right) shows in the FCAL, indicated on the left as structured blue rectangle, an energy deposit in red with a shower shape parallel to the beamline.

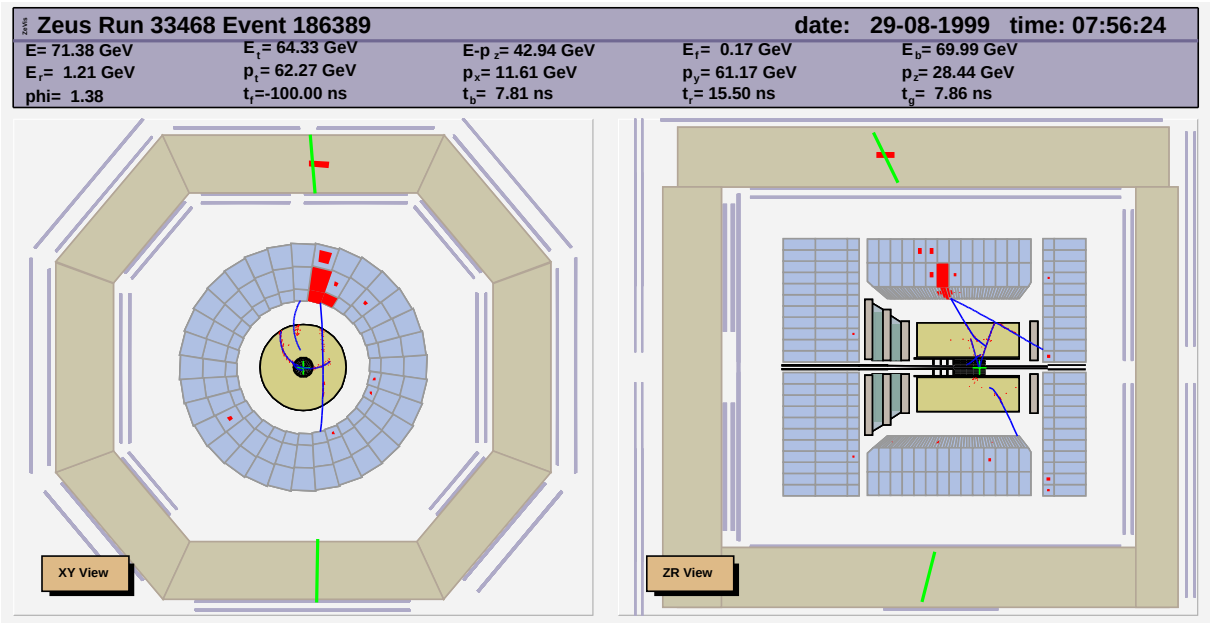

Figure 4.39: Visualized event identified as cosmic event. The lines in the BAC (outer beige boxes) might indicate muons. In the x-y view the track going through BAC, CAL and CTD on both ends but missing the IP is clearly visible.

Sample	N_{total}	$N_{high-\gamma}$	$N_{low-\gamma}$
ZEUS data e^+p 1999/1000	1488	1191	297
Signal MC (ARIADNE)	1488.7	1197.6	291.1
Resolved PHP MC	10.2	9.7	0.5
Direct PHP MC	4.2	3.6	0.6
NC MC	7.9	7.5	0.4
DIS $eu \Rightarrow eX\mu\mu$ di-lepton MC	2.0	1.2	0.8
DIS $e\bar{u} \Rightarrow eX\mu\mu$ di-lepton MC	0.2	0.2	0.0
DIS $ed/s \Rightarrow eX\mu\mu$ di-lepton MC	0.3	0.1	0.1
DIS $e\bar{d}/\bar{s} \Rightarrow eX\mu\mu$ di-lepton MC	0.0	0.0	0.0
Quasi elastic ($M_{\rm had} > 5\,{\rm GeV}$) $\mu\mu$ di-lepton MC	0.0	0.0	0.0
Quasi elastic ($1.08\,{\rm GeV} < M_{\rm had} < 5\,{\rm GeV}$) $\mu\mu$ di-lepton MC	0.7	0.7	0.0
Elastic $\mu\mu$ di-lepton MC	0.5	0.5	0.0
DIS $eu \Rightarrow eX\tau\tau$ di-lepton MC	0.5	0.5	0.1
DIS $e\bar{u} \Rightarrow eX\tau\tau$ di-lepton MC	0.1	0.1	0.0
DIS $ed/s \Rightarrow eX\tau\tau$ di-lepton MC	0.1	0.0	0.1
DIS $e\bar{d}/\bar{s} \Rightarrow eX\tau\tau$ di-lepton MC	0.1	0.1	0.0
Quasi elastic ($M_{\rm had} > 5\,{\rm GeV}$) $\tau\tau$ di-lepton MC	0.0	0.0	0.0
Quasi elastic ($1.08\,{\rm GeV} < M_{\rm had} < 5\,{\rm GeV}$) $\tau\tau$ di-lepton MC	0.3	0.2	0.1
Elastic $\tau\tau$ di-lepton MC	0.4	0.3	0.0
DIS $e^+p \Rightarrow e^+W^-X$ MC	0.7	0.6	0.1
Resolved $e^+p \Rightarrow e^+W^-X$ MC	0.2	0.1	0.0
DIS $e^+p \Rightarrow e^+W^+X$ MC	1.0	0.8	0.1
Resolved $e^+p \Rightarrow e^+W^-X$ MC	0.2	0.2	0.0

Table 4.9: Number of events selected with the final cuts for total, N_{total}, high-γ, $N_{high-\gamma}$, and low-γ sample, $N_{low-\gamma}$ data and MC samples.

shape in the FCAL can be identified to be parallel to the beam line, which can only originate from a halo-muon. In addition, no other energy deposit nor track has been found in the events.

The cosmic events show shower shapes in the CAL corresponding to a line missing the IP. There are some signals in the BAC, probably originating from a muon, however this is not completely reliable and serves only as an indication. No beam-gas event has been found by scanning. No *ep* background events have been rejected by scanning, since they can not be identified unambiguously. However, they have been simulated and handling of the contamination will be explained in Sect. 4.5.3.

4.4 Final event sample

The final CC sample contains a total of 1488 events, of which 1191 are in the high-γ sample and 297 in the low-γ sample. In Table 4.9 the total number of events for signal and background MC samples selected with the cuts are given. The numbers for each bin are given also in the cross section tables in Appendix C. The distribution of the final

event sample in the kinematic plane is shown in Fig. 4.40.

The number of events selected, N_{sel}, and the fraction of all preselected events, ϵ_{Data}, are listed in Table 4.10 for each cut, together with the number of events which are exclusively rejected by the cut, N_{excl}. In additon, the efficiency of the cut in the CC MC, ϵ_{MC}, is given. Since the preselection anticipates some of the cuts, e.g. muon rejection by high P_t/E_t, the efficiency of the final offline cut with respect to the preselected sample might underestimate the background-suppressing power of this type of cut. On the other hand, the efficiency for MC is based on the full generated MC sample, which has as only constraint the minimum generated Q^2 of $Q^2 > 100\,\text{GeV}^2$. This makes the trigger efficiency as given in Table 4.10 differ from the number given in Sect. 4.3.5, which was based on the signal region on generator level. No cut is pronounced in rejecting data events, reducing the sample close to the final size. Only the combination of cuts supresses the background efficiently. On the other hand, the number of events rejected exclusively by only one cut is also limited. In the end, the efficiencies demonstrate a well balanced set of selection-cuts used to isolate the signal.

In Fig. 4.41 the control plots of the key quantities for the final CC sample are displayed. The data are well described by the sum of the signal and background MCs. This justifies the use of the MC for acceptance corrections.

4.5 Cross section measurement

In the previous sections the signal sample has been defined and summarized. Now the procedure from event numbers to differential cross sections is explained. Differential measurements have to be done bin-wise. The definition of the bins in the quantities under study is done according to data statistics and resolution. Based on the MC not only the resolution but also efficiency, acceptance and purity have to be determined bin-wise and used for bin-by-bin unfolding. For the final measurements the background not yet rejected in the signal sample has to be subtracted statistically. The data correspond to the inclusive cross section to all orders. From the theoretical point of view it is favorable to evaluate the cross sections at Born level, which implies that corrections for radiative effects and loops have to be applied. Finally, various sources of systematic uncertainties have to be identified and their influence on the measurement has to be estimated, yielding the systematic uncertainties.

4.5.1 Definition and resolution of bins

For measuring a differential cross section the data which are available event-wise have to be binned in the quantities of interest. This binning has to take into account the statistics of the data. A binning should be balanced such that reasonable numbers of event entries per bin are obtained. The steep drop of the cross section with increasing Q^2 and x, requiring a logarithmic scale for visualization, also suggests equidistant bin borders in $\log Q^2$ and $\log x$.

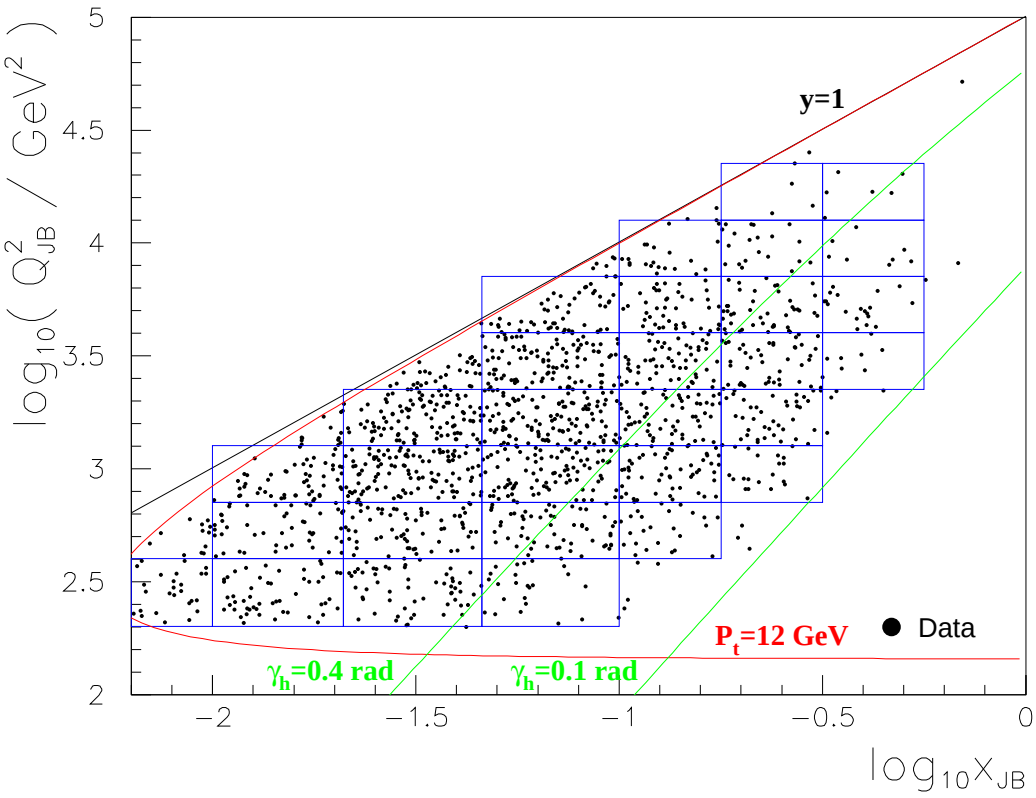

Figure 4.40: Distribution of the final CC event sample in the kinematic plane Q^2 versus x. Examples of lines for constant P_t, $\gamma_{\rm h}$ and y are indicated.

Cut	Type	Section	$N_{\rm sel}$	$N_{\rm excl}$	$\epsilon_{\rm Data}$	$\epsilon_{\rm MC}$
Crossings and Trigger	Technical	4.3.8.2	43675	6	86.1%	79.5%
Spark + dead PM	Technical	4.3.8.1	49647	31	97.9%	100.0%
Event vertex	Beam-gas	4.3.9	33921	56	66.9%	95.7%
Tracking	Beam-gas	4.3.9	9989	215	19.7%	88.6%
High P_t/E_t	Muons	4.3.10	41151	4	81.1%	99.9%
Energy fraction	Muons	4.3.10	50282	0	99.1%	99.9%
MUFFIN	Muons	4.3.10	26133	159	51.5%	100.0%
FCAL shower shape	Muons	4.3.10	28587	75	56.4%	91.5%
P_t/E_t	PHP	4.3.11	30395	185	59.9%	75.2%
Track-calorimeter mismatch	PHP	4.3.11	36275	68	71.5%	89.2%
Track asymmetry	PHP	4.3.11	40531	51	79.9%	87.8%
Electron identification	NC	4.3.12	48926	27	96.5%	99.5%
Q^2	Signal region	4.3.13	46829	23	92.3%	75.0%
y	Signal region	4.3.13	48311	25	95.2%	97.2%
P_t	Signal region	4.3.13	45462	9	89.6%	71.5%
P_t^{ir}	Signal region	4.3.13	33184	133	65.4%	68.3%

Table 4.10: Number of events selected from the preselected data sample, $N_{\rm sel}$, with the corresponding efficiency, $\epsilon_{\rm Data}$, and number of events exclusively rejected, $N_{\rm excl}$, by each cut, together with the efficiency on the not preselected CC MC, $\epsilon_{\rm MC}$.

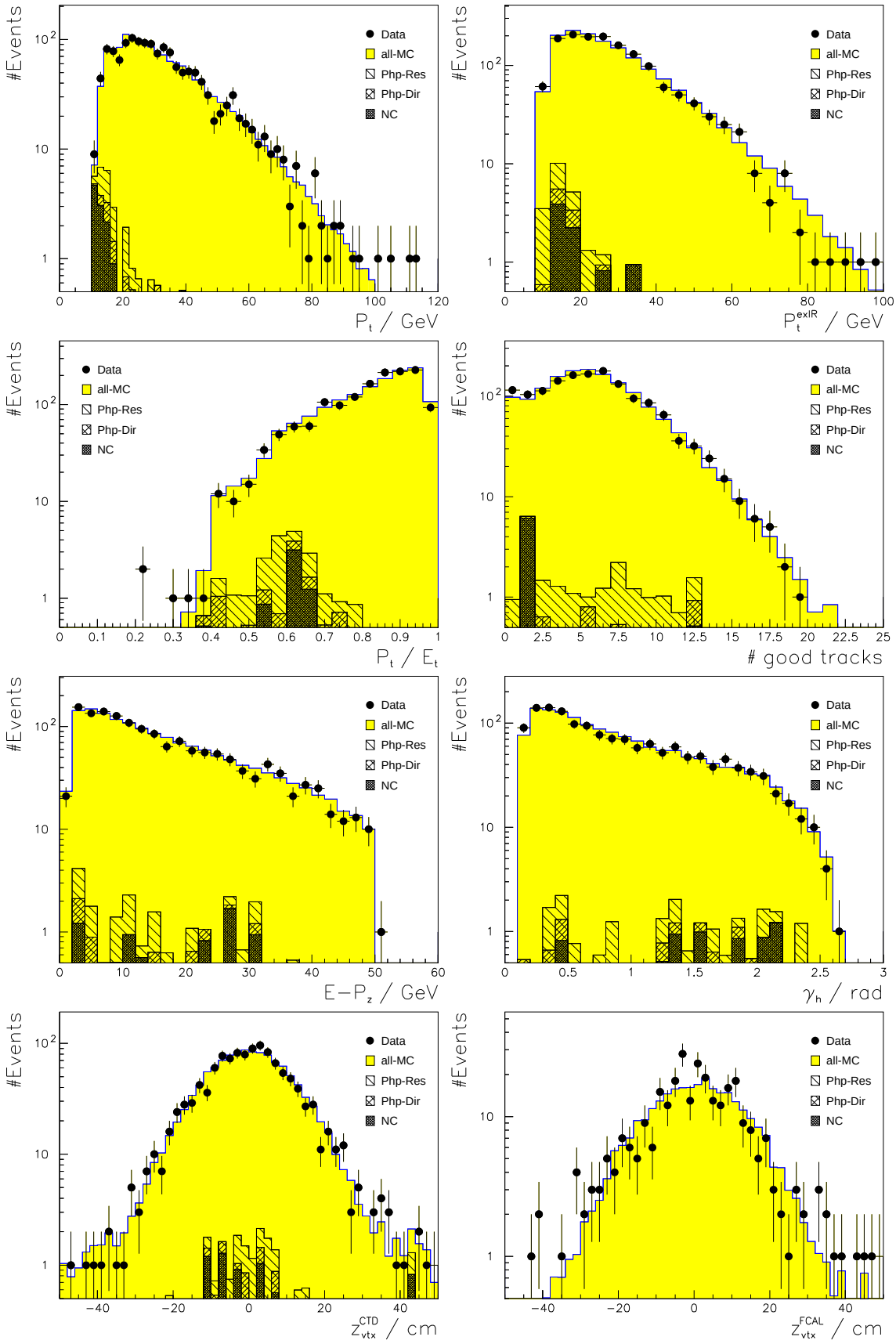

Figure 4.41: Distributions of the key quantities for the final CC event sample.

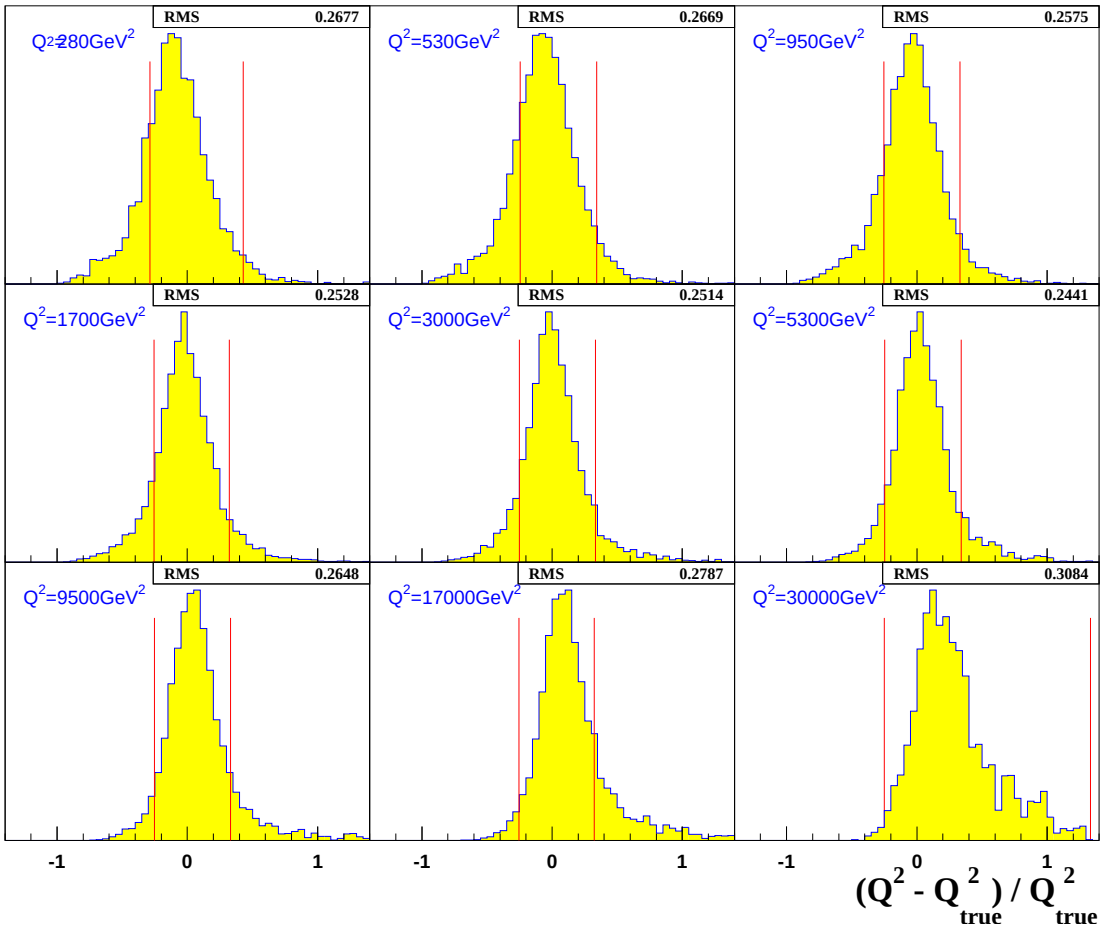

Figure 4.42: Resolution of the measured Q^2 in the bins used for the extraction of $d\sigma/dQ^2$. The lines indicate the fractional distance of the bin borders from bin center.

The bin definitions chosen for this analysis are given in the cross section tables in Appendix C. The bin borders for the double-differential bins coincide with those chosen for the single differential measurements. Their position in the kinematic plane was indicated already in Fig. 4.40, showing the distribution of the signal events. The bin size has also to reflect the resolution of the binned quantity. If the resolution exceeds the bin-size the bin will be dominated by migrations rendering the extracted cross section sensitive to the description of these migrations by the MC. The resolution is obtained with the help of the MC simulation. This requires that the MC is able to describe the data and that the relation between the true event-quantities and the measured ones as extracted from the MC can be accepted as valid also for data. Figures 4.42 to 4.46 show the resolution for the bins. To indicate the bin width lines show the fractional distances of the bin border from the logarithmic center of the bin for the single differential bins. The bin width is larger than the resolution for almost all bins. In case of the bins for the double differential measurement $d^2\sigma/dQ^2\,dx$ the resolutions of Q^2 and x both decrease towards lower P_t.

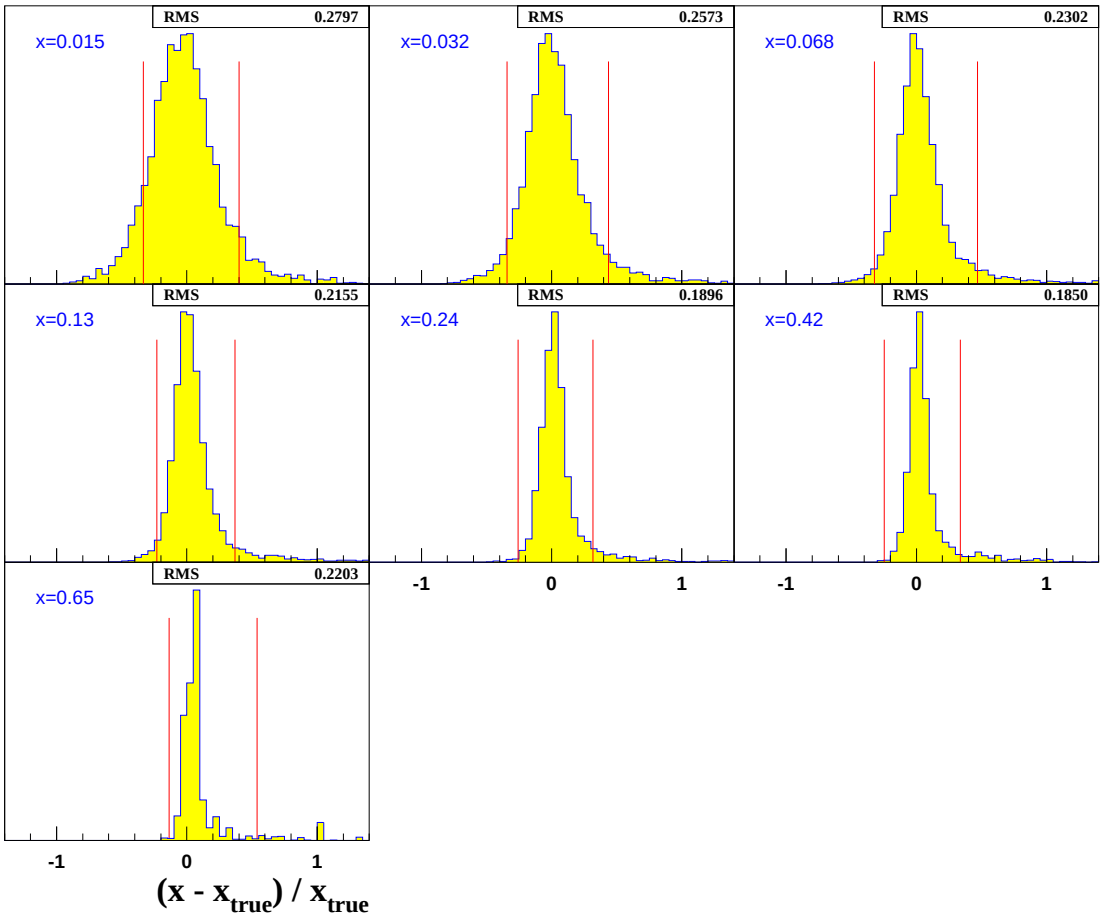

Figure 4.43: Resolution of the measured x in the bins used for the extraction of $d\sigma/dx$. The lines indicate the fractional distance of the bin borders from bin center.

4.5.2 Efficiency, acceptance and purity

Within the bins defined in Sect. 4.5.1 the MC is used to study bin-wise efficiency (ϵ), acceptance ($\mathcal{A}$) and purity ($\mathcal{P}$), defined as follow:

$$\text{efficiency: } \epsilon = \frac{N^{\text{reconstructed}}_{\text{generated}}}{N_{\text{generated}}} \tag{4.33}$$

$$\text{purity: } \mathcal{P} = \frac{N^{\text{reconstructed}}_{\text{generated}}}{N^{\text{reconstructed}}} \tag{4.34}$$

$$\text{acceptance: } \mathcal{A} = \frac{N^{\text{reconstructed}}}{N_{\text{generated}}} = \frac{\epsilon}{\mathcal{P}}. \tag{4.35}$$

In words:

efficiency gives the fraction of events which are generated and reconstructed in the same bin where they are generated,

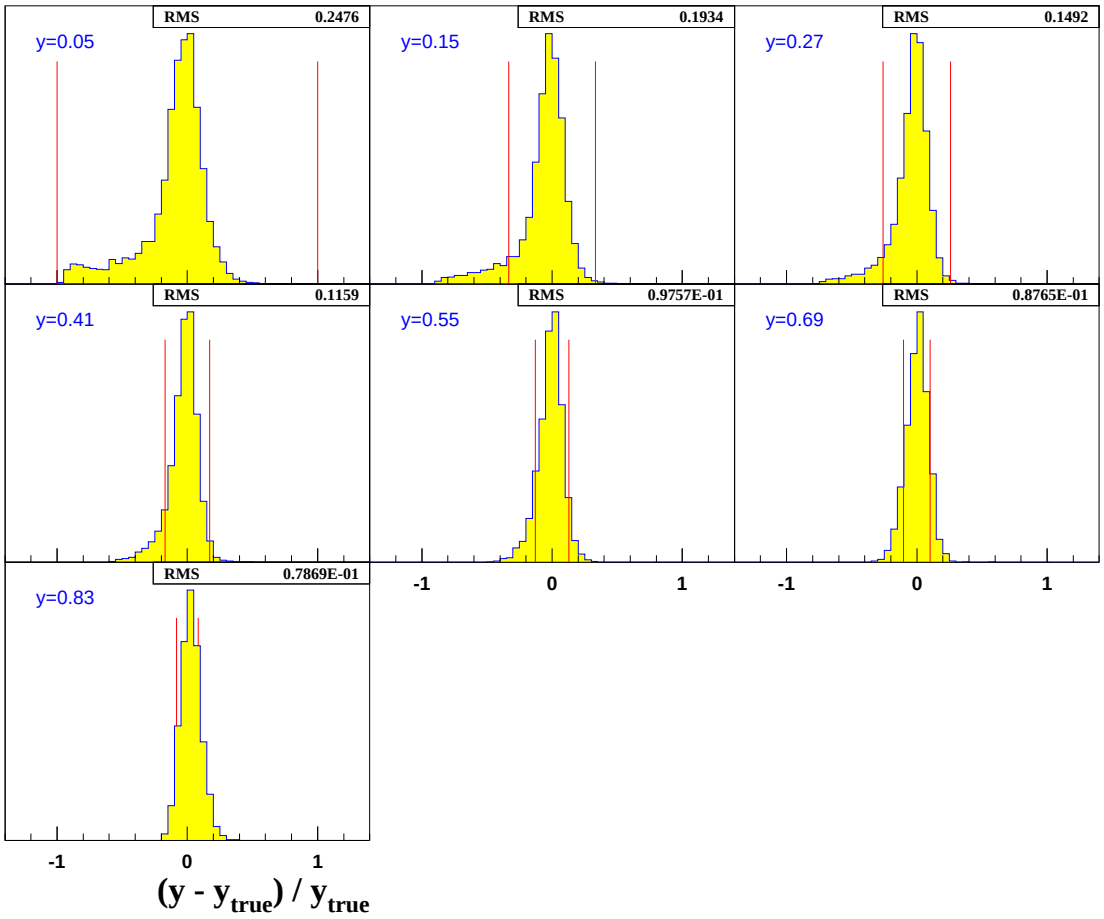

Figure 4.44: Resolution of the measured Q^2 in the bins used for the extraction of $d\sigma/dy$. The lines indicate the fractional distance of the bin borders from bin center.

purity gives the ratio of the events reconstructed and generated in a bin to the events reconstructed in that bin,

acceptance is the quotient of events reconstructed over those generated.

From their definitions efficiency and purity can be at best equal to 1, while acceptance can get larger than 1 due to a net migration into the bin. The results obtained for the signal selection with the signal MC are shown in Figs. 4.47 and 4.48. The purity is almost everywhere above 60%, only dropping to 50% at high x and high Q^2. Of the double differential bins three show purity below 50% at low Q^2 and at the low x end. All bins have an acceptance exceeding 30%. Only one bin does not exceed the acceptance of 40%. The acceptance is rising with Q^2 to 98% in the highest Q^2 and x bin. The bin at lowest Q^2 and x has the lowest purity with 43% and the lowest acceptance of 32%. The low acceptance is due to the P_t-cut of (4.32) which cuts into this bin. But since this kinematic region is unexplored by previous measurements the bin is kept in this analysis.

With the results shown in this section and in Sect. 4.5.1 the binning has been found adequate for the extraction of the cross section.

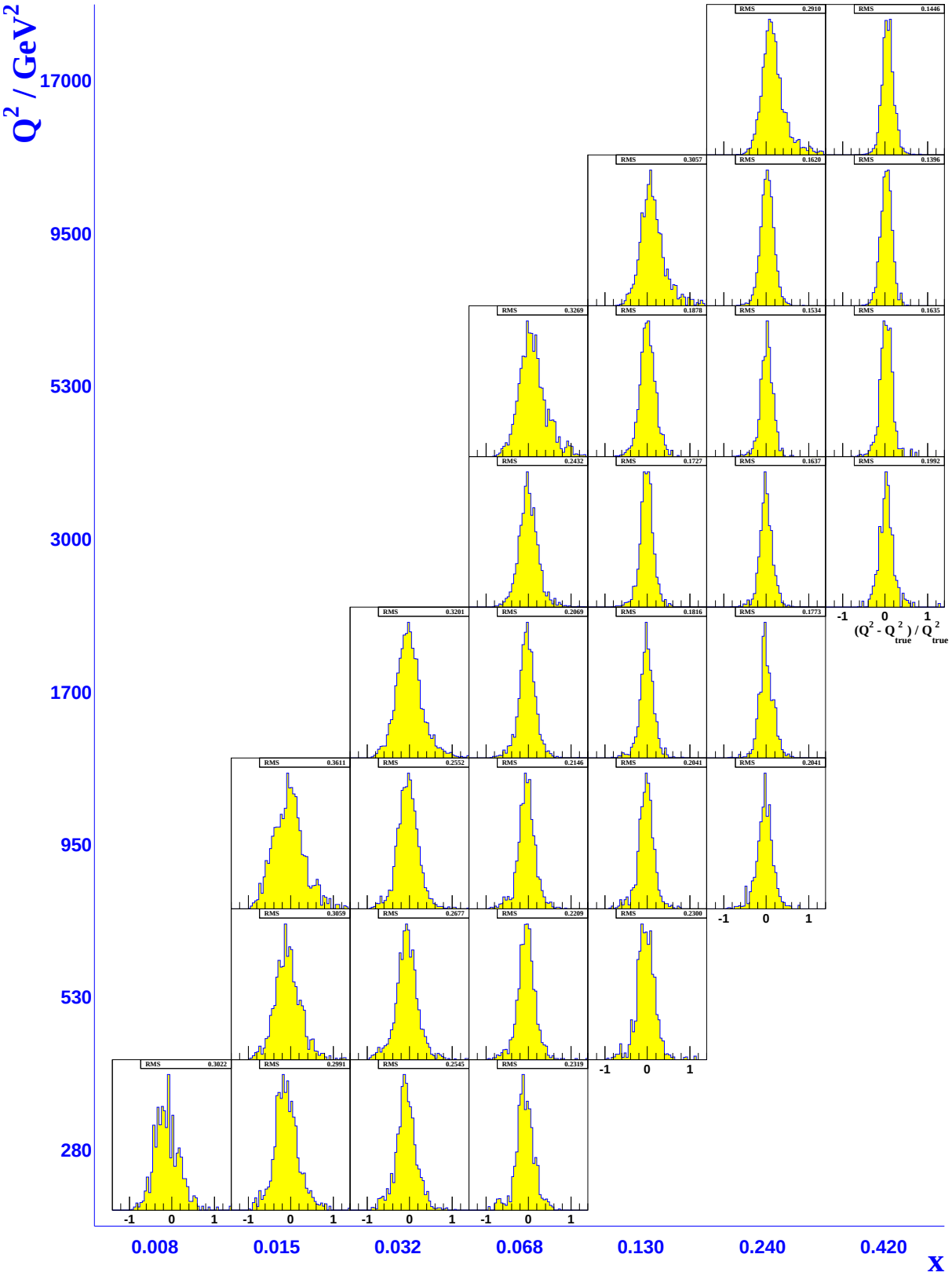

Figure 4.45: Resolution of the measured Q^2 in the bins used for the extraction of $d^2\sigma/dQ^2\,dx$.

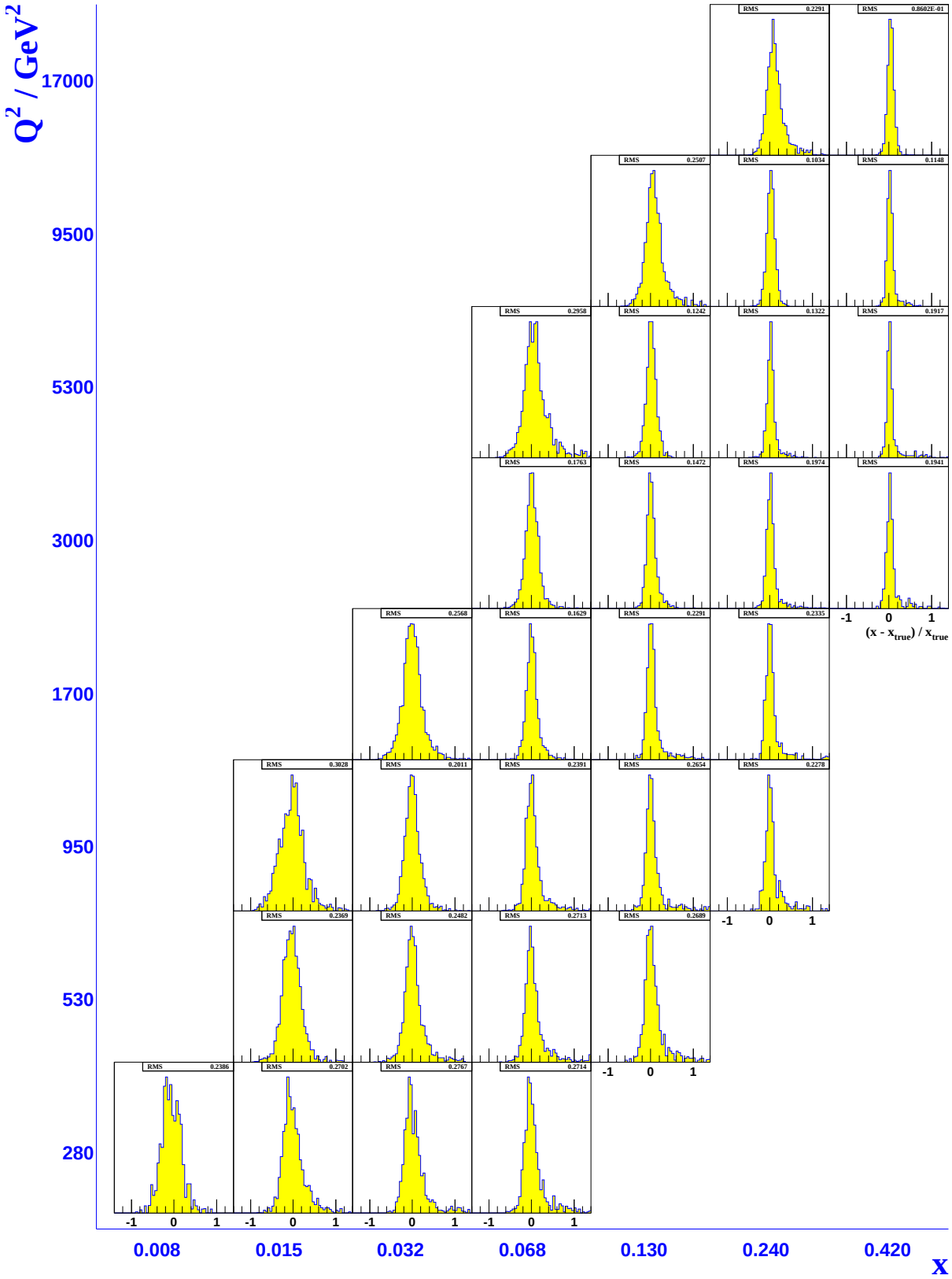

Figure 4.46: Resolution of the measured x in the bins used for the extraction of $d^2\sigma/dQ^2\,dx$.

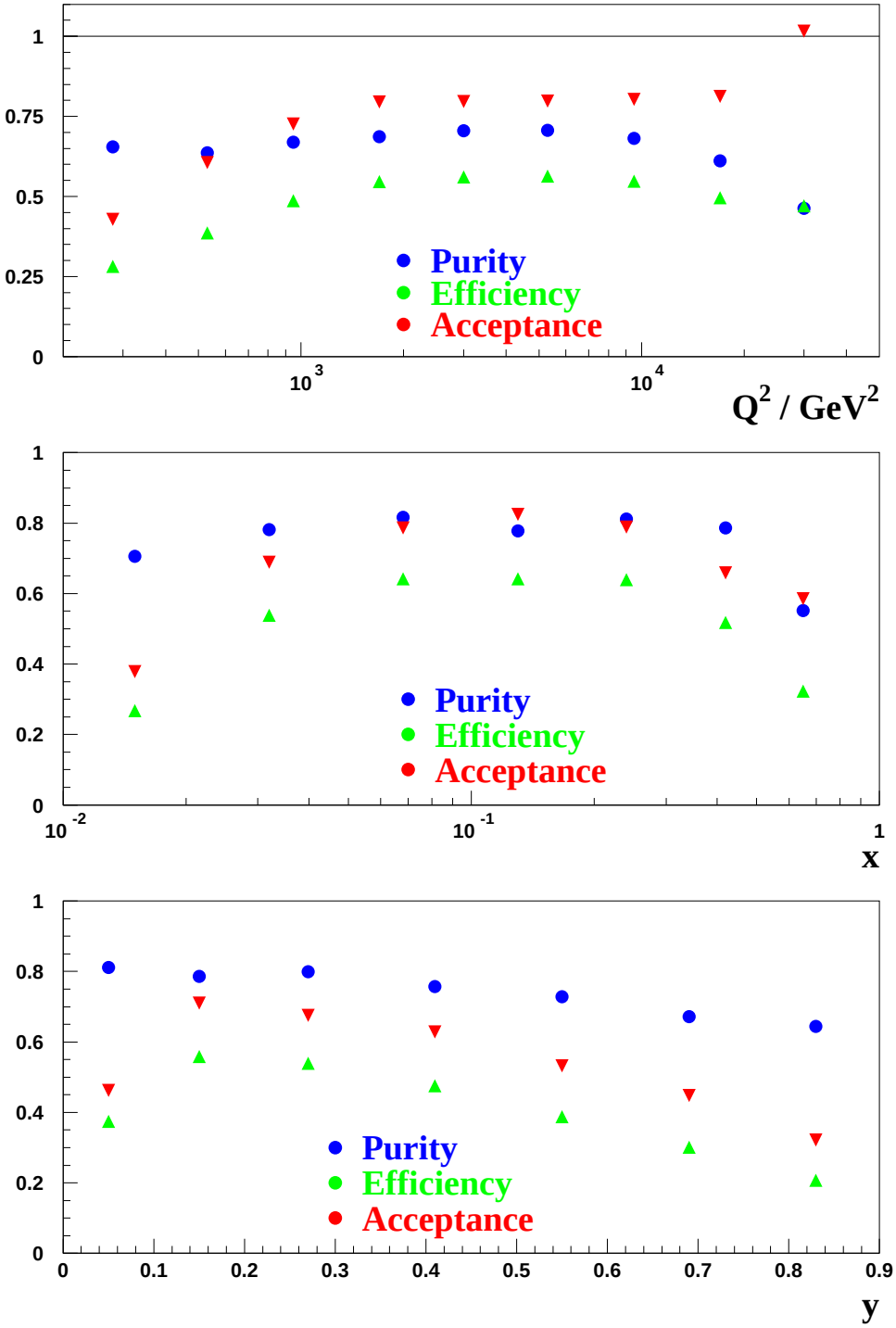

Figure 4.47: Purity, efficiency and acceptance for the bins of the single diffential measurements in Q^2 (top), x (middle) and y (bottom).

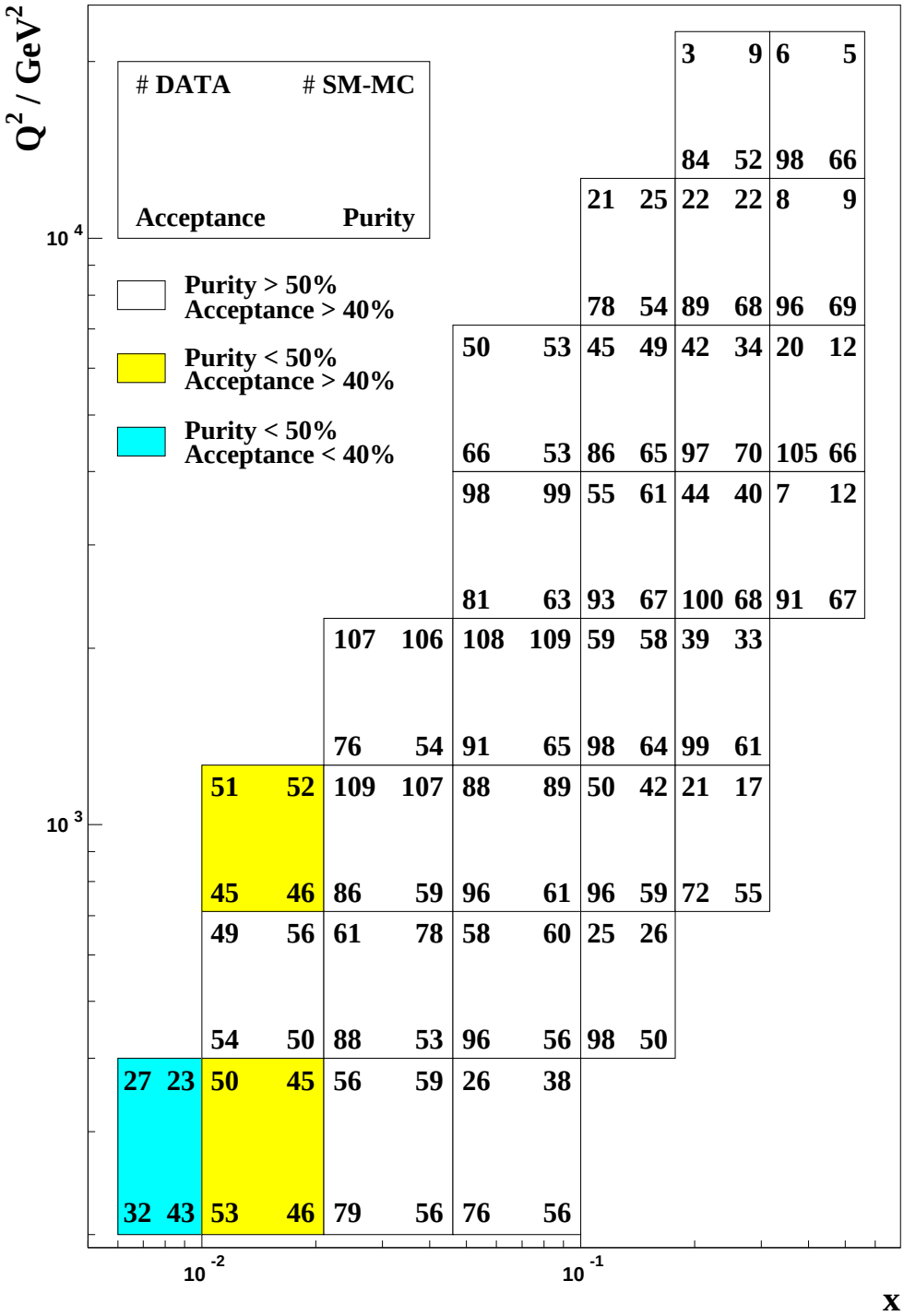

Figure 4.48: Purity and acceptance together with the number of data events and the total events expected from signal plus background MC for the bins of the double differential measurement.

4.5.3 Background subtraction

Non-*ep* background has been successfully suppressed by the selection presented in Sect. 4.3, and the last remaining events where excluded by the visual scanning of the events, as described in Sect. 4.3.14. However, the signal selection has been found to separate the signal not completely from *ep* background. Some *ep* background, like PHP, can not be identified unambiguously by scanning. But they can be simulated and the corresponding MC samples have been introduced in Sect. 4.1. For the measurement of the cross section it is therefore necessary to correct the number of data events for the amount of potential background events. It is estimated by applying the signal cuts to the MC samples. The contamination of the double differential bins with background events is given in Fig. 4.49. Direct and resolved PHP are the biggest contribution. These events are predominantly located at small P_t and Q^2. At high Q^2, however, W production is the only background proccess and gives only a small contamination to the signal sample. Note that the normalization of the PHP MC sample has been determined within this analysis, therefore avoiding an additional uncertainty from the theoretical prediction of the PHP cross section.

In the formulae for the unfolding of the cross section in the following, the number of data events, N_{Data}, used for the extraction of the cross section is the total number of data events passing the selection cuts, $N^{\text{tot}}_{\text{Data}}$, corrected for the number of events from background processes, N_{BG}, as estimated from the MC simulations:

$$N_{\text{Data}} = N^{\text{tot}}_{\text{Data}} - N_{\text{BG}}. \tag{4.36}$$

4.5.4 Radiative corrections

As described in Sect. 3 the measured cross section can not be experimentally isolated from the radiative effects. To extract the cross section at Born level a correction factor, $\mathcal{C}_{\text{rad}}$, is calculated. It is the ratio of the cross section excluding ($\sigma^{\text{theory}}_{\text{excl-rad}}$) and including ($\sigma^{\text{theory}}_{\text{incl-rad}}$) radiative effects. The former is the cross section at Born level ($\sigma^{\text{theory}}_{\text{Born}}$) and the latter the one used for the MC generation ($\sigma^{\text{theory}}_{\text{MC}}$). The correction factor then reads:

$$\mathcal{C}_{\text{rad}} = \frac{\sigma^{\text{theory}}_{\text{excl-rad}}}{\sigma^{\text{theory}}_{\text{incl-rad}}} = \frac{\sigma^{\text{theory}}_{\text{Born}}}{\sigma^{\text{theory}}_{\text{MC}}} \tag{4.37}$$

These factors have been calculated for each bin of the differential measurements. Their values depend on the binning and on experimental conditions like beam energy. The correction is usually less than $\pm 3\%$, reaching up to $+10\%$ at high Q^2 and high x and up to $+7\%$ at high y.

4.5.5 Unfolding of cross sections

To obtain a cross section the event yield measurement has to be unfolded, i.e. corrected for detector acceptance. In general the formula for the cross section of an event-counting

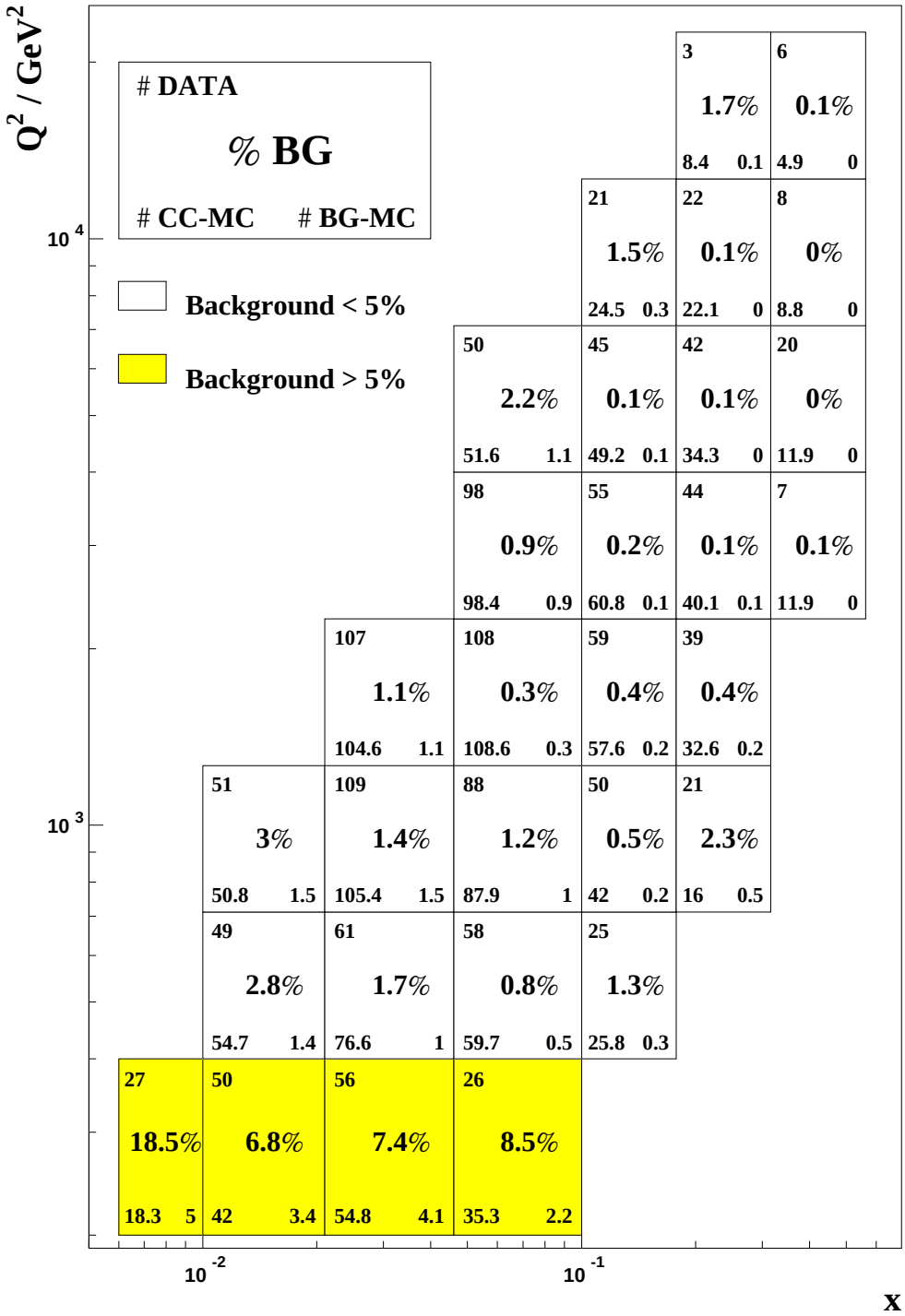

Figure 4.49: Contribution from simulated *ep* background processes to the signal sample in the bins used for the double differential cross section. Given are the number of events selected in data, CC-MC sample and the sum from all samples of simulated background processes, together with the relative contribution of the background to the data events.

experiment is:

$$\sigma^{\text{meas}} = \frac{N}{\mathcal{A} \cdot \mathcal{L}}, \tag{4.38}$$

where N is the number of events measured, $\mathcal{A}$ is the acceptance, here estimated by the MC simulation, and $\mathcal{L}$ is the integrated luminosity as determined in Sect. 4.3.6. Equation (4.38) is valid for both, data and MC. The MC is reweighted to represent the same integrated luminosity as the data, i.e. $\mathcal{L}_{\text{MC}} = \mathcal{L}_{\text{Data}}$. The acceptance is assumed to be the same for both ($\mathcal{A}_{\text{MC}} \equiv \mathcal{A}_{\text{Data}}$). This is justified by the level of accuracy at which in Sect. 4.4 the MC has been shown to decribe the data in the distributions of key quantities. When replacing the acceptance for data in (4.38) by the equivalent equation for MC, the integrated luminosity drops out and one obtains:

$$\sigma^{\text{meas}} = \frac{N_{\text{Data}}}{N_{\text{MC}}} \sigma^{\text{theory}}_{\text{MC}}. \tag{4.39}$$

To be more precise, the cross section that is used for the MC is evaluated for each event individually, i.e. differentially according to the event's kinematic variables. If we restrict (4.39) to a bin, e.g. in Q^2, the theoretical cross section has to be integrated to obtain also the integrated cross section σ_i^{meas} for bin i:

$$\sigma_i^{\text{meas}} = \frac{N_{\text{Data}}}{N_{\text{MC}}} \int_{Q^2{}_{low}}^{Q^2{}_{high}} dQ^2 \, \frac{d\sigma^{\text{theory}}_{\text{MC}}}{dQ^2}. \tag{4.40}$$

This technique offers the possibility to extrapolate the measurement to a kinematical region which is not represented by the data. This is necessarily used for y, since the signal is restricted to $y < 0.9$. Because the integration of $\sigma^{\text{theory}}_{\text{MC}}$ includes the whole y-range the measurements are extrapolated to the full y-range. The bins of the cross section measurements contain from 97% at the lowest Q^2 to 72% at the higest Q^2 of $d\sigma/dQ^2$ and more than 92% of $d\sigma/dx$ of the measured y region. The cross section can be given differentially e.g. for a value Q_0^2 within the Q^2-bin i by dividing the cross section for that bin by the theoretical integrated cross section and multiplying it with the theoretical differential cross section evaluated at Q_0^2. This is sometimes called the bin-centering correction factor $\mathcal{C}_i^{\text{bin}}(Q_0^2)$:

$$\mathcal{C}_i^{\text{bin}}(Q_0^2) = \frac{\left.\frac{d\sigma^{\text{theory}}}{dQ^2}\right|_{Q_0^2}}{\int_{Q^2{}_{low}}^{Q^2{}_{high}} dQ^2 \, \frac{d\sigma^{\text{theory}}_{\text{MC}}}{dQ^2}}. \tag{4.41}$$

This concept is only valid if data and MC distributions agree in that bin. In case of disagreements in the distributions the measurements suffer from different event distributions within the bin. This can be avoided by reweighting the MC to describe the data, if necessary in an iterative procedure. For this analysis the general agreement has been proven in Sect. 4.4, and is indirectly visible from the results when compared to theory, which is approximately equal to the one used for MC generation. It is therefore concluded, that no reweighting is necessary.

Inserting (4.41) in (4.40) the differential cross section yields:

$$\left.\frac{d\sigma^{\text{meas}}}{dQ^2}\right|_{Q_0^2} = \mathcal{C}_i^{\text{bin}}(Q_0^2)\cdot\sigma_i^{\text{meas}} = \frac{N_{\text{Data}}}{N_{\text{MC}}}\cdot\left.\frac{d\sigma^{\text{theory}}}{dQ^2}\right|_{Q_0^2}. \tag{4.42}$$

Including the background subtraction (4.36) from Sect. 4.5.3 and the radiative corrections as described in Sect. 4.5.4 the unfolding proceeds via the formula given here for the differential cross section in Q^2:

$$\left.\frac{d\sigma^{\text{meas}}_{\text{Born}}}{dQ^2}\right|_{Q_0^2} = \frac{N^{\text{tot}}_{\text{Data}} - N_{\text{BG}}}{N_{\text{MC}}}\cdot\left.\frac{d\sigma^{\text{theory}}_{\text{Born}}}{dQ^2}\right|_{Q_0^2}. \tag{4.43}$$

All theoretical cross sections were calculated using the CTEQ5D PDFs.

To estimate the statistical error the uncertainty on the number of data events, $N^{\text{tot}}_{\text{Data}}$, is estimated using Poisson probability. The event numbers for signal MC, N_{MC}, and background MC, N_{BG}, are the sums of the weights, $\sum w_i$. Correspondingly the uncertainty is the square-root of the summed squared weights, $\Delta N_{\text{MC}} = \sqrt{\sum w_i^2}$. The uncertainty for the cross section, $\Delta\left(\left.\frac{d\sigma^{\text{meas}}_{\text{Born}}}{dQ^2}\right|_{Q_0^2}\right)$, is then given by Gaussian error propagation:

$$\Delta\left(\left.\frac{d\sigma^{\text{meas}}_{\text{Born}}}{dQ^2}\right|_{Q_0^2}\right) = \sqrt{\left(\frac{\Delta N^{\text{tot}}_{\text{Data}}}{N_{\text{MC}}}\right)^2 + \left(\frac{\Delta N_{\text{BG}}}{N_{\text{MC}}}\right)^2 + \left(\frac{\Delta N_{\text{MC}}(N^{\text{tot}}_{\text{Data}} - N_{\text{BG}})}{N^2_{\text{MC}}}\right)^2}\cdot\left.\frac{d\sigma^{\text{theory}}_{\text{Born}}}{dQ^2}\right|_{Q_0^2}. \tag{4.44}$$

4.6 Systematic checks

The systematic uncertainties were estimated by varying the appropriate selection or analysis detail and repeating the whole analysis. The complete list of checks is given in Table 4.11. In Appendix B the relative deviation of the cross sections for each check in Figs. B.1 to B.15. The negative or positive deviations from the nominal analysis have been added separately in quadrature for each bin to yield the total systematic uncertainty. To avoid overestimation of the systematic uncertainty by double counting statistical effects only those checks were accounted for the total systematic uncertainty that show bin-by-bin correlated and statistically significant deviations from the nominal cross sections.

4.6.1 Cut variation

To check the influence of several cuts on the analysis results the cut values have been varied typically by ±10%. Especially if data and MC show different behaviors in the distribution around the cut threshold value moving the cut results in a modified acceptance and via unfolding in a different cross section value. Equally, the acceptance might accidentally agree in data and MC if only regarded single-differentially, but correlations

No. of check	Variation	Typ of check
01	$P_t^{\text{low}-\gamma} = 12.6\,\text{GeV}$	Cut variation
02	$P_t^{\text{low}-\gamma} = 15.4\,\text{GeV}$	
03	$P_t^{\text{-}ir,\,\text{low}-\gamma} = 10.8\,\text{GeV}$	
04	$P_t^{\text{-}ir,\,\text{low}-\gamma} = 13.2\,\text{GeV}$	
05	$P_t^{\text{high}-\gamma} = 10.8\,\text{GeV}$	
06	$P_t^{\text{high}-\gamma} = 13.2\,\text{GeV}$	
07	$P_t^{\text{-}ir,\,\text{high}-\gamma} = 9.0\,\text{GeV}$	
08	$P_t^{\text{-}ir,\,\text{high}-\gamma} = 11.0\,\text{GeV}$	
09	$0.293 < \theta^{\text{good}-\text{track}} < 2.85$	
10	$P_t^{\text{good}-\text{track}} = 0.22\,\text{GeV}$	
11	$\Delta\varphi^{\text{low}P_t} = 0.45, \Delta\varphi^{\text{high}P_t} = 1.8$	
12	$\Delta\varphi^{\text{low}P_t} = 0.55, \Delta\varphi^{\text{high}P_t} = 2.2$	
13	$P_t/E_t{}^{\text{low}P_t} = 0.495$	
14	$P_t/E_t{}^{\text{low}P_t} = 0.605$	
15	$P_t/E_t{}^{\text{mid}P_t} = 0.36$	
16	$P_t/E_t{}^{\text{mid}P_t} = 0.44$	
17	$P_t^{P_t/E_t-\text{cut low}P_t} = P_t^{\Delta\varphi} = 18\,\text{GeV}$	
18	$P_t^{P_t/E_t-\text{cut low}P_t} = P_t^{\Delta\varphi} = 22\,\text{GeV}$	
19	$P_t^{P_t/E_t-\text{cut mid}P_t} = P_t^{\text{PHP}} = 27\,\text{GeV}$	
20	$P_t^{P_t/E_t-\text{cut mid}P_t} = P_t^{\text{PHP}} = 33\,\text{GeV}$	
21	$(N_{\text{trk}} - 16)/N_{\text{good-trk}} < 4$	
22	$(N_{\text{trk}} - 24)/N_{\text{good-trk}} < 4$	
23	Vertex left satellite up	Vertex reweighting
24	Vertex left satellite down	
25	Vertex right satellite up	
26	Vertex right satellite down	
27	PHP normalization +20%	PHP normalization
28	PHP normalization -20%	
29	reweight MC to include F_L and F_3	QCD NLO
30	reweight MC by ZEUS-S PDF uncertainty up	PDF
31	reweight MC by ZEUS-S PDF uncertainty down	
32	use MEPS signal MC	Hadronisation
33	reweight CAL energies: F+1%, B+1%, R+2%	CAL energy-scale
34	reweight CAL energies: F-1%, B-1%, R-2%	
35	reweight CAL energies: F+1%, B-1%, R+2%	
36	reweight CAL energies: F-1%, B+1%, R-2%,	
37	reweight CAL energies: FEMC+2%, FHAC-2%	
38	reweight CAL energies: BEMC+2%, BHAC-2%	
39	reweight CAL energies: REMC+2%, RHAC-2%	
40	reweight CAL energies: FEMC-2%, FHAC+2%	
41	reweight CAL energies: BEMC-2%, BHAC+2%	
42	reweight CAL energies: REMC-2%, RHAC+2%	

Table 4.11: List of variations done for systematic checks in analysis details or cut thresholds.

to other quantities could be hidden from view and lead to a systematic shift in the cross sections. The effect can be worsened if the slope of the distribution is large at the cut threshold value. On the other hand we expect the cross section to vary within the statistical uncertainty. Adding quadratically every deviation would increase the systematic uncertainty with each additional check. To this end it is more meaningful to account for the influence of a systematic source like the PHP background not by changing the cut threshold but by varying the normalization of the statistically subtracted PHP MC used for estimating the background contribution, as described in Sect. 4.5.3. The variation of the threshold is presented here as an additional check.

The cut thresholds that have been varied are given in Table 4.11. The important thresholds in the transverse momenta have been varied individually for P_t and P_t^{-ir} as well as for low-γ and high-γ samples (No. 1-8 in Table 4.11). To test the influence of the CTD acceptance the good-track criteria (4.3) have been tightend to a narrower polar-angle region (No. 9) and to higher transverse track momentum (No. 10). The P_t/E_t and $\Delta\varphi$ cuts suppressing mainly PHP have been varied (No.11-16). The threshold in P_t for the lower P_t/E_t cut and $\Delta\varphi$ (No. 17,18) at $P_t = 20\,\text{GeV}$ as well as for the medium P_t/E_t and the PHP-rejection on track asymmetry (No. 19,20) at $P_t = 30\,\text{GeV}$ have been varied to check the sensitivity to the step in the cut. The offset in the 2D cut on the ratio $N_{\text{trk}}/N_{\text{good-trk}}$ that rejects beam gas background has been varied by $\pm 20\%$ (No. 21,22).

As can be seen from the control plots in Appendix B none of the cut variations yields a significant systematic deviation from the nominal analysis compared to the statistical uncertainty. As a consequence they are neglected in the systematic uncertainty.

4.6.2 Diffractive CC contribution

A sub-class of the inclusive CC process are diffractive events, where the lepton interacts via $W^{\pm}$ boson exchange with a hadronic object that is coupled to the proton by exchange of something that carries the quantum numbers of the vacuum, i.e. has no color, which is usually refered to as the Pomeron. The lack of color flow between the proton, that can even stay intact in such an interaction, and the hadronic object scatterd by the $W^{\pm}$ leads to a sizeable separation in the final state. The psudo-rapidity η, as defined in Sect. 2.2, which has the property to conserve the shape of its distribution only shifted by an additive constant under Lorentz transformation, translates this separation in the center-of-mass frame to the laboratory frame, the ZEUS detector. The key signature for a diffractive event is therefore a gap in the rapidity distribution of the energy deposited in the calorimeter. If the proton stays intact it leaves the main detector undetected through the beam pipe. The gap extends from the maximum detectable η to the energy deposit with the maximum η_{max} measured. Because of the proton remnant η_{max} of normal DIS events is close to the maximum detectable η. For diffractive events η_{max} is much smaller.

The signal MC sample contains no explicit simulation of diffractive events. However, diffractive events are a sub-class, included in the inclusive measurement. If the contribution of diffractive events in the data would be sizeable, this would effect the acceptance corrections through migrations in insufficiently described quantities and therefore would

lead to a systematic effect in the cross section measurement. It would not have a direct influence on the measured cross section like background processes, though. To estimate the contribution of diffractive events a sample simulating especially this event-class has been generated using RAPGAP [69]. The distributions expected to be sensitive to diffraction, $\eta_{\max}, x$ and γ_{h}, gave no indication of a considerable diffractive contribution. Since these are the distributions that could in principle lead to an effect on the cross section measurement if underestimation of the diffractive contribution results in an insufficient description, the diffractive contribution is not considered here to yield a systematic effect on the measurement of CC cross sections.

4.6.3 Vertex distribution

To account for the uncertainty in the estimation of the vertex distribution as it is used in the MC the satellites which accompany the main peak are varied in the signal MC. The corresponding parameterizations of the modified vertex distribution are shown in Fig. 4.50.

4.6.4 NLO QCD corrections

The DJANGOH program used for MC generation neglects F_L and the NLO correction to F_3. To estimate the uncertainty due to this feature the signal MC has been reweighted with the ratio of the calculated cross section with and without NLO QCD corrections (No. 29). The biggest influence is seen at high y with 5%.

4.6.5 Uncertainty from PDFs

For MC generation as well as for unfolding the PDFs CTEQ5D have been used. The PDFs can have an influence on the acceptance estimation via event migrations. The effect of the PDFs uncertainties have been estimated by reweighting the signal MC to represent the deviation in the PDFs as allowed by the ZEUS-S fit (No. 30,31). This leads to deviations from the nominal cross sections up to $\pm 10\%$ at high x and $\pm 5\%$ at high Q^2.

4.6.6 Parton-shower scheme

As described in Sect. 4.1.1.1 the signal MC samples were generated using ARIADNE which uses the CDM as parton-shower model. To study the effect this choice of model has on the analysis it has been repeated with an MC sample generated using MEPS (No. 32). This leads to deviations of around $\pm 5\%$, being largest at high Q^2 ($\pm 20\%$) and at high y ($\pm 10\%$). The uncertainties related to the hadronization are the symmetrized deviations from the nominal analysis. Though the statistics of the MC samples is large enough to render the contribution to the statistical uncertainty of the cross section measurement negligible, the

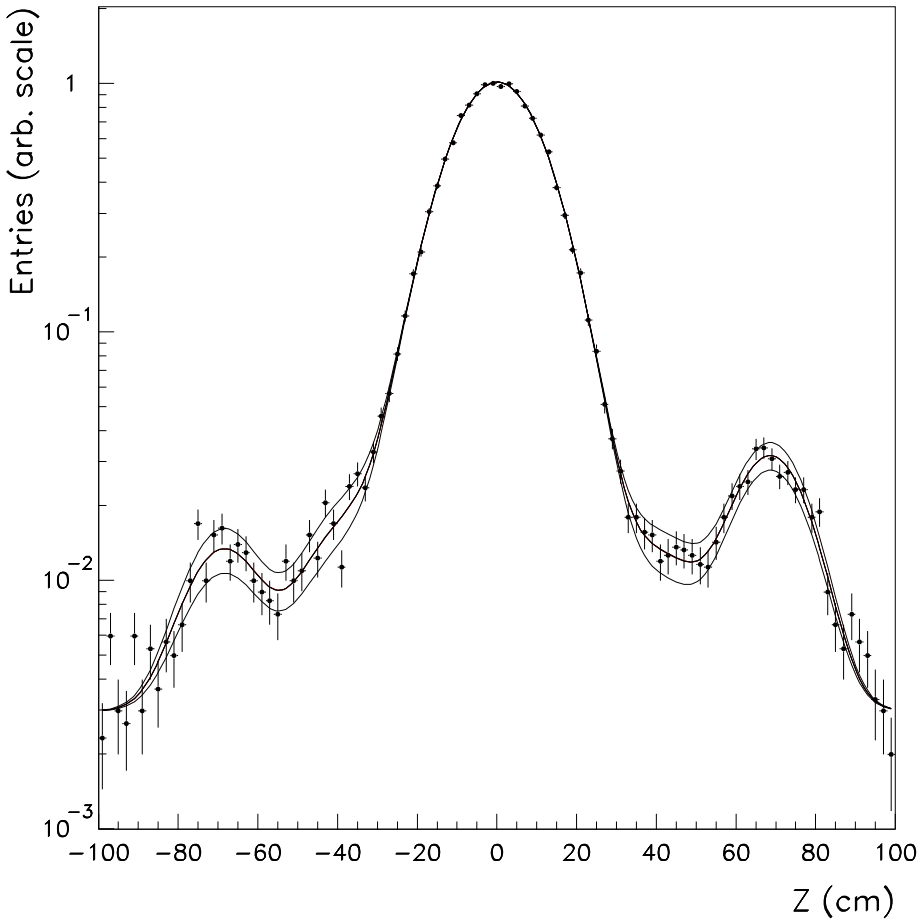

Figure 4.50: Vertex distribution as used in the MC with the parameterizations used for the systematic check. The left and right satellite are each varied up and down. The data are obtained from a minimum bias sample. From [59].

estimation of the hadronization uncertainty suffers from around 1% statistical uncertainty of the MC samples.

4.6.7 Background subtraction

As described in Sect. 4.1.1.2 the normalization of the PHP MC has been established without relying on the theoretical calculation of the cross section by fitting the PHP MC to match the data distribution in P_t/E_t. To estimate the contribution of the uncertainty in the PHP MC normalization to the cross section measurement's uncertainty this normalization has been varied by ±20% (No. 27,28). This corresponds to twice the uncertainty of the fit result.

4.6.8 Calorimeter energy-scale uncertainty

The uncertainty in the overall calorimeter energy scale has been determined to be 2% in RCAL and 1% in FCAL and BCAL [13]. The systematic influence on the estimators for the kinematic variables depends on the correlation of the energy scale variations in the different calorimeter parts and sections. The influence on the measurements are of three kinds. For each kind the configuration of variation in the individual energy scales yielding the maximum effect on the estimator under study has been applied to the MC and the analysis repeated.

- The influence of the total energy scale was studied by varying all parts up or down simultaneously (No. 33, 34 in Table 4.11). The resulting shifts in the cross sections were found to be correlated between kinematic bins.
- The effect of the energy scale on polar angles is maximized if the energy scale of the BCAL is increased while decreasing FCAL and RCAL and vice-versa (No. 35, 36 in Table 4.11). In the first case the hadronic polar angle γ_{h} is pulled towards the transversal direction, in the latter towards the longitudinal direction. The resulting shifts were found to be correlated between kinematic bins.
- The influence of the energy fraction deposited in the electromagnetic and hadronic section is studied by increasing one section while decreasing the other by 2% for each calorimeter part separately (No. 37-42 in Table 4.11).

The uncertainty denoted to the calorimeter energy scale is the square root of the summed deviations from the nominal analysis, where positive and negative deviations were summed separately. The resulting shifts in the cross sections were typically within $\pm 5\%$, but increased towards high Q^2 and high x to about $\pm 20\%$.

4.6.9 Luminosity uncertainty

The uncertainty of the luminosity measurement of 2.25% affects each measured cross section value in equal proportion as an overall normalization uncertainty. The luminosity uncertainty is not included in the systematic uncertainty since it would decrease the information on the point-by-point varying systematic effects. The given measurements can therefore vary in addition to the systematic uncertainty equally within the luminosity uncertainty of 2.25%.

4.6.10 Summary of sytematic checks

In Fig. 4.51 the relative systematic uncertainty is splitted into the contributions of the different classes of systematic checks as denoted in Table 4.11. The systematic uncertainty is for all but one bin in the double differential cross section measurement smaller than the statistical uncertainty. The measurement is therefore statistics limited and its accuracy would considerably improve if more data would become available.

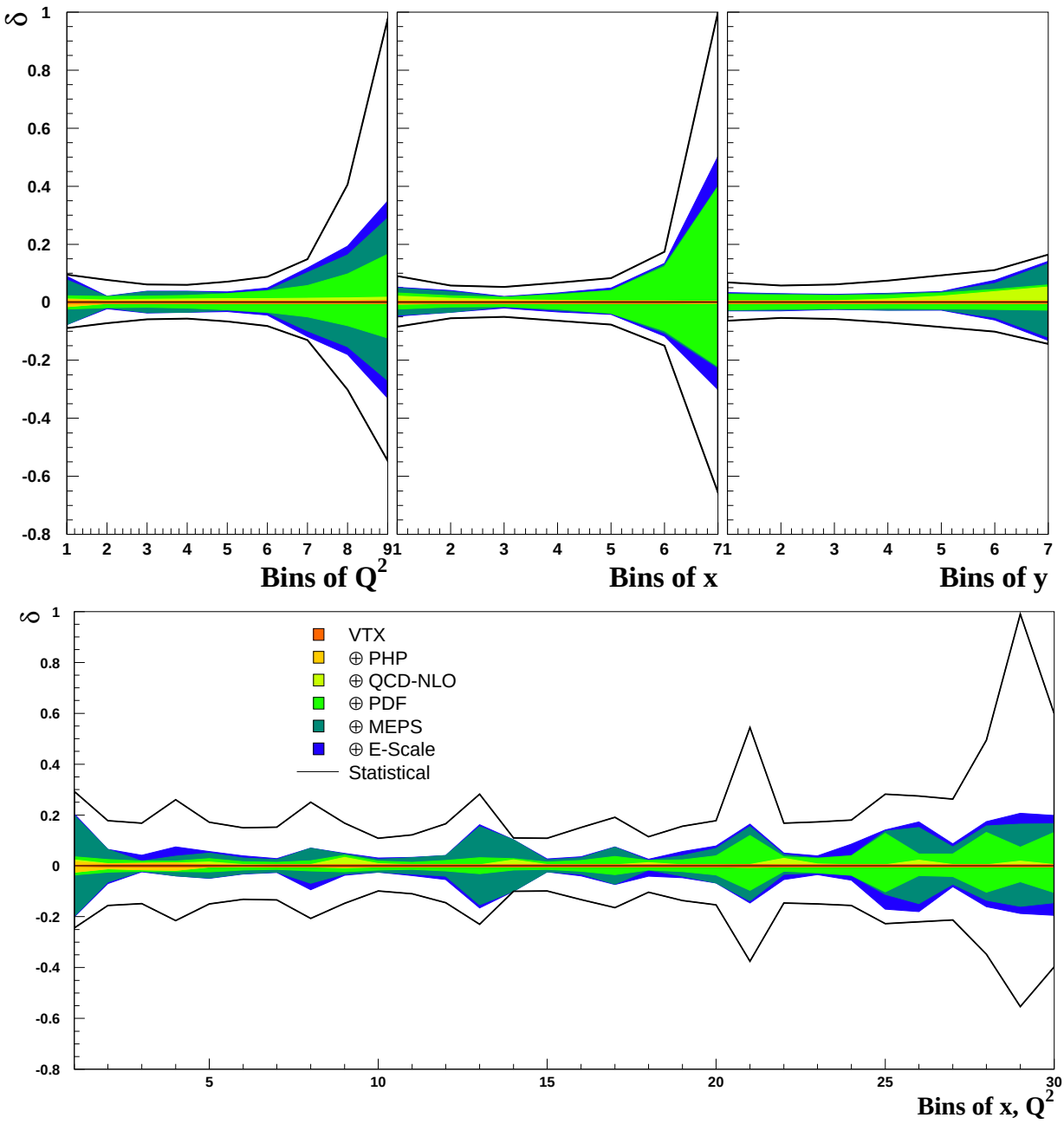

Figure 4.51: Contributions to the relative systematic uncertainty of the cross section measurements from the different classes of systematic checks versus bin number in Q^2 (upper left), x (upper middle), y (upper right) for the single differential measurements and the bin number of the double differential measurement (bottom). The solid lines denote the relative statistical uncertainty.

Chapter 5

Results and discussion

5.1 Single differential cross sections

With the unfolding procedure described in Sect. 4.5.5 the following single differential cross sections are determined and presented:

- $d\sigma/dQ^2$ in Fig. 5.1,
- $d\sigma/dx$ in Fig. 5.2,
- $d\sigma/dy$ in Fig. 5.3.

The statistical uncertainty is evaluated using (4.44). The total error given in the figures is the quadratic sum of the statistical and the systematic uncertainties, the latter as described in Sect. 4.6. The figures show the prediction of the SM evaluated using the ZEUS-S PDFs introduced in Sect. 3.7. The error band indicates the total uncertainty of the ZEUS-S PDFs. For comparison, the SM prediction as evaluated with the alternative PDFs CTEQ6D and MRST(2001) are plotted, too.

The measured cross sections are well described by the SM prediction. This is even more remarkable as the cross section drops e.g. in the case of $d\sigma/dQ^2$ in the measured Q^2 range from $200\,\mathrm{GeV}^2$ to $40\,000\,\mathrm{GeV}^2$ by more than four orders of magnitude.

For closer inspection, in Figs. 5.1 to 5.3 the ratios of the measurements to the SM prediction using ZEUS-S PDFs are shown. For comparison also the ratios of the predictions based on the alternative PDFs to the one evaluated with ZEUS-S are given. These ratios underline the good description by the SM prediction. Though the predictions using different PDFs deviate by more than the total uncertainty denoted to the ZEUS-S PDFs, the precision of the present measurement does not allow to descriminate between either one.

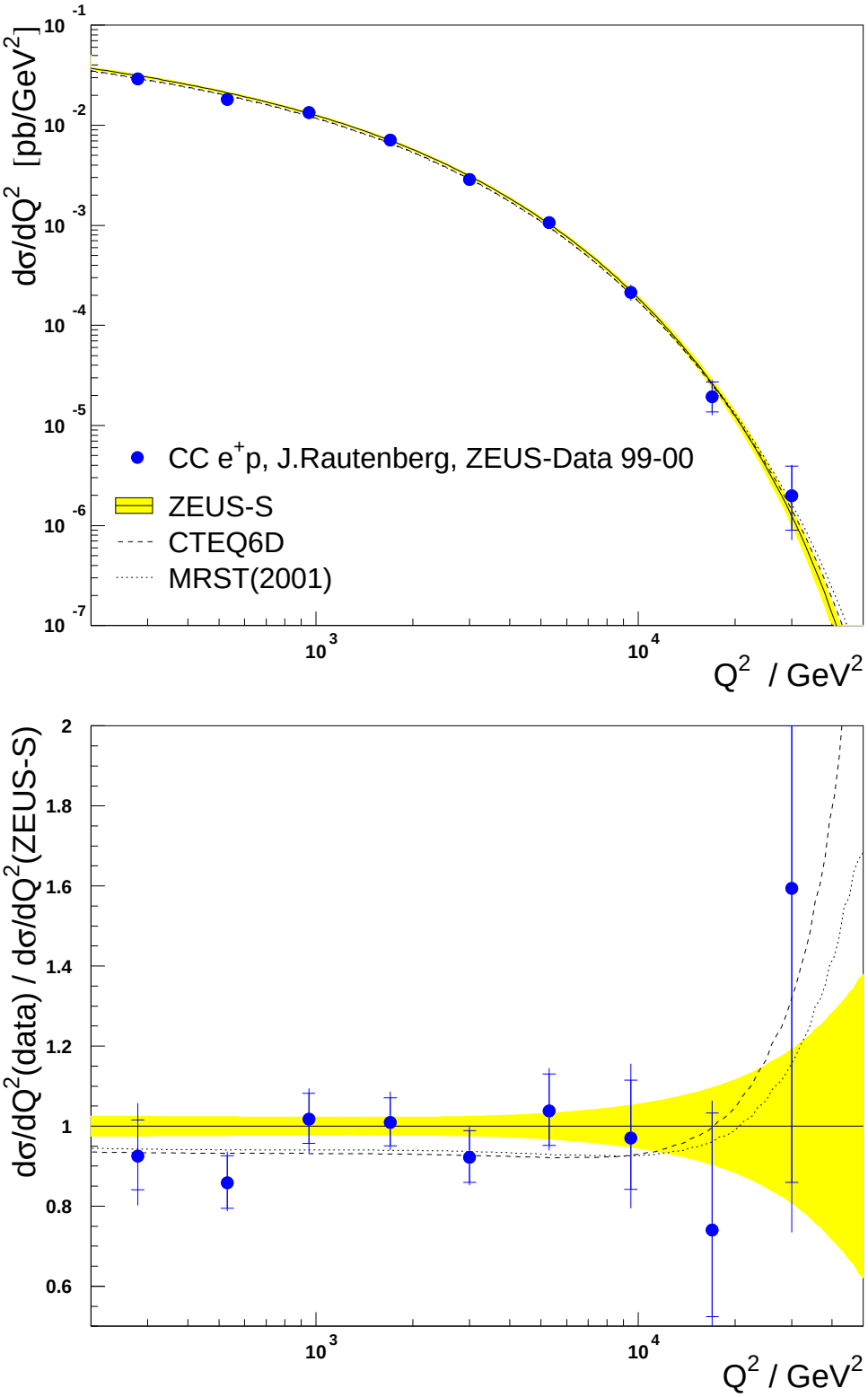

Figure 5.1: CC DIS Born cross section $d\sigma/dQ^2$ (top) and its ratio to the SM prediction using ZEUS-S (bottom) for the measurement based on the e^+p ZEUS-data 99/00, together with the SM predictions using the PDFs ZEUS-S with the error band denoting the total uncertainty, CTEQ6D and MRST(2001)

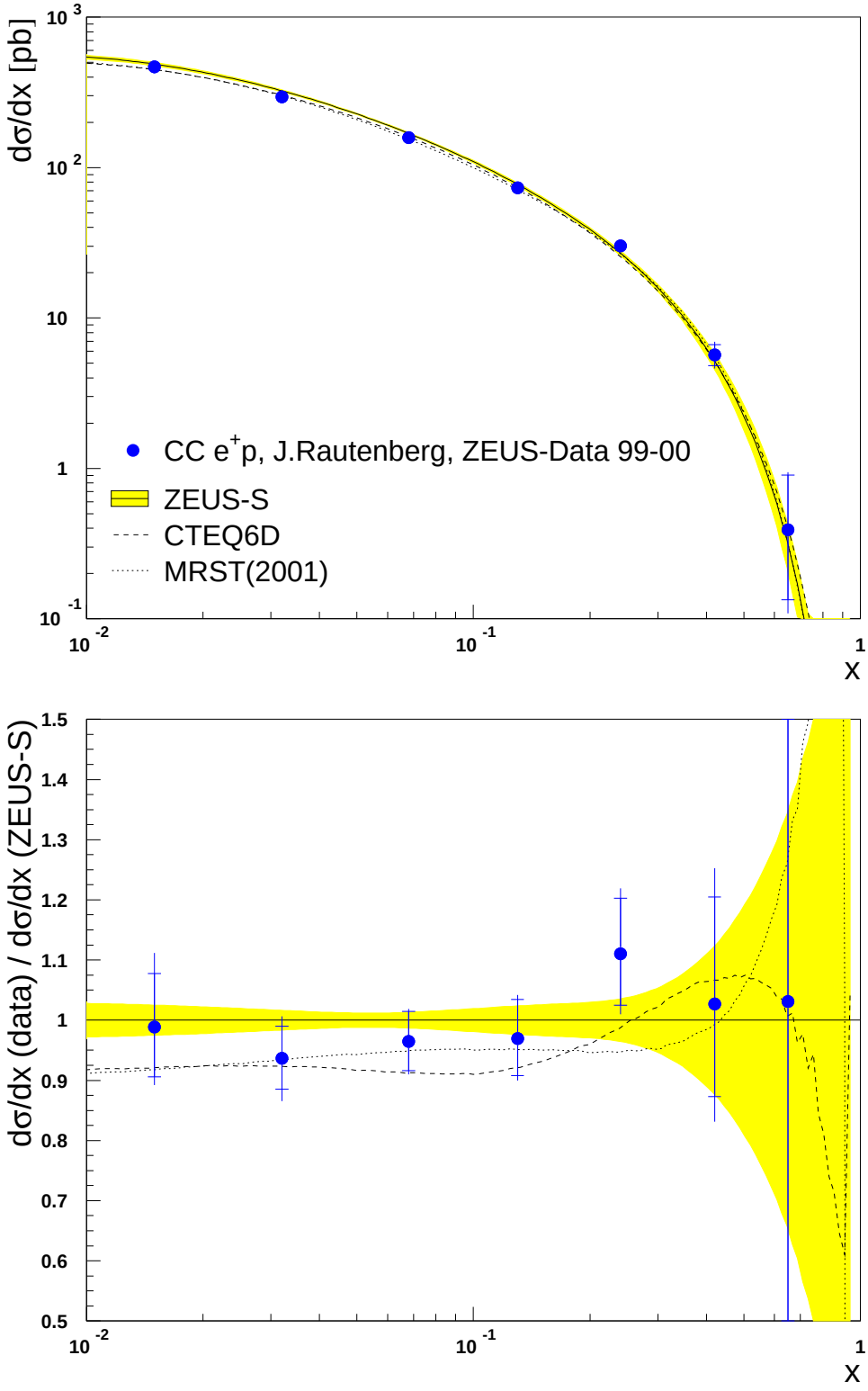

Figure 5.2: CC DIS Born cross section $d\sigma/dx$ (top) and its ratio to the SM prediction using ZEUS-S (bottom) for the measurement based on the e^+p ZEUS-data 99/00, together with the SM predictions using the PDFs ZEUS-S with the error band denoting the total uncertainty, CTEQ6D and MRST(2001)

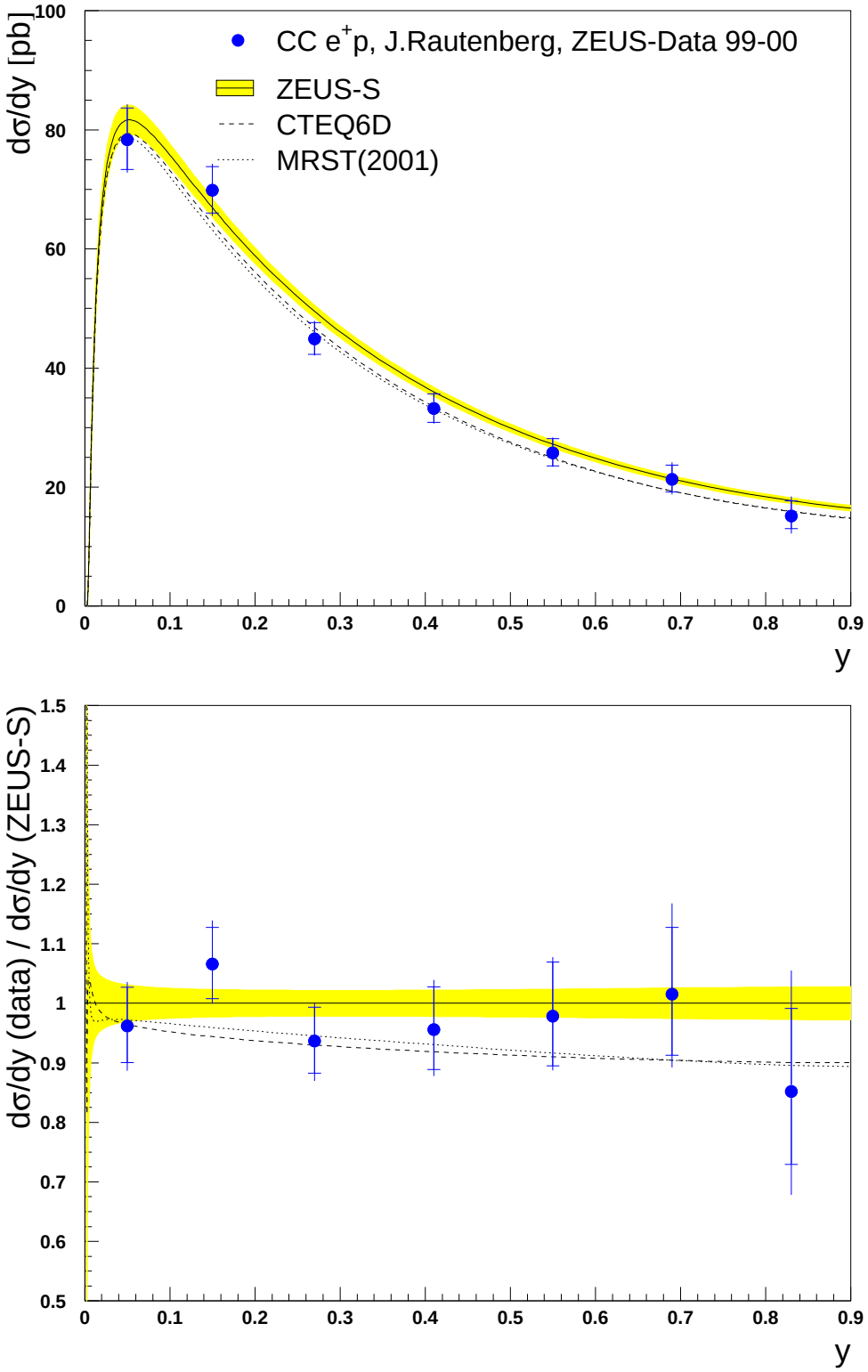

Figure 5.3: CC DIS Born cross section $d\sigma/dy$ (top) and its ratio to the SM prediction using ZEUS-S (bottom) for the measurement based on the e^+p ZEUS-data 99/00, together with the SM predictions using the PDFs ZEUS-S with the error band denoting the total uncertainty, CTEQ6D and MRST(2001)

5.2 Reduced cross sections

In Sect. 3.2 the reduced cross section $\tilde{\sigma}$ (3.22) has been defined, which reflects F_2 in most of the kinematic plane. This double differential cross section is also obtained using the unfolding method of Sect. 4.5.5. It is shown in Fig. 5.4 versus x in 8 bins of Q^2 and in Fig. 5.6 versus Q^2 in 6 bins of x. In addition, the SM predictions evaluated using the ZEUS-S PDFs are shown with the total uncertainty denoted by the error band.

The ratio of the measured cross secrion $\tilde{\sigma}$ to the SM prediction using ZEUS-S is shown in Fig. 5.7 versus Q^2 in bins of fixed x and in Fig. 5.5 versus x in bins of fixed Q^2. In Figs. 5.5 to 5.7 the SM predictions using the alternative PDFs CTEQ6D and MRST(2001) are plotted, too. Again the limited precision of the data does not allow to discriminate between the sets of PDFs. As described in Sect. 3.3 in LO the cross section is interpretable on parton level. There, two major parts of the negatively charged quarks contribute to the cross section, $(\overline{u}+\overline{c})$ and $(d+s)$, the latter being helicity suppressed by the factor $(1-y)^2$. Both parts are plotted separately in Fig. 5.4 as evaluated from the QCD NLO ZEUS-S PDFs. The measurement gives no indication of discrepancy with the composition of the two parts. This issue will be presented in the next section in an improved way.

5.3 Helicity structure

In the previous section the reduced cross section was tested in terms of the quark and anti-quark contributions. This can be visualized even more clearly if the reduced cross section is plotted versus the helicity suppressing factor $(1-y)^2$. Resulting from (3.26) the reduced cross section in the naive parton model gives a straight line with the $(\overline{u}+\overline{c})$ part corresponding to the constant term and the $(d+s)$ part to the linearly rising term. This is shown in Fig. 5.8 for the CC e^+p reduced cross section measured here, as well as for the CC e^-p reduced cross section. Assuming the absence of any sea asymmetry, i.e. $q_{\rm sea} = \bar{q}_{\rm sea}$, the difference in the constants at $(1-y)^2 = 0$ can be interpreted as the u-quark valence distribution and the difference at $(1-y)^2 = 1$ as the difference in u- and d-quark valance distribution. Or, more explicitly, in formulae:

$$\tilde{\sigma}^{\rm CC}_{e^+p} = x\left[(\bar{u}_{\rm sea}+\bar{c}_{\rm sea}) + (1-y)^2(d_{\rm valence}+d_{\rm sea}+s_{\rm sea})\right] \quad (5.1)$$

$$\tilde{\sigma}^{\rm CC}_{e^-p} = x\left[(u_{\rm valence}+u_{\rm sea}+c_{\rm sea}) + (1-y)^2(\bar{d}_{\rm sea}+\bar{s}_{\rm sea})\right] \quad (5.2)$$

$$\left[\tilde{\sigma}^{\rm CC}_{e^-p} - \tilde{\sigma}^{\rm CC}_{e^+p}\right]_{(1-y)^2=0} = x\left[u_{\rm valence}\right] \quad (5.3)$$

$$\left[\tilde{\sigma}^{\rm CC}_{e^-p} - \tilde{\sigma}^{\rm CC}_{e^+p}\right]_{(1-y)^2=1} = x\left[u_{\rm valence} - d_{\rm valence}\right]. \quad (5.4)$$

In this interpretation the valence quark distributions can be read off from Fig. 5.8. The deviations from the straight lines demonstrate, that the validity of the naive parton model is limited to the region of appropiate scaling, i.e. x in the region $x \sim 0.1$. Another indication for the limited validity of the LO interpretation (3.26) is the excess of the up-type contributions over the SM prediction for $\tilde{\sigma}$ at $(1-y)^2$ close to zero in Fig. 5.8.

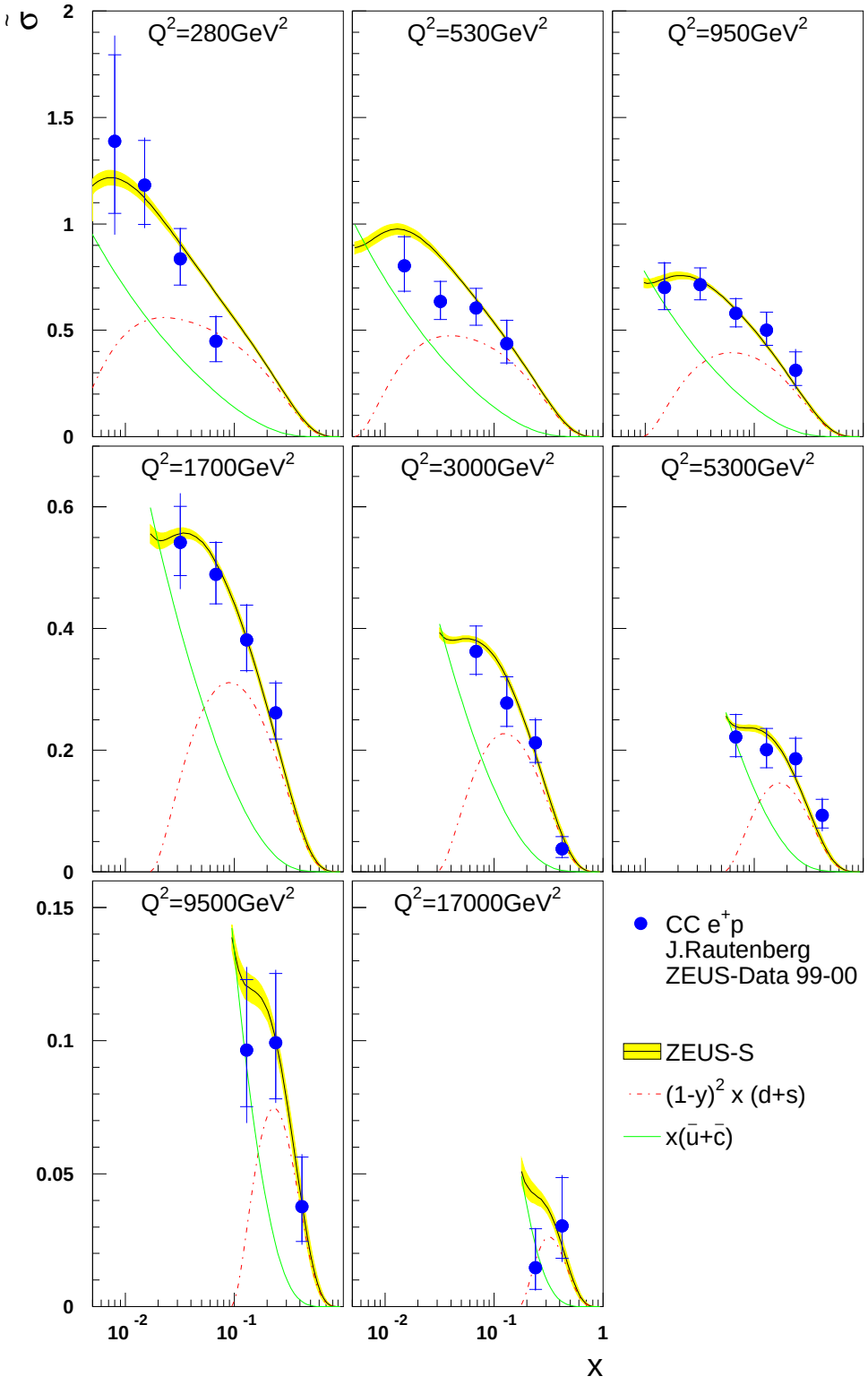

Figure 5.4: The reduced CC DIS Born cross section $\tilde{\sigma}$, for the measurement based on the e^+p ZEUS-data 99/00 as a function of x for 8 different bins of Q^2, together with the SM predictions using the PDFs ZEUS-S with the error band denoting the total uncertainty, the LO quark, $(1-y)^2 x(d+s)$, and anti-quark, $x(\overline{u}+\overline{c})$, contributions.

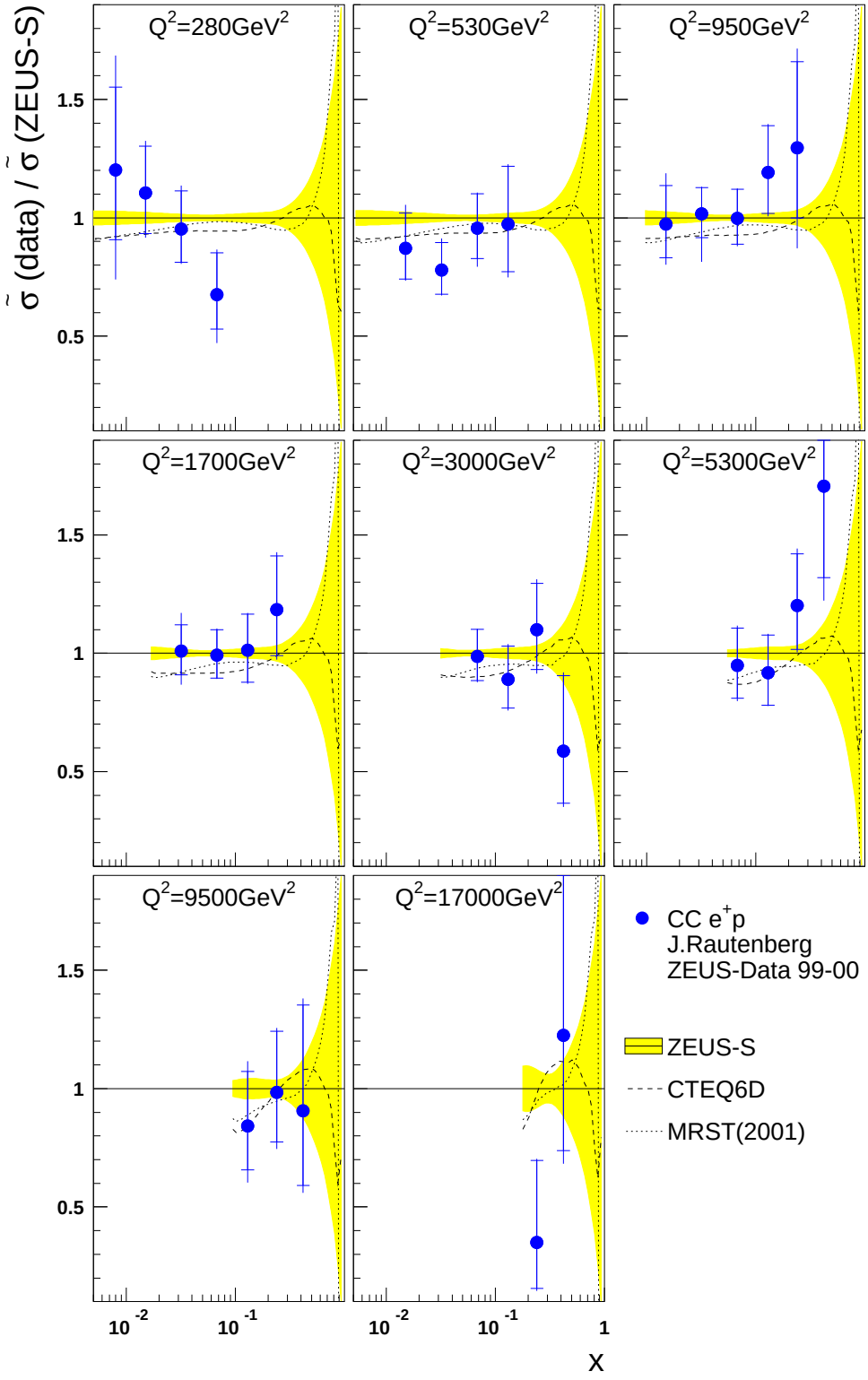

Figure 5.5: The ratio of the reduced CC DIS Born cross section $\tilde{\sigma}$, for the measurement based on the e^+p ZEUS-data 99/00 as a function of x for 8 different bins of Q^2, to the SM predictions using the PDFs ZEUS-S with the error band denoting the total uncertainty together with the expectations evaluated with CTEQ6D and MRST(2001).

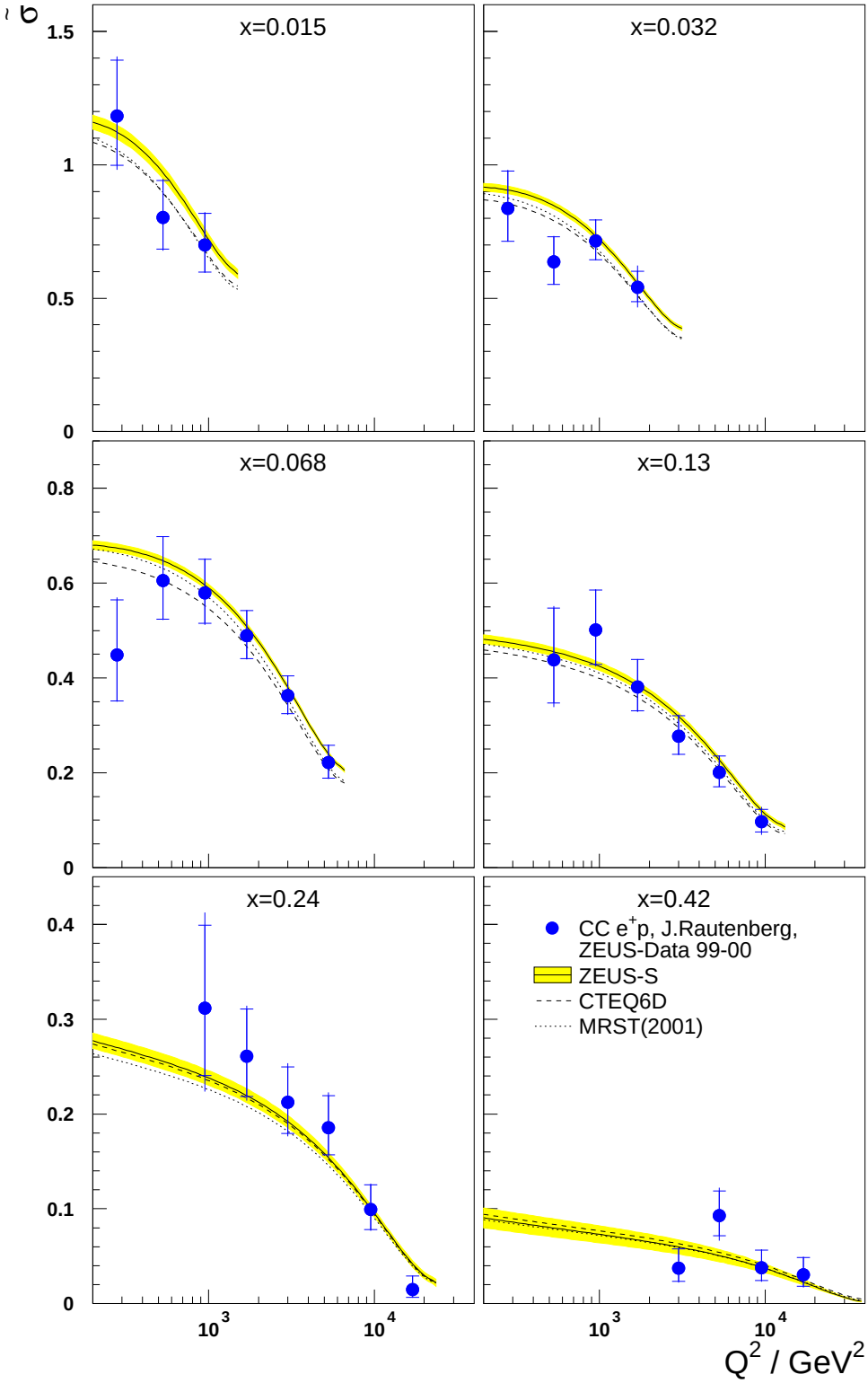

Figure 5.6: The reduced CC DIS Born cross section $\tilde{\sigma}$, for the measurement based on the e^+p ZEUS-data 99/00 as a function of Q^2 for 6 different bins of x, together with the SM predictions using the PDFs ZEUS-S with the error band denoting the total uncertainty, CTEQ6D and MRST(2001).

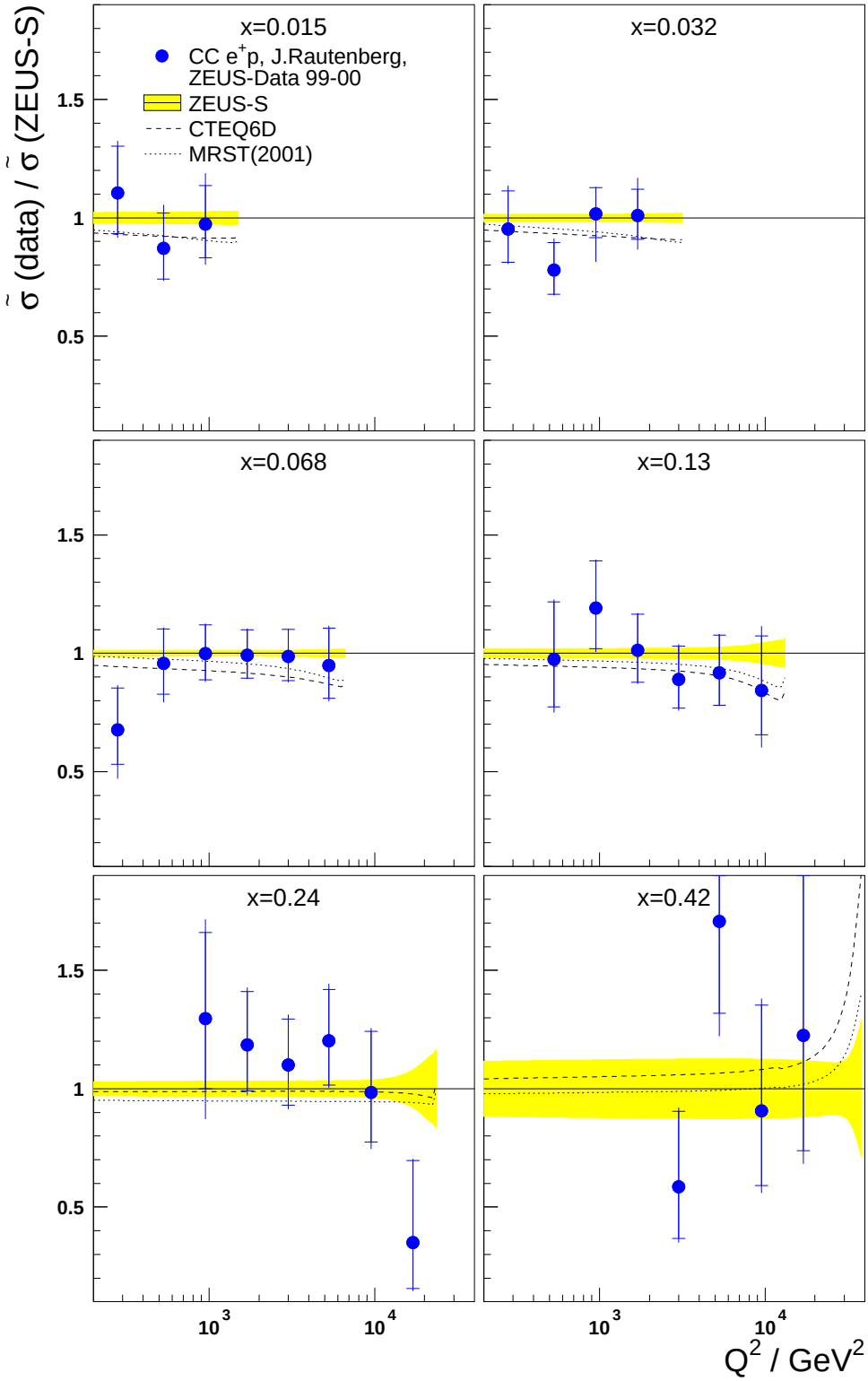

Figure 5.7: The ratio of the reduced CC DIS Born cross section $\tilde{\sigma}$, for the measurement based on the e^+p ZEUS-data 99/00 as a function of Q^2 for 6 different bins of x, to the SM predictions using the PDFs ZEUS-S with the error band denoting the total uncertainty together with the expectations evaluated with CTEQ6D and MRST(2001).

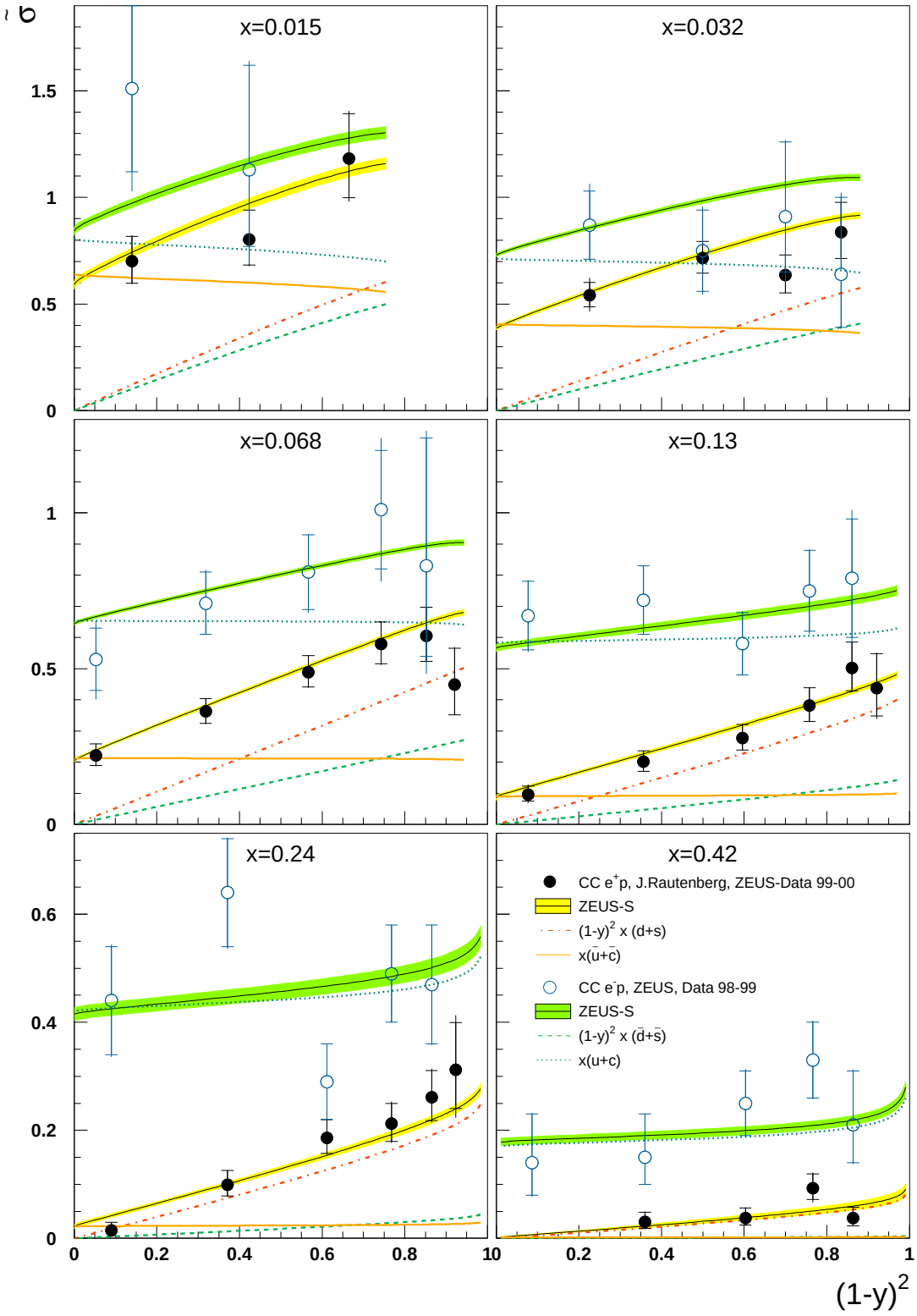

Figure 5.8: The reduced CC DIS Born cross section $\tilde{\sigma}$ for the measurement based on the e^+p ZEUS-data 99/00 (solid points) and for the published e^-p ZEUS-data 98/99 (open points) as a function of $(1-y)^2$ for different values of x together with the SM predictions using the PDFs ZEUS-S with the error band denoting the total uncertainty, the LO quark, $(1-y)^2 x(d+s)$, and anti-quark, $x(\overline{u}+\overline{c})$, contributions.

5.4 Determination of M_W

The Q^2 dependence of the single differential cross section $d\sigma/dQ^2$ as given in (3.21) arises mainly from the factor $\left[(Q^2 + M_W^{2\,2})/M_W^2\right]^2$, while the absolute value of the cross section is determined by the Fermi constant, G_F, and the PDFs. Therefore the meassured cross section $d\sigma/dQ^2$ can be used to extract the propagator mass M_W by fitting the theoretical prediction of the cross section to the measurement with M_W as free fit-parameter.

In this fit G_F is fixed to the PDG value $G_F = 1.16639 \cdot 10^{-5}\,\mathrm{GeV}^{-2}$. The statistical uncertainty of the fit is given by the M_W value where the χ^2 of the fit to the cross section of the nominal analysis is increased by one unit. To estimate the systematic uncertainty the fit has been repeated to the cross sections resulting from the modified analysis accounting for the estimation of the systematic uncertainty in Sect. 4.6. To avoid double counting of the statistical uncertainty the fits to the cross sections of the systematic checks take the relative statistical uncertainty into account as evaluated for the nominal measurement. For the total systematic uncertainty the positive and negative deviations from the nominal M_W are added in quadrature. The luminosity uncertainty, which has been given separately from the systematic point-to-point uncertainties for the cross section measurements, is included here by varying each value up and down by 2.25%. This effects the fit value in a non-trivial way, contrary to the normalization effect on the cross section measurement as described in Sect. 4.6, where it was not included in the systematic uncertainty.

For the cross section measurements the systematic effect of the PDFs as studied in Sect. 4.6 influences only the acceptance estimation via event migrations. This is qualitatively different for the estimate of M_W where it additionally enters directly in the calculation of the theoretical prediction. The uncertainty estimated by fitting a prediction where the calculation is varied by the uncertainty of the ZEUS PDFs is given separately and denoted as PDF.

The result of the total M_W fit is:

$$M_W = \left(80.9^{+2.1}_{-2.0}(\mathrm{stat.})^{+2.0}_{-1.6}(\mathrm{syst.})^{+3.3}_{-2.9}(\mathrm{PDF})\right)\ \mathrm{GeV}. \tag{5.5}$$

The advantage of measuring M_W by using a parameterization choosing G_F as EW parameter is that the higher order weak radiative corrections to the cross sections mainly cancel and are less dependend on m_H and m_t [70]. This way of evaluating M_W is therefore less dependent on higher order corrections than the alternative parameterization using $\cos\theta_\mathrm{W}$. The evaluation of M_W from the ratio of NC to CC has the advantage of being less sensitive to systematic effects since they cancel in the ratio. The ratio is less sensitive to M_W, though, since the M_W dependence which enters σ_NC via the form factor diminishes the M_W sensitivity of σ_CC alone.

The particular interest in measuring M_W in ep-CC-scattering arises from the fact, that here the W exchange is space-like. Even though the precision of the M_W measurement in ep scattering can not challenge the precision obtained from reactions with time-like W-exchanges [24], the measurement of the t-channel propagator mass M_W is a measurement

in its own right, as for the sensitivity of the reaction to an additional hypothetic heavier W' boson [71].

Chapter 6

Summary

In this thesis the charged current (CC) deep inelastic scattering (DIS) e^+p cross sections $d\sigma/dQ^2$, $d\sigma/dx$ and $d\sigma/dy$ have been measured for $Q^2 > 200\,\mathrm{GeV}^2$ at a center-of-mass energy of 318 GeV, as well as the double differential reduced cross section $d^2\tilde{\sigma}/dxdQ^2$ in the kinematic range $280\,\mathrm{GeV}^2 < Q^2 < 17\,000\,\mathrm{GeV}^2$ and $0.008 < x < 0.42$ (bin centers). The measurements are based on ZEUS data corresponding to an integrated luminosity of $61\,\mathrm{pb}^{-1}$, collected in the 1999 and 2000 e^+p HERA running periods.

The MC simulation is a basic tool to analyze detector properties like resolutions and to measure acceptance, efficiency and purity. In addition to the CC signal reaction, several physics processes as sources of background to the CC signal have been simulated to study their contribution to the measurement. The major contamination is due to photoproduction. The normalization of the photoproduction (PHP) sample has been determined from a specially prepared data sample to avoid the theoretical uncertainty of the PHP cross section.

For the reconstruction of the kinematic variables the determination and measurement of the hadronic final state is essential. Sophisticated algorithms for cleaning, correcting and clustering the calorimeter deposits have been employed. The pivot for the polar angle of the hadronic final state is the interaction vertex. Its determination is challenging, since the kinematic region of the measurement exceeds the acceptance of the central tracking detector. For events with the hadronic final state outside the tracking acceptance the vertex has been reconstructed based on the timings of the calorimeter energy deposits.

The selection of the signal sample has the goal to suppress background as much as possible while maintaining a reasonable significance of the signal statistics. A complete separation of signal and background was found to be not possible, though. The limited geometrical acceptance of the central tracking detector made it necessary to split the sample into polar regions where tracking is reliably available and where the vertex has to be reconstructed using alternatively calorimeter timing information. The reconstructed tracking vertex has been determined to be available for $\gamma_0 > 0.4$ rad. The selection criteria have thus been developed separately for a high-γ and a low-γ sample.

For a multi-purpose detector as ZEUS with a wide range of physical programs and a

potential rate for interactions of 60 MHz the dedicated trigger selection for a sub-class of events like CC is vital. The logic of the three leveled trigger has been described and its properties and reliability have been studied in detail. The main focus has been on the run-by-run dependence of the calorimeter FLT and on the efficiency of the FLT slot 60. The performed run selection guarantees a proven run quality for CC analysis. The signal region in the kinematic plane has been defined. Criteria for suppressing the non-*ep* backgrounds, halo and cosmic muons as well as beam gas interactions, have been developed. The contamination of PHP as the main *ep* background has been limited. The rejection of NC events on the basis of a special algorithm for finding the scattered electron has been optimized. All candidate events have been visually scanned and 16 obviously non-*ep* background events were rejected.

The final event sample has been presented and the description by the MC has been verified. This is necessary to guarantee the assumed equivalence of the real detector acceptance needed for the unfolding and the acceptance determined with the MC.

The bin definition for the cross section measurement takes into account the measured resolution of the kinematic variables. Acceptance, efficiency and purity have been determined from the MC. The remaining *ep* background not suppressed by the signal selection has been subtracted statistically. The bin-by-bin unfolding technique presented also corrects for radiative effects.

Systematic effects that could have an effect on the cross section measurements have been studied and the resulting systematic uncertainty estimated. Cut threshold values were found not to have a systematic effect within statistics. Sources of effects taken into account for the estimation of the systematic uncertainty are the satellites of the vertex distribution, the negligence of higher order QCD contributions to the signal MC sample, the PDF uncertainty, the choice of model for the parton showering scheme, the background subtraction and the calorimeter energy scale. The effect of the luminosity uncertainty on the cross section is a trivial overall normalization error and has not been included in the total systematic uncertainty.

The results presented are the single differential CC DIS e^+p cross sections $d\sigma/dQ^2$, $d\sigma/dx$ and $d\sigma/dy$, as well as the double differential reduced cross section $d^2\sigma/dxdQ^2$ for $Q^2 > 200$. The cross sections have been found to be in good agreement with the SM prediction using the ZEUS-S PDFs. The comparison with SM predictions using the alternative PDFs CTEQ6D and MRST(2001) yielded no preference for one of them. The $(1-y)^2$ dependence of the reduced cross section $d^2\sigma/dxdQ^2$ reveals the chiral structure of the SM, which has been investigated. The mass of the space-like W boson propagator is determined from a fit to $d\sigma/dQ^2$ to be $M_W = 78.9 \pm 2.0\,(\text{stat.}) \pm 1.8\,(\text{syst.})\,^{+2.0}_{-1.8}\,(\text{PDF})$ GeV.

As a global result the electroweak sector as well as the QCD part of the standard model have been found to describe the measurements presented here very well and survive the tests performed in this thesis well reinforced.

Appendix A

Examples of CC events

In this section CC example events are presented. They are visualized with the ZEUS software package ZEVis [19]. In figs. A.1 to A.3 an z-r projection of the detector is displayed on the left. This view allows to identify easily the correlation in θ. The protons enter from the right and the electrons from the left. Corresponding to the proton direction the left side is denoted as forward. The calorimeter part on the left is therefore FCAL. The r-ϕ projection on the right side shows azimuthal correlations and transversal imbalance. Only those detector components which are cylindrically shaped and have their longitudinal segmentation in the radial direction are diplayed in this view, i.e. BCAL and CTD but not FCAL/RCAL. The Calorimeter is segmented in the smaller EMC and the bigger HAC sections, as described in Sect. 2.2.2.

Figures A.1 and A.2 show both events of the high-γ sample. Therefore the selection requires good-tracks from a reconstructed vertex. The event of the low-γ sample in Fig. A.3 has to meet no tracking requirement. All three events are part of the signal sample and fulfill the selection criteria as presented in Sect. 4.3.

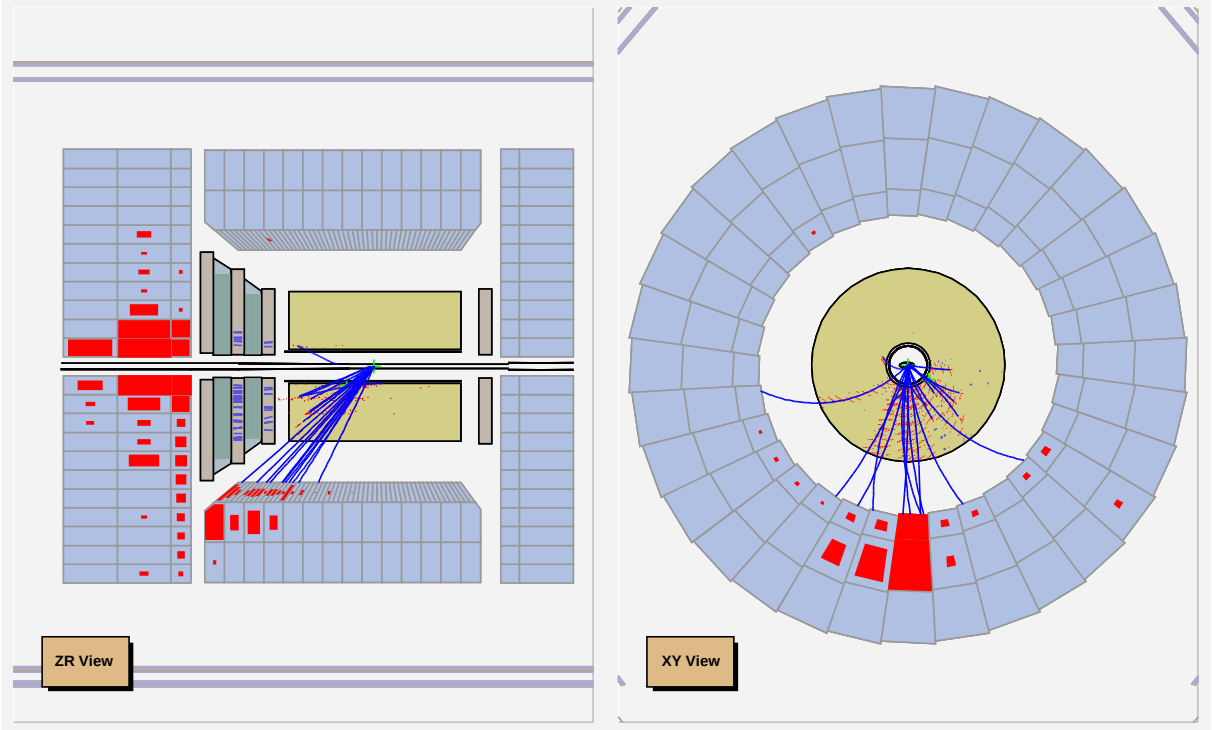

Figure A.1: Visualized CC event number 13581 of run 33423 with the reconstructed kinematic variables $Q^2 = 1517\,\mathrm{GeV}^2$, $x = 0.061$, $y = 0.245$, $\gamma_\mathrm{h} = 0.76$ rad.

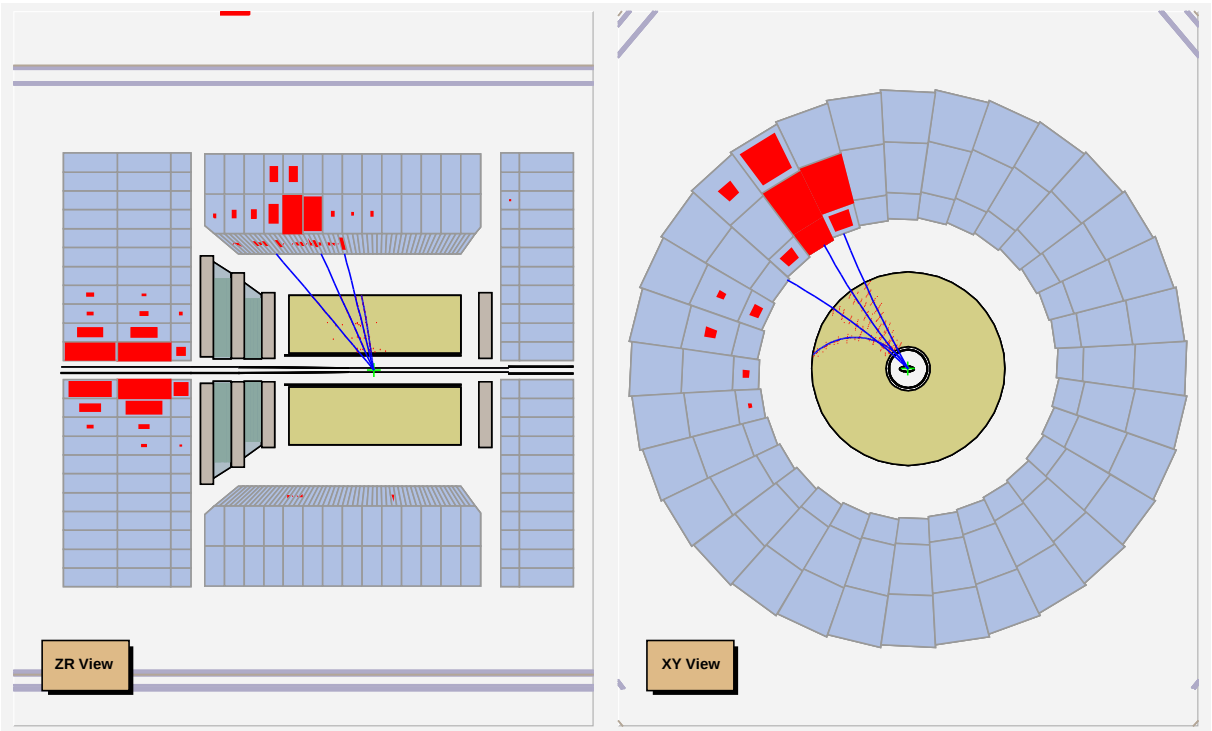

Figure A.2: Visualized CC event number 4820 of run 35066 with the reconstructed kinematic variables $Q^2 = 2441\,\mathrm{GeV}^2$, $x = 0.058$, $y = 0.416$, $\gamma_\mathrm{h} = 1.09$ rad.

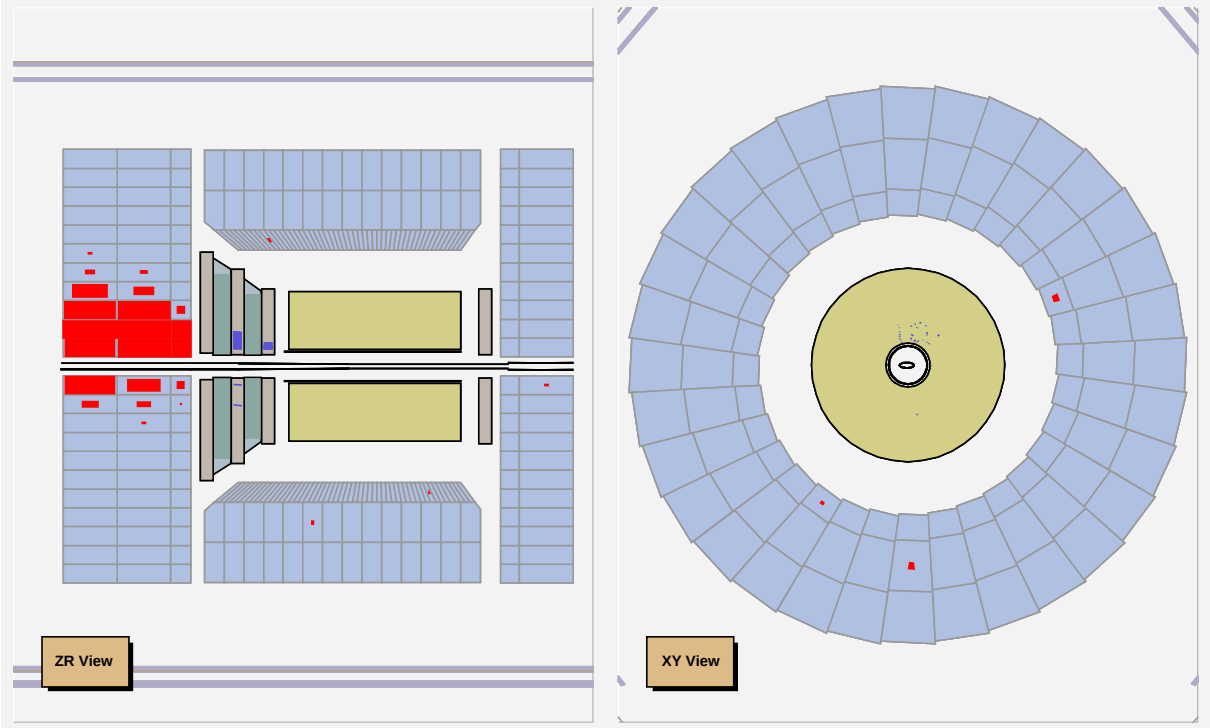

Figure A.3: Visualized CC event number 52885 of run 35043 with the reconstructed kinematic variables $Q^2 = 3252\,\mathrm{GeV}^2$, $x = 0.43$, $y = 0.075$, $\gamma_\mathrm{h} = 0.15$ rad.

Appendix B

Sytematic Checks

In this Appendix the influence of the systematic effects on the measured cross sections are presented as studied for the estimation of the systematic uncertainty in Sect. 4.6. The individual checks have been listed in Table 4.11. In the same order Figures B.1 to B.15 present the relative deviation of the cross sections $d\sigma/dQ^2$, $d\sigma/dx$, $d\sigma/dy$ and $\tilde{\sigma}$ for the analysis repeated under the specific modification.

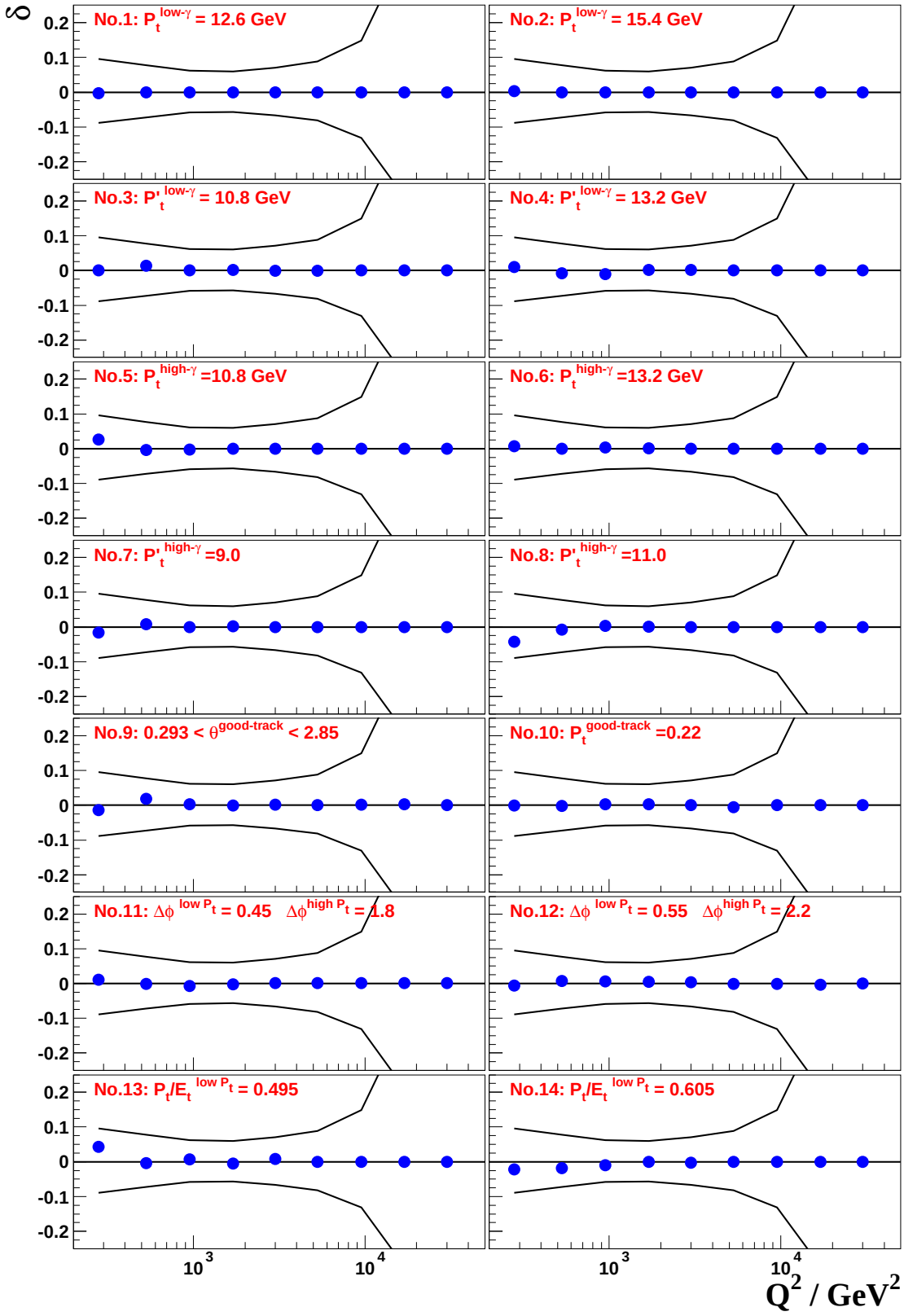

Figure B.1: Relative deviations δ of the cross section $d\sigma/dQ^2$ for systematic checks No.1-14. The line represents the statistical uncertainty.

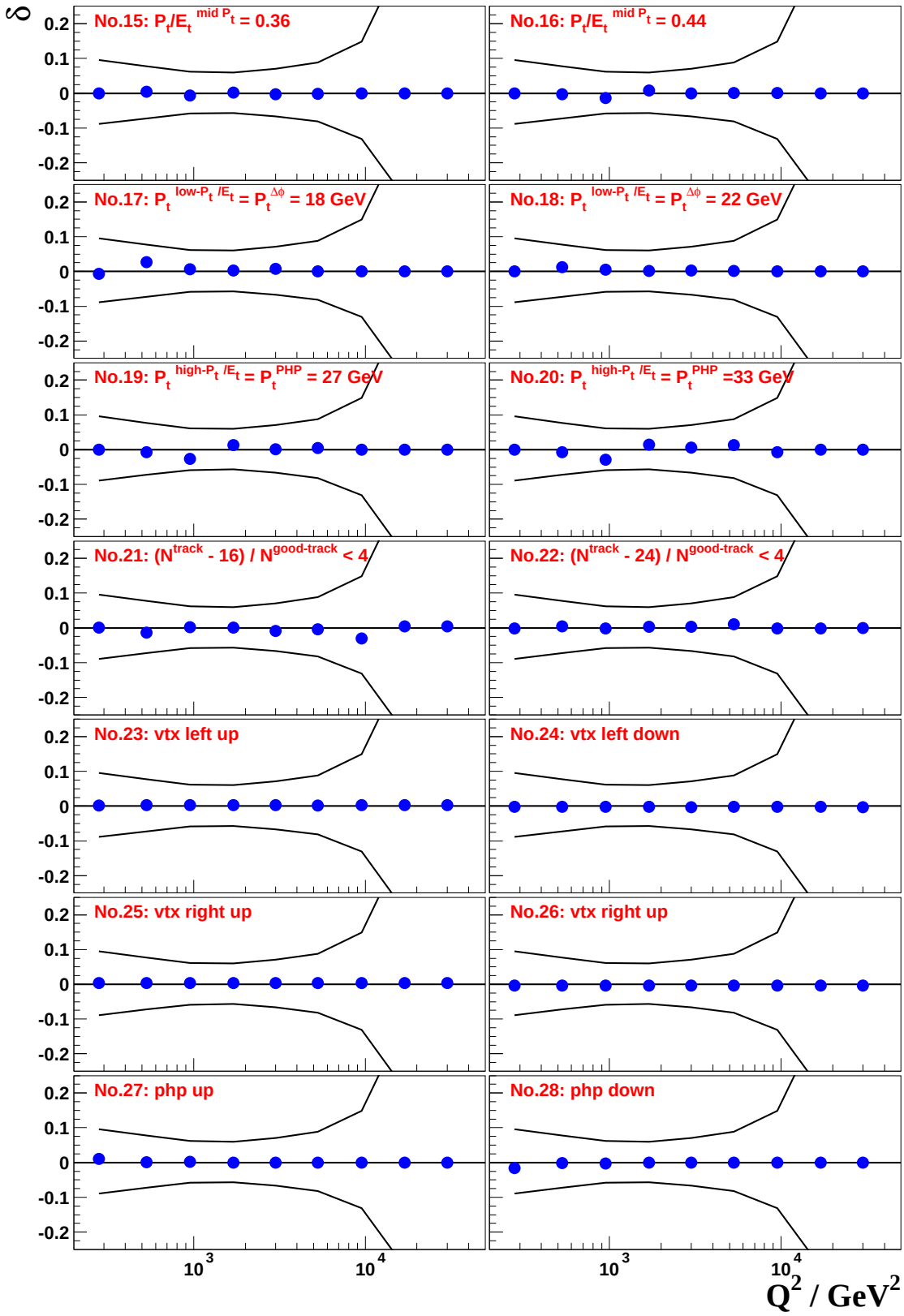

Figure B.2: Relative deviations δ of the cross section $d\sigma/dQ^2$ for systematic checks No.15-28. The line represents the statistical uncertainty.

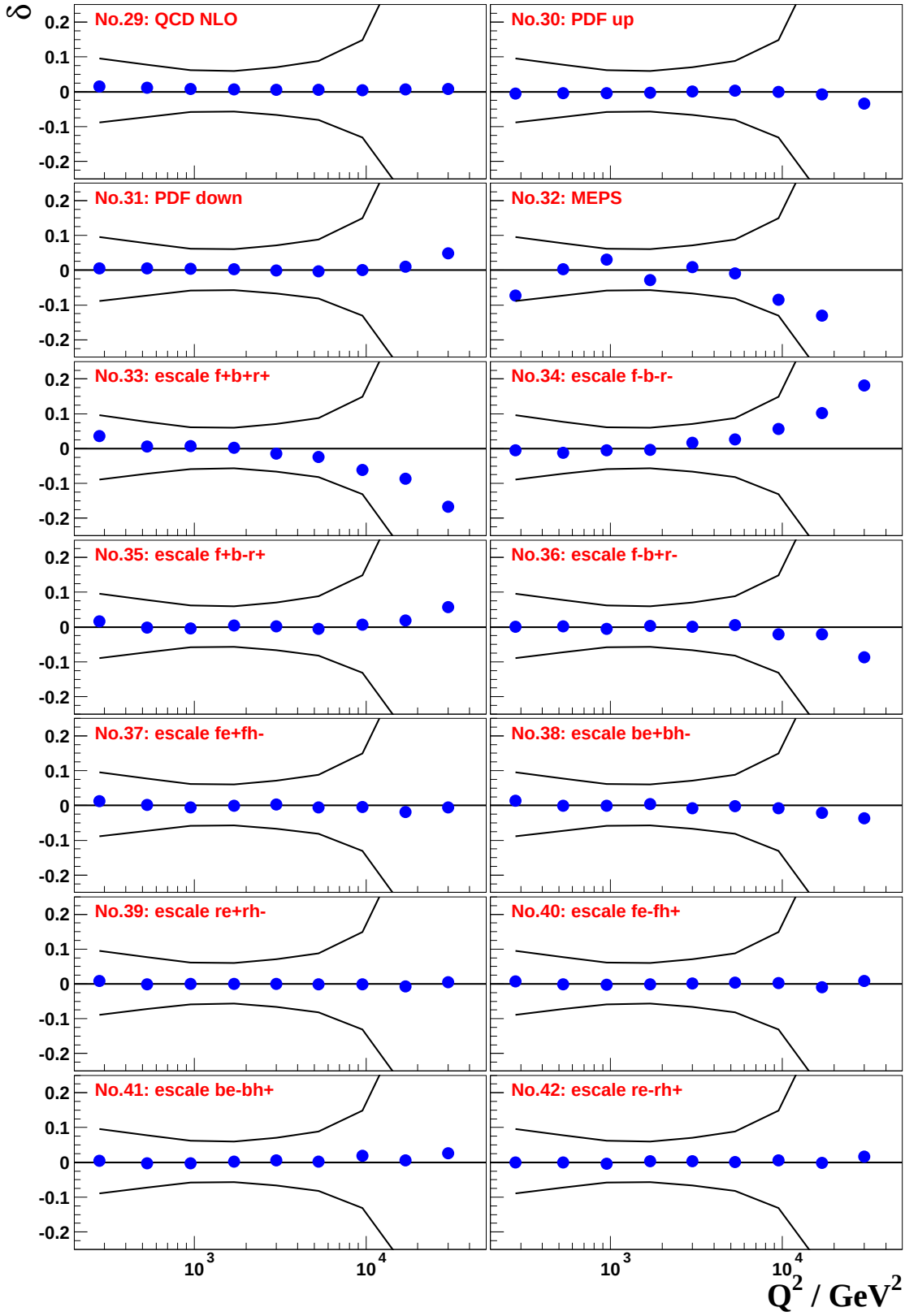

Figure B.3: Relative deviations δ of the cross section $d\sigma/dQ^2$ for systematic checks No.29-42. The line represents the statistical uncertainty.

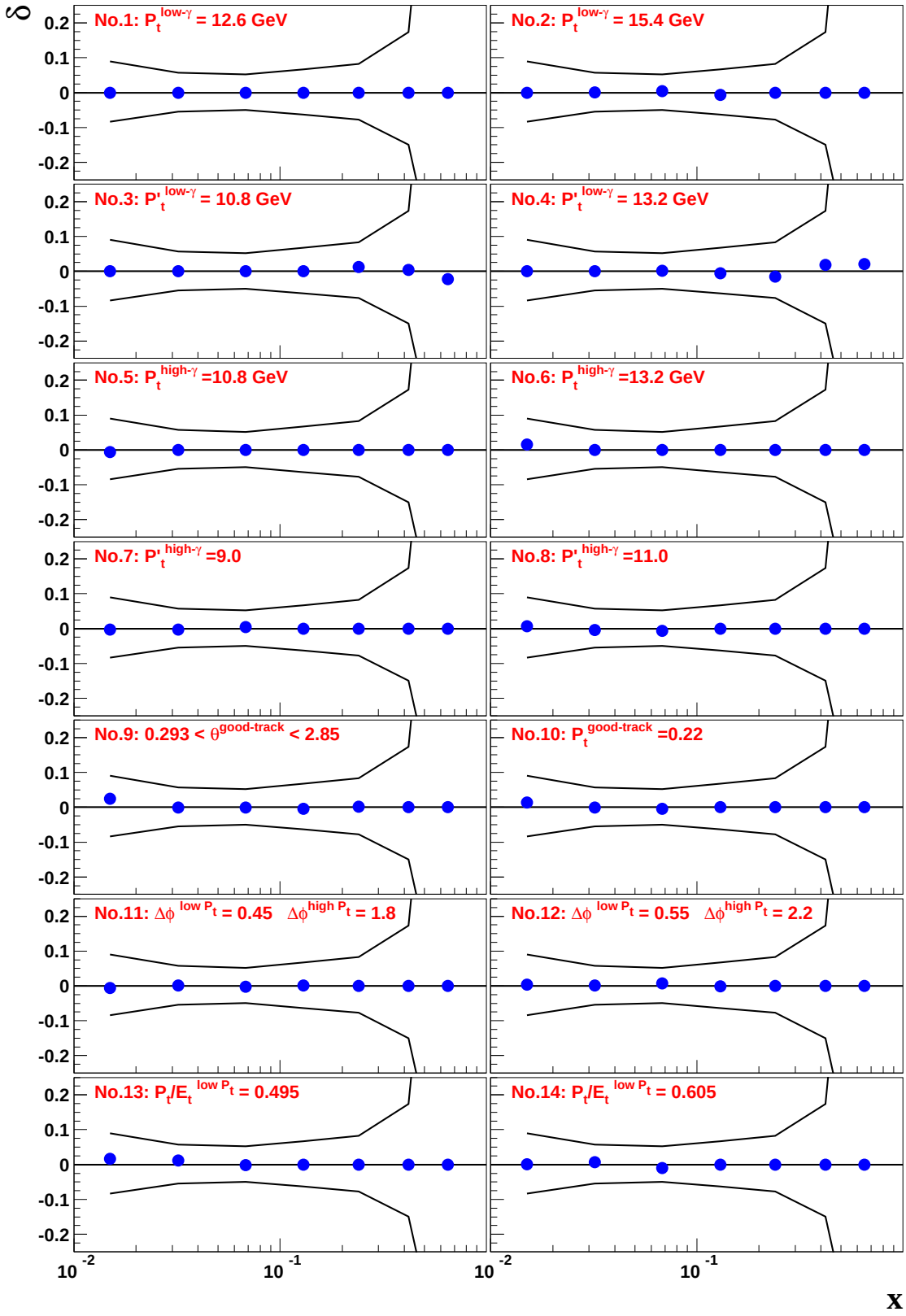

Figure B.4: Relative deviations δ of the cross section $d\sigma/dx$ for systematic checks No.1-14. The line represents the statistical uncertainty.

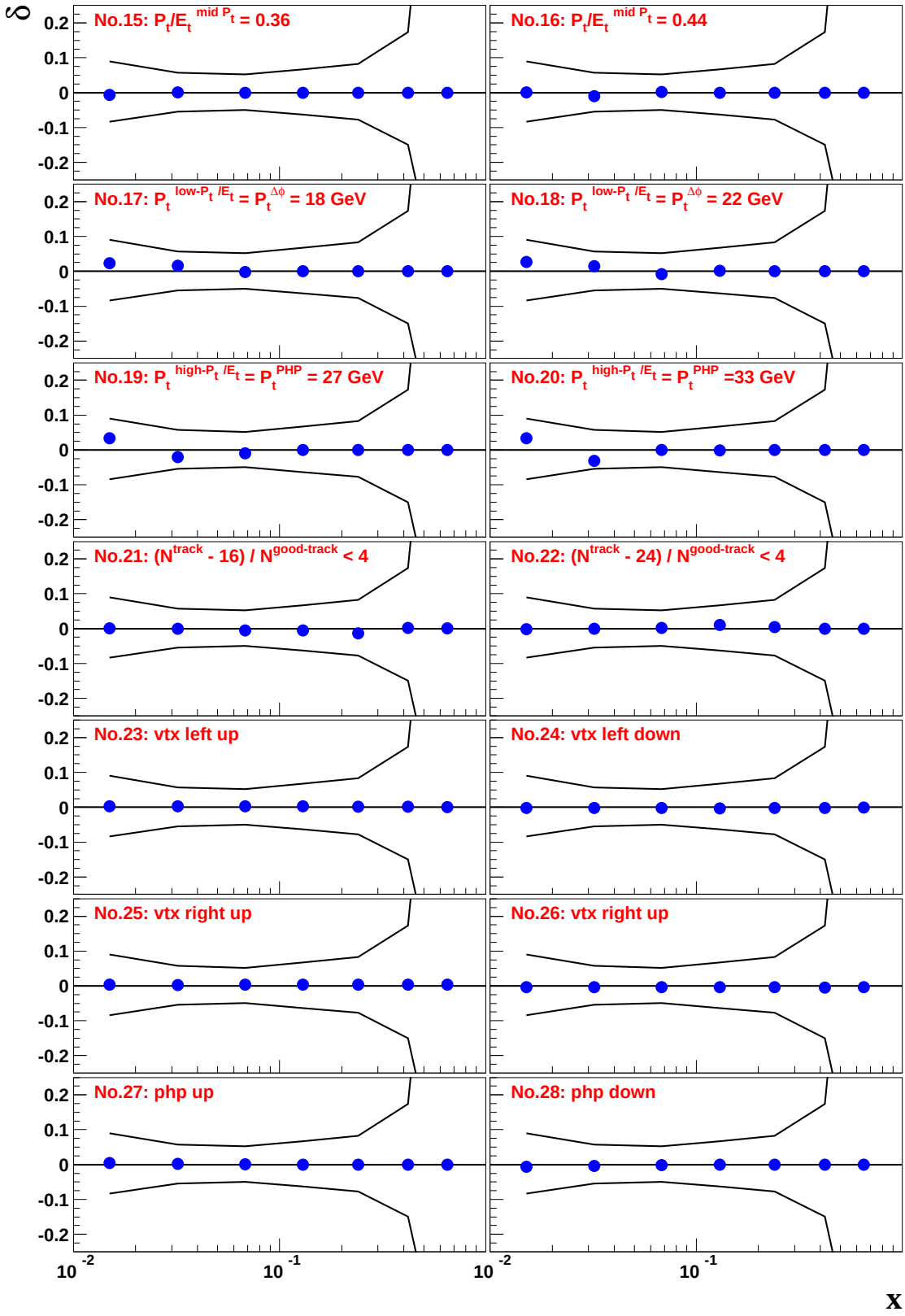

Figure B.5: Relative deviations δ of the cross section $d\sigma/dx$ for systematic checks No.15-28. The line represents the statistical uncertainty.

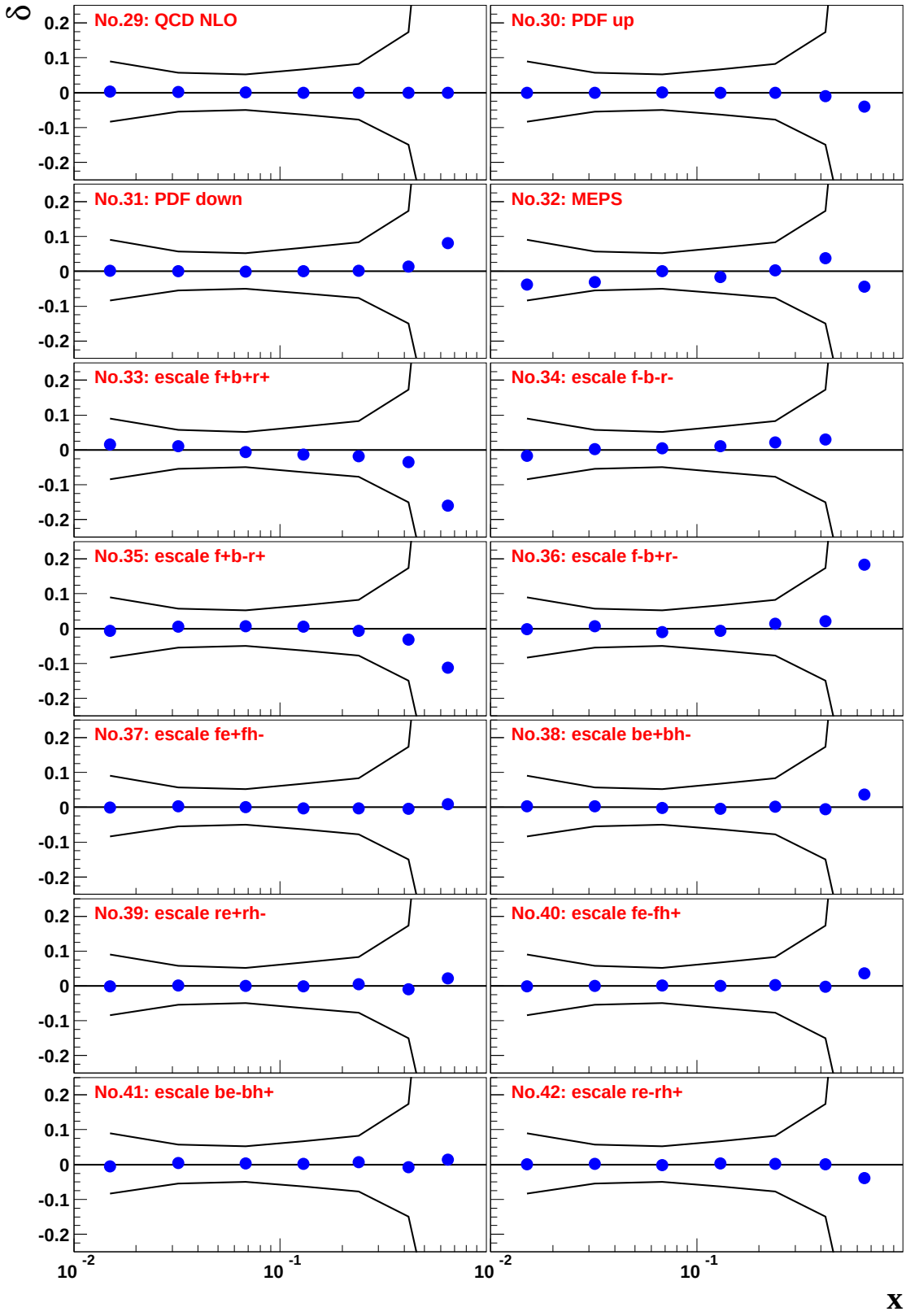

Figure B.6: Relative deviations δ of the cross section $d\sigma/dx$ for systematic checks No.29-42. The line represents the statistical uncertainty.

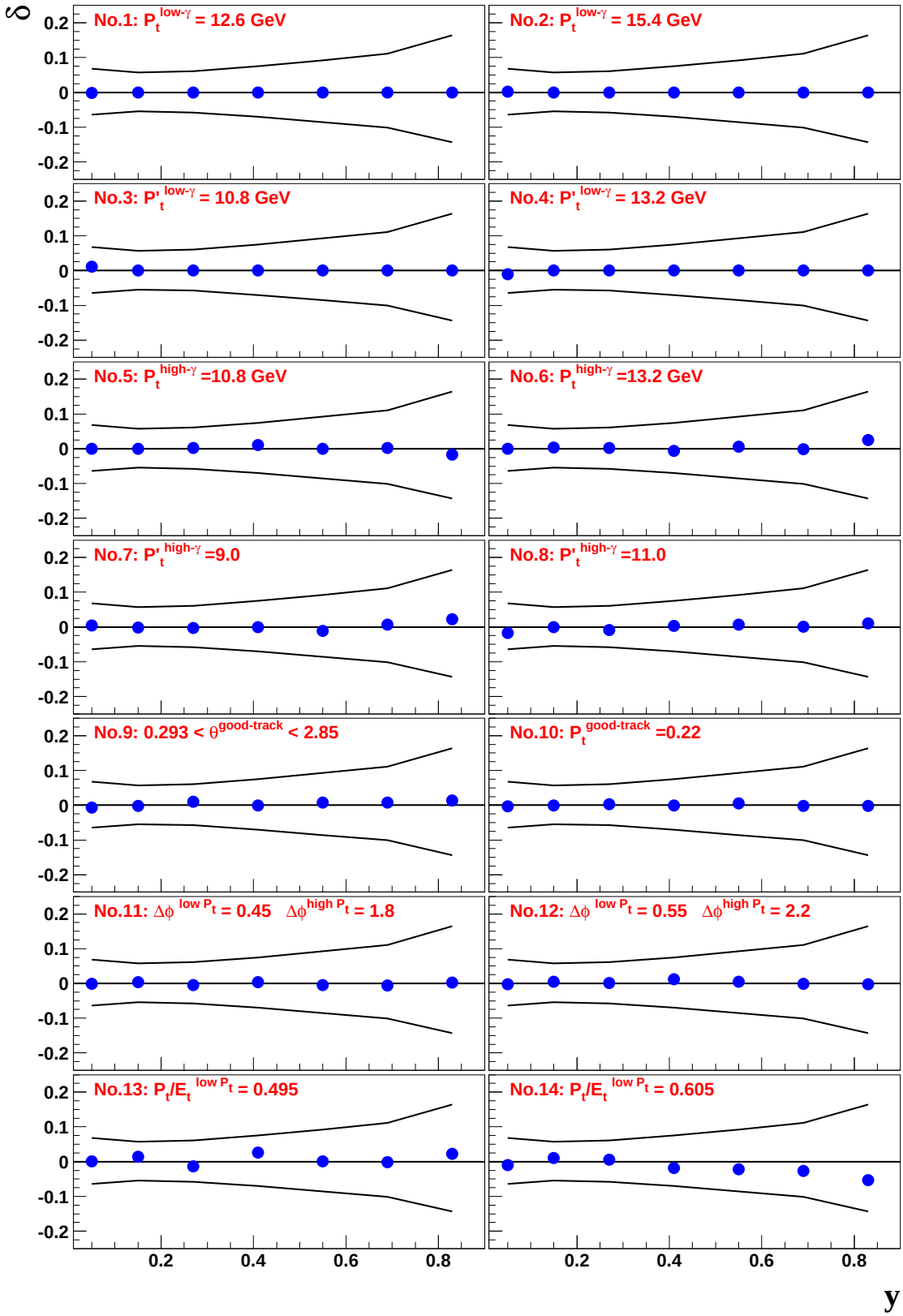

Figure B.7: Relative deviations δ of the cross section $d\sigma/dy$ for systematic checks No.1-14. The line represents the statistical uncertainty.

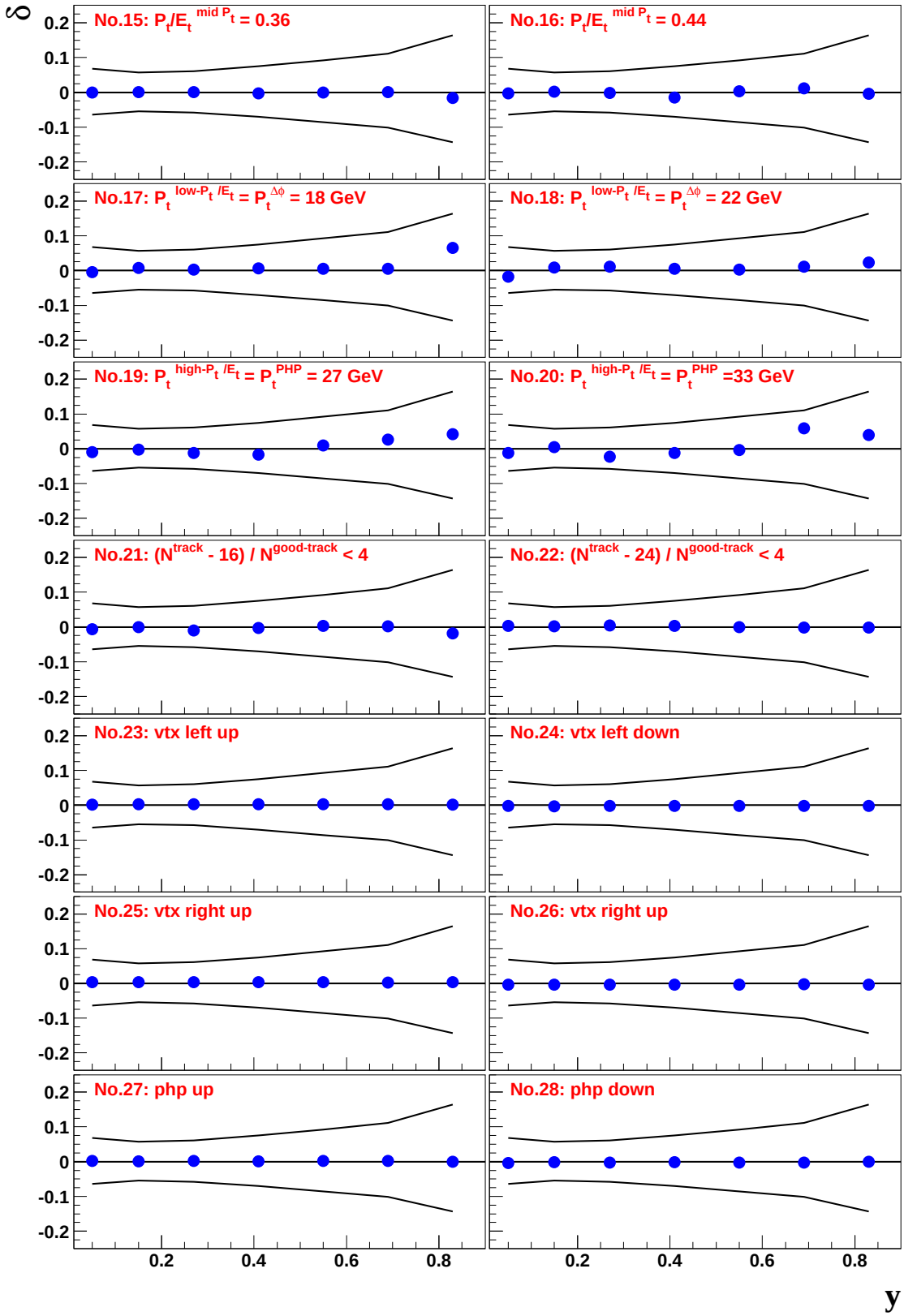

Figure B.8: Relative deviations δ of the cross section $d\sigma/dy$ for systematic checks No.15-28. The line represents the statistical uncertainty.

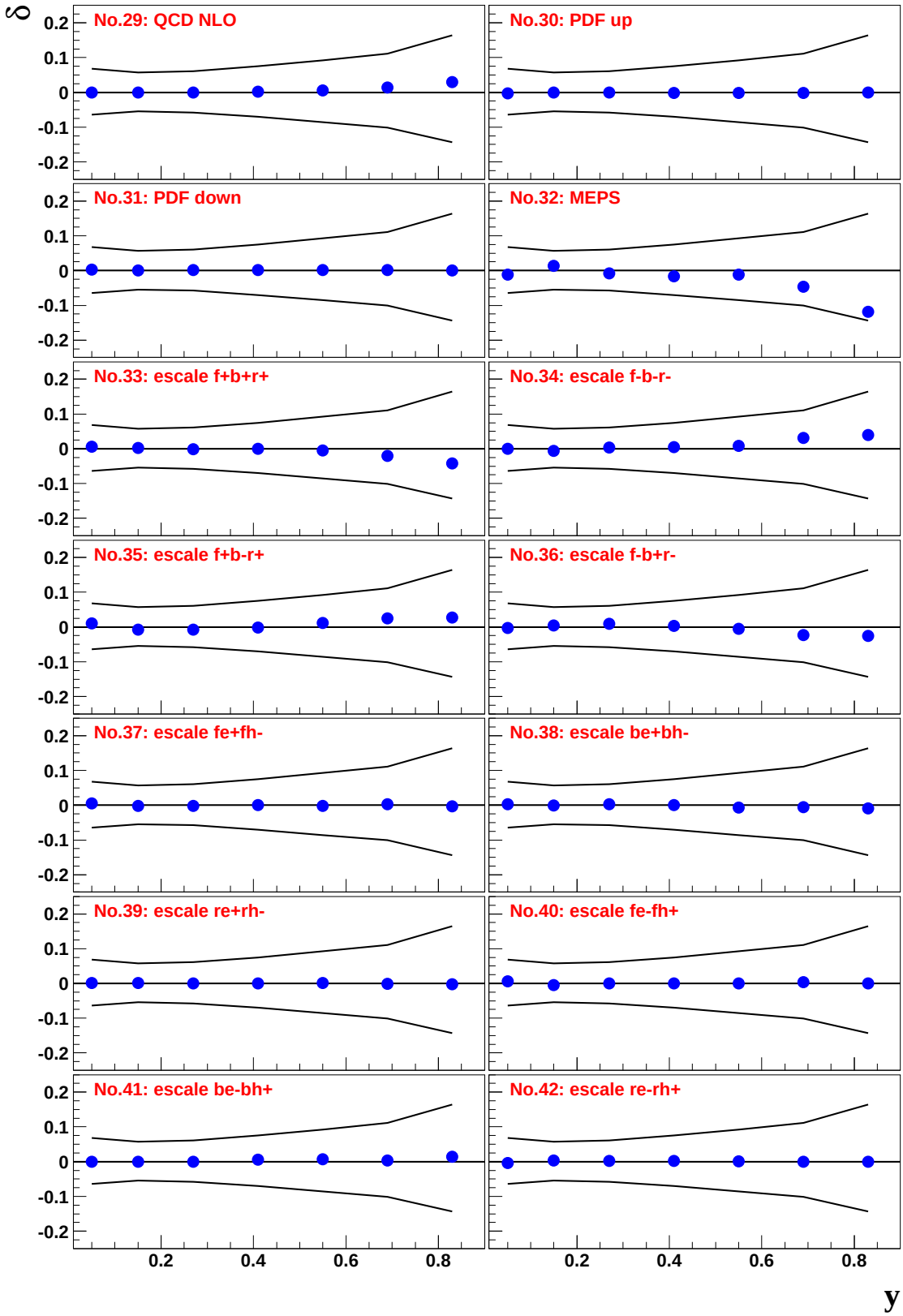

Figure B.9: Relative deviations δ of the cross section $d\sigma/dy$ for systematic checks No.29-42. The line represents the statistical uncertainty.

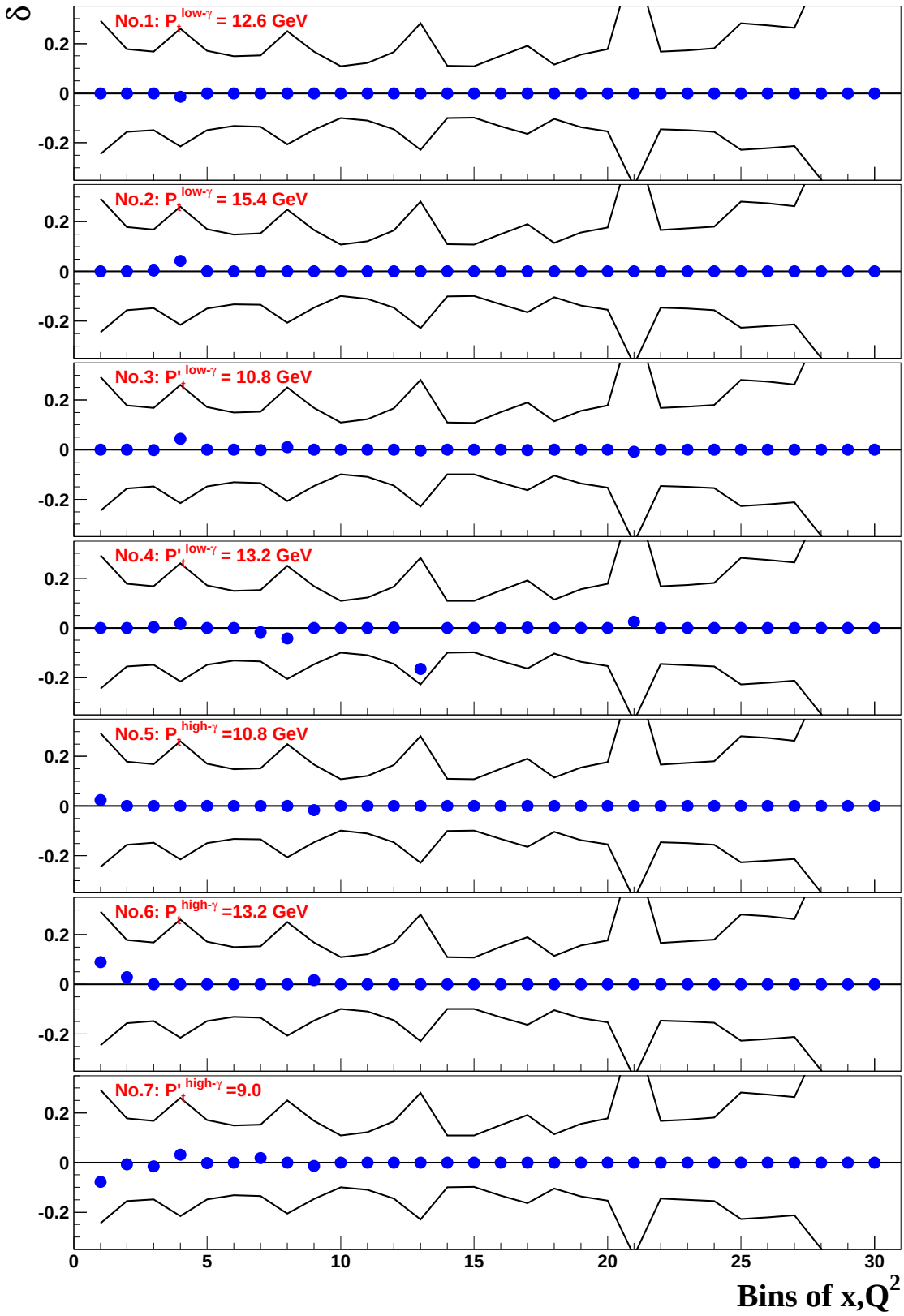

Figure B.10: Relative deviations δ of the cross section $d\sigma^2/dx\,dQ^2$ for systematic checks No.1-7 versus bin index. The line represents the statistical uncertainty.

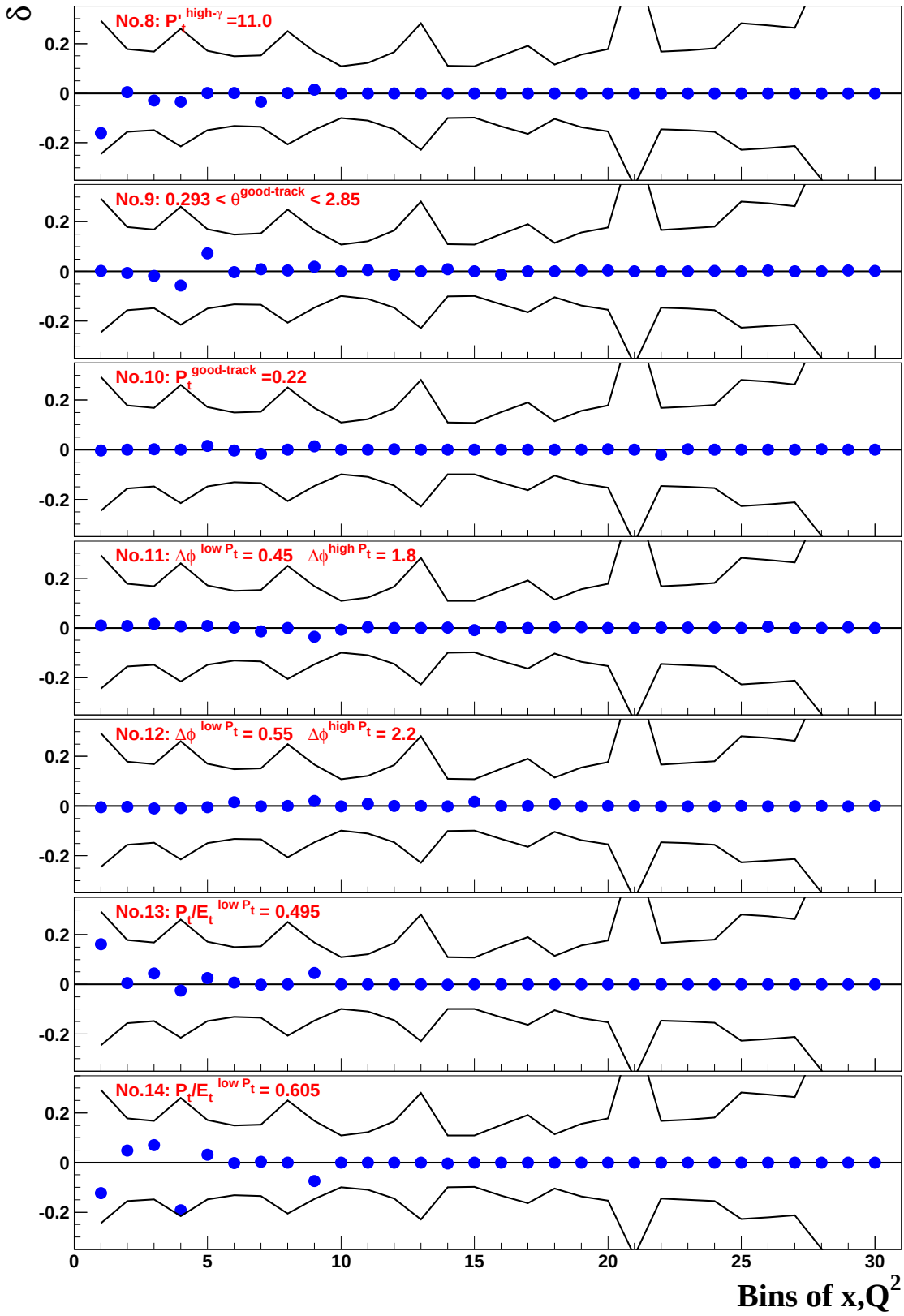

Figure B.11: Relative deviations δ of the cross section $d\sigma^2/dx\,dQ^2$ for systematic checks No.8-14 versus bin index. The line represents the statistical uncertainty.

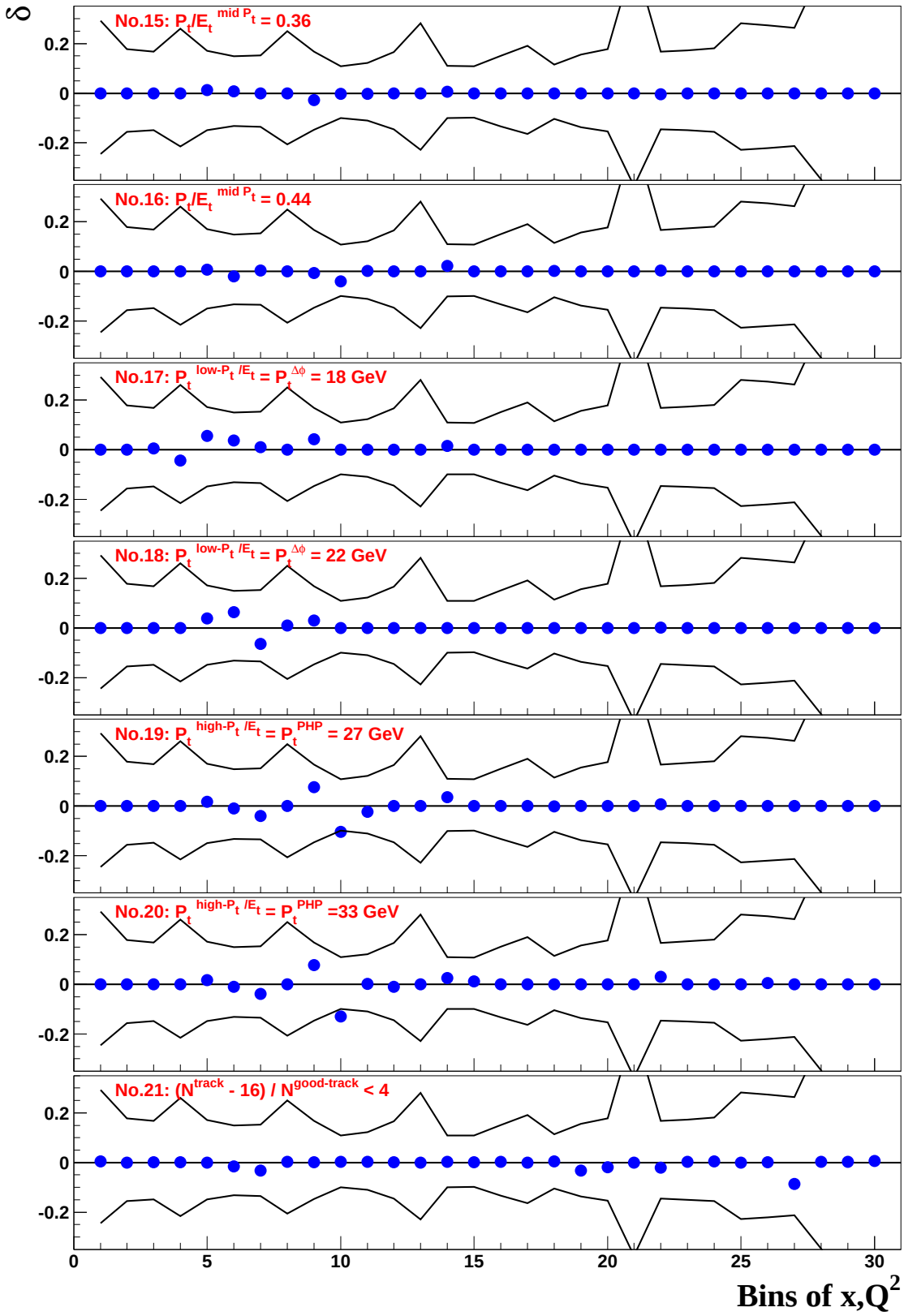

Figure B.12: Relative deviations δ of the cross section $d\sigma^2/dx\,dQ^2$ for systematic checks No.15-21 versus bin index. The line represents the statistical uncertainty.

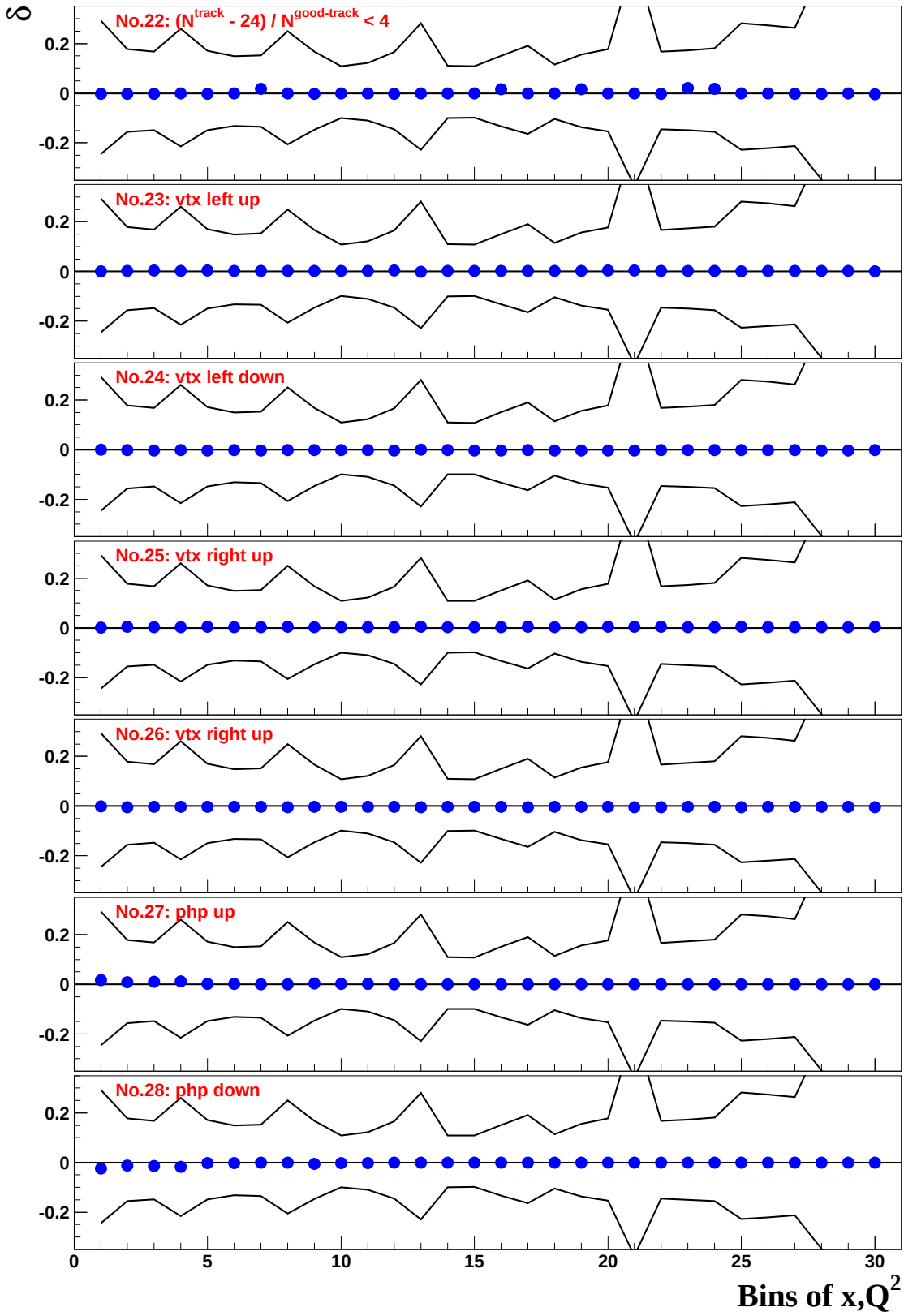

Figure B.13: Relative deviations δ of the cross section $d\sigma^2/dx\,dQ^2$ for systematic checks No.22-28 versus bin index. The line represents the statistical uncertainty.

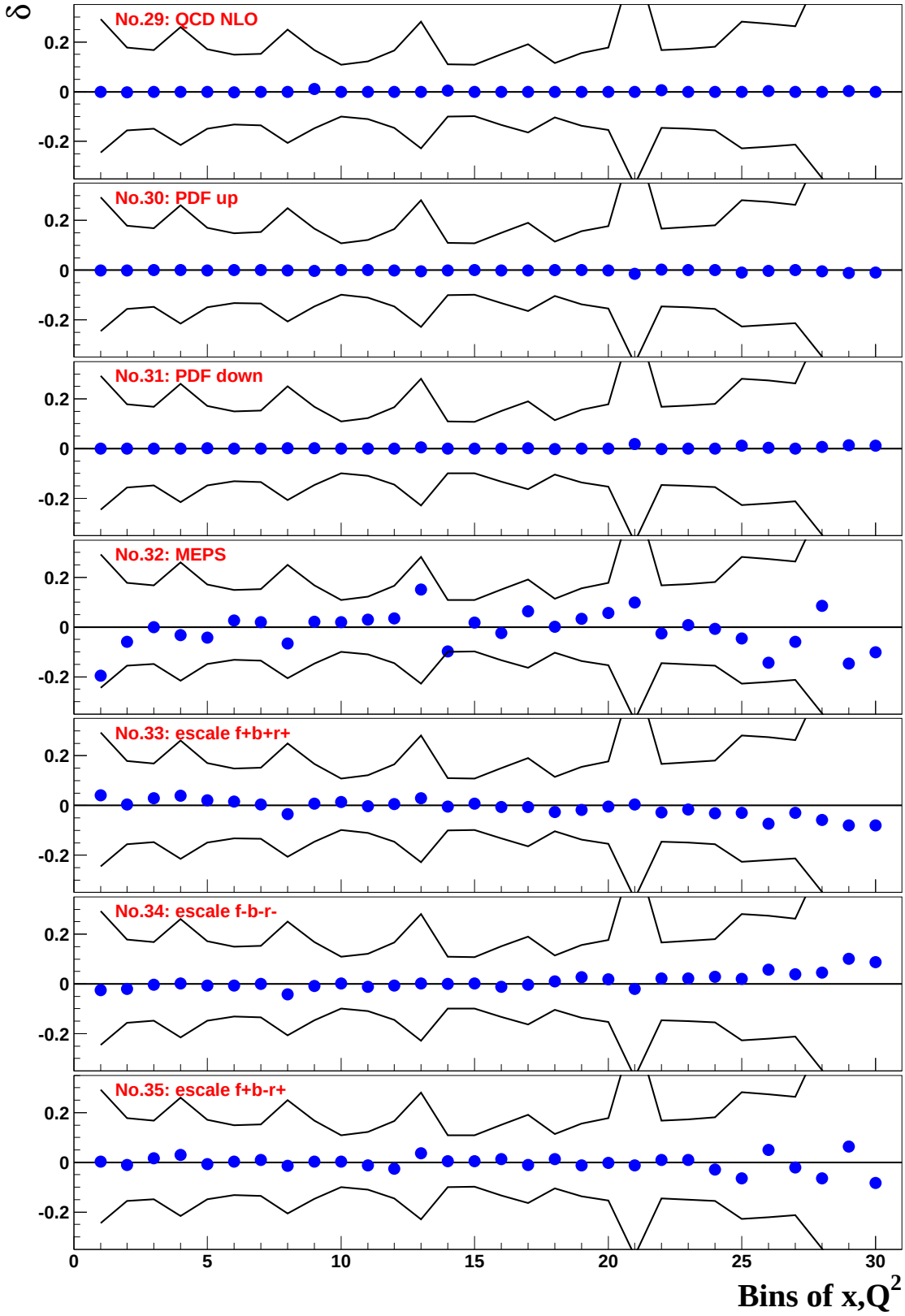

Figure B.14: Relative deviations δ of the cross section $d\sigma^2/dx\,dQ^2$ for systematic checks No.29-35 versus bin index. The line represents the statistical uncertainty.

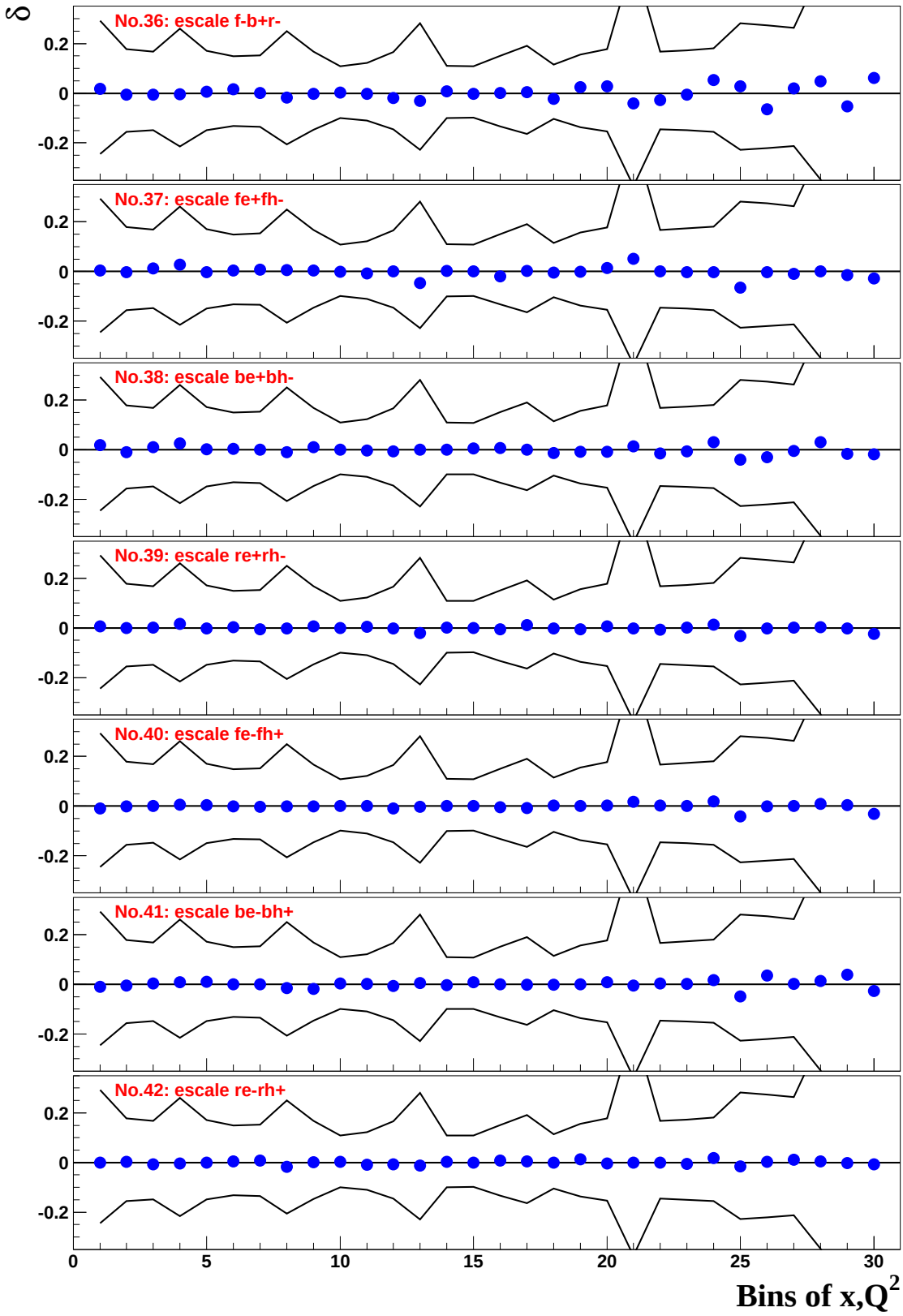

Figure B.15: Relative deviations δ of the cross section $d\sigma^2/dx\,dQ^2$ for systematic checks No.36-42 versus bin index. The line represents the statistical uncertainty.

Appendix C

Measured cross section values

This appendix gives the values for the following cross sections as presented in Sect. 5.1 and 5.2:

- $d\sigma/dQ^2$ (Figure 5.1, Table C.1)
- $d\sigma/dx$ (Figure 5.2, Table C.2)
- $d\sigma/dy$ (Figure 5.3. Table C.3)
- $\tilde{\sigma}$ (Figure 5.4 and 5.6, Table C.4 and C.5)

In Sect. 4.5.1 the definition and the resolution of the bins have been given. Efficiency, acceptance and purity have been discussed in Sect. 4.5.2. Section 4.5.3 introduced the statistical subtraction of the remaining background. The correction for radiative effects has been derived in Sect. 4.5.4. All cross sections where obtained using the unfolding method of Sect. 4.5.5. The systematic uncertainty has been estimated in Sect. 4.6.

$Q^2_{\,center}$ [GeV^2]	Q^2 range [GeV^2]	N_{Data}	$N_{\mathrm{CC-MC}}$	$N_{\mathrm{BG-MC}}$	$\mathcal{A}$	$\mathcal{P}$	$d\sigma/dQ^2$ [pb/GeV^2]
280	$200-400$	164	157.6	15.1	0.43	0.66	$\left(2.90\ ^{+0.28}_{-0.26}\ ^{+0.26}_{-0.22}\right)\cdot 10^{-2}$
530	$400-711$	208	232.0	4.3	0.60	0.64	$\left(1.82\ ^{+0.14}_{-0.13}\ ^{+0.04}_{-0.04}\right)\cdot 10^{-2}$
950	$711-1265$	319	303.3	5.0	0.73	0.67	$\left(1.34\ ^{+0.08}_{-0.08}\ ^{+0.05}_{-0.05}\right)\cdot 10^{-2}$
1700	$1265-2249$	329	317.3	1.9	0.80	0.69	$\left(7.12\ ^{+0.43}_{-0.41}\ ^{+0.27}_{-0.25}\right)\cdot 10^{-3}$
3000	$2249-4000$	238	252.2	1.4	0.80	0.70	$\left(2.87\ ^{+0.20}_{-0.19}\ ^{+0.10}_{-0.09}\right)\cdot 10^{-3}$
5300	$4000-7113$	157	148.2	1.2	0.80	0.71	$\left(1.07\ ^{+0.09}_{-0.09}\ ^{+0.05}_{-0.05}\right)\cdot 10^{-3}$
9500	$7113-2649$	59	59.6	0.5	0.80	0.68	$\left(2.14\ ^{+0.32}_{-0.28}\ ^{+0.25}_{-0.25}\right)\cdot 10^{-4}$
17000	$12649-22494$	11	15.2	0.1	0.81	0.61	$\left(1.94\ ^{+0.79}_{-0.59}\ ^{+0.38}_{-0.35}\right)\cdot 10^{-5}$
30000	$22494-70000$	3	2.2	0.0	1.02	0.46	$\left(1.99\ ^{+1.94}_{-1.09}\ ^{+0.69}_{-0.66}\right)\cdot 10^{-6}$

Table C.1: Values of differential cross sections $d\sigma/dQ^2$ are given together with bin-center, bin range, number of events found in the data as well as expected by the SM for signal and background, acceptance and purity.

Table C.2: Values of differential cross sections $d\sigma/dx$ are given together with bin-center, bin range, number of events found in the data as well as expected by the SM for signal and background, acceptance and purity.

x_{center}	x range	N_{Data}	$N_{\mathrm{CC-MC}}$	$N_{\mathrm{BG-MC}}$	$\mathcal{A}$	$\mathcal{P}$	$d\sigma/dx$ [pb]
0.015	$0.010 - 0.021$	162	157.4	6.3	0.38	0.71	$\left(4.66 \, ^{+0.42}_{-0.39} \, ^{+0.24}_{-0.23} \right) \cdot 10^{2}$
0.032	$0.021 - 0.046$	367	382.6	8.1	0.69	0.78	$\left(2.94 \, ^{+0.17}_{-0.16} \, ^{+0.12}_{-0.10} \right) \cdot 10^{2}$
0.068	$0.046 - 0.100$	435	445.3	6.1	0.79	0.82	$\left(1.59 \, ^{+0.08}_{-0.08} \, ^{+0.03}_{-0.03} \right) \cdot 10^{2}$
0.130	$0.100 - 0.178$	262	268.1	1.4	0.83	0.78	$\left(7.32 \, ^{+0.49}_{-0.46} \, ^{+0.24}_{-0.24} \right) \cdot 10^{1}$
0.240	$0.178 - 0.316$	176	157.3	0.8	0.79	0.81	$\left(3.01 \, ^{+0.25}_{-0.23} \, ^{+0.15}_{-0.13} \right) \cdot 10^{1}$
0.420	$0.316 - 0.562$	45	43.7	0.1	0.66	0.79	$\left(5.69 \, ^{+0.99}_{-0.85} \, ^{+0.76}_{-0.66} \right)$
0.650	$0.562 - 1.000$	2	2.0	0.0	0.59	0.55	$\left(3.90 \, ^{+5.16}_{-2.55} \, ^{+1.96}_{-1.17} \right) \cdot 10^{-1}$

y_{center}	y range	N_{Data}	$N_{\text{CC-MC}}$	$N_{\text{BG-MC}}$	$\mathcal{A}$	$\mathcal{P}$	$d\sigma/dy$ [pb]
0.050	$0.00 - 0.10$	271	275.0	7.6	0.46	0.81	$\left(7.83\ ^{+0.53}_{-0.50}\ ^{+0.26}_{-0.23} \right) \cdot 10^1$
0.150	$0.10 - 0.20$	365	336.6	5.0	0.71	0.79	$\left(6.98\ ^{+0.40}_{-0.38}\ ^{+0.20}_{-0.21} \right) \cdot 10^1$
0.270	$0.20 - 0.34$	322	338.2	4.7	0.68	0.80	$\left(4.49\ ^{+0.27}_{-0.26}\ ^{+0.12}_{-0.11} \right) \cdot 10^1$
0.410	$0.34 - 0.48$	221	226.0	4.6	0.63	0.76	$\left(3.32\ ^{+0.25}_{-0.23}\ ^{+0.10}_{-0.09} \right) \cdot 10^1$
0.550	$0.48 - 0.62$	152	150.4	4.7	0.53	0.73	$\left(2.57\ ^{+0.24}_{-0.22}\ ^{+0.10}_{-0.07} \right) \cdot 10^1$
0.690	$0.62 - 0.76$	105	101.8	1.7	0.45	0.67	$\left(2.13\ ^{+0.24}_{-0.22}\ ^{+0.16}_{-0.13} \right) \cdot 10^1$
0.830	$0.76 - 0.90$	52	59.6	1.3	0.32	0.64	$\left(1.52\ ^{+0.25}_{-0.22}\ ^{+0.21}_{-0.20} \right) \cdot 10^1$

Table C.3: Values of differential cross sections $d\sigma/dy$ are given together with bin-center, bin range, number of events found in the data as well as expected by the SM for signal and background, acceptance and purity.

Table C.4: Values of reduced cross sections $\tilde{\sigma}$ are given together with bin-center, bin range, number of events found in the data as well as expected by the SM for signal and background, acceptance and purity.

Q^2_{center} [GeV^2]	Q^2 range [GeV^2]	x_{center}	x range	N_{Data}	$N_{\mathrm{CC-MC}}$	$N_{\mathrm{BG-MC}}$	$\mathcal{A}$	$\mathcal{P}$	$\tilde{\sigma}$
280	$200-400$	0.008	$0.006-0.010$	27	18.3	5.0	0.32	0.43	$\left(1.39\ ^{+0.41\ +0.28}_{-0.34\ -0.28} \right)$
280	$200-400$	0.015	$0.010-0.021$	50	42.0	3.4	0.53	0.46	$\left(1.18\ ^{+0.21\ +0.08}_{-0.18\ -0.08} \right)$
280	$200-400$	0.032	$0.021-0.046$	56	54.8	4.1	0.79	0.56	$\left(8.37\ ^{+1.41\ +0.35}_{-1.24\ -0.20} \right)\cdot 10^{-1}$
280	$200-400$	0.068	$0.046-0.100$	26	35.3	2.2	0.76	0.56	$\left(4.48\ ^{+1.17\ +0.33}_{-0.96\ -0.18} \right)\cdot 10^{-1}$
530	$400-711$	0.015	$0.010-0.021$	49	54.7	1.4	0.54	0.50	$\left(8.03\ ^{+1.37\ +0.45}_{-1.20\ -0.39} \right)\cdot 10^{-1}$
530	$400-711$	0.032	$0.021-0.046$	61	76.6	1.0	0.88	0.53	$\left(6.36\ ^{+0.95\ +0.25}_{-0.84\ -0.20} \right)\cdot 10^{-1}$
530	$400-711$	0.068	$0.046-0.100$	58	59.7	0.5	0.96	0.56	$\left(6.05\ ^{+0.92\ +0.17}_{-0.81\ -0.15} \right)\cdot 10^{-1}$
530	$400-711$	0.130	$0.100-0.178$	25	25.8	0.3	0.98	0.50	$\left(4.38\ ^{+1.10\ +0.30}_{-0.90\ -0.41} \right)\cdot 10^{-1}$
950	$711-1265$	0.015	$0.010-0.021$	51	50.8	1.5	0.45	0.46	$\left(7.00\ ^{+1.17\ +0.34}_{-1.03\ -0.26} \right)\cdot 10^{-1}$
950	$711-1265$	0.032	$0.021-0.046$	109	105.4	1.5	0.86	0.59	$\left(7.15\ ^{+0.78\ +0.22}_{-0.71\ -0.18} \right)\cdot 10^{-1}$
950	$711-1265$	0.068	$0.046-0.100$	88	87.9	1.0	0.96	0.61	$\left(5.79\ ^{+0.71\ +0.19}_{-0.64\ -0.22} \right)\cdot 10^{-1}$
950	$711-1265$	0.130	$0.100-0.178$	50	42.0	0.2	0.96	0.59	$\left(5.02\ ^{+0.83\ +0.20}_{-0.73\ -0.27} \right)\cdot 10^{-1}$
950	$711-1265$	0.240	$0.178-0.316$	21	16.0	0.5	0.72	0.55	$\left(3.12\ ^{+0.88\ +0.50}_{-0.71\ -0.52} \right)\cdot 10^{-1}$
1700	$1265-2249$	0.032	$0.021-0.046$	107	104.6	1.1	0.76	0.54	$\left(5.41\ ^{+0.59\ +0.56}_{-0.54\ -0.54} \right)\cdot 10^{-1}$
1700	$1265-2249$	0.068	$0.046-0.100$	108	108.6	0.3	0.91	0.65	$\left(4.89\ ^{+0.53\ +0.13}_{-0.48\ -0.11} \right)\cdot 10^{-1}$
1700	$1265-2249$	0.130	$0.100-0.178$	59	57.6	0.2	0.98	0.64	$\left(3.81\ ^{+0.58\ +0.14}_{-0.51\ -0.15} \right)\cdot 10^{-1}$
1700	$1265-2249$	0.240	$0.178-0.316$	39	32.6	0.2	0.99	0.61	$\left(2.61\ ^{+0.50\ +0.19}_{-0.43\ -0.19} \right)\cdot 10^{-1}$

$Q^2{}_{center}$ [GeV^2]	Q^2 range [GeV^2]	x_{center}	$x$range	N_{Data}	$N_{\mathrm{CC-MC}}$	$N_{\mathrm{BG-MC}}$	$\mathcal{A}$	$\mathcal{P}$	$\tilde{\sigma}$
3000	$2249-4000$	0.068	$0.046-0.100$	98	98.4	0.9	0.81	0.63	$\left(3.63\ ^{+0.42\ +0.95}_{-0.38\ -0.15} \right) \cdot 10^{-1}$
3000	$2249-4000$	0.130	$0.100-0.178$	55	60.8	0.1	0.93	0.67	$\left(2.77\ ^{+0.43\ +0.16}_{-0.38\ -0.13} \right) \cdot 10^{-1}$
3000	$2249-4000$	0.240	$0.178-0.316$	44	40.1	0.1	1.00	0.68	$\left(2.12\ ^{+0.38\ +0.17}_{-0.33\ -0.14} \right) \cdot 10^{-1}$
3000	$2249-4000$	0.420	$0.316-0.562$	7	11.9	0.0	0.91	0.67	$\left(3.75\ ^{+2.04\ +0.62}_{-1.40\ -0.55} \right) \cdot 10^{-2}$
5300	$4000-7113$	0.068	$0.046-0.100$	50	51.6	1.1	0.66	0.53	$\left(2.21\ ^{+0.37\ +0.11}_{-0.32\ -0.12} \right) \cdot 10^{-1}$
5300	$4000-7113$	0.130	$0.100-0.178$	45	49.2	0.1	0.86	0.65	$\left(2.01\ ^{+0.35\ +0.08}_{-0.30\ -0.07} \right) \cdot 10^{-1}$
5300	$4000-7113$	0.240	$0.178-0.316$	42	34.3	0.0	0.97	0.70	$\left(1.86\ ^{+0.34\ +0.16}_{-0.29\ -0.11} \right) \cdot 10^{-1}$
5300	$4000-7113$	0.420	$0.316-0.562$	20	11.9	0.0	1.05	0.66	$\left(9.29\ ^{+0.26\ +0.13}_{-0.21\ -0.16} \right) \cdot 10^{-2}$
9500	$7113-12649$	0.130	$0.100-0.178$	21	24.5	0.3	0.78	0.54	$\left(9.65\ ^{+2.64\ +1.66}_{-2.13\ -1.74} \right) \cdot 10^{-2}$
9500	$7113-12649$	0.240	$0.178-0.316$	22	22.1	0.0	0.89	0.68	$\left(9.92\ ^{+2.61\ +0.87}_{-2.11\ -0.81} \right) \cdot 10^{-2}$
9500	$7113-12649$	0.420	$0.316-0.562$	8	8.8	0.0	0.96	0.69	$\left(3.77\ ^{+1.86\ +0.66}_{-1.31\ -0.61} \right) \cdot 10^{-2}$
17000	$12649-22494$	0.240	$0.178-0.316$	3	8.4	0.1	0.84	0.52	$\left(1.47\ ^{+1.46\ +0.31}_{-0.82\ -0.28} \right) \cdot 10^{-2}$
17000	$12649-22494$	0.420	$0.316-0.562$	6	4.9	0.0	0.98	0.66	$\left(3.03\ ^{+1.82\ +0.60}_{-1.21\ -0.59} \right) \cdot 10^{-2}$

Table C.5: Values of reduced cross sections $\tilde{\sigma}$ are given together with bin-center, bin range, number of events found in the data as well as expected by the SM for signal and background, acceptance and purity.

References

[1] CDHS Coll., H. Abramowicz et al., Z. Phys. **C 25**, 29 (1984).

[2] CDHSW Coll., J.P. Berge et al., Z. Phys. **C 49**, 187 (1991).

[3] CCFR Coll., E. Oltman et al., Z. Phys. **C 53**, 51 (1992).

[4] BEBC Coll., G.T. Jones et al., Z. Phys. **C 62**, 575 (1994).

[5] H1 Coll., T. Ahmed et al., Phys. Lett. **B 324**, 241 (1994).

[6] H1 Coll., S. Aid et al., Z. Phys. **C 67**, 565 (1995).

[7] H1 Coll., S. Aid et al., Phys. Lett. **B 379**, 319 (1996).

[8] H1 Coll., C. Adloff et al., Eur. Phys. J. **C 13**, 609 (2000).

[9] H1 Coll., C. Adloff et al., Eur. Phys. J. **C 19**, 269 (2001).

[10] ZEUS Coll., M. Derrick et al., Phys. Rev. Lett. **75**, 1006 (1995).

[11] ZEUS Coll., M. Derrick et al., Z. Phys. **C 72**, 47 (1996).

[12] ZEUS Coll., J. Breitweg et al., Eur. Phys. J. **C 12**, 411 (2000).

[13] ZEUS Coll., S. Chekanov et al., Phys. Lett. **B 539**, 197 (2002).

[14] ZEUS Coll., Eur. Phys. J. **C 27**, 305 (2003).

[15] H1 Coll., C. Adloff et al., Eur. Phys. J. **C 30**, 1 (2003).

[16] M. Eckert, *Spurrekonstruktion in den planaren Driftkammern von ZEUS und Ereignisse der Reaktion $e^+p \to \bar{\nu}_e X$ bei kleinen hadronischen Winkeln.* Ph.D. Thesis, Universität Bonn, 1999. BONN-IB-99-05.

[17] M. Zamponi, *Vergleich von Meßdaten und Simulation der tiefinelastischen Reaktion $e^-p \to \nu_e X$ bei ZEUS.* Diploma Thesis, Universität Bonn, 2001. BONN-IB-01-03.

[18] H. Wessoleck, *Messung der Wirkungsquerschnitte für den tiefinelastischen, inklusiven Prozess $e^+p \to \bar{\nu}_e X$ an der Speicherring-Anlage HERA mit ZEUS-Daten aus den Jahren 1999 und 2000.* Ph.D. Thesis, Universität Bonn, 2002. BONN-IB-02-02.

[19] O. Kind et al., ECONF **C0303241**, MOLT002 (2003).

[20] ZEUS Coll., U. Holm (ed.), *The ZEUS Detector*. Status Report (unpublished), DESY (1993), available on `http://www-zeus.desy.de/bluebook/bluebook.html`.

[21] M. Derrick et al., Nucl. Inst. Meth. **A 309**, 77 (1991);
A. Andresen et al., Nucl. Inst. Meth. **A 309**, 101 (1991);
A. Caldwell et al., Nucl. Inst. Meth. **A 321**, 356 (1992);
A. Bernstein et al., Nucl. Inst. Meth. **A 336**, 23 (1993).

[22] K. Piotrzkowski and M. Zachara, *Determination of the ZEUS Luminosity in 1994* (unpublished). ZEUS-95-138, 1995.

[23] K. Olkiewicz and A. Eskreys, *Off-line Luminosity Calculation in the ZEUS Experiment in 1997, 1998 and 1999* (unpublished). ZEUS-99-44, 1999.

[24] Particle Data Group, K. Hagiwara et al., Phys. Rev. **D 66**, 10001 (2002).

[25] F.E. Close, *An Introduction to Quarks and Partons*. Academic Press Inc. (London) Ltd, 24–28 Oval Road, London NW1, 1979.

[26] E.D. Bloom et al., Phys. Rev. Lett. **23**, 930 (1969).

[27] M. Breidenbach et al., Phys. Rev. Lett. **23**, 935 (1969).

[28] F. Halzen and A.D. Martin, *Quarks and Leptons: An Introductory Course in Modern Particle Physics*. John Wiley & Sons, Inc, 1984.

[29] CCFR/NuTeV Coll., U.K. Yang et al., Phys. Rev. Lett. **86**, 2742 (2001).

[30] U.F. Katz, *Deep-Inelastic Positron–Proton Scattering in the High-Momentum-Transfer Regime of HERA*, Springer Tracts in Modern Physics, Vol. 168. Springer, Berlin, Heidelberg, 2000.

[31] M. Klein and T. Riemann, Z. Phys. **C 24**, 151 (1984).

[32] H. Abramowicz and A. Caldwell, Rev. Mod. Phys. **71**, 1275 (1999).

[33] ZEUS Coll., S. Chekanov et al., Phys. Rev. **D 67**, 012007 (2003).

[34] ZEUS Coll., S. Chekanov et al., Eur. Phys. J. **C 21**, 443 (2001).

[35] BCDMS Coll., A.C. Benvenuti et al., Phys. Lett. **B 223**, 485 (1989).

[36] NMC Coll., M. Arneodo et al., Nucl. Phys. **B 483**, 3 (1997).

[37] E665 Coll., M.R. Adams et al., Phys. Rev. **D 54**, 3006 (1996).

[38] NMC Coll., M. Arneodo et al., Nucl. Phys. **B 487**, 3 (1997).

[39] W.G. Seligman et al., Phys. Rev. Lett. **79** (1997).

[40] G. Gurci, W. Furmanski and R. Petronzio, Nucl. Phys. **B 175**, 27 (1980).

[41] W. Furmanski and R. Petronzio, Phys. Lett. **B 97**, 437 (1980).

[42] W. Furmanski and R. Petronzio, Z. Phys. **C 11**, 293 (1982).

[43] R.S. Thorne, J. Phys. **G 25**, 1307 (1999).

[44] R.G. Roberts and R.S. Thorne, Phys. Lett. **B 421**, 303 (1998).

[45] R.G. Roberts and R.S. Thorne, Phys. Rev. **D 57**, 6871 (1998).

[46] R.G. Roberts and R.S. Thorne, Eur. Phys. J. **C 19**, 339 (2001).

[47] Rautenberg, Julian, *ZEUS results on high Q^2 DIS cross sections and QCD fits*, 2003. To appear in *Proc. 11th Int. Workshop on Deep-Inelastic Scattering* (DIS2003), St.Petersburg, April 2003.

[48] H. Spiesberger, HERACLES *and* DJANGOH*: Event Generation for ep Interactions at HERA Including Radiative Processes*, 1998, available on `http://www.desy.de/~hspiesb/djangoh.html`.

[49] A. Kwiatkowski, H. Spiesberger and H.-J. Möhring, Comp. Phys. Comm. **69**, 155 (1992). Also in *Proc. Workshop Physics at HERA*, 1991, DESY, Hamburg; H. Spiesberger, *An Event Generator for ep Interactions at HERA Including Radiative Processes (Version 4.6)*, 1996, available on `http://www.desy.de/~hspiesb/heracles.html`.

[50] G. Ingelman, A. Edin and J. Rathsman, Comp. Phys. Comm. **101**, 108 (1997).

[51] T. Sjöstrand, Comp. Phys. Comm. **82**, 74 (1994).

[52] CTEQ Coll., H.L. Lai et al., Eur. Phys. J. **C 12**, 375 (2000).

[53] A.D. Tapper, *Measurement of charged current deep inelastic scattering cross sections using the ZEUS detector at HERA*. Ph.D. Thesis, University of London, 2001. (unpublished).

[54] G. Marchesini et al., Comp. Phys. Comm. **67**, 465 (1992).

[55] R. Brun et al., GEANT3, Technical Report CERN-DD/EE/84-1, CERN, 1987.

[56] M. Martinez, *Calorimeter Noisy Cell Study for 1998-2000 ZEUS Data* (unpublished). ZEUS-00-016, internal ZEUS-note, 2000;
A. Savin, *Study of Calorimeter Noise in the 1996 Data* (unpublished). ZEUS-98-007.

[57] G. F. Hartner, *VCTRAK Briefing: Program and Math* (unpublished). Zeus-98-058, internal ZEUS-note, 1998.

[58] G.F. Hartner, *VCTRAK(3.07/04): Offline Output Information* (unpublished). ZEUS-97-064, internal ZEUS-note, 1997.

[59] M. Moritz, *Measurement of the High Q^2 Neutral Current DIS Cross Section at HERA*. Thesis, University Hamburg, 2001.

[60] R. Pawlak, *Vertex reconstruction from FCAL timing* (unpublished). ZEUS-98-040.

[61] R. Schattevoy, *Optimierung, Validation und Analyse der ZEUS-Ereignisselektion unter besonderer Berücksichtigung der Kalorimetrie*. Ph.D. Thesis, Universität Bonn, Report BONN-IR-94-08, 1994.

[62] F. Jacquet and A. Blondel, *Proceedings of the Study for an ep Facility for Europe*, U. Amaldi (ed.), p. 391. Hamburg, Germany (1979). Also in preprint DESY 79/48.

[63] J. Grosse-Knetter, *Energy Correction for Islands* (unpublished). ZEUS-98-031; J. Grosse-Knetter, *Corrections for the Hadronic Final State* (unpublished). ZEUS-98-031, internal ZEUS-note, 1998.

[64] J. Grosse-Knetter. Minutes of ZEUS-SFEW group meeting, 7th of September 1999.

[65] K. Nagano, *Measurement of Charged-Current Deep Inelastic Scattering Cross Sections at* $\sqrt{s} = 300\ GeV$. Ph.D. Thesis, University of Tokyo, 1999. KEK Report 99-11.

[66] A. Kruse, *Charged Current interactions at HERA*. Ph.D. Thesis, Amsterdam University, 1999.

[67] K. Nagano. Minutes of ZEUS-SFEW group meeting, 12th of December 1997.

[68] R. Sinkus and T. Voss, Nucl. Inst. Meth. **A 391**, 360 (1997).

[69] H. Jung, Comp. Phys. Comm. **86**, 147 (1995).

[70] W. Hollik et al., *Proc. Workshop on Physics at HERA*, W. Buchmüller and G. Ingelman (eds.), Vol. 2, p. 923. Hamburg, Germany, DESY (1991).

[71] Kuze, Masahiro and Sirois, Yves, Prog. Part. Nucl. Phys. **50**, 1 (2003).

Acknowledgments

An dieser Stelle möchte ich allen Menschen danken, die zu diesem Werk beigetragen haben.

An erster Stelle gilt mein Dank meinem Doktorvater Erwin Hilger. Seine Betreuung war stets auf das optimale Weiterkommen meiner Forschung und meiner selbst ausgerichtet, ohne persönliche Freiheiten zu verunmöglichen. Ich hatte nie einen Grund, an seiner Unterstützung zu zweifeln, auch in schweren Zeiten.

Wichtiger Bestandteil dieser Arbeit war das tägliche Leben in der Zeus-Cal-Bonn Gruppe, welches während meiner Zeit in der Gruppe im Wesentlichen, aber nicht ausschließlich, von Jim Crittenden, Uli Katz, Robert Kerger, Alexander Kappes, Ainas Weber, Detlef Bartsch, Meng Wang und der Saeco-Café-Maschiene geprägt war. Das Arbeiten in der Gruppe wurde, nicht nur von den genannten Personen, um vielfach hilfreiche, interessante, intelligente, genüßliche oder amüsante Diskussionen, Anreize, Überlegungen im Bereich der Hochenergiephysik, der Physik im allgemeinen aber auch zu Themen des Allags bereichert. Die Gruppenmitglieder standen mir auf ihre Weise immer mit Rat und Tat zur Seite.

Connected with my membership to the ZEUS Collaboration i had many duties, but also a lot of pleasures. I enjoyed working together in changing teams of people with different cultural background in physics groups, special tasks groups, when beeing on data-taking shifts and everywhere else. This reseach would not have been possible without all the people that contributed to the building and maintaining of the detector components and took part in the collection of the data.

I had the pleasure to work closely with Sjors Grijpink and Alex Tapper under the coordination of Ken Long, to achieve the research results towards publication for the collaboration.

Meine Familie hatte einen großen Anteil an meinem Schaffen, wahrscheinlich mehr als sie wahrgenommen hat. Der Versuch, Wissenschaft und Familie zu vereinen, ist nicht trivial. Der Erfolg der einen Hälfte dieses Versuches kann an diesem Werk bemessen werden.